

# Resonant Inelastic X-ray Scattering Studies of Low-Dimensional and Frustrated 3d Transition-Metal Oxides

Présentée le 9 avril 2021

Faculté des sciences de base  
Laboratoire de magnétisme quantique  
Programme doctoral en physique

pour l'obtention du grade de Docteur ès Sciences

par

## Yi TSENG

Acceptée sur proposition du jury

Prof. P. Ricci, président du jury  
Prof. H. M. Rønnow, Dr T. Schmitt, directeurs de thèse  
Prof. J. Chang, rapporteur  
Prof. Ph. Werner, rapporteur  
Prof. M. Grioni, rapporteur

# Acknowledgements

I would like to start by thanking my main thesis supervisor Thorsten Schmitt, who provided guidance for me to learn in his “Spectroscopy of Novel Materials Group” (SNM group) at PSI, while leaving me flexibility to develop my own ideas. His patience and trust in both scientific and personal sides have carried me through my PhD studies. I must also thank my supervisor Henrik Rønnow at LQM, EPFL, who introduced thriving research environments and opportunities to me. The motivation and dedication of both of my supervisors to research, as well as their focus on details, have been inspiring.

I would like to thank Paolo Ricci and Phillip Werner who accepted to be my jury committee, as well as Johan Chang, who also motivated me through several collaboration works and insightful discussions, and Marco Grioni for encouraging me to pursue a scientific career overseas during our first meeting in Taiwan.

For preparing me as an experimental physicist in terms of hands-on practical works, scientific understanding, and the capability to initiate and manage research projects, I would like to acknowledge all the people that worked with me at the RIXS endstation of ADRESS beamline, SLS: Eugenio, Wenliang, Teguh, Daniel, and Marcus. We have spent most of our time together at the beamline in the last few years, and I really appreciate the learning and life lessons from you all. Special thanks are attributed to our technicians, Leo, Andy, and Fritz, and the system controlling engineer Xiaoqiang, for maintaining the beamline operation at regular basis. In the SNM group, I would like to thank: Milan, Vladimir, Marco, Eduardo, Jasmine, Ming, Mengyu, Muntaser, Tianlu, Junzhang, Alla, Mauro, Nick, Hugo, Sandy, Nan, Hang, Haijiang, Stefan, Arian, Niels, Juraj, Wojciech, and Andrew.

It would have not been possible to carry out the work presented in this thesis without support from several groups outside SNM, to which I am greatly indebted. I must thank Steven Johnston and Jinu Thomas from University of Tennessee; Alberto Nocera from University of British Columbia; Umesh Kumar from Los Alamos National Laboratory; and Kai Schmidt from Institute for Theoretical Physics at FAU Erlangen-Nürnberg, for providing theoretical insight to interpret my experimental results. I would also like to thank the people who kindly provided their samples for my experiments: Surjeet Singh and Rabindranath Bag from Indian Institute of Science Education and Research; Ekaterina Pomjakushina and Pascal Puphal from Laboratory for Multiscale Materials Experiments at PSI; Guochu Deng from Australian Centre for Neutron Scattering at Australian Nuclear Science and Technology Organisation; Raman Sankar from Institute of Physics at Academia Sinica (Nankang, Taiwan); and Fang-Cheng Chou from National Taiwan University. I would like to thank the whole LQM group for welcoming me during my visits to EPFL. In particular, I would like to thank Luc Testa and Virgile Favre for helping me at different stages.

I was fortunate to be surrounded by users and collaborators all over the world to learn from during my PhD studies, and I would like to express my gratitude to work with all of them at the ADRESS beamline. I have also benefited from the opportunities to join experiments at numerous facilities outside Switzerland, and I want to thank all people that helped us during those beamtimes. Particularly, I would like to thank Valentina Bisogni and Jonathan Pellciari for stimulating discussions on my thesis results.

Lastly, I would like to thank all my friends and family in Taiwan, particularly my parents, for encouraging and supporting me throughout these years, as this process was never easy. Special thanks are given to my former landlord Abdelouahab Dehbi and his family, as well as my current landlord Eyke Wagner and his late wife Marianne, who have treated me as their own family member.

Taiwan, 17.01.2021



# Abstract

3d transition-metal oxide materials with strong electron correlations and low dimensionality give rise to emerging exotic phases. Resonant inelastic X-ray scattering (RIXS) has developed as a powerful spectroscopic tool for probing the collective excitations in such correlated materials. The RIXS technique provides an ideal approach for assessing electronic instabilities in condensed matter. This thesis comprises the experimental RIXS response of the spin chain-ladder cuprates  $\text{Sr}_{14-x}\text{Ca}_x(\text{Cu}_{1-y}\text{Co}_y)_{24}\text{O}_{41}$  and the (frustrated) honeycomb nickelate  $\text{Na}_2\text{Ni}_2\text{TeO}_6$ .

The spin and charge excitations of  $\text{Sr}_{14-x}\text{Ca}_x\text{Cu}_{24}\text{O}_{41}$  ( $x=0$  &  $12.2$ ) are studied by Cu  $L_3$ -edge RIXS. With increasing Ca content, a crossover from collective two-triplon excitations ( $x=0$ ) to a damped incoherent magnetic spectrum  $\sim 280$  meV ( $x=12.2$ ) in the ladders is uncovered from the RIXS spectra, dominated by spin-flip  $\Delta S=1$  scattering. With model calculations, the localized broad magnetic mode at  $x=12.2$  is shown to be a consequence of enhanced electronic localization. This is supported by polarization-dependent measurements, where the evaluated non-spin-flip  $\Delta S=0$  scattering is showing weight depletion below 1 eV. The RIXS spectral evolution suggests that a suppressed carrier mobility dominates the low-energy physics in the Ca-rich phases.

The low-energy excitations of  $\text{Sr}_{14}\text{Cu}_{24}\text{O}_{41}$  are also studied by O K-edge RIXS at the upper Hubbard band. The RIXS spectra show a sharp dispersing peak of similar energies to the  $\Delta S=1$  two-triplon excitations, and a broad non-dispersive mode at higher-energy. By comparing the experimental results to the existing theories of doped ladders, the observed spectral modes are attributed to interacting holon-spinon quasiparticles, with additional spectral contributions from the  $\Delta S=0$  multi-triplon bound states and continuum. These observations highlight the RIXS capability for resolving composite spin-charge quasiparticles and long-lived  $\Delta S=0$  magnetic excitations, which are difficult to detect by other experiments.

Charge order and phonon excitations for the two-leg ladders of  $\text{Sr}_{14}(\text{Cu}_{1-y}\text{Co}_y)_{24}\text{O}_{41}$  ( $y \leq 0.05$ ) are studied. At the ladder hole peak in O K-edge XAS signal, a concomitant elastic enhancement and phonon-softening is observed across all Co doping levels. The in-plane diffraction and phonon-softening response are found to enhance with increasing Co doping. Moreover, the observed diffraction signal is further characterized by energy- and temperature-dependent measurements. Lastly, given the strong electron-phonon coupling (EPC) observed in O K-edge RIXS spectra, the EPC strength can be analyzed from the RIXS intensity decay of the phonon overtones. The observed in-plane resonant diffraction and inelastic phonon response strongly suggest an enhanced stripe order via magnetic impurities, reminiscent of the reports in  $\text{CuO}_4$  plaquettes.

Electronic structure and EPC of the honeycomb nickelate  $\text{Na}_2\text{Ni}_2\text{TeO}_6$  are studied. Compared with current literature, the localized excitations (1-4.5 eV) in the Ni  $L_3$ -edge RIXS spectra are largely dominated by the crystal-field splitting of a  $\text{Ni}^{2+}$  ion in octahedral coordination. At the O K-edge, the large EPC  $\sim 285$  meV with 5-6 recognizable overtones (frequency of  $\sim 80$  meV) are revealed in the RIXS spectra. The observed modes provide a systematic characterization of charge, orbital and lattice dynamics for a newly proposed frustrated antiferromagnet.

This thesis has been carried out in a collaboration between the Paul Scherrer Institut and the Laboratory for Quantum Magnetism at EPFL.

## Keywords

Low-dimensional/frustrated 3d transition-metal oxides, cuprate ladders, honeycomb nickelates, resonant inelastic X-ray scattering, X-ray absorption spectroscopy, elementary excitations



# Résumé

Avec de fortes corrélations électroniques et une faible dimensionnalité, les phases exotiques et les excitations collectives dans les oxydes de métaux de transition 3d ont été largement explorées. La diffusion inélastique résonante de rayons X (RIXS en anglais) est devenue un puissant outil spectroscopique pour sonder les diverses dynamiques de faible énergie dans les matériaux corrélés. La technique RIXS offre une approche idéale pour évaluer les instabilités électroniques dans la matière condensée. Cette thèse contient l'étude expérimentale de données de RIXS sur les cuprates en chaîne/échelle de spin  $\text{Sr}_{14-x}\text{Ca}_x(\text{Cu}_{1-y}\text{Co}_y)_{24}\text{O}_{41}$  et le nickelate en nid d'abeille  $\text{Na}_2\text{Ni}_2\text{TeO}_6$ .

Les excitations de spin et de charge de  $\text{Sr}_{14-x}\text{Ca}_x\text{Cu}_{24}\text{O}_{41}$  ( $x=0$  et  $12.2$ ) sont étudiées par RIXS au seuil L3 du cuivre. Avec l'augmentation de la teneur en Ca, une transition des excitations collectives de deux-triplons ( $x=0$ ) vers un spectre magnétique incohérent amorti  $\sim 280$  meV ( $x=12.2$ ) est découvert à partir des spectres RIXS des chaînes de spin, dominés par la diffusion spin-flip  $\Delta S=1$ . D'après notre modélisation, le large mode magnétique, localisé à  $x=12.2$ , s'avère être la conséquence d'une localisation électronique accrue. Ceci est corroboré par des mesures en fonction de la polarisation, où la diffusion non-spin-flip ( $\Delta S=0$ ) montre une perte de poids en dessous de  $\Delta E=1$  eV. L'évolution spectrale du signal RIXS suggère qu'une mobilité atténuée des porteurs de charge domine la physique de basse énergie dans les phases riches en Ca.

Les excitations de basse énergie de  $\text{Sr}_{14}\text{Cu}_{24}\text{O}_{41}$  sont étudiées par RIXS au seuil K de l'oxygène, dans la bande de Hubbard supérieure. Les spectres RIXS montrent un pic de dispersion similaires aux excitations  $\Delta S=1$  à deux-triplons, ainsi qu'un mode large non dispersif à énergie supérieure. En comparant les résultats expérimentaux aux théories existantes sur les échelles de spin dopées, les modes spectraux observés sont attribués à des interactions holon-spinons, ainsi qu'à des contributions spectrales supplémentaires provenant des états liés à  $\Delta S=0$  et du continuum. Ces observations mettent en évidence la capacité de la diffusion inélastique résonante de rayons X à résoudre les quasi-particules composites à charge de spin et les excitations magnétiques  $\Delta S=0$  à durées de vie longues, difficilement détectables par des méthodes conventionnelles.

L'ordre de charge et les excitations de phonon dans les échelles de spin  $\text{Sr}_{14}(\text{Cu}_{1-y}\text{Co}_y)_{24}\text{O}_{41}$  ( $y \leq 0.05$ ) sont étudiés. Au sommet du seuil d'absorption K de l'oxygène, dans le signal de spectrométrie d'absorption rayons X, un sursaut du signal élastique et un adoucissement concomitant du phonon sont observés à toutes les valeurs de dopage en Co. La diffraction dans le plan et la diminution de l'intensité du phonon s'avèrent accentuées par l'augmentation du dopage en Co. De plus, le signal de diffraction observé est caractérisé par des mesures en fonction de l'énergie et de la température. Enfin, étant donné le couplage électron-phonon (CEP) fort dans les spectres RIXS, la force du CEP peut être analysée à partir de la décroissance de l'intensité des harmoniques phononiques dans les données RIXS. La diffraction résonnante observée dans le plan et la réponse phononique inélastique suggèrent fortement un ordre de bande amélioré via des impuretés magnétiques, rappelant les constatations faites sur les plaquettes de  $\text{CuO}_4$ .

La structure électronique et le CEP du nickelate en nid d'abeille  $\text{Na}_2\text{Ni}_2\text{TeO}_6$  sont étudiés. Par rapport à la littérature actuelle, les excitations localisées (1-4.5 eV) dans les résultats RIXS au seuil L3 du Nickel sont largement dominées par une levée de dégénérescence dû à l'application d'un champ cristallin sur un ion  $\text{Ni}^{2+}$  dans une symétrie octaédrique. Au seuil K de l'oxygène, le grand CEP  $\sim 285$  meV et ses 5~6 reconnaissables harmoniques sont révélés dans les spectres RIXS. Les modes observés permettent une caractérisation systématique de la dynamique d'un nouvel antiferroaimant frustré.

Cette thèse a été réalisée en collaboration entre l'Institut Paul Scherrer et le Laboratoire de magnétisme quantique de l'EPFL.

## Mots-clés

Oxydes de métaux de transition 3d de faible dimension/frustrés, cuprate à échelles de spin, nickelates en nid d'abeille, diffusion inélastique résonante de rayons X, Spectrométrie d'absorption des rayons X, excitations élémentaires.

# Contents

<b>Acknowledgements</b> .....	<b>i</b>
<b>Abstract</b> .....	<b>iii</b>
<b>Keywords</b> .....	<b>iii</b>
<b>Résumé</b> .....	<b>iv</b>
<b>Mots-clés</b> .....	<b>iv</b>
<b>List of Figures</b> .....	<b>viii</b>
<b>List of Tables</b> .....	<b>xvi</b>
<b>List of Equations</b> .....	<b>xvii</b>
<b>Chapter 1 Introduction</b> .....	<b>1</b>
<b>Chapter 2 Resonant soft X-ray spectroscopy</b> .....	<b>7</b>
2.1 X-ray Absorption Spectroscopy .....	7
2.1.1 Principles of XAS process.....	7
2.1.2 Total fluorescence yield .....	8
2.1.3 Total electron yield .....	9
2.2 Resonant Inelastic X-ray Scattering .....	9
2.2.1 Principles of RIXS process.....	9
2.2.2 RIXS cross section .....	10
2.3 Synchrotron Radiation and Insertion Devices.....	13
2.4 RIXS Endstation at ADRESS Beamline, Swiss Light Source .....	15
2.5 3d Transition-Metal L-edge RIXS.....	17
2.5.1 Polarization-dependent RIXS: Disentanglement between $\Delta S=1$ and $\Delta S=0$ scattering channels .....	19
2.6 Oxygen K-edge RIXS .....	21
2.6.1 Phonon excitations probed by RIXS: Evaluation of electron-phonon coupling .....	22
2.6.2 Energy-resolved quasi-elastic scattering probed by RIXS: Charge density wave order .....	25
2.7 Self-Absorption Correction for the RIXS Spectra .....	26
<b>Chapter 3 Crossover of the high-energy spin fluctuations from collective triplons to localized magnetic excitations in doped <math>\text{Sr}_{14-x}\text{Ca}_x\text{Cu}_{24}\text{O}_{41}</math></b> .....	<b>29</b>
3.1 Project Contribution .....	29
3.2 Preamble .....	29
3.3 Abstract .....	32
3.4 Introduction.....	32
3.5 Experimental Method.....	34
3.6 Results and Discussions .....	34
3.7 Conclusion .....	43
3.8 Acknowledgement.....	44
<b>Chapter 4 Spectroscopic fingerprint for holon-spinon and spin-singlet multi-triplon excitations in the hole-doped ladders of <math>\text{Sr}_{14}\text{Cu}_{24}\text{O}_{41}</math></b> .....	<b>45</b>

4.1	Project Contribution .....	45
4.2	Preamble .....	45
4.3	Abstract .....	49
4.4	Introduction.....	49
4.5	Experimental Method.....	50
4.6	Results and Discussions .....	51
4.6.1	$\Delta S=0$ spin-conserving excitation modes and O K-edge UHB RIXS processes.....	51
4.6.2	O K-edge RIXS spectra with comparison to Cu $L_3$ -edge RIXS results .....	52
4.6.3	Experimental interpretation with holon-spinon and $\Delta S=0$ multi-triplon excitations .....	53
4.6.4	Spectral fingerprint of holon-spinons and $\Delta S=0$ 2T bound state with overlapping energies: Comparison to theories.....	54
4.7	Conclusion .....	58
4.8	Acknowledgement.....	58
<b>Chapter 5</b>	<b>Enhanced charge-stripe order with magnetic impurities in the chain-ladder cuprates <math>\text{Sr}_{14}(\text{Cu}_{1-x}\text{Co}_x)_{24}\text{O}_{41}</math></b>	<b>59</b>
5.1	Projection Contribution .....	59
5.2	Preamble .....	59
5.3	Abstract .....	62
5.4	Introduction.....	63
5.5	Experimental Method.....	64
5.6	Results and Discussions .....	64
5.6.1	Energy-Resolved REXS and RIXS probed: CDW order and phonon excitations .....	64
5.6.2	O K-edge Energy-Resolved REXS: Change of ladder CDW with Co-doping .....	66
5.6.3	Charge order pinning by magnetic impurities? .....	68
5.6.4	Cooperating or competing mechanism of CDW with different spatial and magnetic correlations? .	70
5.6.5	Evaluation of CDW profiles according to co-existent charge order and charge density fluctuations .	71
5.6.6	O K-edge RIXS spectra: Phonon excitations vs. Co-doping.....	72
5.6.7	Evaluation of EPC .....	74
5.6.8	Cu $L_3$ -edge energy-resolved REXS and RIXS results .....	74
5.6.9	Co $L_3$ -edge energy-resolved REXS and RIXS results .....	75
5.7	Conclusion .....	76
5.8	Acknowledgement.....	76
<b>Chapter 6</b>	<b>Electronic structure and electron-phonon coupling of the layered honeycomb nickelate <math>\text{Na}_2\text{Ni}_2\text{TeO}_6</math></b>	<b>81</b>
6.1	Projection Contribution .....	81
6.2	Preamble .....	81
6.3	Abstract .....	83
6.4	Introduction.....	84
6.5	Experimental Method.....	85
6.6	Results and Discussions .....	85
6.7	Conclusion .....	91

6.8	Acknowledgement.....	92
<b>Chapter 7</b>	<b>Conclusion .....</b>	<b>93</b>
7.1	Achieved Results.....	93
7.2	Future Development.....	95
7.2.1	Extended research.....	95
7.2.2	Quantum spin liquid and Majorana excitations .....	96
7.2.3	Further insight into electron-phonon coupling .....	97
<b>References</b>	<b>99</b>	
<b>Curriculum Vitae .....</b>		<b>111</b>

# List of Figures

Figure 1:1 The structural model for hybrid chain-ladder cuprates  $(\text{Sr,Ca,La})_{14}\text{Cu}_{24}\text{O}_{41}$  from ref. [16] (Reprinted by permission from Elsevier publishing group, Journal of Crystal Growth, Bag R., Karmakar K., and Singh S., 458, 16-26, 2017). The materials are composed of alternating edge-sharing  $\text{CuO}_2$  chain layers, two-leg  $\text{Cu}_2\text{O}_3$  ladder layers, and non-magnetic (Sr,Ca,La) atoms. The chain (ladder) subsystem features a Cu-O-Cu bond angle of  $90^\circ$  ( $180^\circ$ ), leading to the magnetic exchange coupling of  $\sim 10$  ( $\sim 100$ ) meV [17]. 2

Figure 1:2 Two-triplon (2T) magnetic excitations of  $\text{Sr}_{14}\text{Cu}_{24}\text{O}_{41}$  probed by Cu  $L_3$ -edge RIXS from ref. [13]. The full momentum-dependent inelastic spectra with a dispersing downturn at zone center, representing the 2T band bottom, are shown in (a). The spectral line fitting in (b) demonstrated a sizable quasi-elastic spectral weight beyond the elastic scattering near the zone center. [Reprinted figure with permission from: J. Schlappa et al., Physical Review Letters, 103, 047401 (2009). Copyright (2009) by the American Physical Society. (<https://doi.org/10.1103/PhysRevLett.103.047401>)] .....2

Figure 1:3 O K- and Cu L-edge resonant elastic X-ray scattering (REXS) study on the (ladder) charge order formation observed in  $\text{Sr}_{14}\text{Cu}_{24}\text{O}_{41}$  from ref. [18]. A commensurate electronic reflection  $\sim 0.2$  (rlu) along the ladder-leg direction was inferred at both O K- and Cu  $L_3$ -edge XAS resonances (Reprinted by permission from Springer Nature publishing group, Nature, Abbamonte P. et al., 431, 1078-1081, 2004). .....3

Figure 2:1 Schematics for X-ray absorption and the two major processes for detection, the fluorescence from X-ray emission and electron yield mainly contributed from Auger processes. The photoelectric transitions (red arrows) from core-level to the unoccupied valence shell (Fermi level labelled by dot-dashed black lines) upon soft X-ray absorption is indicated on the left. The electrons with less energies than the photo-excited electrons (green circles) then annihilate the unstable core-hole to relax the system, which release electromagnetic radiation that correspond to the fluorescence emission. The measured materials can also release energy by allowing electron escape while the lower-energy shells can undergo photoelectric de-excitations to fill the core-hole, and this is connected to the electron yield .....8

Figure 2:2 Schematics for (a) direct and (b) indirect RIXS processes. ....9

Figure 2:3 Schematics for a prototypical synchrotron radiation source from ref. [48]. (Reprinted by permission from John Wiley and Sons, Elements of Modern X-ray Physics 2<sup>nd</sup> edition, Jens Als-Nielsen and Des McMorrow, 2<sup>nd</sup> edition, 2011) .....13

Figure 2:4 Schematics of the collimated radiation released by relativistic accelerated electrons from ref. [48]. (Reprinted by permission from John Wiley and Sons, Elements of Modern X-ray Physics 2<sup>nd</sup> edition, Jens Als-Nielsen and Des McMorrow, 2<sup>nd</sup> edition, 2011) .....14

Figure 2:5 Schematics for (a) undulator and (b) wiggler insertion devices from ref. [48]. (Reprinted by permission from John Wiley and Sons, Elements of Modern X-ray Physics 2<sup>nd</sup> edition, Jens Als-Nielsen and Des McMorrow, 2<sup>nd</sup> edition, 2011) .....14

Figure 2:6 ADDRESS beamline. ....15

Figure 2:7 Schematics of the optical layout of ADDRESS beamline from ref. [54]. [Open access for the reprint of figure available from: Wiley-Blackwell on behalf of the International Union of Crystallography, Journal of Synchrotron Radiation, V. N. Strocov et al., 17, 631–643, 2010 (<https://doi.org/10.1107/S0909049510019862>)] .....15

Figure 2:8 Schematics for the optical elements of SAXES at ADDRESS beamline from ref. [55]. [Open access for the reprint of figure available from: Wiley-Blackwell on behalf of the International Union of Crystallography, Journal of Synchrotron Radiation, V. N. Strocov et al., 18, 134–142, 2011 (<https://doi.org/10.1107/S0909049510054452>)] .....16

Figure 2:9 Energy dependent Cu  $L_3$ -edge RIXS spectra of  $\text{Sr}_2\text{CuO}_3$  modified from ref. [59]. RIXS spectrum taken at  $q_a = 0.189$  (rlu) is highlighted. Low-energy magnetic, inter-orbital crystal field and charge transfer excitations are shown. The local excitations around 1.85, 2.36 and 2.98 eV correspond to the states for xy, xz/yz, and  $3z^2-r^2$  orbitals (Reprinted by permission from Springer Nature publishing group, Nature, Schlappa J. et al., 485, 82-85, 2012). .....18

Figure 2:10 Schematics for the  $\Delta S=1$  single SF magnetic excitations and the inter-orbital transitions during the Cu  $L_3$ -edge RIXS processes in a square-planar copper oxide environment. (Left) A finite cross section of the  $\Delta S=1$  process is allowed due to the strong SOC for the 2p core levels, while the transitions between the crystal field splitting of Cu 3d shells are direct RIXS processes at the Cu  $L_3$ -edge. .... 18

Figure 2:11 Left:  $\Delta S=1$  two-spinon continuum excitations of  $\text{Sr}_2\text{CuO}_3$  probed by Cu  $L_3$ -edge RIXS modified from ref. [59] (Reprinted by permission from Springer Nature publishing group, Nature, Schlappa J. et al., 485, 82-85, 2012). .... 19

Figure 2:12 Schematics of single and double SF magnetic excitations with different timescales modified from ref. [60]. This was previously revealed by a polarization-dependent Cu  $L_3$ -edge RIXS study on the two-spinon continuum excitations in weakly-interacting two-leg ladders  $\text{CaCu}_2\text{O}_3$  [60]. [Reprinted figure with permission from: V. Bisogni et al., Physical Review Letters, 112, 147401 (2014). Copyright (2014) by the American Physical Society. (<https://doi.org/10.1103/PhysRevLett.112.147401>)] ..... 20

Figure 2:13 Overview of O K-edge RIXS spectra on (a) 2D  $\text{Sr}_2\text{CuO}_2\text{Cl}_2$  from ref. [69] and (b) q-1D cuprates  $\text{Li}_2\text{CuO}_2$  and  $\text{CuGeO}_3$  from ref. [70], respectively. The high-energy excitation spectrum above  $\sim 4.5$  eV are dominated by fluorescence signal. The spectral mode  $\sim 3.7$ -4 eV in  $\text{Li}_2\text{CuO}_2$  and  $\text{CuGeO}_3$  were identified as exciton derived from ZRS. [Reprinted figures with permission from: Y. Harada et al., Physical Review B, 66, 165104 (2002). Copyright (2002) by the American Physical Society. (<https://doi.org/10.1103/PhysRevB.66.165104>); C. Monney et al., Physical Review Letters, 110, 087403 (2013). Copyright (2013) by the American Physical Society. (<https://doi.org/10.1103/PhysRevLett.110.087403>)] 21

Figure 2:14 Bimagnon continuum excitations in  $\text{La}_2\text{CuO}_4$  revealed by O K-edge RIXS from ref. [74]. (a)-(b) show the O K-edge XAS and RIXS spectra taken at selected incident X-ray energies, Eu1 and Eu2 here. The blue curves in (b) are smoothing data indicated as a guide-to-eye. (c)-(f) are the momentum- and polarization-dependent RIXS spectra taken at Eu1 along  $(\pi,0)$  and  $(\pi,\pi)$ , with grazing incidence scattering geometry and a scattering angle of  $130^\circ$ . The  $\Delta S=0$  bimagnon continuum shows generally flat dispersions and enhanced with  $\sigma$  polarization. The fitted peak positions along  $(\pi,0)$  and  $(\pi,\pi)$  for the observed  $\Delta S=0$  bimagnon continuum are shown in (g) and (h), respectively [Reprinted figure with permission from: V. Bisogni et al., Physical Review B, 85, 214527 (2012). Copyright (2012) by the American Physical Society. (<https://doi.org/10.1103/PhysRevB.85.214527>)] ..... 22

Figure 2:15 Evaluated EPC for the phonon excitations in  $\text{Li}_2\text{IrO}_3$  probed by O K-edge RIXS from ref. [79]. (a) Fitting for the EPC based on local Einstein phonon modes from ref. [78]. The EPC constant  $g$  and phonon self-energy  $M_0$  are assessed by the decay of high-order phonon overtones. (b) Evaluated  $M_0$  as a function of momentum. (c) Evaluated phonon energies for the harmonic profiles. For the high-order overtones, the deviation from ideal harmonic oscillator for may be derived from the anharmonic effects in the measured materials or contribution of EPC based on other phonon modes. [Reprinted figure with permission from: J. G. Vale et al., Physical Review B, 100, 224303 (2019). Copyright (2019) by the American Physical Society. (<https://doi.org/10.1103/PhysRevB.100.224303>)] ..... 24

Figure 2:16 Cu  $L_3$ -edge RIXS study on the CDW orders and phonon excitations for the SC cuprates  $\text{Bi}_2\text{Sr}_2\text{CaCu}_2\text{O}_{8+x}$  modified from ref. [83]. (From left to right) (a) Energy-resolved elastic and inelastic RIXS spectra as function of momentum. (b) Selected RIXS spectra across the CDW ordering  $\sim 0.3$  rlu along  $(\pi,0)$  with separated elastic scattering and phonons. (c) Quasi-elastic intensity as a function of momentum, with enhanced in-plane diffraction  $\sim 0.3$  rlu. (d) Fitting example for elastic scattering and phonon excitations with a linear background. (e) The fitted phonon energies and widths as function of momentum, showing the phonon softening and broadening in vicinity to CDW ordering (Reprinted by permission from Springer Nature publishing group, Nature Physics, Chaix L. et al., 13, 952-956, 2017). .... 26

Figure 2:17 Illustration for the required parameters when evaluating self-absorption corrections in a given RIXS experimental geometry. .... 27

Figure 3:1  $\Delta S=1$  paramagnon in 2D cuprate  $\text{La}_{2-x}(\text{Ba},\text{Sr})_x\text{CuO}_4$  probed by (a) INS from ref. [95] [Reprinted figure with permission from: S. Wakimoto et al., Physical Review Letters, 98, 247003 (2007). Copyright (2007) by the American Physical Society. (<https://doi.org/10.1103/PhysRevLett.98.247003>)], and (b) Cu  $L_3$ -edge RIXS from ref. [96] (Reprinted by permission from Springer Nature publishing group, Nature Materials, Dean M. D. M. et al., 12, 1019-1023, 2013). .... 30

Figure 3:2 INS measurements for the 1T gap around  $\mathbf{q}=(q_{\text{Leg}}=0.5, q_{\text{Rung}}=0.5)$  of SCCO with (a)  $x=0$  from ref. [17], (b)  $x=11.5$  from ref. [104], and (c)  $x=12.2$  from ref. [105]. From these studies, the 1T excitation energy of SCCO

shows marginal Ca-doping dependence at  $\mathbf{q}=(q_{\text{Leg}}=0.5, q_{\text{Rung}}=0.5)$ , where a spin gap  $\sim 32$  meV persists up to  $x \sim 11-12$ . [Reprinted figures with permission from: R. Eccleston et al., Physical Review Letters, 81, 1702 (1998). Copyright (1998) by the American Physical Society. (<https://doi.org/10.1103/PhysRevLett.81.1702>); S. Katano et al., Physical Review Letters, 82, 636 (1998). Copyright (1998) by the American Physical Society. (<https://doi.org/10.1103/PhysRevLett.82.636>); G. Deng et al., Physical Review B, 88, 014504 (2013). Copyright (2013) by the American Physical Society. (<https://doi.org/10.1103/PhysRevB.88.014504>)]. ..... 31

Figure 3:3 NMR measurements for the 1T gap, Knight shift and  $T_1$  in SCCO as a function of Ca content [106]. A decreasing 1T gap was observed with elevated Ca-doping [Reprinted figure with permission from: K. Magishi et al., Physical Review B, 57, 11533 (1998). Copyright (1998) by the American Physical Society. (<https://doi.org/10.1103/PhysRevB.57.11533>)]. ..... 31

Figure 3:4 Schematics of (a) RIXS experimental geometry with the orientation of the two-leg  $\text{Cu}_2\text{O}_3$  ladders in SCCO. The ladder-leg direction is along c-axis, with lattice constant  $c_{\text{Leg}} \sim 3.9$  Å. (b) Upper panel: Two-leg quantum spin ladders of local antiferromagnetic interactions along the ladder leg and rung, with spins (blue arrows) having equal probability pointing along any directions (for instance, the opposite one denoted as gray arrows). The rung-singlets (purple ellipses) interact through ladder-leg exchange coupling. Bottom panel:  $\Delta S=1$  triplon excitations (orange dashed-line ellipse) in two-leg ladders, consisting of a singlet-triplet excitation with two coherent domain walls (green arrows). (c) Main resonances of Cu  $L_3$ -edge XAS.  $3d^9$  white line is marked by the black dashed-line. (d) Cu  $L_3$ -edge RIXS spectra taken at  $3d^9$  peak of  $q_{\text{Leg}} = -0.31$  (rlu) in  $\sigma$  polarization. Here, a negative (positive) momentum-transfer indicates the RIXS data taken in grazing incidence (emission) geometry. .... 33

Figure 3:5 Cu  $L_3$ -edge RIXS spectra with spectral components taken at  $q_{\text{Leg}} = -0.31$  (rlu) for Sr14 and Sr1.8Ca12.2. From high- to low-energy we observe charge transfer, inter-orbital crystal-field splitting of Cu 3d shell (dd), magnetic excitations and elastic line. .... 34

Figure 3:6 Cu  $L_3$ -edge RIXS spectra with fitting components at selected momenta for (a) Sr14 and (b) Sr1.8Ca12.2. Around the 0 eV energy loss peak comprises the elastic (and diffuse) scattering (green solid lines) along with the quasi-elastic scattering (brown dash lines). 2T excitations of Sr14 are fitted with two Gaussians of one lower-energy sharp (red solid line with shaded-region) mode and a broad high-energy component (red dashed line). 2T profiles in Sr1.8Ca12.2 are fitted by a damped Lorentzian (blue solid line with shaded region). .... 36

Figure 3:7 Fitting results for the magnetic excitations in the Cu  $L_3$ -edge RIXS spectra for Sr14 (red circles) and Sr1.8Ca12.2 (blue squares). The fitted peak positions and widths are plotted in (a) and (b), respectively. 37

Figure 3:8 (a) and (b) shows the rung and ladder (leg) distances for various Ca doping values obtained from different sources (red squares: ref. [16]; green diamonds: ref. [125]; black circles: ref. [123]). (c) shows the rung ratio estimates for Sr1.8Ca12.2, obtained using the ladder rung distances for Sr14 given by two different references [16] and [125] and the procedure described in the text. .... 37

Figure 3:9 O K-edge XAS spectra with fitting components for (a)-(b) Sr14 and (c)-(d) Sr1.8Ca12.2. (e) Experimentally determined number of holes in the ladder subsystem of SCCO, with comparison to the present literature [97,99–103,124,127,128]. .... 38

Figure 3:10 Upper (lower) row panels show the experimental and numerical RIXS results with bicubic interpolation for Sr14 (Sr1.8Ca12.2). The elastic line in each of the experimental spectra is subtracted for clarity. (a) and (d): Momentum-dependent RIXS spectra for Sr14 and Sr1.8Ca12.2 in  $\sigma$  polarization after elastic line subtraction. (b) Calculated  $\Delta S = 1$  RIXS spectra on an undoped ladder cluster for Sr14. (c) and (e): Calculated  $\Delta S = 1$  RIXS spectra on doped ladder clusters with hole doping  $p$  close to the experimentally-determined values from O K-edge XAS results, which are about  $\sim 6\%$  and  $\sim 11\%$  for Sr14 and Sr1.8Ca12.2, respectively. The following set of parameters are applied for Sr14 (Sr1.8Ca12.2) on a  $32 \times 2$  site cluster with spectral convergence:  $t_{\text{Leg}}=340$  meV,  $U=8t$ , and  $r=0.85$  ( $t_{\text{Leg}}=300$  meV,  $U=9t$ , and  $r=1.1457$ ). (f) Calculated  $\Delta S = 1$  RIXS spectra for Sr1.8Ca12 on a  $16 \times 2$  site doped ladder cluster with an impurity potential  $V_{\text{imp}} = 0.5U$ . The same electronic parameters and hole doping applied in (e) are adapted. .... 40

Figure 3:11 (a) Dynamical spin and (b) modified charge structure factors for Sr14 calculated by DMRG. The electronic parameters are chosen as  $t_{\text{Leg}}=340$  meV,  $U=8t$ ,  $r=0.85$ ,  $\eta=0.1379t_{\text{Leg}}$ , and hole doping  $p=6.25\%$ . 41

Figure 3:12 (a)-(e) Dynamical spin and (f)-(j) modified charge structure factors calculated by DMRG for Sr1.8Ca12.2, with  $t_{\text{Leg}}=300$  meV,  $U=9t$ ,  $r=1.1457$ ,  $\eta=0.0.1583t_{\text{Leg}}$ , and hole doping  $p=12.5\%$ . (a) and (f) correspond to (16,17,20,28), (b) and (g) to (6,12,13,17), (c) and (h) to (1,12,24,31), and (d) and (i) to

(7,14,15,24). The averaged $S(\mathbf{q}, \omega+i\eta)$ and $\tilde{N}(\mathbf{q}, \omega+i\eta)$ of the four sets are shown in panel (e) and (j), respectively.....	41
Figure 3:13 RIXS spectra with $\Delta S=1$ (blue-shadowed) and $\Delta S=0$ (red line) channels disentangled for (a)-(b) Sr14 and (c)-(d) Sr1.8Ca12.2 taken at $q_{\text{Leg}} = 0.38$ rlu [(a) and (c)] and $q_{\text{Leg}} = 0.14$ rlu [(b) and (d)]. Experimental data shown here are taken with $\pi$ polarization in grazing emission geometry. ....	42
Figure 3:14 (a)-(d) Polarization-dependent Cu $L_3$ -edge RIXS spectra zoomed in around the low-energy excitations. Here the experimental data are normalized to the total spectral weight of dd excitations with respect to the theoretical cross sections. ....	43
Figure 4:1 (a) Four-spinon continuum excitations outside the Two-spinon continuum boundary in $\text{Sr}_2\text{CuO}_3$ probed by O K-edge RIXS from ref. [77], in comparison with the former Cu $L_3$ -edge RIXS results [59] shown in (b). The O K- and Cu $L_3$ -edge RIXS spectra taken at zone center are displayed in (c). (d) Calculated $\Delta S=0$ RIXS spectra using DMRG on a 22 site t-J chain with periodic boundary conditions. The RIXS intensity is calculated with the Kramers-Heisenberg formalism with core-hole lifetime effects considered. (e)-(f) The comparison between experimental and theoretical O K-edge RIXS response with $q=0.25$ and $q=0$ (rlu), respectively (Open access available at: Springer Nature publishing group, Nature Communications, Schlappa J. et al., 9, 5394, 2018).....	46
Figure 4:2 Schematics for (a) single $\Delta S=1$ processes in INS and (b) Cu $L_3$ -edge RIXS measurements denoted in the hole picture. The 2S and 4S continuum excitations via indirect double spin-flip processes by O K-edge RIXS are shown in (c) and (d), respectively, which are granted by the distinct core-hole potentials of Cu $2p_{3/2}$ and O $1s$ edges [77] (Open access available at: Springer Nature publishing group, Nature Communications, Schlappa J. et al., 9, 5394, 2018). ....	47
Figure 4:3 Calculated modified dynamical charge structure factor ( $\Delta S=0$ ) for undoped and 10% hole-doped t-J ladder $10 \times 2$ site clusters using ED [26]. For both the upper and lower panels, (a)-(f) and (g)-(l) represent the excitations at $q_{\text{Rung}}=0$ and $q_{\text{Rung}}=0.5$ , separately. The $r$ value corresponds to the ratio of the nearest-neighbour magnetic exchange between the rung and leg orientations ( $r=J_{\text{Rung}}/J_{\text{Leg}}$ ). Upper panel: The solid white lines in (a)-(c) indicate the $\Delta S=0$ 2T bound state from the strong to isotropic ( $r=1$ ) rung coupling regime. The solid (dotted) line segments in (d)-(f) and (j)-(l) mark the lower (upper) multi-spinon continuum boundary for the weak rung coupling regime. Lower panel: The white dashed lines in (a)-(c) and (g)-(i) represent the gapless and gapped holon-spinon excitations in the bonding and anti-bonding band from strong to isotropic coupling, respectively. The dotted white lines in (g)-(h) illustrate the boundary for 1T excitations. The solid white lines in (c)-(f) and (j)-(l) highlight the holon excitations when approaching the weak rung coupling limit [Reprinted figure with permission from: Umesh Kumar, Alberto Nocera, Elbio Dagotto, and Steven Johnston, Physical Review B, 99, 205134 (2019). Copyright (2019) by the American Physical Society. ( <a href="https://doi.org/10.1103/PhysRevB.99.205130">https://doi.org/10.1103/PhysRevB.99.205130</a> )].....	48
Figure 4:4 RIXS experimental geometry with the orientation of the two-leg $\text{Cu}_2\text{O}_3$ ladders in Sr14. The ladder-leg direction is along c-axis, with lattice constant $c \sim 3.93$ Å. Inter-site double SF ( $\Delta S=0$ ) and single SF ( $\Delta S=1$ ) processes are indicated by gray arrows in the schematics. ....	50
Figure 4:5 (a)-(c) Schematics for the two-triplon continuum, $\Delta S=0$ two-triplon bound state and holon-spinon excitations in a hole-doped two-leg ladder (from top to bottom, respectively). The ground state rung-singlets (purple ellipses with spin as blue/gray arrows, also see Figure 3:4) can excite into the interacting $S=1$ triplons (orange dashed-line ellipses with spin-triplets, with flipped spins marked as red arrows). This will result in either two delocalized triplons moving away from each other, forming the two-triplon continuum, or two bound triplons with a total spin $S=0, 1$ or $2$ . In this chapter, the $\Delta S=0$ two-triplon bound state (orange dashed-dotted-line square) is of focus given the O K-edge RIXS sensitivity. The formation of triplons do not require holes (pink filled circles). On the other hand, holon-spinon QPs emerge upon the dissociation of bound hole pairs. As the holes hop without spin-flips, the dissociation of hole pairs leave behind two holon-spinon QPs (magenta dashed-dotted-line square) with a total spin-singlet (magenta dashed-line ellipses). (d) O K-edge XAS spectra with UHB marked (black triangle). (e) Schematics of UHB RIXS processes. (ii) and (iii) show the inter-site electron hopping between the adjacent Cu $3d_{x^2-y^2}$ orbitals through the Cu-O-Cu superexchange. ....	51
Figure 4:6 (a) RIXS spectra taken Cu $3d^9$ and UHB resonances of a momentum-transfer $q_{\text{Leg}} = -0.215$ (rlu). (b) A zoom to the low-energy region, including the elastic line (E), phonons (P), MT and QP modes. (c) The corresponding spectral assignment for UHB RIXS spectra. (d) Momentum-dependent UHB RIXS in $\sigma$	



polarization with ( $q_{\text{Leg}}$ ,  $q_{\text{Rung}}$ ) labelled. Black triangles serve as a guide-to-eye for the dispersing sharp peak  $\sim 270$  meV, while the peak maximum at  $q_{\text{Leg}} = -0.215$  (rlu) is marked by a black dotted-line. The “negative” momentum-transfer here indicates that the RIXS spectra are recorded in grazing incidence geometry 53

Figure 4:7 Multi-peak fitting for the O K-edge UHB RIXS spectra at selected momentum-transfer points, where the holon-spinon QP (red shaded peak) is clearly separated from the optical phonons and the 2T continuum. .... 54

Figure 4:8 (a) Normalized momentum-dependent O K-edge RIXS in this work. (b) Cu  $L_3$ -edge RIXS results in ref. [150]. The experimental data are interpolated along  $q_{\text{Leg}}$  with bicubic approximation, and the elastic line is subtracted for clarity. .... 55

Figure 4:9 Fitted peak positions from O K-edge (this work) and Cu  $L_3$ -edge RIXS from chapter 3, overlaid with the energies of the calculated MT scattering densities using CUT ( $J_{\text{Leg}}=130$  meV and  $r=J_{\text{Rung}}/J_{\text{Leg}}=1$ ) modified from ref. [91]. Red (blue) vertical dotted lines indicate the momentum-transfer of  $10^\circ$  grazing incidence at the O  $1s$  (Cu  $2p_{3/2}$ ) edge, serving as references of the experimental kinematic limit of the reachable momentum-space. The orange dot-dashed curve shown from  $q_{\text{Leg}}=0$  to  $q_{\text{Leg}}=0.25$  (rlu) depicts the holon-spinon QPs with the energy dispersion  $\omega(q)=t_{\text{Rung}}(1-\cos(q_{\text{Leg}}c_{\text{Leg}}))$  with sizable  $J_{\text{Rung}}$  [29], where the dispersion branch is shown within the kinematic limit of O K-edge RIXS in this work. Here  $t_{\text{Rung}}$  is taken as 300 meV. The optical signal of  $\Delta S=0$  2T bound state for the hole-depleted ladders in  $\text{Ca}_{14-x}\text{La}_x\text{Cu}_{24}\text{O}_{41}$  from ref. [169] is mostly contributed by the van Hove singularity of 2T DOS weighted by its coupling with phonons, which are peaked at the zone boundary and the maximum of the energy dispersion for  $r \sim 1$  (green dashed circles). The calculated  $\Delta S=0$  2T bound state shows appreciable weight only for  $q_{\text{Leg}} \geq 0.2$  rlu. This momentum region belongs to where the  $\Delta S=0$  2T bound state (red dotted curve) has separated energies from the lower 2T continuum boundary (black solid curve), and therefore free from decaying into the 2T continuum. 56

Figure 4:10 Temperature-dependent O K-edge RIXS spectra taken with  $q_{\text{Leg}} = -0.215$  (rlu) at 20 K (blue) and 280 K (red). RIXS spectra are normalized to total integrated intensity (see caption of Figure 4:8) ..... 57

Figure 4:11 Calculated spectral density for the MT scattering in the  $\Delta S=0$  sector (the calculation data are provided with courtesy by Kai Phillip Schmidt). The rung-to-leg ratio of magnetic exchange  $r=0.8$  is close to the value estimated from the local structural distances ( $r \sim 0.85$  from ref. [26]). The effects of including a cyclic four-spin ring exchange, here defined by  $r_c=J_{\text{Ring}}/J_{\text{Rung}}$ , is taken into consideration with  $r_c=0$ , in the left panel and  $r_c=0.1$  in the right panel, respectively. The momentum- and energy-resolved spectral intensity is similar between the two panels with insignificant dependence on the inclusion of ring exchange. For comparing with the experimental O K-edge RIXS data in this chapter, a  $J_{\text{Rung}}$  value of  $\sim 120$  and 145 meV is taken for the left and right panels, respectively, which are compatible with the magnetic exchange couplings observed in  $\text{Sr}_{14}$  [26] ..... 57

Figure 5:1 The CDW ordering wavevectors  $q_{\text{CDW}}$  as a function of hole-doping  $p$  across a wide span of SC cuprates taken from ref. [23] (Permissions from Annual Reviews, Annu. Rev. Condens. Matter Phys., R. Comin and A. Damaschelli, 7, 369–405, 2016). Two major evolutions are highlighted in the plot. The  $q_{\text{CDW}}$  increase with elevated hole density for the momentum-space ordering type cuprates, coinciding with the La-based cuprates hosting charge-spin cooperative stripe orders. On the contrary, the Bi-, Hg- and Y-based multi-layer cuprates generally show an opposite trend, where the  $q_{\text{CDW}}$  decrease with increasing hole content and are referred to as the real-space ordering cuprates in ref. [23] ..... 60

Figure 5:2 (a) The SC transition temperature  $T_c$  as a function of hole doping in  $\text{La}_{2-x}\text{Sr}_x\text{Cu}_{0.99}\text{M}_{0.01}\text{O}_4$  ( $M=\text{Cu}$ ,  $\text{Ni}$ ,  $\text{Zn}$  and  $\text{Ga}$ ) from ref. [182]. (b)-(c) show  $T_c$  and the depolarization rate (asymmetry ratio) in  $\mu\text{SR}$  measurements as a function of hole-doping for Bi- and Y-based cuprates from ref. [182]. The latter can be translated to the measure of local magnetic field strength. Despite different units for the hole-doping for (b)-(c) compared to (a), a significant suppression of  $T_c$  can be inferred around the  $1/8$  hole-doping level with 1-3% of magnetic doping at the Cu sites for all the measured cuprates (Reprinted by permission from Elsevier publishing group, Physica C: Superconductivity, Koike Y. and Adachi T., 481, 115-124, 2012). .... 61

Figure 5:3 The incommensurate SDW and CDW orders observed in the Fe-doped LSCO using neutron diffraction obtained from ref. [202]. The CDW order observed along  $(0.2 \pm \epsilon, 0)$  with  $\epsilon=0.224 \pm 0.002$  is about twice of the SDW order revealed along  $(0.5 \pm \delta, 0)$  with  $\delta=0.115 \pm 0.003$ , while both orders melt with increasing temperature  $\sim 60$  K. This justifies that the enhanced incommensurate CDW and SDW orders that are absent in the Fe-free LSCO can be induced by magnetic impurity doping (Reprinted by permission from

Figure 5:4 (a)-(c) O K-edge XAS and RIXS spectra showing the probed resonance and the energy-resolved (quasi-) elastic signal. The O K-edge RIXS spectra are recorded at the ladder hole peak  $\sim 528.6$  eV (orange triangle). (d)-(f) Cu  $L_3$ -edge XAS and RIXS spectra showing the probed resonance and the energy-resolved (quasi-) elastic signal. The Cu  $L_3$ -edge RIXS spectra are recorded at the charge-transfer ligand band  $\sim 933$  eV (orange triangle). The chosen XAS resonances at O K- and Cu  $L_3$ -edge are in agreement with the previous REXS reports on SCCO [18,31]. Both measurements are performed with  $\pi$  polarization in the grazing incidence geometry. (b) and (e) reproduce the commensurate ladder CDW  $\sim 0.2$  (rlu) reported for  $x=0$  in ref. [18]. (c) and (f) show an enhanced elastic signal near  $q_{\text{Leg}} \sim 0.135$  (rlu) for  $x=0.03$ , where the diffraction signal is more pronounced at the O K-edge. .... 65

Figure 5:5 (a)-(d) Momentum-dependent O K-edge RIXS spectra revealing the enhanced elastic scattering at certain wavevectors (highlighted by thick solid lines) with optical phonons ( $\sim 65$  meV) across all Co doping levels. .... 65

Figure 5:6 (a) Momentum-dependent O K-edge RIXS measurements showing the in-plane elastic signal in the leg direction for different Co-doped samples. (b)-(c) Normalized O K-edge XAS spectra (see main text) and elastic intensity across the main XAS resonances, respectively, measured in the leg direction for all Co doping levels. The elastic intensities in (c) are recorded at the wavevectors where the elastic signal is maximized for each doping level as shown in (a), while the data are normalized to the integrated RIXS intensity from 10 eV loss to 1 eV gain. The elastic signal taken at the post-edge near UHB ( $\sim 529.3$  eV) is used as the normalization background for comparing the resonant profile of in-plane elastic scattering. .... 66

Figure 5:7 Electrical transport measurements without magnetic field on the single crystal  $\text{Sr}_{14}(\text{Cu}_{1-x}\text{Co}_x)_{24}\text{O}_{41}$  samples for  $x=0$  and  $x=0.05$  (data courtesy: Surjeet Singh and Rabindranath Bag). The horizontal axis represents the inverse of temperature multiplied by 1000, whereas the vertical axis is the resistivity normalized to room-temperature value expressed in the natural logarithmic scale. An overall increased metallicity is inferred with Co doping. .... 67

Figure 5:8 (a)-(d) Momentum-dependent O K-edge RIXS measurements for the in-plane rocking curves around the CDW wavevectors for all Co doping levels (see fitting schemes in section 5.6.2). The elastic intensities are normalized to the integrated RIXS spectral weight from 10 eV loss to 1 eV gain. (e) The evaluated ordering wavevectors (black circles) as a function of Co doping concentration. (f) The fitted CDW correlation lengths (red circles), maximum intensity (blue squares) and integrated intensity (black diamonds) for the ladder CDW as a function of Co doping concentration. The CDW signal is fitted by a Lorentzian function with a linear background. The horizontal lines in (e) represent the  $q_{\text{CDW}}$  obtained from the previous REXS studies on  $\text{Sr}_{14-y}\text{Ca}_y\text{Cu}_{24}\text{O}_{41}$ , where  $q_{\text{CDW}} \sim 0.2$  rlu for  $y=0$  (red dot-dashed) and  $q_{\text{CDW}} \sim 0.33$  rlu for  $y$  of  $10 \sim 12$  (blue dashed) [18,31]. .... 68

Figure 5:9 Magnetic susceptibility for  $\text{Sr}_{14}(\text{Cu}_{1-x}\text{Co}_x)_{24}\text{O}_{41}$  from ref [16], showing an enhanced Curie-Weiss weight in the low-temperature regime upon Co-doping (also see Figure 6 in ref. [213]). This indicates an increased magnetic moment from Co dopants that disrupts the isotropic spin-liquid ground state for the cuprate ladder subsystem, while the increased moment shows clear in-plane/out-of-plane anisotropy. (Reprinted by permission from Elsevier publishing group, Journal of Crystal Growth, Bag R., Karmakar K., and Singh S., 458, 16-26, 2017). .... 68

Figure 5:10 O K-edge RIXS measurements showing the ER-REXS signal around the elastic line for  $x=0.03$  taken at (a) 20 K and (b) 200 K. (c) The CDW rocking curves for  $x=0.03$  are displaying the in-plane resonant diffraction signal for a series of temperatures. The fitting scheme follows Figure 5:8. A linear background is fitted and subtracted from the data. (d)-(f) The fitted peak intensity, peak width and integrated intensity of area below the peak, respectively, for the CDW profiles as a function of temperature. .... 70

Figure 5:11 (a)-(b) CDW fitting with two Lorentzian functions for  $x=0.03$  in  $\text{Sr}_{14}(\text{Cu}_{1-x}\text{Co}_x)_{24}\text{O}_{41}$  taken at 20 K and 200 K, respectively. The fitting scheme is taken from the ref. [180]. Following ref. [180], the BP (red) is assumed to be the temperature-independent charge fluctuations, where the peak position and width are fixed for different temperatures. The SP (blue) is assigned to be the static charge order component that melts with increasing temperature, and its peak position is fixed for all temperatures. .... 72

Figure 5:12 (a)-(c) The fitted peak intensity, peak width and integrated intensity for the SP (red squares) compared to the fitting results with one Lorentzian function for the CDW signal shown in Figure 5:10. .... 72

Figure 5:13 (a)-(b) O K-edge RIXS spectral line fitting. The elastic scattering (purple dot-dashed lines) and the fundamental phonon around 65-70 meV (cyan dashed lines) are well described by two resolution-limited Gaussian functions. The higher-energy peak above 100 meV (cyan dotted lines) is damper than the lower-energy modes, which may originate in high-order multi-phonon scattering or other excitation modes. (c) Momentum-resolved phonon energy for all Co doping levels. .... 73

Figure 5:14 Line fitting for the elastic line and phonon excitations for  $\text{Sr}_{14}(\text{Cu}_{1-x}\text{Co}_x)_{24}\text{O}_{41}$  across all doping levels and momentum-transfer points. .... 77

Figure 5:15 Fitting results of the electron-phonon interactions from the observed phonon excitations in the RIXS spectra. (a) Representative fit for the experimental RIXS results taken for  $x=0.03$  with  $q_{\text{leg}}=0.094$  (r.l.u.). (b) The summary of momentum-resolved EPC as the phonon self-energy across all Co doping levels. The error bars are removed for visual clarity. (c)-(f) The fitted EPC around the CDW ordering vector for  $x=0, 0.01, 0.03$  and  $0.05$ , where the error bars are included. .... 78

Figure 5:16 (a)-(d) Energy-resolved elastic scattering in  $\text{Sr}_{14}(\text{Cu}_{1-x}\text{Co}_x)_{24}\text{O}_{41}$  ( $x=0$  and  $0.03$ ) probed by Cu  $L_3$ -edge RIXS at the  $3d^9$  ( $\sim 931$  eV) and  $3d^{10}L$  ( $\sim 933$  eV) resonances, respectively. (e) Momentum-dependent Cu  $L_3$ -edge RIXS measurements of the 2T magnetic excitations for  $x=0$  and  $x=0.03$ . .... 79

Figure 5:17 (a)-(b) Co L-edge XAS and RIXS measurements for  $x=0.03$ , where the RIXS intensity is plotted for varied incident X-ray energies across the Co  $L_3$ -edge in (b). Both measurements are taken in the grazing  $20^\circ$  incidence geometry. (c) Comparison between O K-edge (ladder hole peak for  $x \leq 0.05$ ) and Co  $L_3$ -edge RIXS spectra (the 3 main resonances labelled in (a) for  $x=0.03$ ). The Co-doping induced peak  $\sim 270$  meV is highlighted (black dashed line) in the O K-edge RIXS experimental data, matching the localized excitations observed in Co  $L_3$ -edge RIXS results. (d) Co  $L_3$ -edge ER-REXS signal for  $x=0.03$  at the 3 main resonances. .... 79

Figure 6:1 (a) Schematic of  $\text{A}(\text{B},\text{B}')\text{O}_3$  cubic in perovskites with (b) truncated projection along  $(111)_{\text{pc}}$  [234]. (c) Effective hexagonal environments along  $(111)_{\text{pc}}$  [Open access for the reprint of figure available from: Online Publikationen der Universität Stuttgart, Matthias Hepting, PhD dissertation, Ordering phenomena in nickelate heterostructures studied by elastic and inelastic photon scattering, 2016 (<http://dx.doi.org/10.18419/opus-8969>)]. .... 81

Figure 6:2 Ni  $L_3$ -edge RIXS spectra on  $\text{NdNiO}_3$  and calculated RIXS response for the Ni  $3d^8L$  ( $L$  is denoted for ligand hole) and  $3d^7$  ground state from ref. [239], respectively. The RIXS spectra are taken at  $3d^8$  electronic configuration, which is labelled as the A resonance in ref. [239] (Open access available at: Springer Nature publishing group, Nature Communications, Bisogni V. et al., 7, 13017, 2016). .... 82

Figure 6:3 O K-edge RIXS study on the phonon excitations of  $\text{Ca}_{2+5x}\text{Y}_{2-5x}\text{Cu}_5\text{O}_{10}$  showing the intertwined lattice, charge and spin degrees of freedom from ref. [154]. (a) The doping-dependent phonon population as a function of EPC strength for  $x=0$  and  $x=0.33$ , which was attributed to the lattice distortions for the O-Cu-O bonds that are sensitive to the charge carrier concentration. (b) The phonon softening for the Cu-O bond-stretching vibrational mode across the Neel temperature  $\sim 30$  K, suggesting the RIXS sensitivities to the rearranged electron-phonon interactions with respect to the magnetic transitions [Reprinted figure with permission from: W. S. Lee et al., Physical Review Letters, 110, 265502 (2013). Copyright (2013) by the American Physical Society. (<https://doi.org/10.1103/PhysRevLett.110.265502>)]. .... 83

Figure 6:4 Crystallographic structure of  $\text{Na}_2\text{Ni}_2\text{TeO}_6$  generated by VESTA [262]. The layers of  $\text{NiO}_6$  octahedra are highlighted with polyhedral surface (Ni: blue spheres; O: red spheres). Te atoms are labelled as clay-brown spheres, while the Na atomic layers are hidden for visible clarity for the  $\text{NiO}_6$  structures. .... 85

Figure 6:5 (a) Ni L-edge XAS spectra normalized at post-edge  $\sim 885$  eV with both  $\sigma$  and  $\pi$  polarization. (b) RIXS spectra taken at selected incident X-ray energies as marked in (a) with  $\sigma$  polarization. (c) A zoom to the local Raman-like excitations in the RIXS spectra measured with  $\sigma$  and  $\pi$  polarization, probed at the Ni  $L_3$ -edge XAS maximum ( $\sim 854$  eV, b resonance). .... 86

Figure 6:6 (a) Calculated local crystal field excitations for a  $\text{Ni}^{2+}$  ion with octahedral lattice environments from ref. [245] [Reprinted figure with permission from: F. M. F. de Groot, P. Kuiper, and G. A. Sawatzky, Physical Review B, 57, 14584 (1998). Copyright (1998) by the American Physical Society. (<https://doi.org/10.1103/PhysRevB.57.14584>)]. The crystal field splitting is taken as 1 eV, while the exchange field for the local spin-flips for the Ni ions is set to be 0.25 eV. The dot-dashed line across simulated RIXS spectra probed at different incident X-ray energies corresponds to the Ni  $L_3$ -edge XAS profiles. (b) Ni  $L_3$ -edge RIXS spectra taken for NiO and  $\text{NiCl}_2$  from ref. [246], where both compound possess octahedra crystal-field

environments for the $\text{Ni}^{2+}$ ions (Reprinted by permission from Springer Nature publishing group, The European Physical Journal - Special Topics, Ghiringhelli G. et al., 169, 199-205, 2009).....	87
Figure 6:7 (a) O K-edge XAS spectra normalized at post-edge $\sim 560$ eV with both $\sigma$ and $\pi$ polarization. (b) RIXS spectra taken at selected incident X-ray energies as marked in (a) with $\sigma$ polarization. The zoom to low-energy regime (below 1 eV loss) are shown in (c) measured with $\sigma$ and $\pi$ polarization. High-energy spectral modes (above 4 eV) are basically fluorescence-like charge excitations, whereas clear multi-phonon overtones for the optical vibrational mode $\sim 80$ meV are observed. ....	87
Figure 6:8 Momentum-dependent O K-edge RIXS measurements taken along the (a) (1, 1) and (b) (1, 0) high-symmetry orientations. The predominant RIXS response are weakly-dispersive multi-phonon excitations from the optical phonon modes, reminiscent of the molecular vibrational spectra. (c) Line fitting for the O K-edge RIXS spectrum taken at (0.148, 0.148) rlu. (d) Fitted phonon energy along the (1,1) orientation with two (filled purple squares) Gaussian functions as shown in (c) and one Gaussian function (open gray squares) to account for the quasi-elastic regime below $\sim 75$ meV loss. (e) Fit for the mode energy of the quasi-elastic component about 25 $\sim$ 35 meV (open brown circles, left axis) with two-component assignment for the elastic line. This is plotted with the peak width of elastic line when it is fitted with only one Gaussian function (open red diamonds, right axis). If the quasi-elastic regime is only fitted with one spectral component, a significant broadening for the elastic peak width of 15 $\sim$ 20% compared to the instrumental energy resolution $\sim 50$ meV (horizontal blue dotted line) is inferred. Alongside the underestimated phonon energy with one-component quasi-elastic fitting, the two-component assignment for the elastic line in (c) justifies a sizable spectral weight for the low-energy excitations between the elastic scattering and the predominant multi-phonon overtones. ....	88
Figure 6:9 (a)-(b) Momentum-resolved fitted peak positions for the fundamental frequency of optical phonon (filled purple squares) and the low-energy mode in the quasi-elastic regime (open brown circles). (c)-(d) Momentum-resolved integrated intensities for the fitted excitation modes. The symbols for notifying the phonon and low-energy excitations follow (a)-(b). (e)-(f) An-harmonicity defined as the deviation for multi-phonon overtones away from the expected energies for a simple harmonic oscillator, which are plotted as the function of momentum-transfer and the $v$ th-order of phonon harmonics. ....	89
Figure 6:10 Temperature-dependent O K-edge RIXS measurements along (h,0) orientation with (a) $\sigma$ and (b) $\pi$ polarization, respectively. Marginal spectral changes are inferred from the optical phonons $\sim 80$ meV, which is in agreement with the previous Raman experiments. ....	90
Figure 6:11 Analysis of EPC from the multi-phonon overtones observed for the oxygen vibrations. (a) illustrates the schematic fit at $\mathbf{q}=(0.06, 0.06)$ rlu, where the RIXS intensity for the multi-phonon scattering adopts the modelling in ref. [78]. (b)-(c) show the momentum-resolved phonon self-energy $M_0$ along (1,1) and (1,0) directions, respectively. ....	91
Figure 7:1 (a) RIXS experimental geometry for probing triplon excitations in the odd-parity scattering channel. The tilted orientation ensures a finite momentum-transfer along the ladder-rung direction (a-axis) for horizontally incident X-rays. (b) The Cu $L_3$ -edge RIXS measurements performed on $\text{Sr}_{14}\text{Cu}_{24}\text{O}_{41}$ taken with and without a rung tilt-angle, while the momentum-transfer along ladder-leg (c-axis) is fixed at $q_{\text{Leg}}=0.378$ (rlu). ....	95
Figure 7:2 Magnetic excitation spectra of an undoped two-leg ladder calculated as a function of the ratio of magnetic exchange between leg and rung orientations (modified from ref. [277]). The black solid lines highlight the boundaries of the multi-particle continuum that follow the formalism of interacting Marojana fermions, which emerge from the intermediate to weak coupling regime. (Note that here $x \equiv J_{\text{Leg}}/J_{\text{Rung}}$ , which is different with the definition of $r$ value in chapter 3 and 4). [Reprinted figure with permission from: D. Schmidiger et al., Physical Review B, 88, 094411 (2013). Copyright (2013) by the American Physical Society. ( <a href="http://dx.doi.org/10.1103/10.1103/PhysRevB.88.094411">http://dx.doi.org/10.1103/10.1103/PhysRevB.88.094411</a> )] ....	97
Figure 7:3 Energy-detuning Cu $L_3$ -edge RIXS measurements of the Cu-O bond-stretching phonon in the AFM $\text{Nd}_{1-x}\text{Ba}_x\text{Cu}_3\text{O}_{7-\delta}$ cuprate, modified from ref. [272]. (Left) The phonon intensity is monotonically suppressed with the detuning $\Omega$ of the incident photon energy towards the pre-edge of the Cu $L_3$ -edge XAS response. (Right) The dimensionless EPC constant $g$ is compared for a variety of extracted values based on the model from Ament et al. in ref. [78] with a Einstein phonon. [Open access for the reprinted figure is available from: L. Braicovich et al., Physical Review Research, 2, 023231 (2020). Copyright (2020) by the American Physical Society. ( <a href="http://dx.doi.org/10.1103/PhysRevResearch.2.023231">http://dx.doi.org/10.1103/PhysRevResearch.2.023231</a> )] ....	98

# List of Tables

Table 5:1 The hole densities in the chain and ladder subsystems evaluated from the O K-edge XAS results based on the model from ref. [99]. The unit p.c.f. indicates that the number is evaluated per chemical formula of  $\text{Sr}_{14}(\text{Cu,Co})_{24}\text{O}_{41}$ . .....67

Table 5:2 Structural lattice parameters for the single crystal samples of  $\text{Sr}_{14}(\text{Cu}_{1-x}\text{Co}_x)_{24}\text{O}_{41}$  obtained from ref. [16]. .....69

# List of Equations

Equation 2:1 Fermi's golden rule at the first order describing the photoelectric XAS process.....	7
Equation 2:2 Differential equation for the photon absorbed in an infinitely thin and uniform material. ....	7
Equation 2:3 Beer-Lambert law. ....	8
Equation 2:4 Fluorescence yield intensity. ....	9
Equation 2:5 Hamiltonian for light-matter interactions. ....	10
Equation 2:6 Fermi's Golden rule in second-order perturbation theory. ....	11
Equation 2:7 Perturbative term in the electron Hamiltonian with photon scattering.....	11
Equation 2:8 Second-order resonant scattering amplitude. ....	11
Equation 2:9 Kramers-Heisenberg equation for the RIXS cross section under dipole approximation. ....	11
Equation 2:10 The RIXS transition operator under dipole approximation.....	12
Equation 2:11 Polarization- and momentum-dependent RIXS intensity expressed as the multiplication between spin-resolved dynamical structure factors and form factors given by the scattering cross section. ....	20
Equation 2:12 Approximation of the RIXS scattering form factors in the single-ion picture. ....	20
Equation 2:13 A generic form of the Hamiltonian describing electron-phonon coupling with the fundamental frequency $\omega_0$ .....	22
Equation 2:14 Dipole operator in the scattering amplitude A. ....	22
Equation 2:15 RIXS amplitude for phonon intensity. ....	23
Equation 2:16 Hamiltonian for electron-phonon interactions of a single Einstein phonon with fundamental frequency $\omega_0$ .....	23
Equation 2:17 RIXS phonon amplitude for an Einstein oscillator.....	23
Equation 2:18 Franck-Condon overlap factors associated with the factorials based on multi-phonon scattering. ....	23
Equation 2:19 Generalized scattering amplitude for the RIXS intensity of dispersive phonons. ....	23
Equation 2:20 The first-order perturbative transition probabilities for the light-matter elastic scattering. ....	25
Equation 2:21 The second-order perturbative transition probabilities for the light-matter elastic scattering. ....	25
Equation 2:22 The fraction of absorbed intensity for the incoming X-rays traveling a total length L, which considers the self-absorption from the samples within an infinitesimal length dL. ....	26
Equation 2:23 The obtained RIXS intensity after including the self-absorption for both the incoming and outgoing X-rays. ....	26
Equation 2:24 The integrated RIXS intensity with self-absorption corrections. ....	27
Equation 3:1 Dynamical spin structure factor probed by RIXS. ....	37
Equation 3:2 Modified dynamical charge structure factor probed by RIXS. ....	37
Equation 7:1 RIXS intensity for considering a single Einstein phonon mode as a function of detuned-energy for the incident X-rays. ....	98



# Chapter 1 Introduction

Due to their strong electronic correlations, low-dimensional transition-metal oxides (TMOs) have been a focus in condensed matter physics with enduring interest for decades. Despite a simple low-dimensional geometry, their rich electronic phase diagrams have provided an ideal platform for examining theoretical models in solid-state physics. Based on this, their high flexibility and potential for tailoring functionalized materials have also introduced exciting opportunities for device applications. The underlying electronic correlations of these TMOs comprise the entangled spin, charge, orbital and lattice degrees of freedom (DOF), in the presence of low-dimensional crystallographic environments. In the enclosed thesis, these low-energy electronic instabilities are studied with X-ray spectroscopy. Resonant soft X-ray spectroscopies have been widely demonstrated to be extremely sensitive to charge and orbital DOFs. With the photo-electric transitions involving the core-level electrons and valence band, this enables an elemental sensitive probing of the electronic structure for a wide range of materials. Additionally, momentum- and energy-resolved resonant inelastic X-ray scattering (RIXS) has extended this by its unique spectral capability to resolve various elementary collective excitations, e.g. magnons and phonons, while the RIXS field is still developing rapidly in the recent years. Therefore, studies using RIXS have opened up exciting new opportunities in correlated TMOs that demand spectroscopic sensitivities beyond traditional experimental probes, giving rise to new fields that have yet to develop in fundamental research, as well as for future device applications. A brief overview for the RIXS technique and relevant experimental observations in TMOs will be addressed in chapter 2.

The thesis starts with the study focusing on the spin fluctuations in the low-dimensional antiferromagnetic (AFM) systems. Quantum magnetism is one of the intensively studied low-energy instabilities in low-dimensional correlated electronic materials. This was arising already from the early theoretical studies, which pointed out that the prototypical Heisenberg model is not sufficient to account for finite-range spin interactions in low-dimensionality (e.g. two- or one-dimensions, 2D or 1D) [1]. Conceptually, the thermally excited spin wave excitations essentially hinder the existence of long-range magnetic order in 2D or 1D systems [2]. The existing experimental literature deal with a large class of other low-dimensional magnetic materials with significantly reduced ordered moment at low-temperature, indicative of strong zero-temperature quantum spin fluctuations [2]. A potentially crucial role for the phonons is also proposed from the divergent thermal excitations and sound waves for 1D or 2D systems [1]. The microscopic modelling for describing these unconventional magnetic systems is beyond trivial and remains challenging nowadays. For TMOs, the magnetism is mediated by the strong Coulomb repulsion of the transition-metal (TM)  $d$  electrons, where an effective magnetic exchange emerges via the inter-orbital hopping (superexchange) [3,4]. This is the direct consequence of the strong orbital hybridization between the TM  $d$  orbitals and oxygen  $p$  orbitals, which can lead to magnetic exchange couplings as large as  $\sim 1000$  K observed in the layered copper oxides (cuprates) [5–7]. Accordingly, the magnetic fluctuations  $\sim 100$  meV in the layered cuprates have also posed the spin dynamics in a crucial spot for studying the electronic instabilities of these cuprates, e.g. high-temperature superconductivity (HTSC) [8].

In addition to  $\text{CuO}_2$  plaquettes in the 2D cuprates hosting HTSC, special attention has been paid to the quasi-one-dimensional (q-1D) cuprate spin ladders (or coupled-chains) for decades [Figure 1:1], which has been conceptualized as the crossover between two- and one- dimension [9]. Each “leg” consists of a chain with antiferromagnetically coupled spins. These two parallel chains are in turn antiferromagnetically coupled along the transverse “rung” direction, forming a singlet ground state on each rung [9–11]. Given the low-dimensionality, there is no magnetically-ordered ground state opposed to the 2D cuprates due to the manifested quantum fluctuations. For spin ladders with even-number of legs, long-range ordering is replaced by short-range spin-spin correlations [9–11]. As a result, collective spin excitations are of main interest as they describe the low-energy behavior. For the low-energy magnetic fluctuations in the ladders, the



spin dynamics is dominated by the singlet-to-triplet excitations (triplons) that propagate through the ladder-leg directions with momentum dispersion [12,13]. Alongside numerous early experimental reports using inelastic neutron scattering (INS) and nuclear magnetic resonance (NMR) spectroscopy [14,15], the collective triplon excitations have also been previously observed by RIXS as shown for the chain-ladder cuprate  $\text{Sr}_{14}\text{Cu}_{24}\text{O}_{41}$  in Figure 1:2 [13].

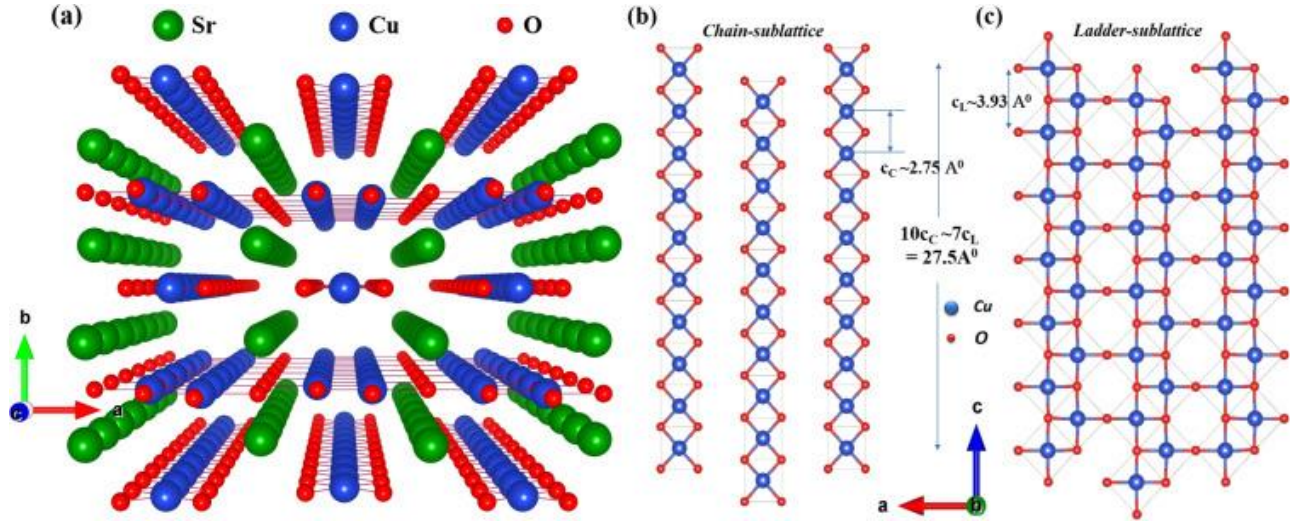


Figure 1:1 The structural model for hybrid chain-ladder cuprates  $(\text{Sr,Ca,La})_{14}\text{Cu}_{24}\text{O}_{41}$  from ref. [16] (Reprinted by permission from Elsevier publishing group, Journal of Crystal Growth, Bag R., Karmakar K., and Singh S., 458, 16-26, 2017). The materials are composed of alternating edge-sharing  $\text{CuO}_2$  chain layers, two-leg  $\text{Cu}_2\text{O}_3$  ladder layers, and non-magnetic  $(\text{Sr,Ca,La})$  atoms. The chain (ladder) subsystem features a Cu-O-Cu bond angle of  $90^\circ$  ( $180^\circ$ ), leading to the magnetic exchange coupling of  $\sim 10$  ( $\sim 100$ ) meV [17].

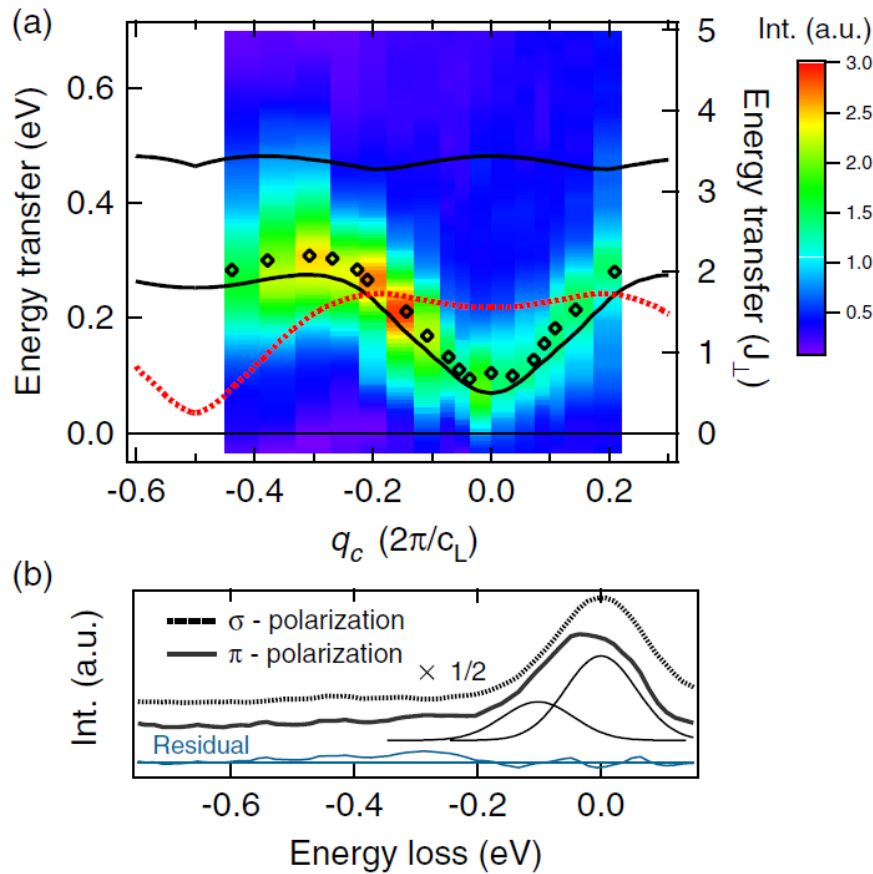


Figure 1:2 Two-triplon (2T) magnetic excitations of  $\text{Sr}_{14}\text{Cu}_{24}\text{O}_{41}$  probed by Cu  $L_3$ -edge RIXS from ref. [13]. The full momentum-dependent inelastic spectra with a dispersing downturn at zone center, representing the 2T band bottom, are shown in (a). The spectral line fitting in (b) demonstrated a sizable quasi-elastic spectral weight beyond the elastic scattering near the zone center. [Reprinted figure with permission from: J. Schlappa et al., Physical Review Letters, 103, 047401 (2009). Copyright (2009) by the American Physical Society. (<https://doi.org/10.1103/PhysRevLett.103.047401>)]

Alongside the magnetic origin for its novel ground state, the spin ladder also serves as a platform for many-body collective physics. Even-leg ladders form a gap in the spin excitation spectrum, unlike the 1D spin chains with the Luttinger liquid phase and distinct holon/spinon DOFs [9–11]. Early theories connected the evolution of the spin gap upon hole doping to pairing fluctuations, analogous with the resonance-valence-bond (RVB) spin-liquid state proposed for the HTSC in cuprates [9–11]. Based on this, a competing charge density wave (CDW) order state and superconductivity (SC) was also predicted, and has been later confirmed experimentally [9–11]. As shown in Figure 1:3, a commensurate charge order was previously uncovered using O K- and Cu L<sub>3</sub>-edge resonant elastic X-ray scattering (REXS) in the ladders of Sr<sub>14</sub>Cu<sub>24</sub>O<sub>41</sub> [18]. On the other hand, a SC state was discovered in Sr<sub>0.4</sub>Ca<sub>13.6</sub>Cu<sub>24</sub>O<sub>41.84</sub>, with T<sub>c</sub>=12 K at an applied pressure of ~3 GPa [19,20]. The crystallization of bound holes is considered to play a crucial role for the low-energy regime of doped spin ladders, as it has often been taken as the minimal interacting model for stripe order in 2D cuprates [21,22]. This highlights the collective electronic localization for the ground state, where the total system energy is minimized with respect to certain spontaneous symmetry breaking, e.g charge- and spin density wave (SDW) observed in the low-dimensional cuprates and nickelates [23].

Another quantum manifestation realized in ladders is the possibility to manipulate the interactions of elementary excitations. Quasiparticles in solids have been formulated as the basis of numerous theories describing many-body phenomena in correlated materials, e.g. HTSC, disentanglement between elementary DOFs, etc [24,25]. At the strong ladder-rung coupling limit of the charge-doped ladders, the low-energy excitations are dominated by interacting holons and coherent spinons (triplons), resulting in exotic excitations predicted by calculations, e.g. a holon-spinon continuum or dispersive antiholon excitations [26]. Assessing the evolution of the low-energy charge and magnetic fluctuations with doping in the spin ladders constraints the scaling of the correspondent pairing order parameter, where impeding efforts have been made in early studies [24,27–29]. The importance of understanding the details of the excitation spectrum was addressed by mean-field theoretical studies. It was pointed out that two major types of distinct excitations, the collective triplon mode and a holon bound to a spinon with charge |e| and spin 1/2, evolve differently as a function of hole density [28,29]. These calculations showed that the bound holon-spinon preserves particle-hole symmetry in a large fraction of the Fermi surface, similar with the Bogoliubov quasiparticles in BCS theory [28,29]. These findings re-emphasize the importance of resolving the low-energy excitations for understanding the essence of ladder physics.

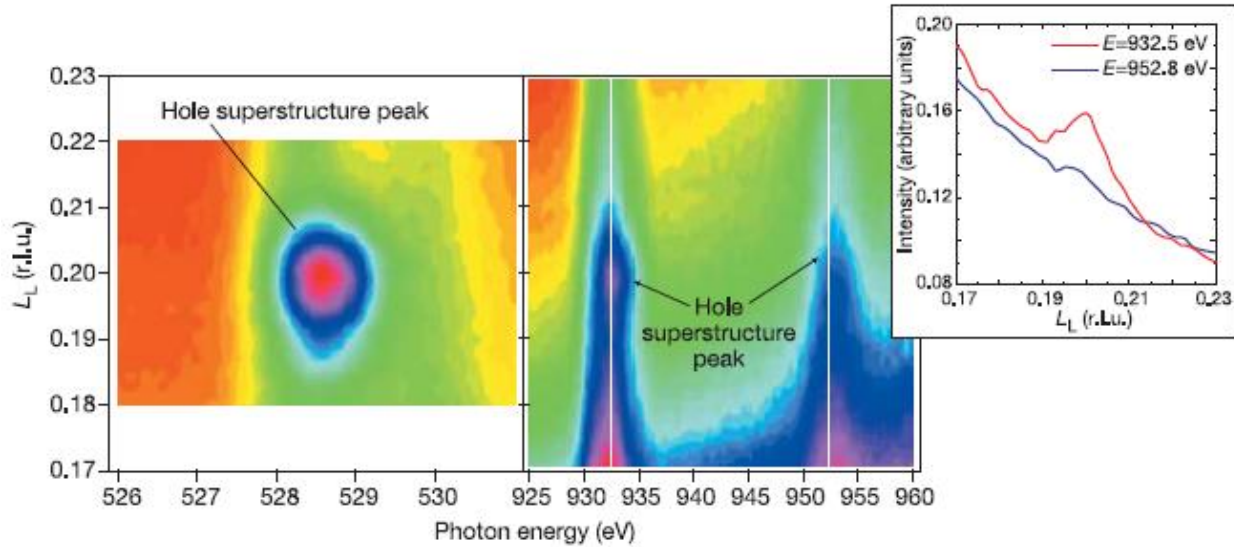


Figure 1:3 O K- and Cu L-edge resonant elastic X-ray scattering (REXS) study on the (ladder) charge order formation observed in Sr<sub>14</sub>Cu<sub>24</sub>O<sub>41</sub> from ref. [18]. A commensurate electronic reflection ~0.2 (rlu) along the ladder-leg direction was inferred at both O K- and Cu L<sub>3</sub>-edge XAS resonances (Reprinted by permission from Springer Nature publishing group, Nature, Abbamonte P. et al., 431, 1078-1081, 2004).

The hybrid spin chain-ladder material Sr<sub>14</sub>Cu<sub>24</sub>O<sub>41</sub> is the main focus in this thesis. The crystallographic structure is composed of alternating layers of two-leg Cu<sub>2</sub>O<sub>3</sub> ladders and edge-sharing CuO<sub>2</sub> chains [Figure 1:1]. The chain and ladder subsystems are internally strained due to the incommensuration of the lattice spacing between the two sublattices [30]. Due to the long chemical formula, it is commonly referred to as the telephone number compound (TNC) in literature.

TNC host numerous intriguing phenomena that have been experimentally confirmed, including gapped  $S=1$  triplons in the ladders [13,17], CDW order [18,31], spin dimerization in the chain subsystem coupled with Zhang-Rice singlet (ZRS) formation [32,33], sliding density wave motions between the chains and ladders [34], etc. In particular, a SC phase was previously inferred upon Sr-Ca substitution in high-pressure transport measurements [19,20]. This connects to the early mean-field studies suggesting that the hole-doped spin ladders should host competition between charge and pair density fluctuations with modified d-wave superconductivity, which are similar to the proposed theories for 2D HTSC in cuprates [9–11]. Conceptually, one can think of the even-leg ladders as the 2D  $\text{CuO}_2$  plaquette planes with arrays of line defects introduced in the structures, where the pairing correlations are expected to emerge upon hole-doping with a different temperature scale compared to 2D cuprates [10,11]. Recently, the experimental signature of long-range quantum entanglement in the chain subsystem was also reported, giving significant importance to understanding the quantum computation theory [35]. Many of these exotic properties are central to the fact that the TNC is a self-hole-doped compound, with doped holes residing in the ladder and chain subsystems [36]. Given the overall charge neutrality of the material, one can obtain an average Cu valence of +2.25 that is beyond the limit of an idealized  $\text{Cu } 3d^9$  configuration, leading to roughly 6 additional holes per chemical formula (pcf) [36]. It has been widely believed that about 70~80% of the holes are distributed in the chain subsystem owing to its relatively positive electrical potentials, consistent with the current experimental studies [37].

In chapter 3, the triplon response is studied by comparing the parent chemical phase  $\text{Sr}_{14}\text{Cu}_{24}\text{O}_{41}$  with a phase of high Ca doping  $\text{Sr}_{1.8}\text{Ca}_{12.2}\text{Cu}_{24}\text{O}_{41}$ . With the momentum- and polarization-dependent Cu  $L_3$ -edge RIXS measurements, the excitation spectrum evolves from collective two-triplon spin excitations ( $x=0$ ) to a localized magnetic mode with significant damping at  $x=12.2$ . With the help of model calculations using density matrix renormalization group (DMRG), the dispersion-less magnetic mode at  $x=12.2$  is consistent with a physical scenario signifying significant carrier localization. This is further supported by the polarization analysis of experimental RIXS data, where the spin-conserving  $\Delta S=0$  charge scattering is disentangled from the dominant non-spin-conserving  $\Delta S=1$  signal, and shows clear weight depletion with Ca-doping. By resolving momentum-resolved magnetic and charge excitations at the heavily Ca-doped phases, these results highlight that the localized hole-pairs play a crucial role for the prerequisite of electron pairing via elevated pressure.

In chapter 4, the possibility to study the co-existent low-energy charge and spin-singlet magnetic excitations in the doped ladders of  $\text{Sr}_{14}\text{Cu}_{24}\text{O}_{41}$  is covered. At the upper Hubbard band (UHB) resonance in O K-edge XAS signal, the RIXS spectra reveal a series of excitation modes, including a sharp dispersing peak  $\sim 270$  meV and a broad non-dispersive mode at higher-energy  $\sim 400$ -500 meV. With comparison to the current theories on the magnetic and charge dynamics of doped ladders, the observed RIXS response show close resemblance to the interacting holons-spinons, likely accompanied by the bound states and continua derived from multi-triplon scattering. The main experimental result comprises the RIXS capability of likely delivering a spectroscopic signature of composite spin-charge quasiparticles and momentum-resolved long-lived spin-singlet magnetic excitations. The spectroscopic determination of the observed excitations are generally difficult in conventional experiments, owing to the lack of understanding on the respective scattering cross section for these modes.

In chapter 5, the observation and manipulation of the electronic charge order via low-doping of magnetic impurities are demonstrated for the ladders of  $\text{Sr}_{14}(\text{Cu}_{1-y}\text{Co}_y)_{24}\text{O}_{41}$ . Using a high-resolution experimental setup of the RIXS probe, allows discussing the interplay between the observed diffraction signal and low-energy phonon excitations. At the pre-edge peak representing the ladder hole content in the O K-edge XAS spectra, the RIXS spectra show concurrent elastic enhancement and phonon-softening for the Cu-O bond-stretching mode for all Co-doping levels ( $y=0, 0.01, 0.03$  and  $0.05$ ). The observed in-plane diffraction and phonon-softening become stronger with increasing Co dopants, while the diffraction wavevector continuously decreases upon elevated Co impurities. With energy-detuned and temperature-dependent RIXS measurements, the in-plane diffraction signal is shown to be resonantly enhanced at the ladder hole XAS peak and melts with increasing temperature, suggesting its possible electronic origin rather than solely from Bragg diffraction. Additionally, the electron-phonon coupling (EPC) about  $\sim 220$ -240 meV is analyzed systematically as a function of Co-doping and momentum-transfer, given the clear RIXS phonon signal. With magnetic impurities, these observations are reminiscent of a strengthened charge-stripe order assisted by significant phonon interactions, which are reminiscent of the experimental reports on 2D SC cuprates.

In chapter 6, the electronic structure and phonon excitations of a geometrically frustrated honeycomb nickelate  $\text{Na}_2\text{Ni}_2\text{TeO}_6$  are discussed [38]. Recently, there has been increasing attention to frustrated magnetic materials owing to their novel electronic phases [39,40], e.g. bond-directional magnetic exchange in Kitaev systems [41], long-range entanglement with fractionalized excitations [42], etc (see more information in section 6.2). The Ni valence shell is characterized by Ni  $L_3$ -edge RIXS, showing a series of localized excitations similar to studies on the crystal field splitting of  $\text{Ni}^{2+}$  ions with an octahedral site symmetry. Moreover, the higher-energy inelastic RIXS response reveals fluorescence-like excitations, which are consistent of charge-transfer states observed in other nickel oxides of  $\text{Ni}^{2+}$  configuration. On the other hand, the O  $K$ -edge RIXS spectra reveal strong EPC with clear phonon overtones up to 5-6 harmonics. An EPC of  $\sim 285$  meV that is weakly-dependent to momentum is observed for the optical phonon excitations, with phonon frequency about 80 meV. The RIXS sensitivities to orbital and charge-transfer excitations, as well as momentum-resolved EPC, provide valuable information for the dynamical properties that are difficult to probe by other experimental techniques. With temperature and polarization analysis, the RIXS study on such frustrated antiferromagnets will help to elucidate the crucial excitation modes that are directly associated with the novel magnetic ground state.

---

## Chapter 2 Resonant soft X-ray spectroscopy

In this chapter, the principles of soft X-ray spectroscopy applied in this thesis and details of the experimental methodology are briefly introduced. The spectroscopic methods, X-ray absorption spectroscopy (XAS) and resonant inelastic X-ray scattering (RIXS), along with the RIXS endstation of the Advanced Resonant Spectroscopies (ADRESS) beamline at the Swiss Light Source (SLS), will be described. Additionally, a brief review of the spectral response of elementary excitations for 3d metal L<sub>3</sub>- and oxygen K-edge RIXS in 3d transition-metal oxides is given.

### 2.1 X-ray Absorption Spectroscopy

#### 2.1.1 Principles of XAS process

X-ray absorption spectroscopy (XAS) is a powerful technique for studying the electronic structure in solids, molecules and gases [43–45]. Generally, the microscopic processes consist of the excitation of the core-level electrons to the valence states above the Fermi level. By illuminating the measured samples with X-rays of varied incident energies, one can infer the underlying chemical composition from the increase of absorption coefficients, which correspond to certain resonant transitions between the electronic states. For comprehensive understanding, the readers are referred to references [43–46]. With the given electronic materials, the charge particles can react to the presence of interacting photons and oscillate with respect to the electromagnetic fields. The transition probability from a certain initial state  $i$  to the final state  $f$  can be described by the Fermi's golden rule at the first order that reads

$$w_{fi} = \frac{2\pi}{\hbar} |\langle f | T | i \rangle|^2 \delta(E_f - E_i - \hbar\omega).$$

Equation 2:1 Fermi's golden rule at the first order describing the photoelectric XAS process.

Here  $T$  represents the transition operator that determines the matrix elements for the photon absorption process, which are directly reflective of the involved electronic states with certain orbital symmetry [1]. In combination with utilizing the X-ray polarization and experimental geometry, the XAS sensitivity allows direct access to the unoccupied states for various symmetries. This enables the XAS capability to assess the local electronic configuration alongside the oxidation states and coordination environments [43–45]. The XAS edges are defined by the relevant transitions involved in the photoelectric excitation. For the context of this thesis, the  $2p \rightarrow 3d$  and  $1s \rightarrow 2p$  atomic transitions for the 3d transition-metal and oxygen ions separately are of the main topics, corresponding to the L and K XAS edges, respectively. For the oxides composed of the first-row transition metal ions, these elemental absorption edges are within the soft X-ray regime ( $< 1$  keV). Given that the frontier atomic wavefunctions for the valence band and Fermi level are largely contributed by the metal 3d and O 2p orbitals, the 3d metal L- and O K-edge XAS edges are suitable for evaluating the electronic structure for the cuprates and nickelates discussed in this thesis.

In the typical hard X-ray XAS measurements, the absorption coefficient can be taken as the measure of intensity ratio between the outgoing and incoming photon, namely operated in a transmission geometry. This is rationalized by the Beer-Lambert law, where the amount of photon absorbed  $dI$  in a thin slice of sample with thickness  $dz$  can be expressed as:

$$\frac{dI}{dz} = -I(z)\mu(\omega)$$

Equation 2:2 Differential equation for the photon absorbed in an infinitely thin and uniform material.

$I_0$  is the incoming photon intensity, and  $\mu(\omega)$  is the absorption coefficient that is associated with energy. By solving this differential equation, one obtains the Beer-Lambert law as:

$$I = I_0 e^{-\mu(\omega)z}.$$

Equation 2:3 Beer-Lambert law.

For soft X-ray, however, the typical penetration depth of photon is of 10-100 nm scale. This would imply that a thin film sample is mandatory for the practical measurements, therefore hinders the experimental application. In the following two sections, the alternative approaches for detecting XAS by fluorescence and electron yield are introduced. Given by the considerable cross section in the soft X-ray regime, the fluorescence emission and Auger electron escape are the two major ways to relax total energy for condensed matter [47]. Both methods are based on the assumption that the photoabsorption is proportional to the number of core-holes created. This can be measured by the correspondent emitted photons or electrons due to the annihilation of these unstable core-holes via different energy relaxation channels in the samples.

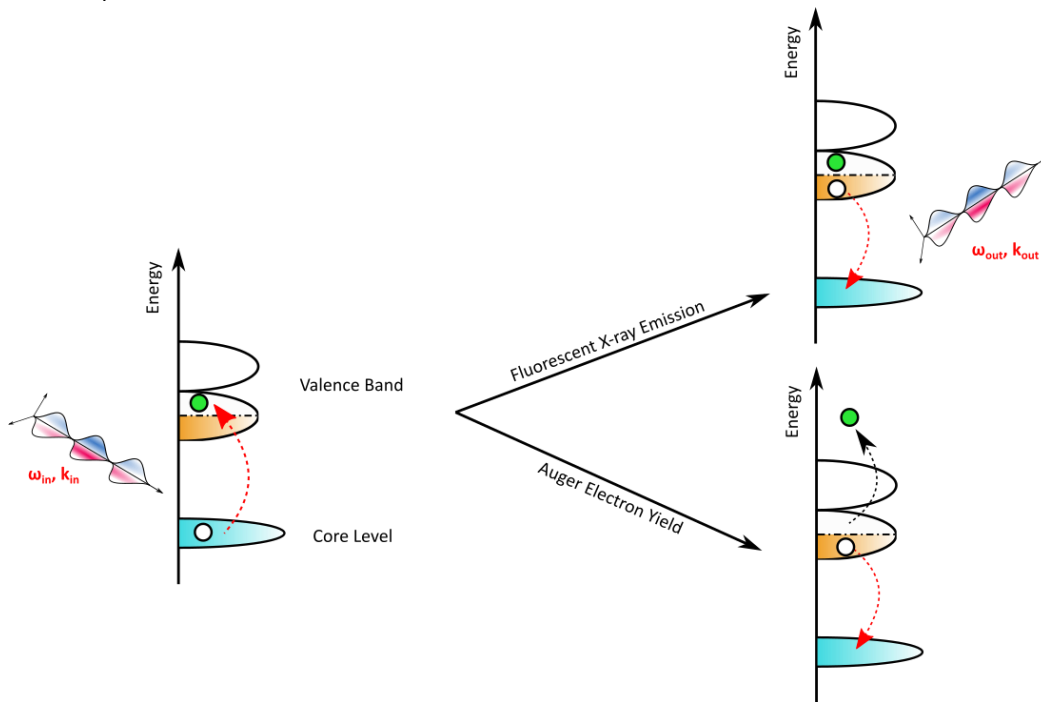


Figure 2:1 Schematics for X-ray absorption and the two major processes for detection, the fluorescence from X-ray emission and electron yield mainly contributed from Auger processes. The photoelectric transitions (red arrows) from core-level to the unoccupied valence shell (Fermi level labelled by dot-dashed black lines) upon soft X-ray absorption is indicated on the left. The electrons with less energies than the photo-excited electrons (green circles) then annihilate the unstable core-hole to relax the system, which release electromagnetic radiation that correspond to the fluorescence emission. The measured materials can also release energy by allowing electron escape while the lower-energy shells can undergo photoelectric de-excitations to fill the core-hole, and this is connected to the electron yield.

### 2.1.2 Total fluorescence yield

One simple approach to perform XAS measurements is to probe the fluorescence yield (Figure 2:1). Followed by the photoelectric excitation of electrons, the radiation emitted through the annihilation of the created core-hole filled by electrons from outer shell is described as fluorescence [46,48]. In this manner, the fluorescence yield is proportional to the photoelectrons resonantly excited by the incoming photon, thereby allowing the evaluation of XAS signature of the measured samples. In practice, this is commonly conducted with a photodiode to collect the outgoing photons within a solid angle, with respect to the finite energy spread for the detector. This corresponds to the total fluorescence yield (TFY), which assumes that the emission lines are featureless for the elements that are non-resonantly excited for the given incoming photon energy. The TFY detection mode is essentially bulk-sensitive, determined by the probing depth of the incoming photon for X-ray. As a result, it is less invasive and relatively inert to the surface treatment or roughness of the samples. One major drawback for TFY mode is the self-absorption effects for the incoming and outgoing photons

during the light-matter interactions. This leads to distortion on the X-ray emission signal due to the damping from the measured samples, which depends on the geometrical configuration for experiments. Given that the measured materials in this thesis are reasonably insulating, the XAS data from chapter 3 to 6 are taken with TFY mode unless specified. The fluorescence yield intensity normalized to the incident photon intensity can be expressed as:

$$\frac{I(E_g, E_f)}{I_0(E_g)} = C \sum_i \int_0^z \Omega_i(E_g, E_f) \frac{\mu_i(E_g)}{\sin(\alpha)} e^{-\left(\frac{\mu_i(E_g)}{\sin(\alpha)} + \frac{\mu_i(E_f)}{\sin(\beta)}\right)z'} dz'.$$

Equation 2:4 Fluorescence yield intensity.

Here  $E_g$  and  $E_f$  stand for the incoming and outgoing photon energies, respectively.  $\Omega_i$  is the fluorescence yield coefficient for element  $i$ , while  $\mu_i(E)$  is the absorption coefficient for energy  $E$ .  $\alpha$  and  $\beta$  are the incidence and emission angles with respect to the sample surface, separately, which will affect the self-absorption for the incoming and outgoing photon. This matters for the probed region for the sample of thickness  $z$  for the self-absorption effects of the fluorescence signal. The constant  $C$  accounts for the quantum yield efficiency of the photon events on detector covered in the solid angle.

### 2.1.3 Total electron yield

Another way to measure XAS is to detect the electron yield signal (Figure 2:1). This is realized through the Auger decay processes that establish an electron current between the measured sample and the experimental ground. In general, the strength of Auger signal is proportional to the number of photons absorbed. Therefore, by measuring the drain current signal of total electron yield (TEY), one can obtain an approximated XAS profile that is sensitive to the Auger electron escape paths. This method will require a moderate electrical conduction between the measured samples and the experimental ground. Moreover, due to the limited escape length of electrons that is scaled by the inelastic mean free path (IMFP)  $\sim 1$  nm, the TEY detection for XAS is surface sensitive and influenced by contamination on the sample surface [46,48]. For the context of this thesis, the measured samples are insulating bulk single crystals, and thereby the TEY signal is mostly weak and irrelevant to the actual XAS processes.

## 2.2 Resonant Inelastic X-ray Scattering

### 2.2.1 Principles of RIXS process

RIXS is a resonant X-ray spectroscopy with two-step light-matter interactions. It has shown great potential to be capable of probing various elementary excitation modes in condensed matter [47,49]. The scattering processes consist of two subsequent photo-induced atomic transitions as shown in Figure 2:2. It starts with resonantly exciting a core-level electron into the valence band. This creates a highly unstable intermediate state with a core-hole, scaled by a lifetime scale about few fs. This is then filled by an electron from the valence band then emitting radiation. The energy of the emitted photon can be equivalent or smaller than the incoming photon, where the latter corresponds to a resonant inelastic process. The generally weak scattering cross section for such dynamical processes is enhanced due to the anomalous scattering when the incident X-ray is tuned to XAS edges. This overcomes the low count rates for the scattered-photon events observed in non-resonant X-ray scattering.

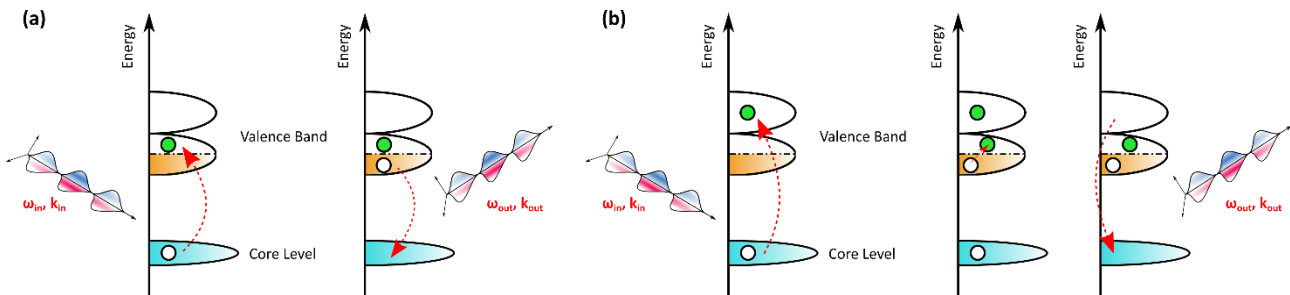


Figure 2:2 Schematics for (a) direct and (b) indirect RIXS processes.



By resolving the RIXS signal with energy and polarization dependence, one can study the underlying electronic structure with symmetry analysis. Furthermore, the application of high-energy X-ray scattering not only enables the exchange of photon energy but also the transfer of momentum. In combination of the momentum and energy conservation laws between the photon and measured samples, one can extract the momentum-resolved RIXS spectral weight which allows the evaluation of energy dispersions for collective excitations. These establish RIXS as a powerful spectroscopic tool for studying spin, charge, orbital and lattice dynamics in diverse electronic materials, where small-volume samples of  $\sim 1\text{mm}^3$  are sufficient for spectral statistical efficiency. A finite cross section is available provided that the scattering process is charge-neutral, which poses RIXS free from the charging issues for photoemission experiments in insulators due to the removal of electrons. By tuning the incoming photon with respect to the elemental XAS edges, RIXS probe is element- and orbital-specific for the measured excitation modes. This is advantageous to disentangle the intricate electronic correlations in condensed matter.

Figure 2:2 describes the direct RIXS processes corresponding to the aforementioned paragraphs. The excited state is highly unstable after absorbing a photon with a core-hole, then quickly decays from such intermediate state with few femtoseconds. An inelastic process is achieved when an electron with different energy in the valence state annihilates the unstable core-hole. The so-called direct RIXS is governed by the fact that the two-step processes show substantial coupling between the core and valence states, e.g. K-edge ( $1s \rightarrow 2p$ ) for light elements (carbon, oxygen, nitrogen, etc) and L-edge ( $2p \rightarrow 3d$ ) for transition metals. When the photoelectric transitions between the core and valence states are weak, another mechanism referred as the indirect RIXS can occur as depicted in Figure 2:2. The core-level electron is excited up to several electron volts above the Fermi level, where the system decays from this intermediate state (e.g.  $1s \rightarrow 4p$  K-edge transition for metals). This leads to shake-up/shake-off excitations during the RIXS process. In most cases including this thesis, the RIXS signal is dominated by the direct RIXS process.

The major obstacle for RIXS studies is the low photon signal derived from the second-order light-matter interactions. The necessity for high resolution from a synchrotron beamline with high-resolving power spectrometer further elevates the challenges for the overall spectral throughput. Thanks to the rapid improvement with the advent of optimized optics specifically for high-resolution RIXS setup, nowadays the detection of low-energy modes about tens of meV (e.g. magnetic or vibrational modes) within few-hour acquisition have been realized. This opens up the opportunities for studying fields that were previously specialized for inelastic neutron scattering (INS) or non-resonant inelastic X-ray scattering (IXS).

### 2.2.2 RIXS cross section

In this section, the RIXS scattering cross section described by Kramers-Heisenberg formula is briefly introduced. For more comprehensive discussions, the references from [49] and [47] are recommended. To illustrate the underlying interactions between photons and electrons with simplicity, we make the following approximations. First of all, non-relativistic bound electrons are considered, which are in agreement with the applied X-ray of third-generation synchrotron radiation in this thesis. Secondly, the light-matter interactions are treated as small perturbations with the form of time-dependent electromagnetic waves. Such semi-classical picture may not be valid for stronger field strength achieved in light scattering, e.g. free-electron laser (FEL). In SI units, the Hamiltonian for  $N$  electrons with a presence of electromagnetic field  $\mathbf{A}(\mathbf{r}, t)$  can be written as:

$$H = \sum_i^N \left( \frac{(\mathbf{p}_i + e\mathbf{A}(\mathbf{r}_i))^2}{2m} + \frac{e\hbar}{2m} \boldsymbol{\sigma}_i \cdot \mathbf{B}(\mathbf{r}_i) + \frac{e\hbar}{2(2mc)^2} \left( \mathbf{E}(\mathbf{r}_i) \times (\mathbf{p}_i + e\mathbf{A}(\mathbf{r}_i)) - (\mathbf{p}_i + e\mathbf{A}(\mathbf{r}_i)) \times \mathbf{E}(\mathbf{r}_i) \right) \right) + \frac{e\hbar^2 \rho(\mathbf{r}_i)}{8(mc)^2 \epsilon_0} + H_{\text{Coulomb}} + \sum_{\mathbf{k}, \epsilon} (a_{\mathbf{k}, \epsilon}^\dagger a_{\mathbf{k}, \epsilon} + \frac{1}{2}).$$

Equation 2:5 Hamiltonian for light-matter interactions.

Here,  $\mathbf{p}_i$  and  $\mathbf{r}_i$  are the momentum and position operators for the electrons, and  $\boldsymbol{\sigma}_i$  are the Pauli matrices.  $\mathbf{A}(\mathbf{r}_i)$  is the vector potential, with correspondent electric field  $\mathbf{E}(\mathbf{r}_i) = -\nabla\varphi(\mathbf{r}_i) - \partial\mathbf{A}(\mathbf{r}_i)/\partial t$  and magnetic field  $\mathbf{B}(\mathbf{r}_i) = \nabla \times \mathbf{A}(\mathbf{r}_i)$ .  $a_{\mathbf{k}, \epsilon}^\dagger$  and  $a_{\mathbf{k}, \epsilon}$  are the creation and annihilation operators for photons with wavevector  $\mathbf{k}$ , polarization  $\epsilon$ , and energy  $\hbar\omega_{\mathbf{k}} = c|\mathbf{k}|$ , where  $c$  is the light speed. The first term in the brackets describes the kinetic energies for the electrons, and the second term accounts for the Zeeman splitting. The third term is responsible for the spin-orbit coupling (SOC), relevant for

electrons with finite orbital moments ( $\mathbf{L} \neq 0$ ). The fourth term is the Darwin term that modifies the effective potential for the nucleus, which is more relevant for s-wave orbitals due to their finite scattering probability at nuclei. The  $H_{\text{Coulomb}}$  term is associated with the electron response to other sources of external field, e.g. the atomic cores. The last term summarizes the summation of photon quanta with energy of  $\hbar\omega$ .

The scattering cross section can be calculated by assuming the interactions between light and measured sample  $H'$  are small compared to the unperturbed dynamics of the photons and electrons  $H_0$ , where the total Hamiltonian  $H = H_0 + H'$ . Here, the momentum and energy for initial (final) state of a single photon before (after) the scattering processes are assumed as  $\hbar\mathbf{k}$  ( $\hbar\mathbf{k}'$ ) and  $\hbar\omega_k$  ( $\hbar\omega_{k'}$ ), with polarization  $\boldsymbol{\epsilon}$  ( $\boldsymbol{\epsilon}'$ ). This gives rise to a photon transfer for the measured sample with the momentum and energy transfer expressed as  $\hbar\omega = \hbar\omega_k - \hbar\omega_{k'}$  and  $\hbar\mathbf{q} = \hbar\mathbf{k} - \hbar\mathbf{k}'$ , respectively. As a consequence, under the framework of perturbation theory, the transition rate  $w$  for the two-step processes can be described by the Fermi's Golden rule expanded at the second order:

$$w = \frac{2\pi}{\hbar} \sum_f \left| \left( \langle f | H' | g \rangle + \sum_n \frac{\langle f | H' | n \rangle \langle n | H' | g \rangle}{E_g + \hbar\omega - E_n} \right) \right|^2 \delta((E_f + \hbar\omega_{k'}) - (E_g + \hbar\omega_k)),$$

Equation 2:6 Fermi's Golden rule in second-order perturbation theory.

$|n\rangle$  correspond to the available intermediate states summed over the given atomic transitions. Here  $|n\rangle$  are eigenstates for  $H_0$  with energies of  $E_n$ . The first term represents the non-resonant inelastic scattering, while the second term depicts the resonant scattering. The former generally outweighs the latter except for  $\hbar\omega \sim (E_n - E_g)$ . With a nearly zero denominator, the second-order resonant scattering term is largely enhanced in vicinity to the resonant condition.

To evaluate the perturbative  $H'$ , one collects the terms in  $H$  that are linear in vector potential  $\mathbf{A}$ . Although the first and third term possess both linear and quadratic order of  $\mathbf{A}$ , the relevant contribution is of order  $\alpha^{3/2}$  and therefore neglected. Here  $\alpha = e^2/4\pi\epsilon_0\hbar c \sim 1/137$  is the dimensionless fine structure constant. As a result, all terms that are independent of  $\mathbf{A}$  are included in  $H_0$ , where the remaining terms read:

$$H' = \sum_i \left( \frac{e}{m} \mathbf{A}(\mathbf{r}_i) \cdot \mathbf{p}_i + \frac{e^2}{2m} (\mathbf{A}(\mathbf{r}_i))^2 + \frac{e\hbar}{2m} \boldsymbol{\sigma}_i \cdot \nabla \times \mathbf{A}(\mathbf{r}_i) - \frac{e^2\hbar}{(2mc)^2} \boldsymbol{\sigma}_i \cdot \left( \frac{\partial \mathbf{A}(\mathbf{r}_i)}{\partial t} \times \mathbf{A}(\mathbf{r}_i) \right) \right)$$

Equation 2:7 Perturbative term in the electron Hamiltonian with photon scattering.

Here the Gauge is fixed with  $\nabla \cdot \mathbf{A} = 0$ , leading to  $\mathbf{A} \cdot \mathbf{p} = \mathbf{p} \cdot \mathbf{A}$ . By inserting this into the Equation 2:6, we obtain the second-order amplitude for the resonant scattering as

$$\frac{e^2\hbar}{2m^2V\epsilon_0\sqrt{\omega_k\omega_{k'}}} \sum_n \sum_{i,j}^N \frac{\left| \langle f | e^{-ik' \cdot \mathbf{r}_i} (\boldsymbol{\epsilon}'^* \cdot \mathbf{p}_i - \frac{i\hbar}{2} \boldsymbol{\sigma}_i \cdot \mathbf{k}' \times \boldsymbol{\epsilon}') | n \rangle \right| \left| \langle n | e^{ik \cdot \mathbf{r}_j} (\boldsymbol{\epsilon}^* \cdot \mathbf{p}_j + \frac{i\hbar}{2} \boldsymbol{\sigma}_j \cdot \mathbf{k} \times \boldsymbol{\epsilon}) | g \rangle \right|}{E_g + \hbar\omega - E_n + i\Gamma_n}$$

Equation 2:8 Second-order resonant scattering amplitude.

$V$  is the volume for the system considered. The core-hole lifetime broadening  $\Gamma_n$  is introduced to account for the non-radiative processes. Thus prevents an infinitely large scattering amplitude that is unphysical, making the intermediate states short-lived in nature. For simplicity,  $\Gamma_n$  are taken as independent among the intermediate states for the following derivation ( $\Gamma_n = \Gamma$ ). Furthermore, one can simplify the resonant scattering amplitude by neglecting the magnetic contribution  $\boldsymbol{\sigma}_i \cdot \mathbf{k}' \times \boldsymbol{\epsilon}'$ , which has been demonstrated to be generally weaker than the non-magnetic scattering [49]. Lastly, the original  $\mathbf{p}$  operator is replaced by  $i m [\mathbf{H}_0, \mathbf{r}] / \hbar$  through the commutator relation, giving rise to  $\langle n | \boldsymbol{\epsilon} \cdot \mathbf{p} | g \rangle \approx m\omega \langle n | \boldsymbol{\epsilon} \cdot \mathbf{r} | g \rangle$ . Consequently, with the dipole approximation ( $e^{i\mathbf{k} \cdot \mathbf{r}} = 1 + i\mathbf{k} \cdot \mathbf{r} + \dots$ ), the Kramers-Heisenberg RIXS cross section can be obtained by normalizing to the photon density of states with respect to the solid angle  $\Omega$  and by photon flux, which reads:

$$\frac{d^2\sigma}{d(\hbar\omega)d\Omega} = r_e^2 m^2 \omega_k \omega_{k'}^3 \sum_f \left| \sum_n \sum_{i,j}^N \frac{\langle f | \boldsymbol{\epsilon}'^* \cdot \mathbf{r}_j | n \rangle \langle n | \boldsymbol{\epsilon} \cdot \mathbf{r}_i | g \rangle}{E_g + \hbar\omega - E_n + i\Gamma} \right| \delta(E_g - E_f + \hbar\omega).$$

Equation 2:9 Kramers-Heisenberg equation for the RIXS cross section under dipole approximation.

The relevant transition operator can be written as:

$$D = \frac{1}{im\omega k} \sum_{i=1}^N e^{ik \cdot r_i} \epsilon \cdot p_i$$

Equation 2:10 The RIXS transition operator under dipole approximation.

Here  $r_e$  is the classical electron radius  $e^2/4\pi\epsilon_0 c^2$ . To examine the validity of dipole approximation for a local-transition picture, the typical scale of radiation wavelength for soft X-ray of few nm is still reasonably larger than the common lattice spacing ( $\sim \text{\AA}$ ) in solids. Nevertheless, the sizable contributions from multipole expansions will arise when entering towards higher incoming photon energies. The two-step RIXS processes, consisting of the transitions between the initial, highly unstable intermediate and the excited final state, are described by the multiplication of overlapping wavefunctions between dipole operators in a Frank-Condon fashion. The RIXS cross section is highly dependent on the intermediate state core-hole potentials. This poses the RIXS selection rule beyond the scope of the conventional optical spectroscopy, and allows the detection of optically-forbidden excitation modes. The probed excitations are not affected by the core-hole broadening in the intermediate state, but their own intrinsic lifetime scales. By analysing the energy for incoming and outgoing photon, one can map out the excitation spectrum as a function of energy loss by collecting the scattered photon events at given scattering geometry. With the varied polarization, energy and incidence angle for the incoming photon, one can study the comprehensive RIXS cross section for the probed excitations that are sensitive to the above variables.

The evaluation of the RIXS intensity has been beyond trivial. Several approximation have been so far applied for calculating the Kramers-Heisenberg scattering amplitude in current studies. The most straightforward approach is to directly compute the exact scattering amplitude and RIXS intensity [47,49]. In this case, the complex electronic correlations and intermediate states are largely approximated to a simplified system. For instance, one solution is to describe the underlying electronic interactions with an isolated single ion. The atomic orbitals are often taken into account for the consideration of local lattice symmetry. This is commonly utilized with the usage of local density approximation and calculated in the *ab initio* fashion, approximating the interacting electrons with an effective potential. With the lack of core-hole potentials and intermediate state effects in the formalism, this essentially provides a measure for the convolution of occupied and unoccupied states. Therefore, this has been demonstrated for early studies on the wide band insulators and semiconductors. In this scenario, the intermediate states consist of an exciton with core-hole and valence electron for band insulators and semiconductors, while the creation for such low-energy electron-hole excitations can also effectively screen the intermediate core-hole potentials for metallic systems.

Another approach relies on the exact diagonalization (ED) on the local clusters [47,49]. This is useful for strongly correlated electronic materials, as the assumption of non-interacting electrons in the single-ion approximation is no longer valid due to the sizable Coulomb interactions. In these calculations, it requires a properly chosen basis for the studied systems. Then, one sets up the model Hamiltonian for the investigated properties, where the parameters are often extracted from numerical methods, e.g. *ab initio* or Hartree-Fock approximation. Finally, the Hamiltonian is diagonalized for the the given electronic states involved in the two-step photoelectric transitions during the RIXS processes. This approach directly tackles the many-body phenomena in the studied systems compared to the single-ion method. However, the amount of required computation memory increases rapidly with the basis set and number of states involved, therefore often limited to the studies on small clusters (e.g. 5~6 CuO<sub>2</sub> plaquettes for edge-sharing cuprate chains). The main task for this approach is to decide the crucial electronic states that are sufficient to describe the studied excitations. For the transition metal L- and M-edge, the RIXS processes are direct and optically-allowed for diopole transitions. Therefore, the core-hole in the intermediate states are strongly bound to the excited valence electrons, leading to the direct access of a variety of elementary excitations.

Except for directly computing the scattering amplitude in the simplified systems, another way to approximate the RIXS cross section is to apply effective theory for the intermediate state core-hole propagator [47,49]. This takes advantages of being capable of tackling large size clusters beyond the reach of state-of-art ED calculations. In particular, this gives the access to the collective excitations during RIXS processes, which are limited for small clusters with the potential finite-size effects. By simulating the intermediate states with an interaction model possessing reduced degrees of freedom, one can obtain the effective RIXS response to compare with the experimental results. In recent years, the usage of density-matrix renormalization group (DMRG) for calculating the effective RIXS cross section has been

demonstrated for the q-1D systems, where a large cluster size up to hundreds of sites is achievable. This will be shown in chapter 3 and 4, where the low-energy magnetic and charge excitations in the doped two-leg ladders are well described by the DMRG calculations. As the introduction of DMRG method is beyond the context of this thesis, the readers are referred to the enclosed references [50–52].

Lastly, a commonly applied approximation for calculating the RIXS cross section is introduced here. In the wide band insulators and semiconductors, the RIXS response is simplified as the electron-hole pairs with effectively projected density of states from the two subsequent electronic transitions in the RIXS processes [47,49]. Given the considerable intermediate state interactions for strongly correlated electronic materials, which suits the context of this thesis, this physical picture is not valid. Nevertheless, the predominant dipole contributions for the RIXS scattering amplitude still hold for the transition metal L- and M-edge. With this, one intuitive approximation is to simplify the intermediate state interactions by assuming an ultrafast core-hole lifetime (UCL). With the approximated fast-collision limit, the intermediate state propagator can be replaced by a resonant factor, which remains a constant determined by the given electronic states. Recent theories expanded this with the polarization-resolved RIXS scattering channels, where it has been shown that the dynamical magnetic ( $\Delta S=1$ ) and charge ( $\Delta S=0$ ) correlations can be discussed separately from the RIXS spectra [53]. This is covered in the context of chapter 3.

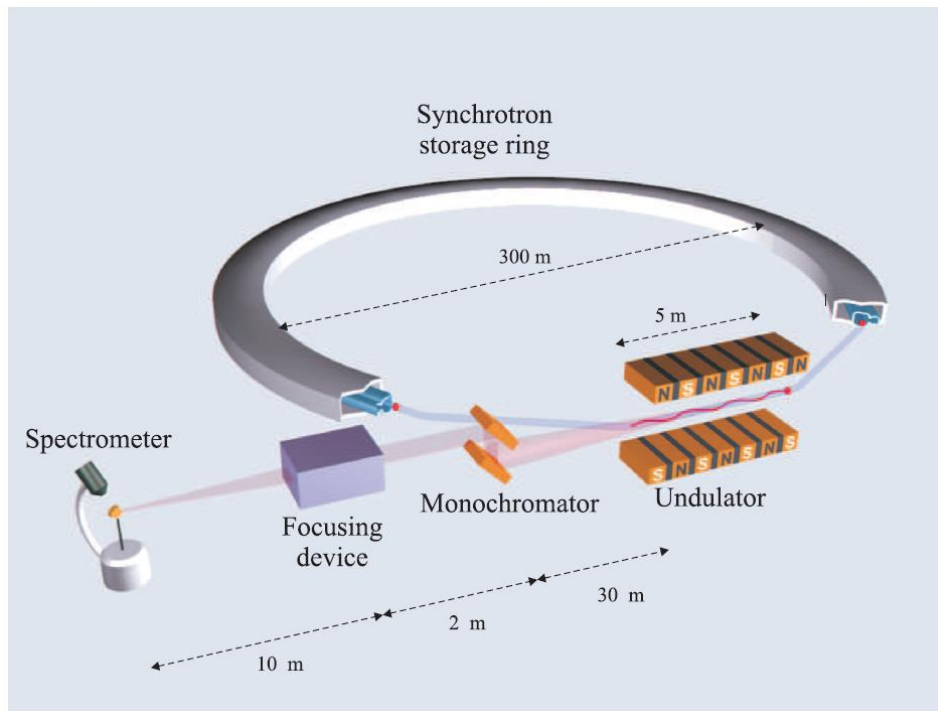


Figure 2:3 Schematics for a prototypical synchrotron radiation source from ref. [48]. (Reprinted by permission from John Wiley and Sons, Elements of Modern X-ray Physics 2<sup>nd</sup> edition, Jens Als-Nielsen and Des McMorrow, 2<sup>nd</sup> edition, 2011)

## 2.3 Synchrotron Radiation and Insertion Devices

In order to perform soft X-ray RIXS measurements in condensed matter, a stable photon source with high flux and collimation is required. The synchrotron radiation facilities provide the ideal source for such purposes. For more comprehensive studies, the readers are referred to the recommended reference [46,48]. Figure 2:3 shows the schematics of typical synchrotron radiation source with its components. The working concept relies the electromagnetic radiation released by charge particles accelerated to the relativistic limit by a linear accelerator up to 1~2 GeV scale. The accelerated electrons are then injected into the storage ring, and maintain a circular motion which is forced by magnets. With this, the electromagnetic wave is released along the tangential direction of the circular motion for the electrons, and then guided to the experimental endstation for measurements. Under relativistic limit, the emitted radiation from the electrons undergoes an extreme sharpening scaled by the inverse of Lorentz factor  $\sim 1/\gamma$  (Figure 2:4). This is caused by the relativistic Doppler effects that modify the spatial profile of the electromagnetic wave, leading to

a highly collimated photon beam seen by an observer. The energy the emitted radiation seen by an observer is roughly peaked at a frequency determined by the inverse of the traversal time, which is defined as visible time interval for the radiation cone for an observer in the laboratory frame. The exact formulation can be written as:  $\omega_c = 3eB\gamma^2/2m$ , where  $\omega_c$  is the critical frequency,  $B$  is the magnetic field,  $m$  is the electron mass and  $e$  is the electron charge. For sufficiently large  $\gamma$ , the energy spectrum is peaked at a frequency in the X-ray regime

During this process, the loss of kinetic energies of accelerating electrons will be compensated by the radio frequency (RF) cavities, which replenish the electron energy through the electric field that is in-phase with the transverse time of electron motion in the RF cavities. This can be seen in the so-called top-up operational mode for a typical third-generation synchrotron radiation source. Additionally, this also gives rise to a discrete distribution for the electrons in time structure as separated bunches, where the time scale  $\sim 2$  ns between electron bunches is determined by the typical working frequency of the RF cavity ( $\sim 500$  MHz). Due to the repulsive interactions between the electrons, the length for an electron bunch is usually extended up to  $\sim 100$  ps.

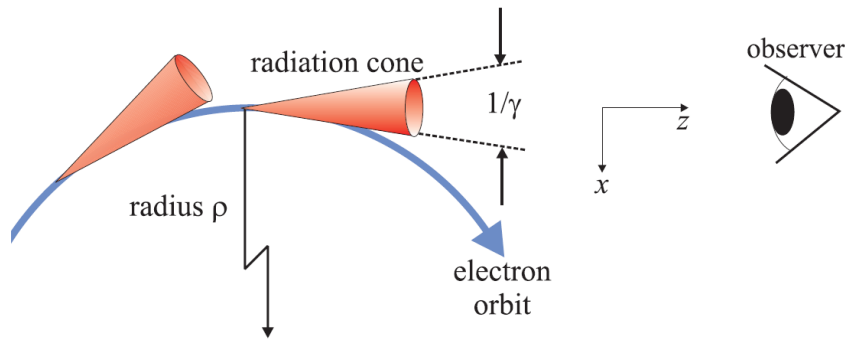


Figure 2:4 Schematics of the collimated radiation released by relativistic accelerated electrons from ref. [48]. (Reprinted by permission from John Wiley and Sons, Elements of Modern X-ray Physics 2<sup>nd</sup> edition, Jens Als-Nielsen and Des McMorrow, 2<sup>nd</sup> edition, 2011)

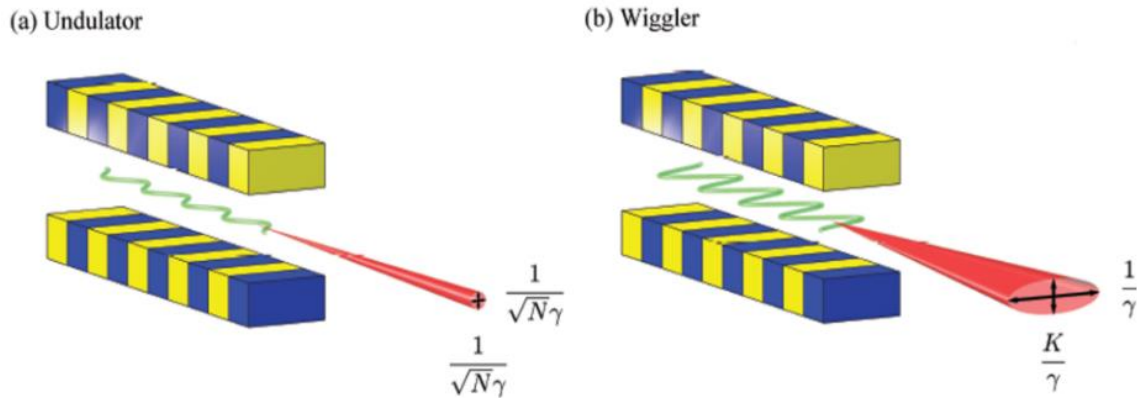


Figure 2:5 Schematics for (a) undulator and (b) wiggler insertion devices from ref. [48]. (Reprinted by permission from John Wiley and Sons, Elements of Modern X-ray Physics 2<sup>nd</sup> edition, Jens Als-Nielsen and Des McMorrow, 2<sup>nd</sup> edition, 2011)

After the electron acceleration, the emitted photons are deflected into a corresponding beamline by the Lorentz force bending the electrons under magnetic fields. Despite the usage of typical bending magnets are sufficient for X-ray studies, the demand for higher intensity and narrow beam size require further assistance from the instrumental side. By combining a series of magnets, manipulation on the photon energy spectrum can be achieved. This is conceptualized as periodically arranged magnets, where the magnitude and periodicity of the applied field can introduce different condition for constructive interference of the emitted light depending on the scientific purpose. For such "insertion devices", the emitted radiation cone can be wider than the directed beam from the bending magnets, or possess an even narrower angular excursion. The former corresponds to the so-called wigglers, whereas the latter represents the undulators (Figure 2:5). The energy spectrum of an undulator is more sharply peaked at a specific frequency compared to the original accelerated electrons. The fundamental wavelength is approximately scaled by  $\lambda' = \lambda/2\gamma^2$ , where  $\lambda$  is the periodicity of the magnets. The magnet periodicity is firstly Lorentz contracted back to the reference frame for the



unmodulated electrons. Then, the emitted radiation undergoes the Doppler shift with respect to the lab frame. In practice, this relation does not include the contribution of actual electron path through the undulator, and possible non-sinusoidal components of the electron trajectory. The latter may lead to higher-order harmonic contributions. Modern undulators are capable of producing X-ray radiation with arbitrary polarization properties by inducing additional phase shifts in the magnetic field that cause the electron trajectory to move out of the plane of the storage ring.

## 2.4 RIXS Endstation at ADDRESS Beamline, Swiss Light Source

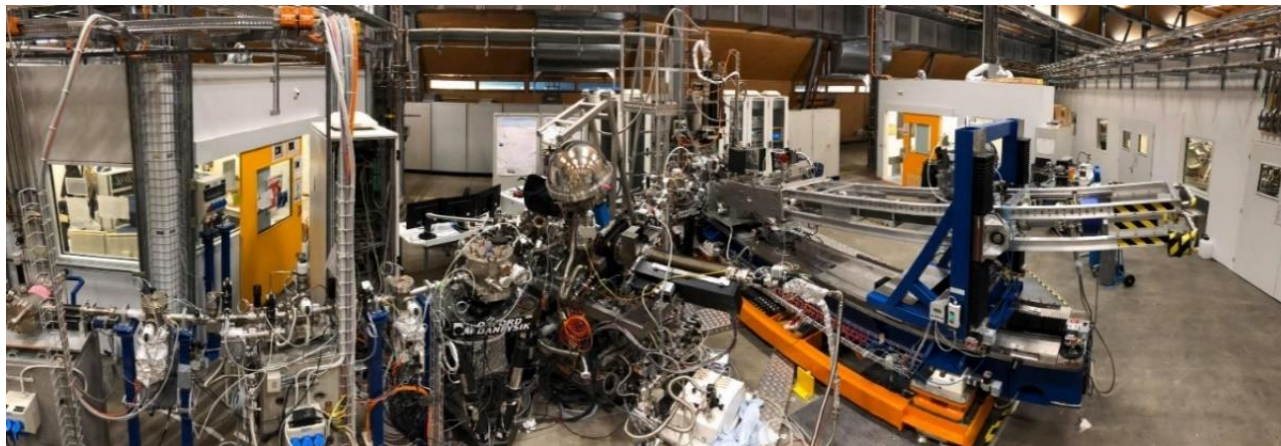


Figure 2:6 ADDRESS beamline.

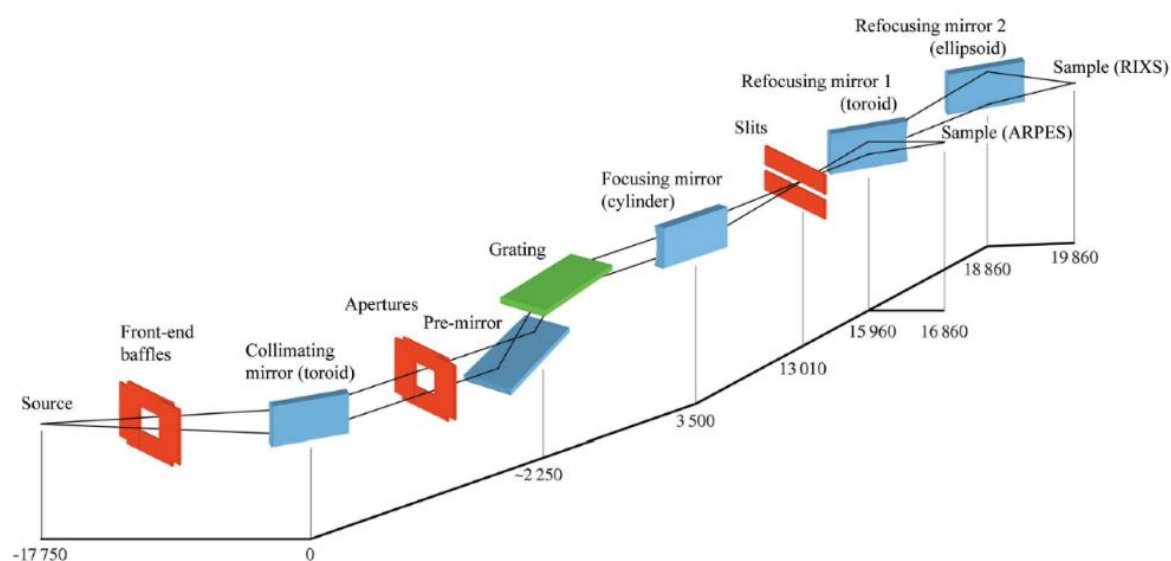


Figure 2:7 Schematics of the optical layout of ADDRESS beamline from ref. [54]. [Open access for the reprint of figure available from: Wiley-Blackwell on behalf of the International Union of Crystallography, Journal of Synchrotron Radiation, V. N. Strocov et al., 17, 631–643, 2010 (<https://doi.org/10.1107/S0909049510019862>)]

The major obstacle for RIXS measurements is the overall weak signal. This is caused by the nature of second-order light-matter interactions in RIXS processes. Therefore, a highly monochromatized beamline with high photon flux, in combination of high-resolution spectrometer for detecting scattered photon, is required. Here the setup of RIXS endstation in soft X-ray ADDRESS beamline at SLS, Paul Scherrer Institut (PSI), is briefly covered (Figure 2:6). The storage ring is operated at the top-up mode, maintaining constant injection of the accelerated electron bunches with a ring current of 400 mA. All the components for the beamline and spectrometer are operated under ultra high vacuum (UHV) because soft X-rays are absorbed by air. To resolve the energy of a photon beam in the soft X-ray range, the use of gratings is mandatory. The characteristic length scale for X-ray diffraction in solid crystals is incompatible with the soft

X-ray photon, leading to a low efficiency for crystal-based energy analyzers. A brief overview is covered in the following, while the technical details can be found in references [54–58].

For the front-end insertion devices, the beamline is equipped with a fixed gap undulator with 75 periods of 44 mm. It provides light with linear (horizontal and vertical) and circular (left and right) polarization with equivalent flux. A series of optical elements are placed to monochromatize and focus the incoming photon beam (see Figure 2:7). The first element is a toroidal collimating mirror that focus the divergent beam, then passing the beam through the exit-slit and onto the monochromator horizontally. The beam passes through an aperture then enters the plane pre-mirror component of the monochromator. The pre-mirror ensures the compensation of emittance angle across different photon energies. The beam is later attenuated by passing through the energy selection channels of a subsequent plane grating, where the energy dispersion is displayed vertically. Here one can choose the probing photon energy for the X-ray beam. There are two choices of monochromator grating available at ADRESS beamline: a blazed 800 line/mm grating and a laminar 2000 line/mm grating. With increasing line density for the grating, the resolving power increases while the photon flux decreases. The last component in the monochromator sector, a cylindrical cylinder, directs the beam horizontally to an ellipsoidal refocusing mirror before the sample chamber. With this setup, a beam size  $\sim 50 \times 4 \mu\text{m}^2$  (horizontal and vertical dimension, respectively) is delivered onto the sample stage with an exit-slit of  $10 \mu\text{m}$ . At 1000 eV, the resultant photon flux is about  $10^{13}$  ph/s/0.01%BW with ring current of 400 mA, representing one of the most high-brilliance sources of the world in the soft X-ray range.

Upon shining X-ray beam onto the sample, the light-matter scattering results in the emitted radiation of different X-ray energies. This includes the elastic and inelastic scattering processes. To discriminate the scattered photon in energies, it requires an optical element to disentangle the outgoing beam with mixed spectral components. For this purpose, the Super Advanced X-ray Emission Spectrometer (SAXES) for the RIXS measurements at ADRESS beamline is briefly addressed here.

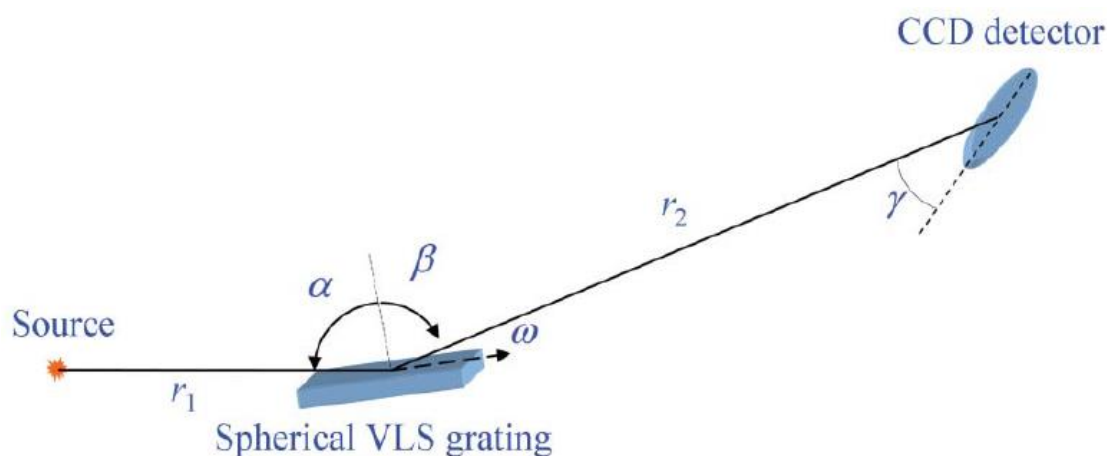


Figure 2:8 Schematics for the optical elements of SAXES at ADRESS beamline from ref. [55]. [Open access for the reprint of figure available from: Wiley-Blackwell on behalf of the International Union of Crystallography, Journal of Synchrotron Radiation, V. N. Strocov et al., 18, 134–142, 2011 (<https://doi.org/10.1107/S0909049510054452>)]

The schematics of the SAXES setup is illustrated in Figure 2:8. The RIXS spectrometer consists of a variable line spacing (VLS) grating and a charge coupled device (CCD) camera for detecting the scattered photon from the sample. The sample is mounted on a Carving manipulator in UHV. Six degrees of freedom including three orthogonal translations and rotations of polar, azimuthal and tilt orientations. The sample stage can be cooled down to a base temperature about 20 K by a Janis liquid helium cryostat, while the temperature is controlled in the range 20–350 K with a heater filament. The first element for the scattered beam to pass through from the sample is a movable mask that selects the correspondent fraction of the VLS grating. This aims to exclude non-ideal regions for the subsequent photon illumination onto the grating, e.g. geometrical edges. The grating is designed to spatially discriminate the energies of scattered photon in terms of vertical height differences on the CCD. In this geometry, the horizontal plane provides the constant-energy orientation. The optimization of energy resolution is achieved by tweaking the incidence pitch angle between the scattered beam and the grating. This is conducted in parallel with compensating the distances from the sample to the spectrometer grating, and the subsequent optical path from the grating to CCD. There are two choices of gratings

installed in the SAXES spectrometer, depending on the purpose of high resolution (3000 line/mm) or high throughput experimental configuration (1500 line/mm). The CCD camera is applied to record the positions of the scattered photons that were previously resolved by the spectrometer grating. To improve the energy resolution, a fine grid is implemented for the CCD readout that provides sub-pixeling in the energy axis. This will lead to overlapping scattered photon events that may cause damping and distortions in the recorded spectra, which are artificial effects onto the measured signal. Therefore, an algorithm specialized for the single-photon counting for centroiding the photon events is applied. The CCD camera is connected to a compressor circulating liquid nitrogen for cooling at -110 °C. This aims for reducing the thermal and electrical noise during the readout of the scattered photon events.

## 2.5 3d Transition-Metal L-edge RIXS

RIXS signal is highly dependent on the probed elemental absorption edges. The complicated cross section is sensitive to the underlying spin, charge, orbital and lattice environments in the measured samples. Particularly, distinct core-hole potentials in the intermediate state pose different criteria for the detectable excitation modes in the RIXS spectra. In this section, a short review of the case studies using metal L-edge RIXS is presented. This comes with the anticipated excitations predicted by theories that were later confirmed in experiments. For relevance to the enclosed thesis, the Cu L<sub>3</sub>-edge RIXS response in the experimental reports on low-dimensional cuprates and nickelates are specifically highlighted.

Charge transfer (CT) excitations have been widely confirmed at the metal absorption edges. The early experiments revealing charge transfer in wide band-gap insulators play the role for showing spectral feasibility of the RIXS technique. At the metal L-edge, a core-hole is introduced at the metal site, which quickly decays and gets annihilated by the charge moving from the surrounding ligands. This leads to the rearranged charge clouds with CT exciton during such indirect RIXS processes, with the main scattering channels of  $\alpha|\underline{c}d^{n+1}\rangle + \beta|\underline{c}d^{n+2}\underline{L}\rangle$  character [47,49]. Here  $\underline{c}$  and  $\underline{L}$  denote the core-hole and ligand un-occupancy, respectively. The electron excited into the 3d shell can directly screen the core-hole without the screening from neighbouring metal sites. Therefore, the observed CT at the metal L-edge mostly occur between the bonding and anti-bonding states of the metal sites, while the non-local screening is quite small in the cross section (see Figure 3:5 in chapter 3).

RIXS enables the detection of crystal field splitting from inter-orbital excitations. This is achieved by the core-hole potentials in the short-lived intermediate state that can allow optically-forbidden processes [47,49]. The coupling between the shake-up exciton in the intermediate state to the inter-orbital transitions is usually weak and unclear for indirect RIXS processes at the metal M-edge. This, however, is relatively well understood for the direct RIXS transitions at the metal L-edge, e.g. inter-orbital excitations for Cu 3d shells (Figure 2:10). A localized picture provides good approximation for a single ion interacting with the crystal field, or the surrounding ligand environments [47,49]. Despite the poor resolution compared to optical spectroscopy, the generally enhanced cross section for dd excitations in RIXS has reproduced clearly defined spectral lines for the crystal field excitations in several transition-metal compounds. Furthermore, these experimentally observed dd excitations can often be well described by the numerical approaches based on a single ion or small clusters [47,49]. The dd signal probed by RIXS allows the characterization of the underlying local distortions and orbital symmetry. This provides a powerful tool to analyse the electronic structure.

Magnetic excitations can also be probed by RIXS, which comprise the main results for chapter 3 and 4 in this thesis. Despite that the spin-spin interactions between the photons and electrons are generally weak, the photon spin can effectively couple to the orbital angular momentum for the electrons. With the presence of the additional field, e.g. spin-orbital interactions, the spin and orbital moments mix such that the spin and orbital angular momentum are no longer well defined quantum numbers [47,49]. For instance, the transfer of spin moment between the incoming photon and electrons in the samples can be achieved at the Cu L<sub>3</sub>-edge RIXS processes (Figure 2:10), given the strong spin-orbital interactions of Cu 2p<sub>3/2, 1/2</sub> core-levels.

A crude physical picture for the single SF processes probed by Cu L<sub>3</sub>-edge RIXS is shown in Figure 2:10. With spin-orbital interactions, the spin and orbital quantum numbers S and L are no longer well-defined, and should be replaced by the total angular momentum  $J = L + S$ . Therefore, by resonantly exciting an electron from Cu 2p<sub>3/2</sub> core-level to Cu 3d



orbitals, this creates a core-hole that can have mixed spin-up and spin-down states in its wavefunction. As a result, a finite cross section of single SF processes ( $\Delta J=0$  and  $\Delta S=1$ ) are allowed in the scattering matrix elements.

This gives unique opportunities for RIXS to measure magnetic excitations with different spin-resolved scattering channels (e.g. total spin  $S=0, 1$  and  $2$ ). In neutron scattering measurements, the dynamical spin-spin correlations between neutron probe and atom nucleus with spin  $1/2$  can lead to a total spin change of  $0$  or  $1$ . For RIXS, on the contrary, an incoming light with total angular momentum  $L=1$  may give rise to the SF processes of  $0, 1$ , and  $2$  [47,49]. Provided by the conservation laws of total angular momentum, this creates the co-existing single and double spin-flip (SF) excitations granted by the RIXS processes [47,49]. With element- and orbital-specific cross section, RIXS can probe inelastic processes beyond the conventional two-site correlation functions, which will be addressed specifically in Chapter 4. Furthermore, studying magnetic excitations using RIXS does not require large sample volume. Experiments for neutron-absorbing materials are also allowed. Combining with the improved optical elements for better RIXS energy resolution, these establish RIXS as a powerful spectroscopic tool for studying low-energy magnetic excitations. In early Cu  $L_3$ -edge RIXS studies on q-1D and 2D cuprates, dispersing  $\Delta S=1$  single SF excitations comparable to the INS works were revealed (see section 3.2). In chapter 3, the  $\Delta S=1$  two-tripion magnetic excitations in the two-leg ladders of the hybrid chain-ladder  $\text{Sr}_{14-x}\text{Ca}_x\text{Cu}_{24}\text{O}_{41}$  materials are studied.

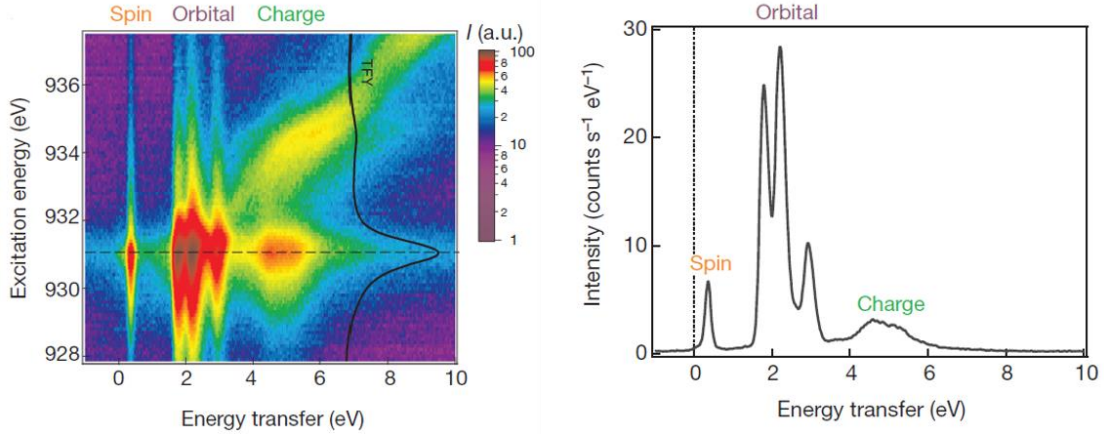


Figure 2:9 Energy dependent Cu  $L_3$ -edge RIXS spectra of  $\text{Sr}_2\text{CuO}_3$  modified from ref. [59]. RIXS spectrum taken at  $q_a = 0.189$  (rlu) is highlighted. Low-energy magnetic, inter-orbital crystal field and charge transfer excitations are shown. The local excitations around 1.85, 2.36 and 2.98 eV correspond to the states for  $xy$ ,  $xz/yz$ , and  $3z^2-r^2$  orbitals (Reprinted by permission from Springer Nature publishing group, Nature, Schlappa J. et al., 485, 82-85, 2012).

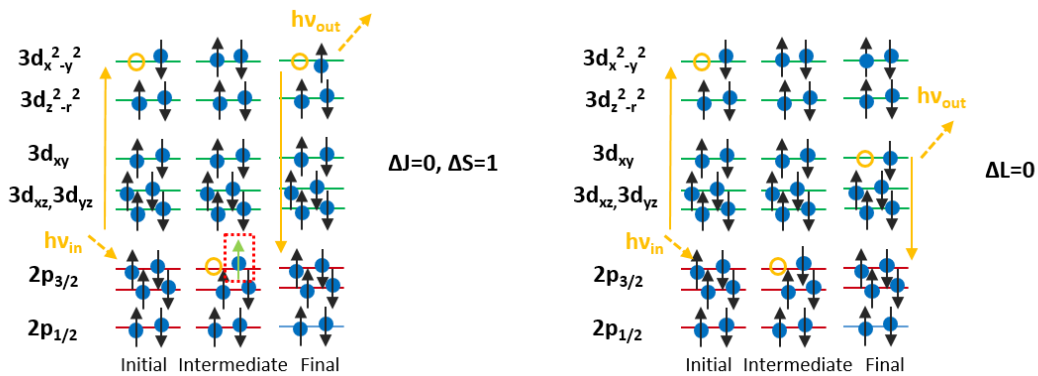


Figure 2:10 Schematics for the  $\Delta S=1$  single SF magnetic excitations and the inter-orbital transitions during the Cu  $L_3$ -edge RIXS processes in a square-planar copper oxide environment. (Left) A finite cross section of the  $\Delta S=1$  process is allowed due to the strong SOC for the  $2p$  core levels, while the transitions between the crystal field splitting of Cu  $3d$  shells are direct RIXS processes at the Cu  $L_3$ -edge.

Lastly, by utilizing the polarization analysis of the incoming and outgoing photon, one can further reveal the character of the probed excitations by RIXS. In recent years, there have been accumulative experimental realization of such polarimetric analysis in the RIXS signal thanks to the rapid instrumental progress. Polarization-dependent RIXS measurements have been demonstrated to be capable of resolving the entangled spin, charge and orbital character for the

probed excitations with overlapping energies [60–65]. Currently, there are three approaches present in existing literature for this type of studies. The first case starts with the assumption that the dynamical structure factors can be approximated by the local fluctuations along with a sufficiently fast core-hole lifetime. An example on the disentanglement between  $\Delta S=1$  and  $\Delta S=0$  scattering channels of magnetic excitations can be found in ref. [60]. In this picture, the RIXS cross section with respect to polarization and momentum dependence can be calculated in the single-ion fashion. Here the symmetry of atomic orbitals are taken into account for the approximated magnetic and charge RIXS cross section by local spin-flip and elastic scattering, respectively [66]. One can thereby extract the de-coupled dynamical spin/charge structure factor by performing the RIXS measurements with different polarization for the incident X-rays (Figure 2:12). **In chapter 3, this analysis is applied for the magnetic excitations in the two-leg ladders of the hybrid chain-ladder  $\text{Sr}_{14-x}\text{Ca}_x\text{Cu}_{24}\text{O}_{41}$  materials.** The next section will give a brief introduction to this method.

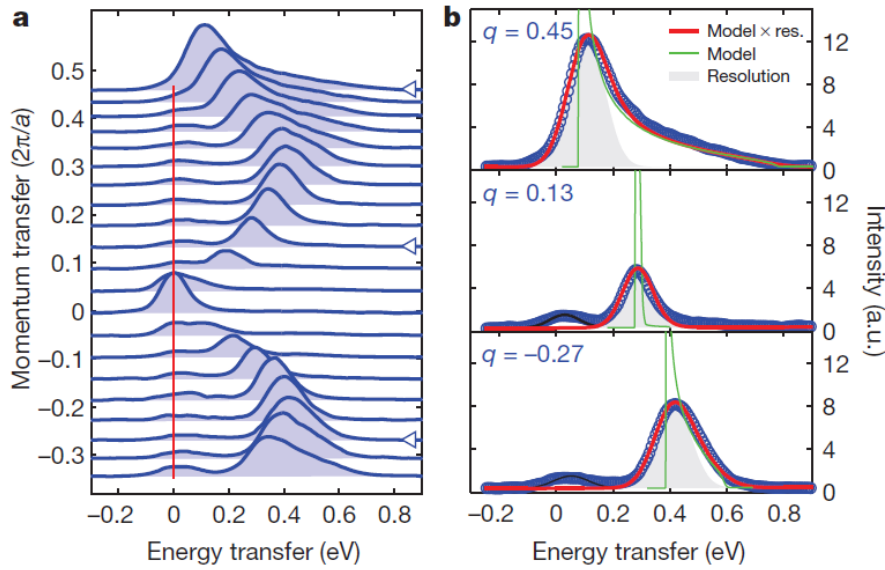


Figure 2:11 Left:  $\Delta S=1$  two-spinon continuum excitations of  $\text{Sr}_2\text{CuO}_3$  probed by Cu  $L_3$ -edge RIXS modified from ref. [59] (Reprinted by permission from Springer Nature publishing group, Nature, Schlappa J. et al., 485, 82-85, 2012).

In first case, the scattered photon remains depolarized with mixed scattering channels. The second method directly tackles this by employing a polarizer with the CCD [73]. This provides the polarization selection for both the incoming and outgoing photon, enabling the mapping for excitations modes with complete polarization dependence [65]. Due to the generally weak RIXS signal, alongside the extra attenuation of the scattered photon from the polarimeter, the existing reports mostly measure at the elemental edges with strong fluorescence yield, e.g. transition-metal L-edge. A third approach has been recently at play in this field. It de-convolutes the spin/charge and inter-orbital RIXS signal by sampling the angular dependence of the RIXS cross section at a given scattering geometry [67]. With this, one can transform the polarization- and azimuthal-dependent RIXS signal into the spin-, charge-, and orbital-resolved dynamical structure factors [67]. This is achieved by solving the equations of RIXS intensity with varied polarization and azimuthal-angle, where the solution provides the scaling relation among different scattering channels based on the scattering tensors at given experimental geometry [67].

### 2.5.1 Polarization-dependent RIXS: Disentanglement between $\Delta S=1$ and $\Delta S=0$ scattering channels

In order to decompose the non-spin-conserving  $\Delta S=1$  and spin-conserving  $\Delta S=0$  scattering of magnetic and charge excitations with overlapping energies, the polarization-dependent Cu  $L_3$ -edge RIXS measurements are applied for the two-spinon continuum excitations of pseudo two-leg ladders  $\text{CaCu}_2\text{O}_3$  demonstrated in ref. [60]. The RIXS spectra are measured with incident X-rays in  $\sigma$  and  $\pi$  polarization at the same geometry. These yield the polarization-dependent magnetic RIXS intensity  $I(\epsilon, q)$  for the low-energy excitations.  $\epsilon$  and  $q$  represent the polarization of the incident X-rays and momentum-transfer, respectively. For practical purposes, the  $\Delta S=1$  and  $\Delta S=0$  scattering disentanglement is

performed with RIXS experiments measured in the grazing emission geometry ref. [60]. This reduces the errors from intensity fluctuations or unphysical results due to the small differences between  $I(\sigma, q < 0)$  and  $I(\pi, q < 0)$  in the grazing incidence geometry [71]. Additionally, the spectral differences from self-absorption effects by applying  $\sigma$  and  $\pi$  polarization for the incident X-rays are also reduced in grazing emission geometry [60]. As described in the ref. [72], the RIXS intensities can be written as:

$$I(\epsilon, \mathbf{q}) = G(\Delta S, E, \epsilon, \mathbf{q}) F(\Delta S, \epsilon, \mathbf{q}).$$

Equation 2:11 Polarization- and momentum-dependent RIXS intensity expressed as the multiplication between spin-resolved dynamical structure factors and form factors given by the scattering cross section.

With the corresponding form factors  $F(\epsilon, \mathbf{q})$  for respective  $\Delta S=1$  and  $\Delta S=0$  scattering, one could solve the dynamical structural factors  $G(\Delta S, E, \epsilon, \mathbf{q})$  from  $I(\epsilon, \mathbf{q})$  that are obtained from RIXS measurements. The key assumption in this method is that the form factors  $F(\epsilon, \mathbf{q})$  are approximated by local SF and charge scattering probabilities  $P(\epsilon, \mathbf{q})$  as:

$$F(\Delta S = 1, \epsilon, \mathbf{q}) \approx P_{SF}(\epsilon, \mathbf{q}); F(\Delta S = 0, \epsilon, \mathbf{q}) \approx P_{EL}(\epsilon, \mathbf{q}).$$

Equation 2:12 Approximation of the RIXS scattering form factors in the single-ion picture.

which can be calculated in the single-ion approximation [66]. The atomic symmetries of core-hole p and valence d orbitals for the  $\text{Cu}^{2+}$  ion are taken into account in these calculations. In this scenario, the momentum-dependence is associated with the changes of projection of atomic orbitals for the initial and final state with varying scattering geometry. *For the given RIXS experimental geometry, this works well for the majority of  $\text{Cu}^{2+}$  electronic configuration in the underdoped ladder subsystem in chapter 3.* The RIXS spectra are normalized with respect to the theoretical dd cross section before evaluating  $G(\Delta S, E, \epsilon, \mathbf{q})$ . This follows the data treatment of the experimental RIXS results in ref. [60] (normalized to dd excitations from 1.5 to 3 eV loss). The error bars for evaluating the extracted spectra are assuming Poisson statistics [60]. The elastic line is removed from the RIXS spectra before the dynamical structure factors  $G(\Delta S, E, \epsilon, \mathbf{q})$  are evaluated from the RIXS intensities  $I(\epsilon, \mathbf{q})$ .

With this approach, the  $\Delta S=1$  and  $\Delta S=0$  RIXS scattering channels were previously resolved in the magnetic excitations of the two-leg pseudo-ladder  $\text{CaCu}_2\text{O}_3$  ( $J_{\text{Leg}} \sim 134$  meV;  $J_{\text{Run}} \sim 11$  meV) in ref. [60] (Figure 2:12). On the left panel, one can see the  $\Delta S=1$  and  $\Delta S=0$  RIXS scattering processes at Cu L<sub>3</sub>-edge with evolution in time. The initial state with  $\text{Cu } 2p^6 3d^9$  configurations evolves into the intermediate state with  $\text{Cu } 2p^5 3d^{10}$ , creating a doublon with two electrons of anti-parallel spins. The  $\Delta S=1$  and  $\Delta S=0$  magnetic scattering corresponds to the situation where the spin-orbit coupling of  $\text{Cu } 2p_{3/2, 1/2}$  core-levels effectively flips/conserves the spins. On the right panel, one can see the disentangled  $\Delta S=1/\Delta S=0$  scattering channels from the polarization-resolved Cu L<sub>3</sub>-edge RIXS measurements. With comparison to calculations, the momentum-dependence of the evaluated spin-resolved spectral intensities were rationalized with distinct time scales of  $\Delta S=1$  and  $\Delta S=0$  scattering channels.

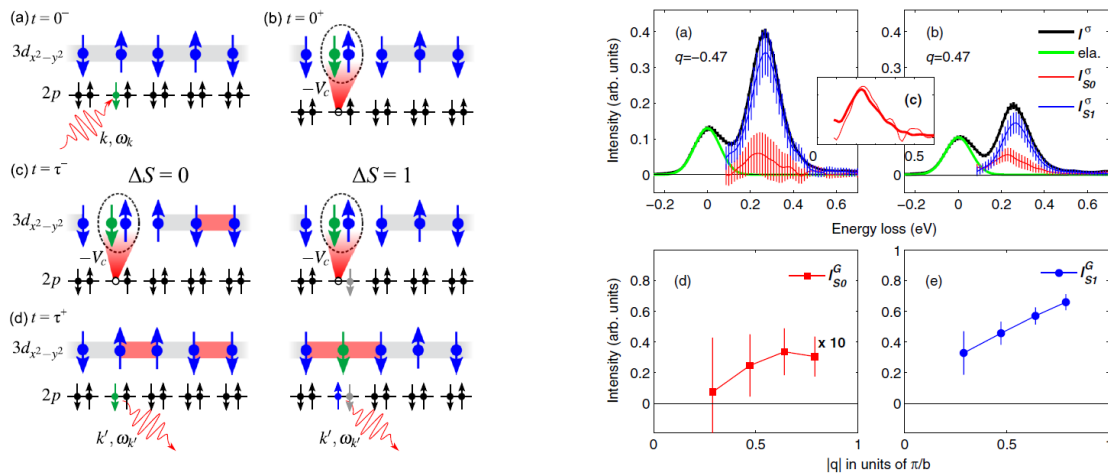


Figure 2:12 Schematics of single and double SF magnetic excitations with different timescales modified from ref. [60]. This was previously revealed by a polarization-dependent Cu L<sub>3</sub>-edge RIXS study on the two-spinon continuum excitations in weakly-interacting two-leg ladders  $\text{CaCu}_2\text{O}_3$  [60]. [Reprinted figure with permission from: V. Bisogni et al., Physical Review Letters, 112, 147401 (2014). Copyright (2014) by the American Physical Society. (<https://doi.org/10.1103/PhysRevLett.112.147401>)]

## 2.6 Oxygen K-edge RIXS

O K-edge RIXS studies on correlated transition metal oxides have been sporadic compared to the metal L-edge. This is in part due to the weak fluorescence yield at the O K-edge that hampers the statistical efficiency for the RIXS signal. The CT excitations probed at O K-edge for low-dimensional oxides are generally predominant in the spectral signal (Figure 2:13). The intermediate state hosts an annihilated O 2p hole that is strongly coupled to the metal d shell, followed by a O 2p electron with different energy quickly filling the unstable intermediate state. This is a direct RIXS process. Experimental observations for high-energy fluorescence based on the above charge transitions have been observed in early studies [47,49]. Furthermore, with the relatively large on-site Coulomb potential for the Cu sites, the O content are predominant for the underlying charge order and fluctuations for the q-1D and 2D cuprates. The ground state of CT type insulator for doped cuprates is of  $\alpha|3d^9>+\beta|3d^{10}\bar{\text{L}}>$  character, where  $\bar{\text{L}}$  is denoted as a ligand hole for the O site [68]. RIXS probe allows the spectroscopic probing for the dynamical charge correlations across the momentum-space, providing information beyond the localized optical processes. This has led to the experimental observations of low-energy charge excitations manifested at the O K-edge, which has been referred to the direct consequences of sensitivity to the charge carriers that are mostly of O 2p nature in the wavefunction [47,49]. Experimental observation of charge-like exciton with Zhang-Rice singlet (ZRS) formalism, electron-hole continuum derived from inter-band transitions, and collective plasmon excitations have been so far reported from the low-dimensional cuprate studies using O K-edge RIXS [69–73].

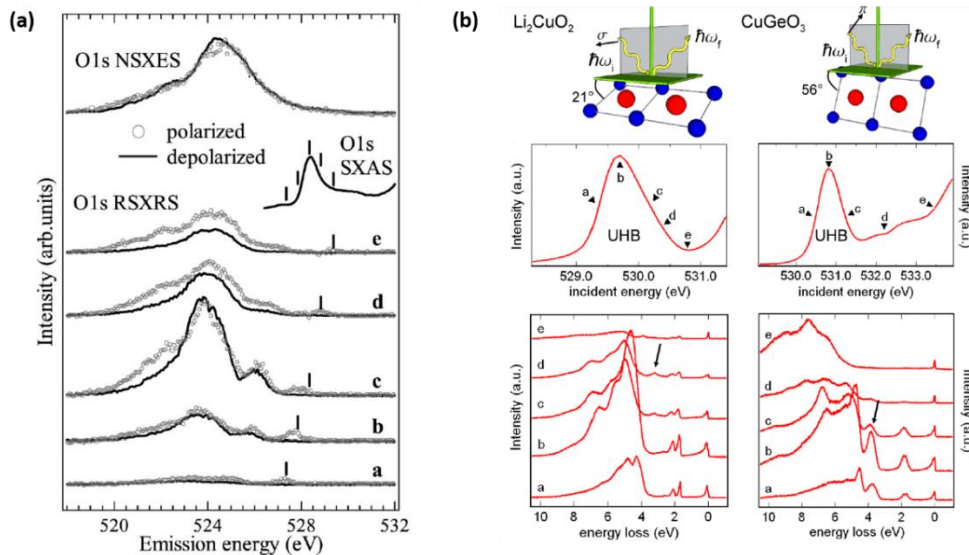


Figure 2:13 Overview of O K-edge RIXS spectra on (a) 2D  $\text{Sr}_2\text{CuO}_2\text{Cl}_2$  from ref. [69] and (b) q-1D cuprates  $\text{Li}_2\text{CuO}_2$  and  $\text{CuGeO}_3$  from ref. [70], respectively. The high-energy excitation spectrum above  $\sim 4.5$  eV are dominated by fluorescence signal. The spectral mode  $\sim 3.7$ –4 eV in  $\text{Li}_2\text{CuO}_2$  and  $\text{CuGeO}_3$  were identified as exciton derived from ZRS. [Reprinted figures with permission from: Y. Harada et al., Physical Review B, 66, 165104 (2002). Copyright (2002) by the American Physical Society. (<https://doi.org/10.1103/PhysRevB.66.165104>); C. Monney et al., Physical Review Letters, 110, 087403 (2013). Copyright (2013) by the American Physical Society. (<https://doi.org/10.1103/PhysRevLett.110.087403>)]

As mentioned in the previous section, double SF processes with a total  $\Delta S=0$  can also be probed by RIXS. Given the weak SOC for the O 1s core level, the cross section for non-spin-conserving  $\Delta S=1$  magnetic excitations is low. In low-dimensional cuprates, this can be conceptualized by the inter-site double SFs through the Cu-O-Cu superexchange when probing at the Cu-O hybridization band (see section 4.6.1). With their higher-order nature, the  $\Delta S=0$  magnetic excitations observed in K-edge RIXS are mostly damped in the spectral profiles, showing a short-lived character. The substantial high-energy spectral weight observed in O K-edge is mostly inaccessible at the metal L-edge, which is directly related to the longer core-hole lifetime at the O K-edge compared to metal L-edge. The high-energy upper bound for the two-magnon (2M) continuum excitations have been reported in undoped and underdoped 2D cuprates [69,74–77] (Figure 2:14, also see section 4.6.1), which was previously shown to be compatible with the calculated 2M spectral density [47,49]. **In chapter 4, the identification of low-energy charge and  $\Delta S=0$  magnetic excitations in the doped cuprate spin ladders of  $\text{Sr}_{14}\text{Cu}_{24}\text{O}_{41}$  are highlighted.**

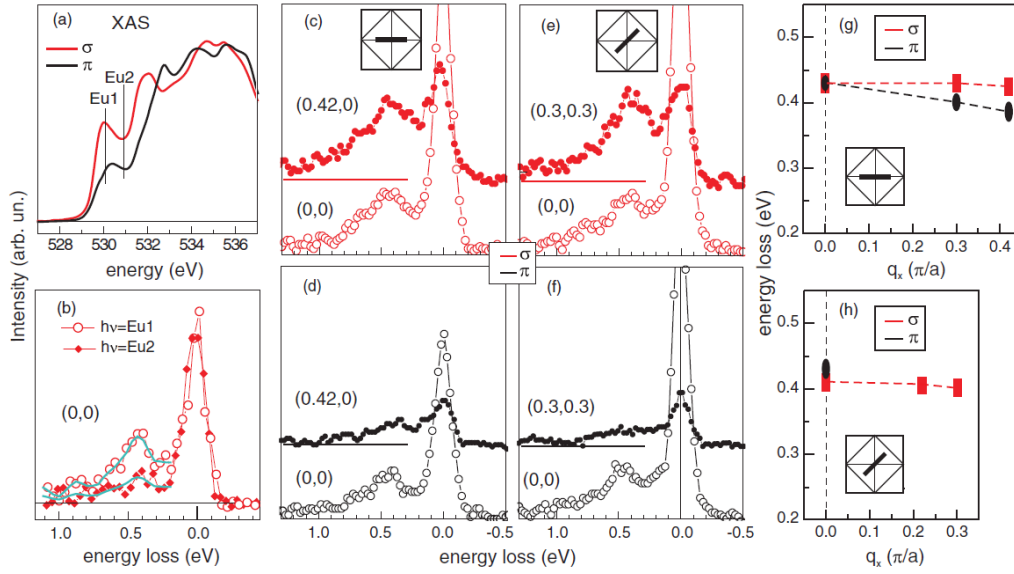


Figure 2:14 Bimagnon continuum excitations in  $\text{La}_2\text{CuO}_4$  revealed by O K-edge RIXS from ref. [74]. (a)-(b) show the O K-edge XAS and RIXS spectra taken at selected incident X-ray energies, Eu1 and Eu2 here. The blue curves in (b) are smoothing data indicated as a guide-to-eye. (c)-(f) are the momentum- and polarization-dependent RIXS spectra taken at Eu1 along  $(\pi,0)$  and  $(\pi,\pi)$ , with grazing incidence scattering geometry and a scattering angle of  $130^\circ$ . The  $\Delta S=0$  bimagnon continuum shows generally flat dispersions and enhanced with  $\sigma$  polarization. The fitted peak positions along  $(\pi,0)$  and  $(\pi,\pi)$  for the observed  $\Delta S=0$  bimagnon continuum are shown in (g) and (h), respectively [Reprinted figure with permission from: V. Bisogni et al., *Physical Review B*, 85, 214527 (2012). Copyright (2012) by the American Physical Society. (<https://doi.org/10.1103/PhysRevB.85.214527>)].

### 2.6.1 Phonon excitations probed by RIXS: Evaluation of electron-phonon coupling

Phonon excitations can be probed by RIXS as well. RIXS probes phonon excitations in a Frank-Condon fashion, where the matrix elements are governed by the overlapping wavefunctions during the two-step photoelectric transitions [78]. The lattice distortion during the intermediate state is translated into the RIXS signal through the sensitivity to the fast rearranged charge cloud. This sets RIXS apart from the conventional techniques for measuring lattice vibrations (e.g. INS and IXS), where the spectral signal is dominated by the electron-phonon coupling (EPC) with respect to the excited orbitals at the given resonance [78]. RIXS takes the advantage of studying phonon excitations owing to the direct probing of momentum-resolved EPC strength among different phonon modes. With the improved energy resolution for the RIXS beamlines in recent years (resolving power 20000 for practical measurements), this has opened up opportunities for investigating the interplay between phonons and other electronic order and excitations in correlated oxides. The multi-phonon scattering can be detected as harmonic satellites in the energy loss spectra using RIXS (Figure 2:15). This grants the direct assessment of the EPC strength from the decay of high-order phonon overtones compared to the fundamental phonons, which has also been extended to the scattering between different vibrational modes demonstrated in recent theories [78].

In this paragraph, the formalism of EPC response in RIXS is briefly covered. For further reading, the interested readers are referred to recommended references [49,78]. To understand the phonon response probed by RIXS, one can start with the electron-phonon interaction Hamiltonian as:

$$H = \sum_{k,q,\lambda} \omega_0 b_{q,\lambda}^\dagger b_{q,\lambda} + M_{q,\lambda} c_{k-q,\lambda}^\dagger c_{q,\lambda} (b_{q,\lambda}^\dagger + b_{-q,\lambda}).$$

Equation 2:13 A generic form of the Hamiltonian describing electron-phonon coupling with the fundamental frequency  $\omega_0$ .

The summation runs over phonons with different momentum  $q$  and branches  $\lambda$  where  $M_{q,\lambda}$  stand for the corresponding EPC self-energies.  $b^\dagger$  ( $b$ ) and  $c^\dagger$  ( $c$ ) are the creation (annihilation) operators for phonons and electrons, respectively. Under dipole approximation, one can denote the dipole operator for two-step RIXS processes as [78]:

$$\hat{D} = \sum_R (e^{-ik_{in}R} c_R^\dagger p_R + e^{ik_{out}R} c_R p_R^\dagger),$$

Equation 2:14 Dipole operator in the scattering amplitude  $A$ .

where  $\hat{D} \sim \mathbf{p} \cdot \mathbf{A}$  where  $\mathbf{p}$  is the momentum operator and the scattering amplitude  $\mathbf{A}$  is

$$A_q = \sum_n \frac{\langle f | \hat{D} | n \rangle \langle n | \hat{D} | i \rangle}{\omega_{det} - E_n + i\Gamma}.$$

Equation 2:15 RIXS amplitude for phonon intensity.

Here  $i$ ,  $n$  and  $f$  stand for initial, intermediate and final states.  $\omega_{det}$  is the detuning energy away from XAS resonance, and  $\Gamma$  is the inverse of core-hole lifetime. For systems described by a single Einstein phonon, the Hamiltonian is reduced with summation over lattice positions  $R$  as

$$H = \sum_R \omega_0 b_R^\dagger b_R + M_R c_R^\dagger c_R (b_R^\dagger + b_R).$$

Equation 2:16 Hamiltonian for electron-phonon interactions of a single Einstein phonon with fundamental frequency  $\omega_0$ .

Despite that a crude physical picture of the local Einstein phonon modes is introduced here, it captures the main spirit of the context discussed in this thesis and the current literature. When a core-level electron is excited to the valence shell, it can locally modifies the neighbouring charge density distribution during the intermediate state. After the fast subsequent annihilation of the unstable intermediate state with a core-hole, there is a finite probability that the system is left behind with an excited state governed by combination of the available populated phonons. This is determined by the symmetry for the atomic orbitals of the initial and final state wavefunctions, leading to the weight factors that dependent on the excited orbitals and vibrational modes involved during the RIXS processes. Therefore, the RIXS phonon intensity is thus proportional to the EPC strength for the excited photoelectrons and the phonons, which can also be affected by the intermediate core-hole potentials. For the simplified picture of an Einstein phonon, suitable for the weakly-dispersive optical phonons that have been reported in updated RIXS experimental reports, the RIXS scattering amplitude for exciting  $n'$  phonon overtones can be expressed as:

$$A_q = \sum_{n=0}^{\infty} \frac{B_{\max(n',n),\min(n',n)}(g) B_{n0}(g)}{z + (g - n)\omega_0},$$

Equation 2:17 RIXS phonon amplitude for an Einstein oscillator.

where the functions  $B_{mn}(g)$  are:

$$B_{mn}(g) = (-1)^m \sqrt{e^{-g} m!} \sum_{l=0}^n \frac{(-g)^l \sqrt{g}^{m-n}}{(n-l)! l! (m-n+l)!}.$$

Equation 2:18 Franck-Condon overlap factors associated with the factorials based on multi-phonon scattering.

$g$  is the dimensionless EPC constant where  $g = M^2 / \omega_0^2$ .  $z = \omega_{det} + i\Gamma$ . The core-hole lifetime for copper/nickel metal  $L_3$ -edge and oxygen K-edge are about  $\sim 0.3$  and  $\sim 0.1$  eV, respectively. For the usual self-energies of the optical phonons  $\sim 30$ -100 meV, the phonon self-energy obtained by soft X-ray RIXS are usually of a few tens meV scale, which is sufficiently smaller than the core-hole lifetime broadening. This sets the criteria for the experimental observation of phonons probed by RIXS, which is empirically supported by the dispersive magnetic excitations reported by RIXS studies on the 3d correlated oxides. The energy dispersions for collective excitations should be overwhelmed by the corresponding lattice vibrations, if the natural timescales for EPC are beyond the core-hole lifetime for given RIXS processes. For dispersive phonons, Equation 2:16 can be generalized into:

$$A_q = \sum_R e^{iq \cdot R} \sum_m \left( \frac{\Pi_{k,\lambda} \langle n'_{k,\lambda} | e^{-S_{R,k,\lambda}} | n_{k,\lambda}(m) \rangle \langle n_{k,\lambda}(m) | e^{S_{R,k,\lambda}} | n_{k,\lambda}^0 \rangle}{z + \sum_{k,\lambda} (g_{k,\lambda} - n_{k,\lambda}(m)) \omega_{k,\lambda}} \right),$$

Equation 2:19 Generalized scattering amplitude for the RIXS intensity of dispersive phonons.



where  $n_{k\lambda}^0$ ,  $n_{k\lambda}$  and  $n'_{k\lambda}$  are the occupation numbers of specific phonon modes with momentum  $k$  and branches  $\lambda$  for the initial, intermediate and final state in the RIXS processes.

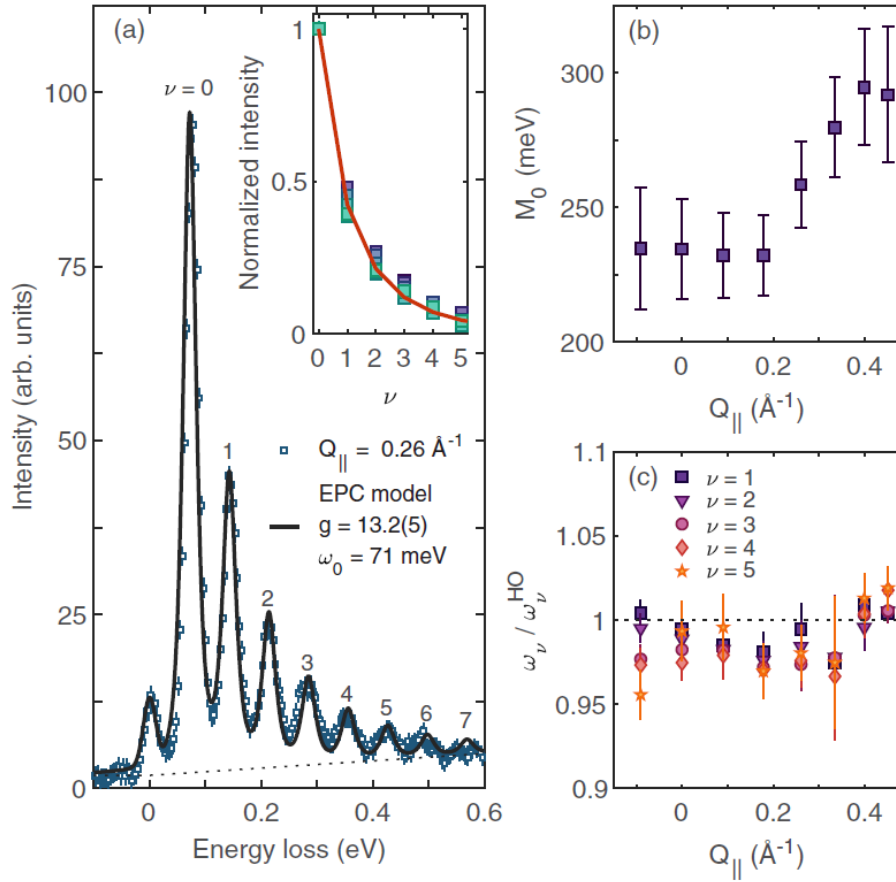


Figure 2:15 Evaluated EPC for the phonon excitations in  $\text{Li}_2\text{IrO}_3$  probed by O K-edge RIXS from ref. [79]. (a) Fitting for the EPC based on local Einstein phonon modes from ref. [78]. The EPC constant  $g$  and phonon self-energy  $M_0$  are assessed by the decay of high-order phonon overtones. (b) Evaluated  $M_0$  as a function of momentum. (c) Evaluated phonon energies for the harmonic profiles. For the high-order overtones, the deviation from ideal harmonic oscillator for may be derived from the anharmonic effects in the measured materials or contribution of EPC based on other phonon modes. [Reprinted figure with permission from: J. G. Vale et al., Physical Review B, 100, 224303 (2019). Copyright (2019) by the American Physical Society. (<https://doi.org/10.1103/PhysRevB.100.224303>)]

With the reasonably fast core-hole lifetime for most 3d transition-metal L-edges, however, the higher-order overtones are often hampered in the scattering cross section. In this case, alternative method for evaluating EPC based on detuning RIXS measurements was recently suggested, and will be introduced in chapter 7. *From the given RIXS experimental configuration in this thesis, the phonon excitations measured by 3d metal  $L_3$ -edge RIXS mainly contributed as the low-energy asymmetry for the quasi-elastic scattering, which will not be the main focus for the experimental results.* For O K-edge RIXS studies on low-dimensional oxides, on the other hand, phonon excitations have been revealed with intense harmonic profiles from multi-phonon scattering. This has been related to the weak charge screening and longer core-hole lifetime for the RIXS processes, which grants the substantial weight for the short-lived multi-phonon processes. Alongside the weak charge screening given by the low-dimensionality, the moderate core-hole lifetime grants the clear detection for vibrational modes at the light O element, including the short-lived higher-order harmonics. This was confirmed in experiments on q-1D cuprate spin-chains, where harmonics of optical phonon modes  $\sim 60$ -70 meV were resolved.

**In chapter 5, the optical phonon excitations are revealed and analysed from the O K-edge RIXS spectra for the q-1D two-leg ladders in the  $\text{Sr}_{14}(\text{Cu},\text{Co})_{24}\text{O}_{41}$  materials.** With the RIXS capability, the site-selective EPC and interplay with other excitation modes have also been discussed using RIXS. **In chapter 6, the molecular-like EPC with predominant multi-phonon vibrational spectra are demonstrated in a geometrically frustrated honeycomb nickelate  $\text{Na}_2\text{Ni}_2\text{TeO}_6$ .**

This is in line with the recent report on O K-edge study on the quantum spin liquid candidate of honeycomb iridates, where the lattice interactions were predicted to play a crucial role for its frustrated magnetism [80].

## 2.6.2 Energy-resolved quasi-elastic scattering probed by RIXS: Charge density wave order

Lastly, the possibility of studying charge density wave (CDW) orders using RIXS is briefly introduced. There have been increasing numbers of experimental reports showing the possibility to study charge- and spin-orders using RIXS as an alternative approach for energy-resolved resonant elastic X-ray scattering (REXS). Here the principle of REXS and its advantage over conventional X-ray diffraction for probing electronic orders is briefly covered, while the interested readers are suggested to refer to the recommended references [23]. One can start with a general picture of the light-matter interactions as derived in section 2.2.2, which involves the terms with linear and quadratic orders of the vector potential  $\mathbf{A}(\mathbf{r}, t)$  and the Hamiltonian described in Equation 2:7. By collecting the terms with linear order of  $\mathbf{A}(\mathbf{r}, t)$ , this constitutes the major contribution for the perturbation of the electrons under the presence of electromagnetic waves. The central element to the elastic scattering here is the transition probabilities for the interacting electrons and photons. Here the initial and final states are assumed to stay in the electronic ground states. Thus, the scattering probabilities can be described by the Fermi's golden rule as in Equation 2:6. The predominant contribution at the first-order in the perturbative formalism reads

$$w^{(1)} = 2\pi \left| \frac{e^2}{2mc^2} \langle \psi_i | \sum_j \mathbf{A}(\mathbf{r}_j, t)^2 | \psi_f \rangle \right|^2,$$

Equation 2:20 The first-order perturbative transition probabilities for the light-matter elastic scattering.

while the second-order term is

$$w^{(2)} = 2\pi \left| \left( \frac{e}{mc} \right)^2 \sum_M \frac{\langle \psi_i | \sum_j \mathbf{A}(\mathbf{r}_j, t) \cdot \mathbf{p}_j | \psi_M \rangle \langle \psi_M | \sum_k \mathbf{A}(\mathbf{r}_k, t) \cdot \mathbf{p}_k | \psi_f \rangle}{E_i - E_M + i\Gamma_M} \right|^2.$$

Equation 2:21 The second-order perturbative transition probabilities for the light-matter elastic scattering.

$E_M$  stands for the available transitions while  $\Gamma_M$  represent the corresponding lifetimes. In the soft X-ray regime, the second-order term is composed of the excitation of the core-level electrons to the valence shell, which is followed by a subsequent re-emission of photons due to the annihilation of the unstable core-hole. One can think of Equation 2:18 as a special case for Kramers-Heisenberg formula. The first-order term, on the other hand, does not involve the excitation of an intermediate state. This is essentially responsible for the Thompson scattering that summarizes the non-resonant scattering from the electronic densities in the ground state. Furthermore, the REXS intensity has a strong energy-dependence in general, where the signal is maximized at the XAS resonances as seen from Equation 2:18. In this manner, the second-order term describes the resonant atomic transition processes, which are directly sensitive to the partial charge modulations of specific element and orbitals. On the contrary, the first-order term sums the total electronic states over the lattice, where the spatial electronic contrast is less significant as it only contributes via structural distortions from both the core and valence electrons. This has the advantage of studying electronic orders with respect to certain ions or orbital-symmetry, where the enhancement in the elastic scattering amplitude  $w^{(2)}$  can be larger than the non-resonant X-ray diffraction  $w^{(1)}$  by a factor  $\sim 100$  in cuprates [81,82].

Compared to prototypical resonant elastic X-ray scattering (REXS), the elastically-scattered outgoing photon in RIXS does not preserve an overall coherence as in the diffraction processes. The pristine elastic charge scattering is indeed one of the major source for the elastic scattering. Other than that, the spectral contribution may also be derived from the diffuse scattering (e.g. surface roughness of the measured samples), and the superstructure reflection of electronic modulation. The latter can enhance the elastic intensity with proximity to the diffraction ordering wavevector. Such resonant enhancement that mimics the anomalous diffraction observed in REXS studies, which have been widely demonstrated for cuprates and nickelates with electronic orders of broken-symmetry ground states, has also been confirmed using RIXS (Figure 2:16). With the spectroscopic capability, the disentanglement between the elastic signal and high-energy inelastic fluorescence poses RIXS as a unique tool for studying CDW orders. Additionally, the concomitant elastic and inelastic scattering channels in RIXS allows the direct assessment of dynamical response in vicinity to the



electronic orders. *In chapter 5, the CDW formation alongside their interplay with phonon excitations in the two-leg ladders of  $\text{Sr}_{14}(\text{Cu}_{1-x}\text{Co}_x)_{24}\text{O}_{41}$  are revealed by O K- and Cu L<sub>3</sub>-edge RIXS.*

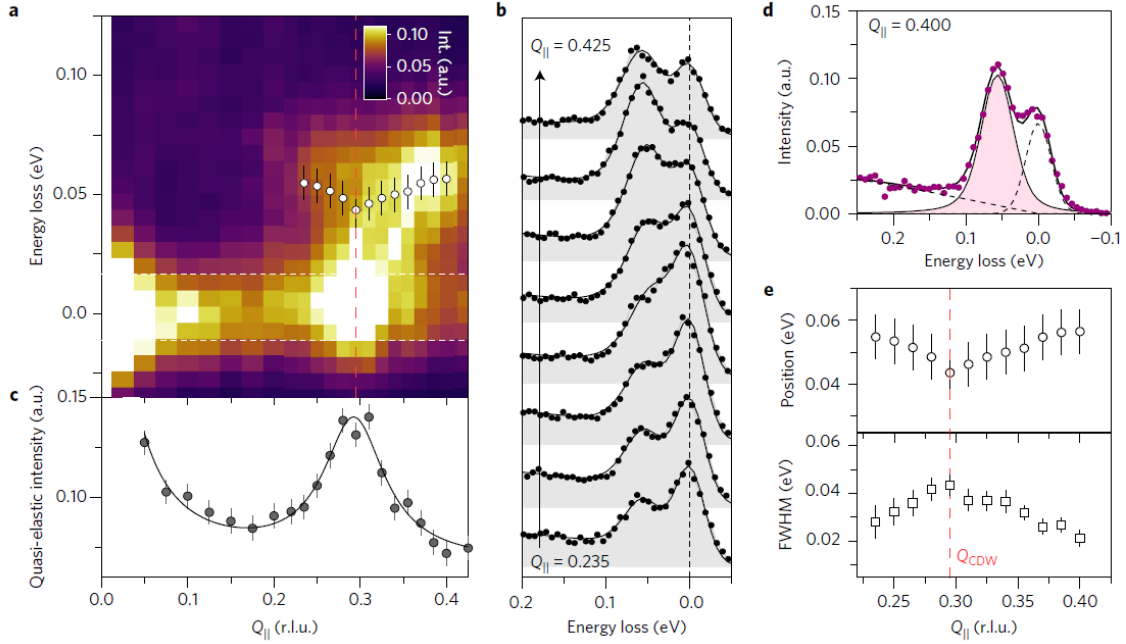


Figure 2:16 Cu L<sub>3</sub>-edge RIXS study on the CDW orders and phonon excitations for the SC cuprates Bi<sub>2</sub>Sr<sub>2</sub>CaCu<sub>2</sub>O<sub>8+x</sub> modified from ref. [83]. (From left to right) (a) Energy-resolved elastic and inelastic RIXS spectra as function of momentum. (b) Selected RIXS spectra across the CDW ordering  $\sim 0.3$  rlu along  $(\pi, 0)$  with separated elastic scattering and phonons. (c) Quasi-elastic intensity as a function of momentum, with enhanced in-plane diffraction  $\sim 0.3$  rlu. (d) Fitting example for elastic scattering and phonon excitations with a linear background. (e) The fitted phonon energies and widths as function of momentum, showing the phonon softening and broadening in vicinity to CDW ordering (Reprinted by permission from Springer Nature publishing group, Nature Physics, Chaix L. et al., 13, 952-956, 2017).

## 2.7 Self-Absorption Correction for the RIXS Spectra

In this section, the RIXS spectral treatment to account for the self-absorption effects is briefly covered. In principle, when collecting the inelastically scattered photon from the samples, the outgoing X-rays can be re-absorbed by the measured samples through the penetrated region. This leads to a damping for the emitted photon signal that distorts the RIXS spectral, which depends on the experimental geometry as well as the energies for the incoming and outgoing X-rays [61,84]. Particularly, the quasi-elastic regime in the RIXS signal suffer the most from the self-absorption distortions, given the strong absorption coefficients for the emitted photon energy near the XAS resonances. The self-absorption processes can be described in two steps. Firstly, from Figure 2:17, the incident photons will experience the exponential reduction in intensities due to the absorption from the samples, which can be expressed as

$$dI \propto -\mu(E_i)e^{-\mu(E_i)l}dl.$$

Equation 2:22 The fraction of absorbed intensity for the incoming X-rays traveling a total length  $L$ , which considers the self-absorption from the samples within an infinitesimal length  $dL$ .

$E_i$  is the incident photon energy.  $\mu(E_i)$  is the energy-dependent absorption coefficient for the incoming X-rays. If one focuses on an infinitesimal length along the light path for interior of illuminated samples, a certain fraction of the outgoing X-rays will get absorbed again by the measured samples, therefore result in the RIXS intensity in as:

$$dI(E_i, E_f, l) \propto \mu(E_i)e^{-\left(\mu(E_i) + \mu(E_f)\frac{\sin(\alpha)}{\sin(\beta)}\right)L}dL.$$

Equation 2:23 The obtained RIXS intensity after including the self-absorption for both the incoming and outgoing X-rays.

$E_f$  is the emitted photon energy.  $\mu(E_f)$  is the energy-dependent absorption coefficient for the outgoing X-rays.  $\alpha$  and  $\beta$  are the incidence and emission angles for the incoming and outgoing X-rays with respect to the sample surface, respectively. By integrating the probed sample region, one obtains the total RIXS intensity as

$$I(E_i, E_f) \propto \left( 1 + \frac{\mu(E_f) \sin(\alpha)}{\mu(E_i) \sin(\beta)} \right)^{-1}.$$

Equation 2:24 The integrated RIXS intensity with self-absorption corrections.

In the practical XAS experiments, the relative absorption intensities compared to the pre-edge and post-edge XAS signal, which are generally structure-less background that provide background signal level for normalizing the absorption coefficients. For specific evaluation, these values are commonly compared and normalized to the tabulated photoelectric absorption cross section [85]. Generally speaking, the absorption coefficients are functions of the orientations for the light polarization vectors with respect to the crystallographic directions. In a simplified scenario, the dichroism is either negligible for an isotropic sample [84]. However, for low-dimensional materials, emission light with different polarizations ( $\sigma$  and  $\pi$  in this thesis) give distinctive self-absorption attenuation [84]. The polarization analysis of outgoing photon in the RIXS processes requires the polarimeter at the photon detector, which is beyond the scope of the enclosed thesis. To minimize the self-absorption effects from the outgoing photon, RIXS measurements in this thesis are mostly performed with grazing incidence scattering geometry such that the major self-absorption attenuation is dominated by the incoming photon [84], where the light polarization is known.

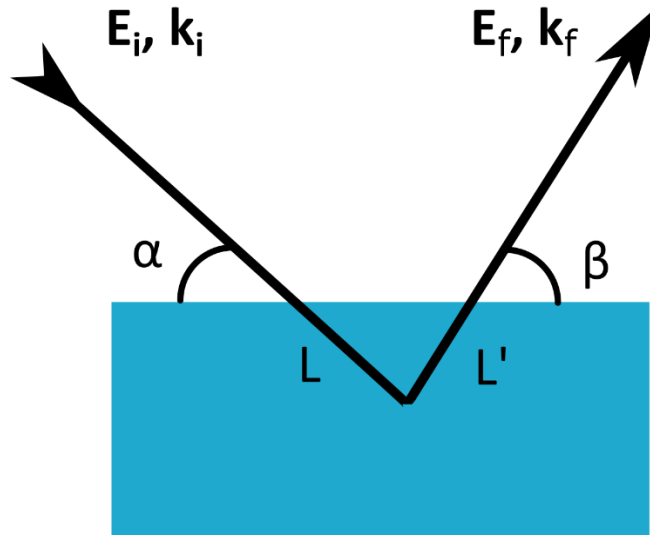


Figure 2:17 Illustration for the required parameters when evaluating self-absorption corrections in a given RIXS experimental geometry.



# Chapter 3 Crossover of the high-energy spin fluctuations from collective triplons to localized magnetic excitations in doped $\text{Sr}_{14-x}\text{Ca}_x\text{Cu}_{24}\text{O}_{41}$

## 3.1 Project Contribution

The content of this chapter is based on an article manuscript that has been submitted to the journal Physical Review Letters. In this chapter, I investigate the high-energy momentum-resolved magnetic excitations in the two-leg ladders of the hybrid chain-ladder material  $\text{Sr}_{14-x}\text{Ca}_x\text{Cu}_{24}\text{O}_{41}$  (SCCO,  $x=0$  & 12.2) using Cu  $L_3$ -edge RIXS. In this work, I, Yi Tseng, am responsible for the experiment planning, preparation of the experimental setup, alignment and in-situ cleaving of the samples, performing the RIXS measurements and the experimental data analysis. Calculated RIXS spectra using DMRG method were provided by Jinu Thomas, supervised by Steven Johnston and Alberto Nocera. The paper is written by me as the main responsible with input from Jinu Thomas, Steven Johnston and Thorsten Schmitt. Section 3.2 serves as an additional introduction giving extended background information for the context of this work, including the figures 3:1 - 3:3. The submitted paper includes the content from section 3.3 to 3.8, including the figures 3:4 - 3:14.

## 3.2 Preamble

The motivation of studying magnetic excitations in the ladder subsystem of SCCO lies in their close resemblance to  $\Delta S=1$  paramagnon modes in hole- and electron-doped 2D SC cuprates. With an energy range of the magnetic superexchange interactions up to  $\sim 100$  meV, the occurrence of SC phases by doping long range ordered antiferromagnetic compounds have promoted high-energy magnetic fluctuations as a compelling candidate for mediating HTSC in cuprates [8]. Despite the large efforts made in both experimental and theoretical studies in the last two decades, the role of magnetism in the emergence of pairing fluctuations in cuprates remains elusive. The undoped antiferromagnetic phases display  $\Delta S=1$  spin-wave fluctuations that not only persist with doping but survive up to the overdoped phases, transforming into the so-called damped paramagnon excitations (Figure 3:1). The character of the itinerant paramagnon response, with a non-uniform doping evolution across different momentum/energy regimes, remains heavily debated. This has led to proposals involving other possible sources to reconcile the minimal-interaction models for HTSC based on singlet-pairing, e.g. interplay with dynamical charge correlations of overlapping excitation energies [62], non-negligible inter-layer magnetic exchange interactions [86] and quantum criticality for spin susceptibility around the optimal doping [61,87]. On the other hand, the concurrent local magnetic moments and itinerant quasiparticles have also posed great difficulties to current theory in reconciling the dynamics of charge-doped cuprates. The inclusion of high-order electron hopping can improve the calculated dynamical spin structure factor, but may provide unphysical higher-order parameters that are not well-defined observables to examine experimentally [88,89]. To sum up, the role and nature for magnetism in the HTSC phase of cuprates is still elusive.

In this respect, Cu  $L_3$ -edge RIXS studies on cuprate ladders provide unique opportunities to tackle this issue. Given the strong spin-orbital interactions in Cu 2p core levels, numerous works have demonstrated Cu  $L_3$ -edge RIXS as an effective tool for investigating the dispersing  $\Delta S=1$  magnetic excitations in cuprates, comparable to experiments with INS [49]. Furthermore, with the help of polarimetric analysis of the incoming and scattered photons, polarization-resolved RIXS enables the disentanglement of the magnetic and charge sectors for the dynamical structure factors with doping [60–65]. On the other hand, cuprate ladders represent the ideal alternative models to study cuprates. In early theories, even-leg ladders were conceptualized as the 2D  $\text{CuO}_2$  planes with arrays of line defects introduced, resulting in similar d-wave SC with a different temperature scale [9–11]. Along with several similarities to 2D cuprates, e.g. high-energy magnetic exchange [17] and non-Fermi liquid transport behaviour [90], a SC phase was also confirmed in SCCO with high Ca content ( $x>11$ ) and applied static pressure of about few GPa [19,20]. Lastly, the quasi-one-dimensional (q-1D) lattice environments of spin ladders significantly reduce the complications for theoretical studies. Measuring the

magnetic excitations of cuprate ladders will thereby provide valuable insight into the role of magnetism for HTSC in cuprates.

In spite of the extensive studies on cuprate ladders, the exact relation between hole content, chemical doping (e.g. Sr replaced by Ca, Y, and La in SCCO) and magnetic excitations at different energy scales are still inconclusive. The magnetic exchange couplings for the ladder subsystem in SCCO were confirmed to be in close vicinity to the isotropic limit ( $J_{\text{Rung}}=J_{\text{Leg}}$ ), where the gapped  $\Delta S=1$  singlet-to-triplet processes (triplons) reasonably capture the essence of the elementary excitations [9,91]. Despite being fundamentally different from the Goldstone mode spin-wave excitations in 2D cuprates, the magnetic excitations in ladder compounds display stark similarities with the 2D cuprates in the high-energy regime [21,22,92]. Mean-field based studies predicted a larger spin gap in spin ladders upon doping, and suggested its high importance to pairing correlations [10,27]. Numerical works, however, indicated a decrease of the triplon gap with elevated hole carrier levels [93,94].

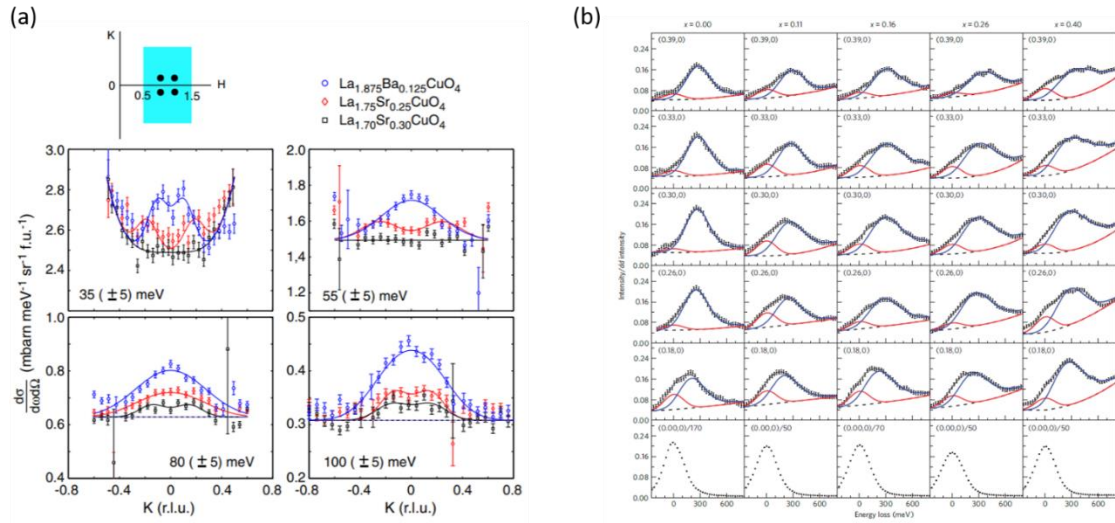


Figure 3:  $\Delta S=1$  paramagnon in 2D cuprate  $\text{La}_{2-x}(\text{Ba,Sr})_x\text{CuO}_4$  probed by (a) INS from ref. [95] [Reprinted figure with permission from: S. Wakimoto et al., Physical Review Letters, 98, 247003 (2007). Copyright (2007) by the American Physical Society. (<https://doi.org/10.1103/PhysRevLett.98.247003>)], and (b) Cu  $L_3$ -edge RIXS from ref. [96] (Reprinted by permission from Springer Nature publishing group, Nature Materials, Dean M. D. M. et al., 12, 1019-1023, 2013).

The doping level is a parameter directly connected with the band filling and therefore, it is fundamental in the physics of Mott insulators, as it ultimately determine the ground state electronic properties. The experimental methods for quantifying doping and its effect on the magnetic fluctuations have remained similarly debated. Optical and transport measurements inferred an increased low-energy weight and suppressed resistivity in SCCO with isovalent Sr-Ca substitution [90,97]. This was interpreted as enhanced conductivity from increasing hole density in the ladder subsystem by increased Ca content, as the transport behaviour was suggested to be dominated by the two-leg ladders with their  $180^\circ$  Cu-O-Cu bond angles [97]. This was further supported by bond-valence sum and Madelung potential calculations [36,98]. Similar with 2D cuprates, the quantification of hole content in q-1D SCCO can be carried out by O K-edge XAS analysis, as the doped hole carriers are mostly of O 2p character and form pre-edge peaks in the O  $1s \rightarrow 2p$  XAS process [99–102]. However, a recent *ab initio* study revealed that the interaction with charge localization and antiferromagnetic order in the chains should be taken into consideration to evaluate the hole content [103]. Compared to the phenomenological modelling of early XAS studies, large errors up to a factor up to  $2\sim 5$  was inferred by including/excluding the charge and magnetic correlation effects for Sr14 [103]. An error for estimating the ladder hole density up to a factor of 2-5 was predicted by not considering the charge and magnetic correlations in the chain subsystem from these first-principle calculations [103].

Additionally, the understanding of magnetic excitations as a function of doping in cuprate ladders is unclear. Only scarce experimental information associated with momentum-dependent spin excitations does so far exist. Experiments using INS showed an unchanged triplon gap energy  $\sim 32$  meV at ( $q_{\text{Leg}}=\pi$ ,  $q_{\text{Rung}}=\pi$ ) from  $x=0$  to  $x=12.2$  (Figure 3:2) [104,105], suggesting an Ca-doping-independent behaviour for the  $S=1$  triplon excitations. Studies using NMR, on the contrary, revealed a decrease in the triplon gap energy with increasing Ca content [106], which developed into a

gap collapse at elevated static pressure (Figure 3:3) [107]. Additionally, both techniques have so far addressed the doping dependence of triplons close to the momentum region where ( $q_{\text{Leg}} \sim \pi$ ,  $q_{\text{Rung}} \sim \pi$ ). More detailed, experimental studies are still lacking on the doping evolution of spin fluctuations in the ladders, covering a large fraction of the Brillouin zone. These uncertainties hamper the understanding of the initial electronic condition of SCCO before emergence of a SC phase as well as the role of chemical and static pressure for the electron-pairing.

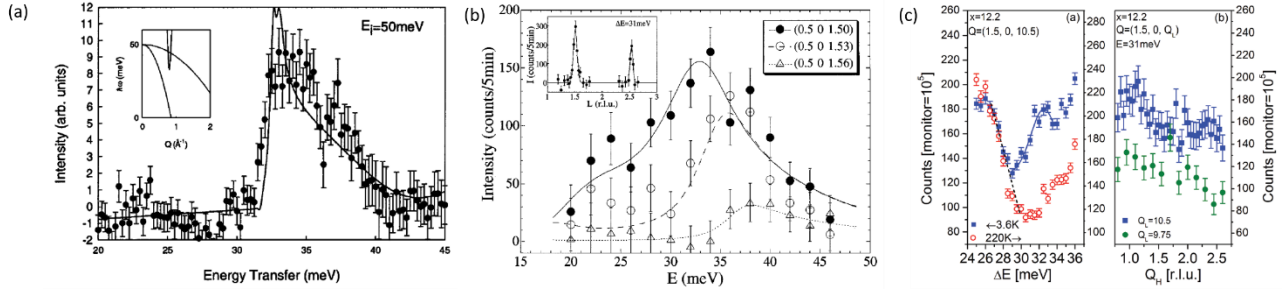


Figure 3:2 INS measurements for the 1T gap around  $q=(q_{\text{Leg}}=0.5, q_{\text{Rung}}=0.5)$  of SCCO with (a)  $x=0$  from ref. [17], (b)  $x=11.5$  from ref. [104], and (c)  $x=12.2$  from ref. [105]. From these studies, the 1T excitation energy of SCCO shows marginal Ca-doping dependence at  $q=(q_{\text{Leg}}=0.5, q_{\text{Rung}}=0.5)$ , where a spin gap  $\sim 32$  meV persists up to  $x \sim 11-12$ . [Reprinted figures with permission from: R. Eccleston et al., *Physical Review Letters*, 81, 1702 (1998). Copyright (1998) by the American Physical Society. (<https://doi.org/10.1103/PhysRevLett.81.1702>); S. Katano et al., *Physical Review Letters*, 82, 636 (1998). Copyright (1998) by the American Physical Society. (<https://doi.org/10.1103/PhysRevLett.82.636>); G. Deng et al., *Physical Review B*, 88, 014504 (2013). Copyright (2013) by the American Physical Society. (<https://doi.org/10.1103/PhysRevB.88.014504>)).

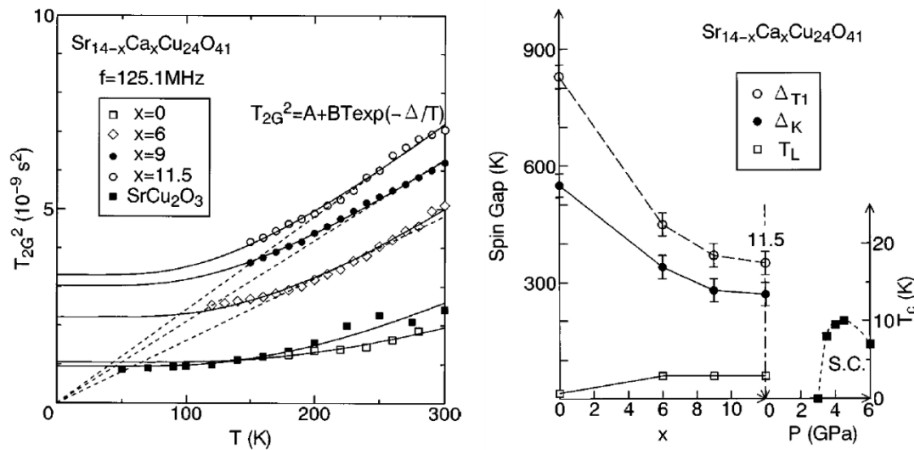


Figure 3:3 NMR measurements for the 1T gap, Knight shift and  $T_1$  in SCCO as a function of Ca content [106]. A decreasing 1T gap was observed with elevated Ca-doping [Reprinted figure with permission from: K. Magishi et al., *Physical Review B*, 57, 11533 (1998). Copyright (1998) by the American Physical Society. (<https://doi.org/10.1103/PhysRevB.57.11533>)).

In this chapter, the magnetic spectral evolution from collective two-triplon (2T) excitations ( $x=0$ ) to incoherent damped modes with larg gap near zone center ( $x=12.2$ ) is revealed by Cu  $L_3$ -edge RIXS measurements. In this work, the scattering geometry is chosen with  $q_{\text{Rung}}=0$ , i.e. with a negligible projection of the exchanged momentum along the rung direction, such that the multi-triplon scattering with even-parity is enhanced [91]. This is achieved due to the selection rule for the scattering cross section of the multi-triplon response in momentum- and energy-resolved spectroscopies [91], e.g. INS and RIXS [12,13,108]. This contributes a direct doping dependent assessment of spectral changes in the high-energy magnetic RIXS response towards the zone center with  $q_{\text{Rung}}=0$ , which has not been covered in the current literature. A previous Cu  $L_3$ -edge RIXS study at  $x=0$  had revealed that the high-energy magnetic excitations are dominated by the triplon excitations in the ladders [13]. With the help of model DMRG calculations on doped ladder clusters, we interpret the presence of weakly-dispersive damped magnetic excitations at  $x=12.2$  as due to a suppressed carrier mobility, despite an increase in the hole content determined from O K-edge XAS. In SCCO, the RIXS spectra calculated considering an exchange coupling ratio  $r=J_{\text{Rung}}/J_{\text{Leg}} \sim 1$ , estimated from structural data and doping levels determined from XAS, show a clear downturn in the momentum dispersion of the magnetic excitations closed to zone center upon doping. This prediction is not compatible with the experimental observation, suggesting that other factors beyond

charge doping, e.g. enhanced hole localization, are required to account for the observed flattened dispersions and spectral broadening in the RIXS response. [26]. Polarization-dependent RIXS studies have shown how the spin-conserving  $\Delta S=0$  scattering channel undergoes a spectral weight depletion for the low-energy dynamical charge response. This result is reflective of a hole-immobilized scenario which is also captured by the model DMRG calculations. Despite the important insight into the magnetic and charge dynamics, a comprehensive understanding of their momentum and (chemical) doping dependence in doped ladders is still lacking. With the experimental RIXS results in this chapter, I will tackle this open question in SCCO that have been revealed with SC phases upon applied pressure [18,19].

### 3.3 Abstract

We studied the magnetic excitations in the quasi-one-dimensional (q-1D) self-hole-doped ladder subsystem of the hybrid chain-ladder material  $\text{Sr}_{14-x}\text{Ca}_x\text{Cu}_{24}\text{O}_{41}$  (SCCO) using Cu  $L_3$ -edge resonant inelastic X-ray scattering (RIXS). By comparing momentum-resolved RIXS spectra without ( $x=0$ ) and with high Ca content ( $x=12.2$ ), we track the evolution from collective two-triplon (2T) excitations ( $x=0$ ) to weakly-dispersive gapped modes at an energy  $\sim 280$  meV ( $x=12.2$ ). Density matrix renormalization group (DMRG) calculations of the RIXS response suggest that the flat magnetic dispersion and the damped excitation profile observed upon doping originates from enhanced hole localization. This result is supported by polarization-dependent measurements, where we disentangle the spin-conserving  $\Delta S=0$  scattering from the predominant  $\Delta S=1$  signal in the RIXS spectra. The extracted  $\Delta S=0$  channel shows spectral weight depletion in the low-energy dynamical charge response, when Sr is replaced by Ca, consistent with the suppressed carrier mobility. Our study characterizes the magnetic and charge fluctuations for the precursor of pairing fluctuations in SCCO, for which superconductivity is achieved at elevated pressure.

### 3.4 Introduction

Antiferromagnetic spin fluctuations are a promising candidate for mediating high-temperature superconductivity (HTSC) in cuprates [8]. However, despite extensive studies, the precise relationship between magnetism and SC across the phase diagram of copper oxides remains unclear. This is in part due to the fact that modelling the competition between local moment formation and itinerant quasiparticles with charge doping is a tremendously difficult problem. The quasi-one-dimensional (q-1D) spin ladders [Figure 3.4(b)] serve as an ideal platform to tackle this issue. In fact, doped cuprate ladders share several similarities with two-dimensional (2D) SC cuprates, such as high-energy spin-fluctuations [17], d-wave pairing [9–11], non-Fermi-liquid transport behavior [90], and magnetic exchange couplings  $\sim 100$  meV [17]. At elevated pressure of in the range 1.5 to 8 GPa, a SC phase was confirmed in the hybrid chain-ladder materials  $\text{Sr}_{14-x}\text{Ca}_x\text{Cu}_{24}\text{O}_{41+\delta}$  (SCCO) for  $11 < x < 14$  [19,20]. Therefore, the low-dimensional SCCO contains the fundamental ingredients for cuprate superconductivity, providing a unique playground for exploring the role of dimensionality, lattice connectivity and spin-charge coupling in this class of materials. Moreover, their low dimensionality makes the q-1D spin ladders easier to model with respect to their 2D counterpart, making the problem easier to approach from the theoretical side [9–11,109]. For the above reasons, characterizing the magnetic excitations in doped cuprate ladders, and their evolution with doping, will help us reaching a better understanding of HTSC in cuprates.

Magnetic excitations in even-leg ladders can be viewed as coupled-spinons, i.e. triplons, due to the intra-ladder exchange interactions across their rungs [Figure 3:4(b)] [9–11]. The expected gapped excitation spectrum associated with these triplons has been identified by several experimental works [91], and suggested to be central for the SC fluctuations upon doping [9–11,27,93]. Early studies also showed that the collective triplon excitations in the high-energy regime closely resemble the prototypical “hourglass” magnetic excitations in 2D SC cuprates [21,22,92]. However, a complete description of the evolution of the triplon excitations and relative dispersion relations upon doping is still lacking. Inelastic neutron scattering (INS) experiments discovered that the one-triplon (1T) gap at  $(q_{\text{Leg}}=\pi, q_{\text{Rung}}=\pi)$  survives up to  $x=12.2$ , and remains nearly unchanged compared to  $x=0$  in SCCO [104,105]. Nuclear magnetic resonance (NMR) studies, on the other hand, indicated a decreasing triplon gap with increasing Ca content, which further developed into a gap collapse at elevated pressure [106,107,110]. Furthermore, although dispersive triplon excitations have been reported in the nearly undoped ladder  $\text{Sr}_{10}\text{La}_4\text{Cu}_{24}\text{O}_{41}$  using INS [12], their corresponding doping-dependence across the reciprocal space is still lacking. The spectral response of the spin fluctuations in cuprates reacts to doping in



a non-uniform fashion across different energy and momentum regimes [8]. Therefore, a systematic assessment of the triplon response across a large fraction of the Brillouin zone, along with the exact relation to chemical pressure (induced by Ca-substitution), is of high importance to understand the role of spin fluctuations for the pairing in SCCO.

Additionally, the experimental quantification of the hole doping as a function of the Ca content remains inconclusive. In early experiments on SCCO, an increase in the low-energy Drude-like weight in conductivity and enhanced metallicity in transport measurements were observed with elevated Ca content, which led to the conclusion that the holes get transferred from the chain to the ladder subsystem upon isovalent Sr-Ca substitution [36,97,98]. In fact, the 180° Cu-O-Cu bond angle in two-leg ladders may result in the ladder subsystem dominating the transport characteristics [19,20,90]. Recent studies, however, revealed that errors up to a factor of 2 to 5 can occur in quantifying the ladder hole content when the interplay with charge and magnetic correlations in the chains is not taken into consideration [103].

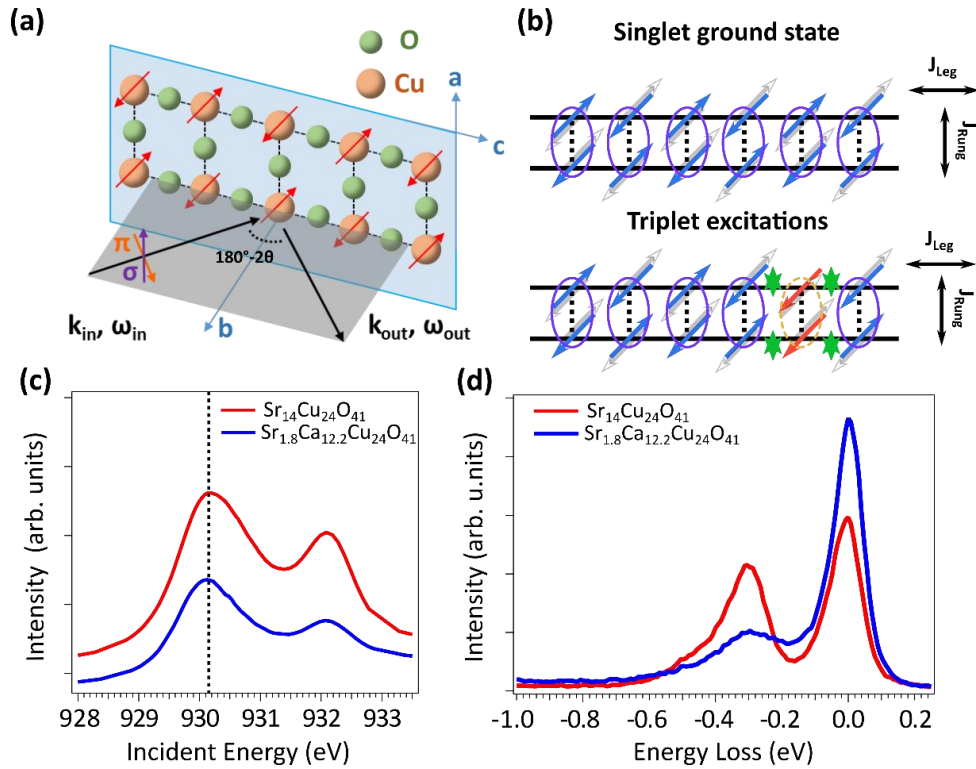


Figure 3:4 Schematics of (a) RIXS experimental geometry with the orientation of the two-leg Cu<sub>2</sub>O<sub>3</sub> ladders in SCCO. The ladder-leg direction is along c-axis, with lattice constant  $c_{leg} \sim 3.9$  Å. (b) Upper panel: Two-leg quantum spin ladders of local antiferromagnetic interactions along the ladder leg and rung, with spins (blue arrows) having equal probability pointing along any directions (for instance, the opposite one denoted as gray arrows). The rung-singlets (purple ellipses) interact through ladder-leg exchange coupling. Bottom panel:  $\Delta S=1$  triplon excitations (orange dashed-line ellipse) in two-leg ladders, consisting of a singlet-triplet excitation with two coherent domain walls (green arrows). (c) Main resonances of Cu L<sub>3</sub>-edge XAS. 3d<sup>9</sup> white line is marked by the black dashed-line. (d) Cu L<sub>3</sub>-edge RIXS spectra taken at 3d<sup>9</sup> peak of  $q_{leg} = -0.31$  (r.l.u) in  $\sigma$  polarization. Here, a negative (positive) momentum-transfer indicates the RIXS data taken in grazing incidence (emission) geometry.

Owing to the strong spin-orbit coupling (SOC) in Cu 2p<sub>3/2</sub> core-level, a multitude of Cu L<sub>3</sub>-edge RIXS studies on layered cuprates have resolved the momentum-dependent magnetic excitations in the non-spin-conserving channel ( $\Delta S=1$ ) [49]. Due to the distinct energy scales of magnetic exchange in the ladder ( $\sim 100$  meV) and chain subsystem ( $\sim 10$  meV), a previous Cu L<sub>3</sub>-edge RIXS study on Sr<sub>14</sub>Cu<sub>24</sub>O<sub>41</sub> showed that the high-energy magnetic excitations are dominated by the ladder triplons when probed at the Cu 3d<sup>9</sup> resonance [13].

In this letter, we present a Cu L<sub>3</sub>-edge resonant inelastic X-ray scattering (RIXS) study on the ladders in SCCO with varied Ca content, Sr<sub>14</sub>Cu<sub>24</sub>O<sub>41</sub> (Sr14) and Sr<sub>1.8</sub>Ca<sub>12.2</sub>Cu<sub>24</sub>O<sub>41</sub> (Sr1.8Ca12.2). We observe a clear response of the magnetic excitations, evolving from a sharp collective two-triplon (2T) to a damped and weakly-dispersive mode upon heavy substitution of Ca in place of Sr. By comparing the RIXS spectra with numerical calculations on doped ladder clusters, we find that the flattened dispersion and broadened excitation profiles with high Ca content are characteristic of an enhanced hole-localization. With introduction of localization by electrical potentials, the calculated RIXS cross section is



compatible with the observed incoherent spin fluctuations for Sr<sub>1.8</sub>Ca<sub>12.2</sub>. Additionally, exploiting the polarization dependence of the RIXS spectra, we detect the depletion of the spin-conserving ( $\Delta S=0$ ) charge-like scattering in the low-energy regime, in agreement with the scenario of a suppressed carrier mobility. This can be naturally connected to the observation of low-temperature insulating behaviour in Ca-doped compounds, despite the expected increase of holes in the ladder subsystem [19,20,90]. This observation is in contrast to the case of a system hosting CuO<sub>2</sub> plaquettes, where metallicity and superconductivity emerge upon moderate charge-doping. The SCCO serves as one of the few cuprate materials that achieves pairing correlations without a CuO<sub>2</sub> plaquette structure, representing a bridge between the q-1D quantum fluctuations and HTSC in 2D planar environments. By shedding light on the interplay between spin fluctuations and chemical pressure, our study provides important information towards the understanding of the emergence on superconductivity in SCCO and, more generally, in the family of cuprates.

### 3.5 Experimental Method

Single crystals of Sr<sub>14</sub> and Sr<sub>1.8</sub>Ca<sub>12.2</sub> are grown with the traveling-solvent floating zone method [16,111]. Top-post cleavage is performed *in-situ* before all measurements in a vacuum pressure of better than  $5 \times 10^{-10}$  mbar. Cu L<sub>3</sub>-edge RIXS and X-ray absorption spectroscopy (XAS) measurements were performed at the Advanced Resonant Spectroscopies (ADDRESS) beamline at the Swiss Light Source (SLS), Paul Scherrer Institut [54–56]. The total energy resolution of the RIXS experiment was 95 meV at the Cu L<sub>3</sub>-edge ( $\sim 930$  eV). The RIXS spectrometer was fixed at a scattering angle  $2\theta$  of  $130^\circ$ . In this work, we fix our RIXS experimental geometry with b- and c- orientations in the scattering plane [Figure 3:4(a)]. This allows no momentum-transfer along the ladder-rungs and selectively enhances the multi-triplon (MT) RIXS response with even-parity along  $\mathbf{q} = (q_{\text{Leg}}, q_{\text{Rung}}=0)$  [13,108]. RIXS measurements are acquired with 15 minutes per spectrum, and normalized to the total spectral weight of the crystal-field excitations.  $\sigma$  polarization is employed for the incident X-rays if not specified differently. XAS spectra are recorded in total fluorescence yield (TFY) mode. All measurements are taken at base temperature  $\sim 20$  K.

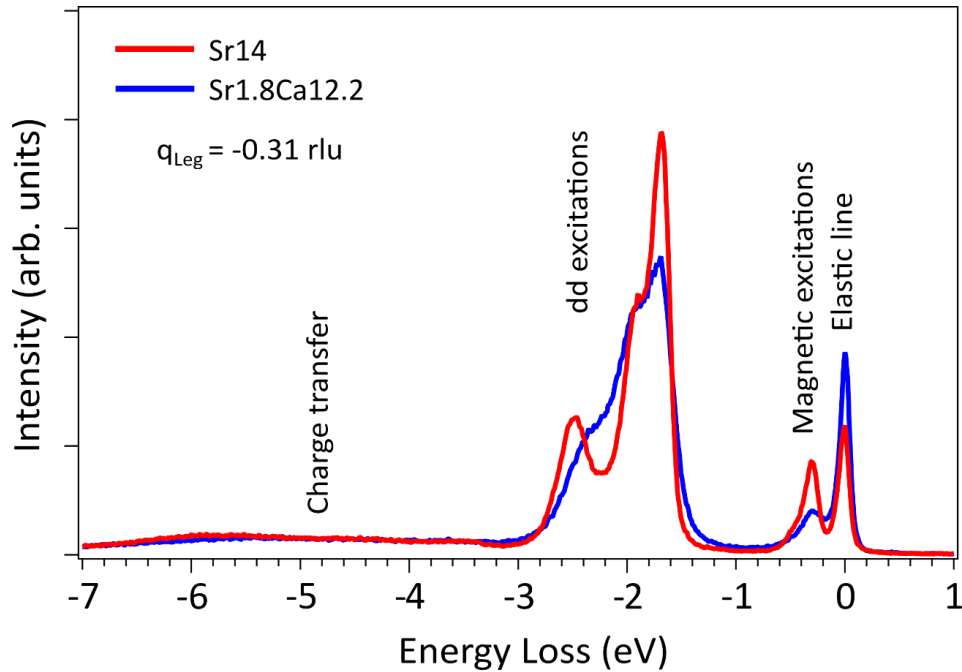


Figure 3:5 Cu L<sub>3</sub>-edge RIXS spectra with spectral components taken at  $q_{\text{Leg}} = -0.31(\text{rlu})$  for Sr<sub>14</sub> and Sr<sub>1.8</sub>Ca<sub>12.2</sub>. From high- to low-energy we observe charge transfer, inter-orbital crystal-field splitting of Cu 3d shell (dd), magnetic excitations and elastic line.

### 3.6 Results and Discussions

Figure 3:4(d) shows magnetic excitations, appearing around 200-400 meV in the low-energy loss Cu L<sub>3</sub>-edge RIXS spectra, with reduced spectral weight and increased broadening, when Sr is replaced by Ca. Both RIXS spectra are taken

at the 3d<sup>9</sup> main resonance ~930 eV indicated in Figure 3.4(c) and for a momentum transfer of  $q_{\text{Leg}} = -0.31$  (rlu). The high-energy inelastic structures, including the local crystal-field splitting of Cu 3d orbitals [dd excitations] from 1.5-3 eV loss and the broad charge transfer (CT) excitations around 4 eV and above, are shown in Figure 3:5. One can find the dd electronic excitations become broader with Ca-doping. This is consistent with the experimental reports suggesting the increasing ladder holes upon Ca-doping in SCCO, as the transport and low-energy optical properties (below charge gap ~2 eV for Sr<sub>14</sub>) were ascribed to be dominated by the ladder subsystem [36,96,97] (also see section 3.2). Figure 3:6(a) display the momentum-dependent RIXS experimental results along  $\mathbf{q} = (q_{\text{Leg}}, q_{\text{Rung}}=0)$  at selected q-points. For Sr<sub>14</sub> [Figure 3:6(a)], the magnetic spectra from collective 2T excitations are observed. For Sr<sub>1.8</sub>Ca<sub>12.2</sub> [Figure 3:6(b)], the excitations are broadened and exhibit a flattened dispersion around 280 meV loss across the momentum space [Figure 3:6(b)]. Due to the broad RIXS lineshape of Sr<sub>1.8</sub>Ca<sub>12.2</sub>, we will use the peak maximum as a reference to identify the mode energy. With the combined energy- and momentum-space sensitivity of Cu L<sub>3</sub>-edge RIXS, we reveal the  $\Delta S=1$  2T spectral changes near the zone center and up to ~300 meV, which are generally inaccessible by INS, NMR, and Raman spectroscopy. Due to the weak momentum-dependence, it is tempting to compare such incoherent magnetic response in Sr<sub>1.8</sub>Ca<sub>12.2</sub> to the itinerant paramagnon excitations in doped 2D cuprates along the nodal direction [112–120].

In the following, we present the Cu L<sub>3</sub>-edge RIXS responses below 1 eV loss for SCCO at selected momentum-transfer vectors. For one momentum transfer vector along the leg direction, Figure 3:5 shows RIXS spectra extending up to 10 eV loss. Figure 3:6 shows the momentum-dependent RIXS measurements of SCCO at selected momentum-transfer points. In Figure 3:6(a), we decompose the excitation modes of Sr<sub>14</sub> into the elastic line around 0 eV loss and magnetic excitations in the range of 150-400 meV. The elastic line has contributions from elastic scattering, including pure charge and diffuse scattering due to surface roughness, and quasi-elastic weight accounting for the low-energy asymmetry of the elastic line. The latter is attributed to the unresolved low-energy excitations, such as phonons and magnetic excitations in the chains [13]. Both components are described by Gaussian functions with a width of the overall instrumental energy resolution. The magnetic excitations are fitted with a resolution-limited Gaussian profile for the predominant sharp peak, and a broad Gaussian peak of ~250 meV full-width to half-maximum (FWHM) for the residual higher-energy weight that becomes more distinguishable with increasing momentum. With these procedure, we manage to fit the sharp 2T peak position with errors no greater than 10 meV. The fitted results are plotted in Figure 3:7. The momentum-dependent 2T excitations is in agreement with the peak energy and dispersion evaluated from the previous Cu L<sub>3</sub>-edge RIXS work [13]. The width of the 2T excitations increases towards the zone boundary. This may be caused by the enhanced scattering of the higher-energy component, which could be contributed by the high-order MT scattering or charge excitations [26,91]. Another possibility for the high-energy spectral weight near zone boundary could be the excitation of confined spinons, as suggested by the magnetic exchange couplings being close to isotropic limit from our experimental and numerical results [26]. Further investigations would be required to clarify this.

The fitting strategy for the magnetic excitations described above does not hold for the heavily Ca-doped compound. The increased Ca content leads to a broadening of the magnetic RIXS response causing large uncertainties in the estimation of the peak position. As shown in Figure 3:6(b), we keep the two-component contributions to fit the elastic line, and a damped Lorentzian of 350~400 meV FWHM for the magnetic excitation spectra. This gives us a fitting error of no greater than 30 meV for the magnetic excitations of Sr<sub>1.8</sub>Ca<sub>12.2</sub> across the momentum-space.

A natural explanation of the broadened lineshape due to Ca-doping may be localization effects connected to the Ca dopants. To better understand this mechanism, we performed model calculations of the RIXS response using density matrix renormalization group (DMRG) [50,51]. DMRG has been shown to be powerful for studying elementary excitations in q-1D systems with large cluster sizes [52,121,122]. For Sr<sub>14</sub>, the magnetic exchange parameters were previously determined to be close to the isotropic limit with  $r=J_{\text{Rung}}/J_{\text{Leg}} \sim 0.85$  and to follow a weak-coupling behavior [26]. For Sr<sub>1.8</sub>Ca<sub>12.2</sub>, the weakly-dispersive magnetic excitations can be simulated by an increasing  $r$ , which evolves towards a rung-dimer phase [26]. However, in order to reproduce the localized gapped dimer spectrum, the present theory requires a large  $r$  value ( $\geq 2$ ) that is incompatible with the structural modulation in SCCO [26,123]. In fact, our perturbative approach estimates  $r$  to be around ~1.15 for reaching consistency with local Cu-O bond distances in the ladders. From polarization-dependent O K-edge XAS measurements, we estimated the nominal ladder hole densities in Sr<sub>14</sub> and Sr<sub>1.8</sub>Ca<sub>12.2</sub>. This is achieved by the atomic sensitivity of XAS to the distinct Cu-O bonding environments in the chain and ladder subsystems, enabling the evaluation of their hole content with O 2p character [99–101,103]. Using the

model in [99], we obtain an increasing ladder hole concentration with of  $\sim 0.06$  and  $\sim 0.11$  (per Cu atom) for Sr14 and Sr.18Ca12.2, respectively, in agreement with previous literature [124]. The DMRG and XAS methods will be discussed in the following sections.

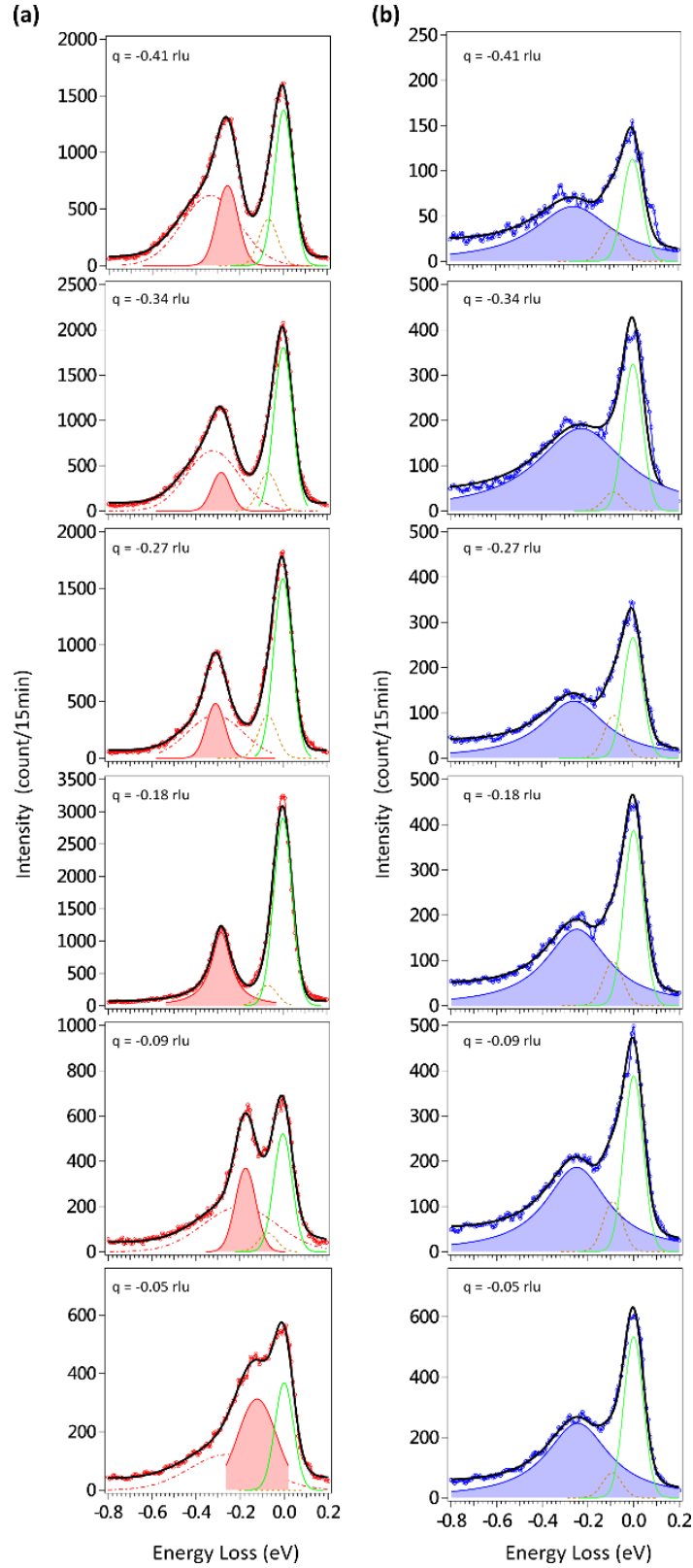


Figure 3:6 Cu  $L_3$ -edge RIXS spectra with fitting components at selected momenta for (a) Sr14 and (b) Sr1.8Ca12.2. Around the 0 eV energy loss peak comprises the elastic (and diffuse) scattering (green solid lines) along with the quasi-elastic scattering (brown dash lines). 2T excitations of Sr14 are fitted with two Gaussians of one lower-energy sharp (red solid line with shaded-region) mode and a broad high-energy component (red dashed line). 2T profiles in Sr1.8Ca12.2 are fitted by a damped Lorentzian (blue solid line with shaded region).

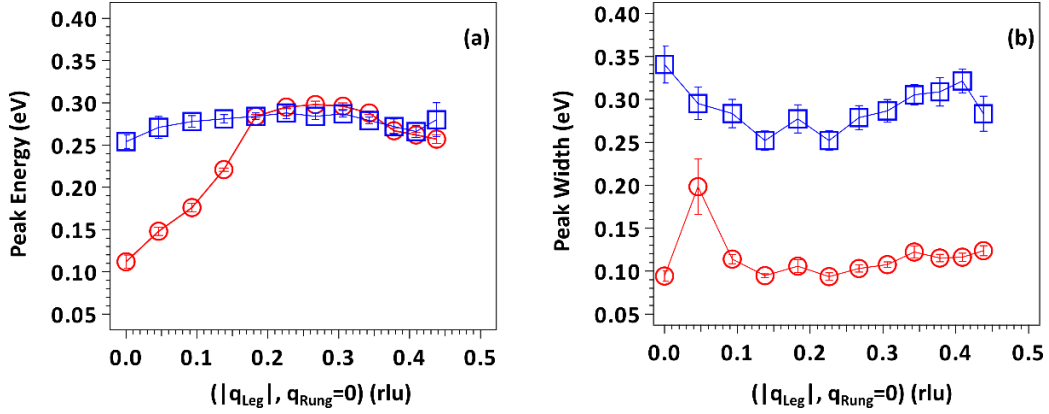


Figure 3:7 Fitting results for the magnetic excitations in the Cu  $L_3$ -edge RIXS spectra for Sr14 (red circles) and Sr1.8Ca12.2 (blue squares). The fitted peak positions and widths are plotted in (a) and (b), respectively.

The RIXS intensity in the Kramer's-Heisenberg formalism can be expanded using the ultra-short core-hole (UCL) approximation. For the low-energy excitations in the Cu  $L_3$ -edge RIXS spectra of layered cuprates, the non-spin-conserving  $\Delta S=1$  channel of RIXS has been shown to provide a good approximation at lowest order of the dynamical spin structure factor  $S(\mathbf{q}, \omega)$ , while the spin-conserving  $\Delta S=0$  channel can be approximated by a modified dynamical charge structure factor  $\tilde{N}(\mathbf{q}, \omega)$  [62]. This has been extended to the magnetic and charge excitations in spin ladders recently in ref. [26]. These structure factors are calculated as:

$$S(\mathbf{q}, \omega) = \sum_f |\langle f | S_{\mathbf{q},\sigma}^z | g \rangle|^2 \delta(E_f - E_g + \omega)$$

Equation 3:1 Dynamical spin structure factor probed by RIXS.

and

$$\tilde{N}(\mathbf{q}, \omega) = \sum_f |\langle f | \tilde{n}_{\mathbf{q},\sigma} | g \rangle|^2 \delta(E_f - E_g + \omega),$$

Equation 3:2 Modified dynamical charge structure factor probed by RIXS.

where  $\tilde{n}_{\mathbf{q},s} = n_{\mathbf{q},s} - n_{\mathbf{q},s} n_{\mathbf{q},s'}$ ,  $s$  is the spin index,  $|g\rangle$  and  $|f\rangle$  are the initial and final state of the scattering process, respectively,  $E_g$  and  $E_f$  are their respective energies, and  $\mathbf{q}$  and  $\omega$  are the net momentum and energy transfer into the system [26].  $S_{\mathbf{q},s}^z$  and  $n_{\mathbf{q},s}$  are the Fourier transforms of the local spin and charge operators, respectively.

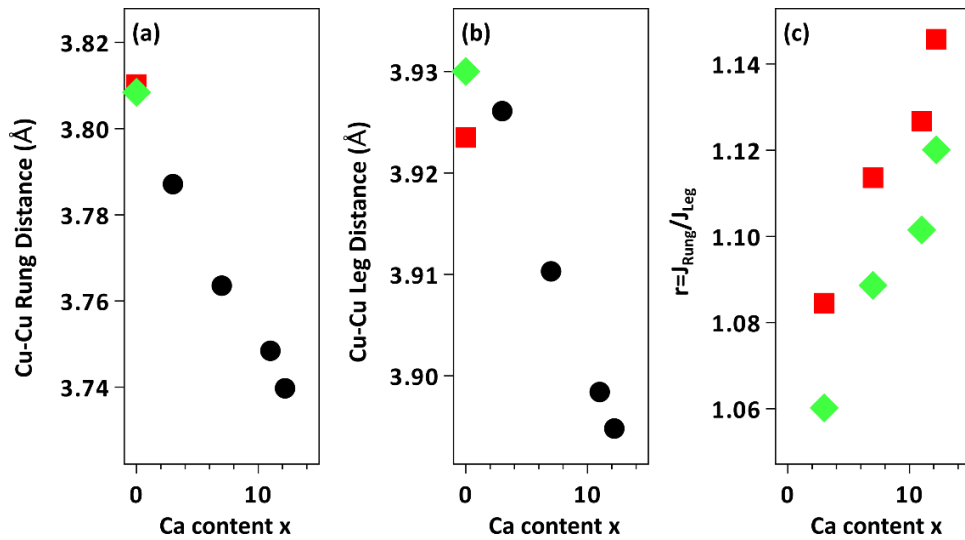


Figure 3:8 (a) and (b) shows the rung and ladder (leg) distances for various Ca doping values obtained from different sources (red squares: ref. [16]; green diamonds: ref. [125]; black circles: ref. [123]). (c) shows the rung ratio estimates for Sr1.8Ca12.2, obtained using the ladder rung distances for Sr14 given by two different references [16] and [125] and the procedure described in the text.

The Sr14 data is well described by adopting a rung ratio  $r = J_{\text{Rung}}/J_{\text{Leg}} = \sqrt{t_{\text{Rung}}/t_{\text{Leg}}}$  that is slightly less than one, consistent with prior estimates [26]. The flattened dispersion of the excitation spectrum of Ca12 might be explained by adopting a large  $r$ , which would result in the formation of localized spin dimers along the rungs [26]; however, we have found that such a large rung ratio is inconsistent with the available crystal structure data. To demonstrate this, we estimated  $r$  from the available structural data for SCCO using perturbation theory. Here, the superexchange parameter  $J$  can be obtained by  $J = \frac{4t_{pd}^4}{\Delta^2} \left( \frac{1}{\Delta} + \frac{1}{U_d} \right)$  [126], where  $\Delta$  is the charge transfer energy,  $U_d$  is the on-site Coulomb repulsion on the Cu site, and  $t_{pd}$  is the Cu-O hopping integral. The rung and the ladder Cu-Cu distances for Sr14 and the various Ca-doped systems were obtained from refs. [16,123,125]. The Cu-O distance was taken to be half this value. We then adopted  $t_{pd} = t_{pd}^0 (1 + \delta d_{\text{Cu-O}}/d_{\text{Cu-O}})^{-3}$ , where  $t_{pd}$  is the Cu-O hopping in the Ca-doped system,  $t_{pd}^0$  and  $d_{\text{Cu-O}}$  are the hopping and Cu-O distance in the parent compound Sr14, respectively, and  $\delta d_{\text{Cu-O}}$  is the change in Cu-O distance in the Ca-doped system with respect to Sr14. For further simplification,  $t_{pd}^0$ ,  $\Delta$ , and  $U_d$  were treated as constants. Using this approach, we estimate  $r < 1.15$  for all Ca concentrations (Figure 3:8). In this work, we adopt  $r = 1.15$  as a conservative estimate.

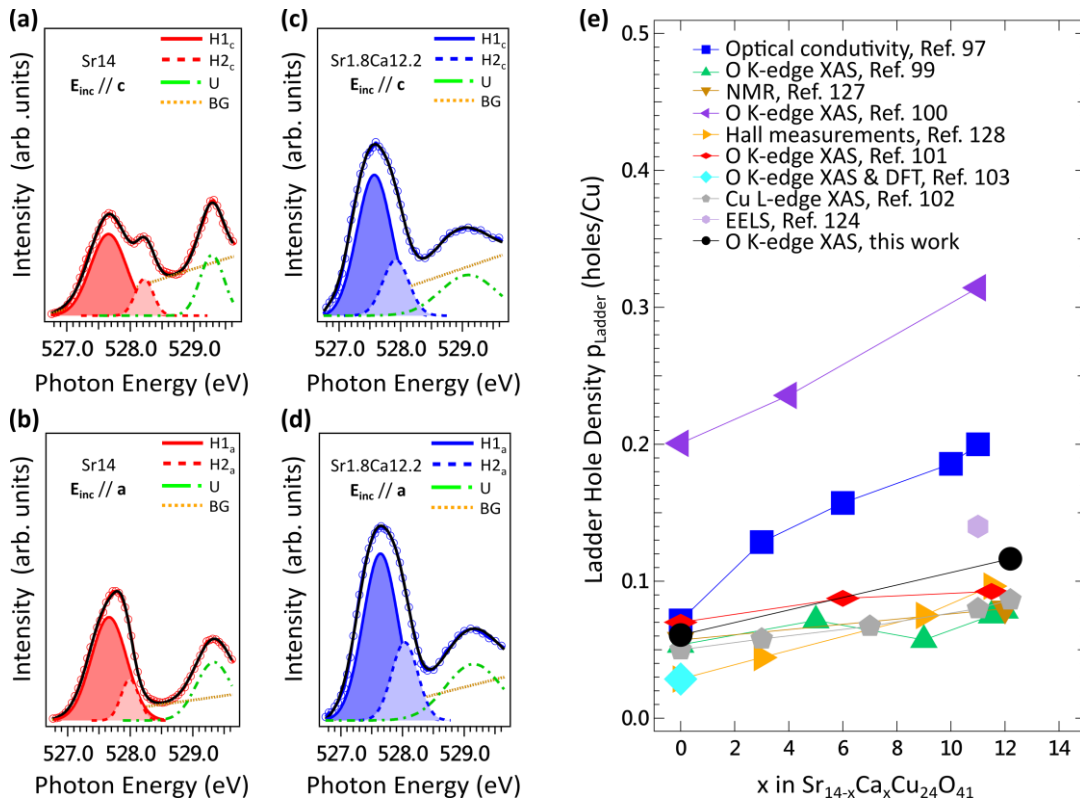


Figure 3:9: O K-edge XAS spectra with fitting components for (a)-(b) Sr14 and (c)-(d) Sr1.8Ca12.2. (e) Experimentally determined number of holes in the ladder subsystem of SCCO, with comparison to the present literature [97,99–103,124,127,128].

To quantify the ladder hole content, the polarization-dependent O 1s XAS is applied. It has been shown to be effective for distinguishing the local Cu-O bonding environments between the edge-sharing  $\text{CuO}_2$  chains and two-leg  $\text{Cu}_2\text{O}_3$  ladders for the self-hole-doped SCCO. The character of the holes in low-dimensional cuprates is mostly of O 2p nature, due to the relatively high repulsion energy at Cu sites. Here we apply the fitting model established in ref. [99] to estimate the hole densities in nearly hole-depleted Sr14 and moderately hole-doped Sr1.8Ca12.2. The obtained values will serve as the starting parameters of the doping levels for our model cluster calculations of RIXS spectra. In the model of [100], an overall overestimated ladder hole concentration was shown [Figure 3:9(e)]. This is incompatible with the experimental observations for the sharp collective magnetic excitations observed in Sr14 from our work and other reports, reflective of an underdoped or nearly undoped character [12,13], thus is not applied here.

In Figure 3:9 (a)-(d), the intensity and peak position of the lower-energy pre-edge hole peak (called H1 in what follows) is polarization-independent. The H1 peak was interpreted as related to doped holes in the chains, due to their  $90^\circ$  Cu-O-Cu bond angle [99]. As a result, the linear dichroism is vanishing in the spectral contributions from the chains. On the

other hand, the higher-energy component in the double-peak structure, labelled as H2, was argued to be mainly originating from the hole content in the ladders [99]. H2 is enhanced when the polarization of incident X-ray  $E_{inc}$  is parallel to the ladder-leg orientation (c-axis), in line with the increasing number of accessible O 2p orbitals in the ladder subsystem [4]. The spectral weight in the energy region  $\sim 529.25$  eV represents the upper Hubbard band (UHB) [99]. The linear dichroism in O 1s XAS is suppressed with Ca doping, as shown in Figure 3:9 (c)-(d) and in agreement with literature [99–102]. This was speculated to originate from lattice distortions in the ladder subsystem, creating an increasing quasi-2D electronic character resemble to the CuO<sub>2</sub> planes [99] that may provide a link to the observed SC phases in SCCO [19].

One thing worth notice is that this modelling might fail to describe the hole content across a wide range of chemical doping, as the approach follows a phenomenological basis. Shown in Figure 3:9(c) and Figure 3:9(d), whether the two-component assignment still reasonably captures the chain-ladder hole distribution for nearly complete replacement between Sr and (Y,La,Ca) is not known. For Sr<sub>1.8</sub>Ca<sub>12.2</sub>, the spectral components representing the hole content did not show a clear separation between the chain and ladder contributions, as explained in previous XAS reports [99]. Another possible source of errors for estimating the hole content of SCCO by O K-edge XAS is the role of slightly decreasing resistivity with Ca-doping [19,20]. Despite that SCCO remain insulating with Ca-doping (without applied pressure), early transport measurements revealed the slight flattening for the resistivity slope with respect to temperature [19,20]. This indicated that the itineracy is not constant with Ca-doping, which can lead to differences in the post-edge fluorescence signal level (up to 70 eV above the main XAS edge  $\sim 530$  eV in this section). In the XAS analysis of SCCO from literature, the post-edge XAS signal with structure-less background is normally taken as the normalization reference, where its uncertainties could cause evaluation errors of the hole density in chain and ladder subsystems. For the analysis in Figure 3:9, we adapt the assumptions in ref. [99] that the two-component assignment for the hole content from XAS peaks is valid for all doped phases, which ignores the possible changes in itineracy.

We compare our estimated hole contents with existing experimental reports in Figure 3:9(e). The number of ladder holes  $n_{Ladder}$  per chemical formula (pcf) are estimated as the following:  $n_{Ladder} = 6 \cdot (H2_a + H2_c) / (H1_a + H1_c + H2_a + H2_c)$  [99]. Here the subscript labels a and c represent the H1 and H2 spectral weights measured with the polarization vector of incident X-rays parallel to the rung or leg orientations shown in Figure 3:9(a)-(d). The factor 6 represents the total number of excess holes pcf. Early studies concluded that the Sr-Ca substitution does not change the total numbers of holes, but rather transfer the holes from chains to ladders due to the altered electrical potential in SCCO [97]. Therefore, we extract 0.85 and 1.43 ladder holes pcf for Sr<sub>14</sub> and Sr<sub>1.8</sub>Ca<sub>12.2</sub>, respectively. This leads to an estimate of 6% and 11% ladder hole densities  $p_{Ladder}$  in Sr<sub>14</sub> and Sr<sub>1.8</sub>Ca<sub>12.2</sub>, respectively.

In Figure 3:10 we compare the experimental Cu L<sub>3</sub>-edge RIXS data with DMRG calculations of the dynamical spin structure factor for Hubbard models in two-leg ladder geometry. Here, we consider both undoped and doped ladders, using the doping level determined by our O K-edge XAS analysis. The RIXS spectra for Sr<sub>14</sub> are fairly well described by both the undoped [Figure 3:10(b)] and doped [Figure 3:10(c)] models. As in previous studies, the  $\Delta S=1$  scattering channel clearly dominates the spectral signal [49]. However, we observe a slight increase in the broadening of the dispersing 2T excitations towards the zone boundary between the undoped and 6% hole-doped ladder, which may be caused by the mixing with charge or Stoner-like continuum excitations like in the 2D cuprates [96,129]. Overall, the experimental Sr<sub>14</sub> Cu L<sub>3</sub>-edge RIXS spectra are better described by the DMRG calculation of the 6% nominally doped ladder.

We find that the weakly-dispersive mode of Sr<sub>1.8</sub>Ca<sub>12.2</sub> in Figure 3:10(d), on the other hand, may either reflect an effective hole-depletion or significant localization in the ladders both of which are not intrinsically considered in the DMRG calculations. Comparing the undoped ladder calculations for Sr<sub>1.8</sub>Ca<sub>12.2</sub> in Figure 3:10(e) and the 11% hole-doped ladder calculation in Figure 3:10(f), we identify a more diffuse spin excitation profile with increasing holes. However, increased ladder hole doping also produces a pronounced downturn of the maximum RIXS intensity in the calculations close to the zone center, which does not occur in our experimental RIXS data on Sr<sub>1.8</sub>Ca<sub>12.2</sub>. Despite the residual low-energy weight, the overall magnetic excitations in Figure 3:10(d) are clearly gapped. This indicates that the observed broadening of magnetic excitations for high Ca content may not be solely driven by the increased ladder hole content, namely other factors should be included to explain both the flattened dispersion and broadened RIXS lineshape in Sr<sub>1.8</sub>Ca<sub>12.2</sub>, e.g. electronic localization, defect scattering defects, spin-lattice relaxation, damping from high-order or frustrated magnetic exchange interactions, etc. [91,130,131]. This result connects to a recent *ab initio* study revealing that charge localization and antiferromagnetic order in the chains favor a ladder hole-depletion due to the chain-hole

attraction, which could not be concluded solely from a phenomenological XAS analysis for assigning spectral components [103]. From the structural data [123], the obtained magnetic exchange couplings suggest that the flat magnetic dispersion cannot be entirely triggered by the localization of triplons, as the strong rung dimerization scenario for  $r \geq 2$  [26] is not yet reached at  $x=12.2$  [Figure 3:8].

We use the DMRG method to calculate the structure factors in real space and Fourier transform the results to momentum space following the procedure outlined in ref [121]. For Sr14, we use a  $32 \times 2$  ladder cluster and keep up to  $m=1000$  states and a maximum truncation error of  $10^{-7}$ . The artificial broadening parameter is set to  $\eta=47.5$  meV to match the experimental resolution. All calculations here are performed in the electron language. We find that the spin structure factor captures the major spectral features of the RIXS data [Figure 3:10]. The modified dynamical charge structure factor is one order of magnitude smaller than  $S(\mathbf{q}, \omega)$  in doped ladders [Figure 3:11].

From Figure 3:10(d)-(f), the increased ladder hole content determined from our O 1s XAS explains the magnetic spectral broadening of RIXS response, but is incompatible with the localized character observed in the experimental excitation spectrum. The question is what mechanism could explain these results. In order to better reproduce the experimental momentum-resolved RIXS spectra for Sr1.8Ca12.2 [Figure 3:10(d)], we consider a sizable electronic localization with carrier-immobility in Ca-rich phases, likely linked to modulations in the electrical potentials. Our assumption is corroborated by transport studies in which the resistivity of SCCO with  $x>11$  showed a linear decrease down to  $100 \sim 150$  K, followed by an abrupt upturn with further cooling [19,20]. The latter was interpreted as the indication of carrier localization at low temperature [20]. To account for the localized hole content, we perform DMRG calculations on ladders by adding impurity potentials. In particular, we parametrize of the impurity potential with  $V_{\text{imp}} \sim 0.5U$ , with a  $\sim 12.5$  % coverage of hole-occupied defects. The simulated RIXS map for the  $\Delta S=1$  channel (shown in Figure 3:10(f)) captures well the spectral broadening observed experimentally upon increased hole density. Additionally, the spectral weight with dispersing downturn near zone center observed in Figure 3:10(f) becomes less defined in Figure 3:10(g), while the momentum-resolved intensity distribution also becomes flattened closed to the zone boundary. Therefore, taking into account electronic localization in the DMRG calculations captures the evolution of the RIXS spectra for Sr1.8Ca12.2. Our results clearly point out that other factors beyond charge doping need to be at play for explaining the evolution of the magnetic RIXS response with increasing Ca content. These findings challenge the current speculations for the role of the magnetic fluctuations in the pairing mechanism of SCCO when replacing Sr by Ca.

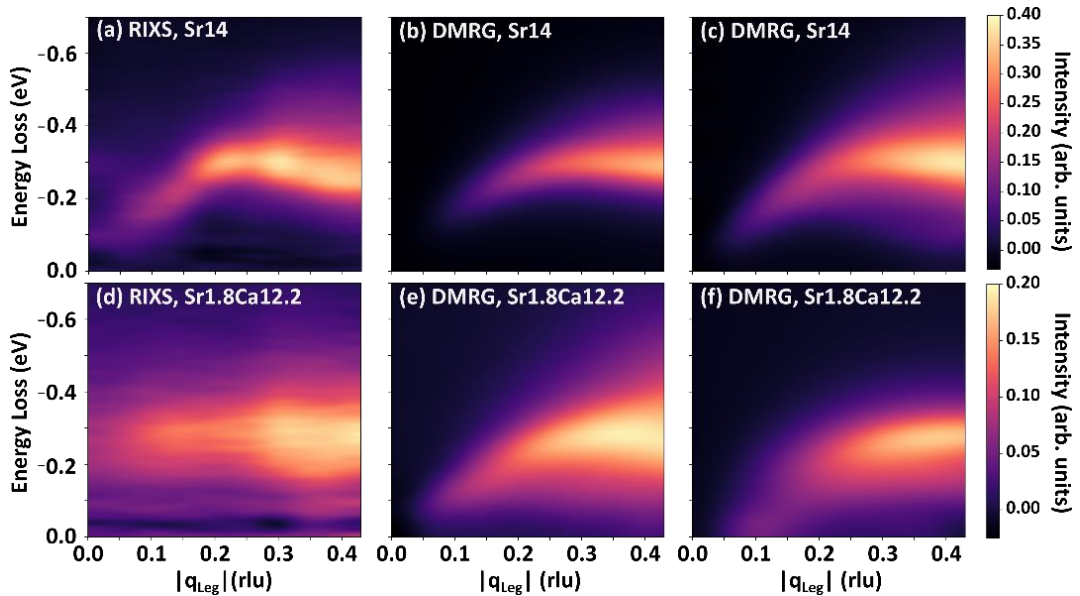


Figure 3:10 Upper (lower) row panels show the experimental and numerical RIXS results with bicubic interpolation for Sr14 (Sr1.8Ca12.2). The elastic line in each of the experimental spectra is subtracted for clarity. (a) and (d): Momentum-dependent RIXS spectra for Sr14 and Sr1.8Ca12.2 in  $\sigma$  polarization after elastic line subtraction. (b) Calculated  $\Delta S = 1$  RIXS spectra on an undoped ladder cluster for Sr14. (c) and (e): Calculated  $\Delta S = 1$  RIXS spectra on doped ladder clusters with hole doping  $p$  close to the experimentally-determined values from O K-edge XAS results, which are about  $\sim 6\%$  and  $\sim 11\%$  for Sr14 and Sr1.8Ca12.2, respectively. The following set of parameters are applied for Sr14 (Sr1.8Ca12.2) on a  $32 \times 2$  site cluster with spectral convergence:  $t_{\text{leg}}=340$  meV,  $U=8t$ , and  $r=0.85$  ( $t_{\text{leg}}=300$  meV,  $U=9t$ , and  $r=1.1457$ ). (f) Calculated  $\Delta S = 1$  RIXS spectra for Sr1.8Ca12 on a  $16 \times 2$  site doped ladder cluster with an impurity potential  $V_{\text{imp}} = 0.5U$ . The same electronic parameters and hole doping applied in (e) are adapted.



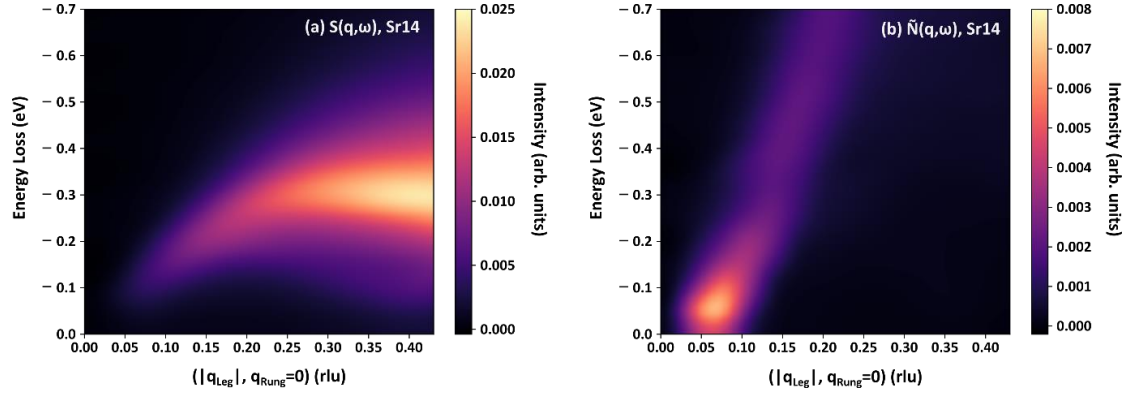


Figure 3:11 (a) Dynamical spin and (b) modified charge structure factors for Sr14 calculated by DMRG. The electronic parameters are chosen as  $t_{\text{Leg}}=340$  meV,  $U=8t$ ,  $r=0.85$ ,  $\eta=0.1379t_{\text{Leg}}$ , and hole doping  $p=6.25\%$ .

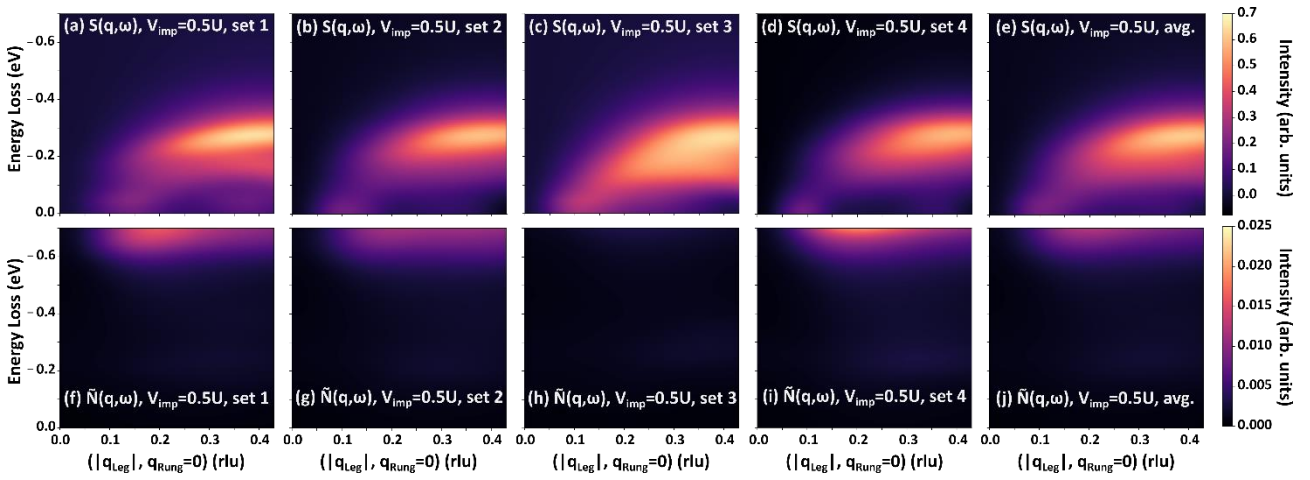


Figure 3:12 (a)-(e) Dynamical spin and (f)-(j) modified charge structure factors calculated by DMRG for Sr1.8Ca12.2, with  $t_{\text{Leg}}=300$  meV,  $U=9t$ ,  $r=1.1457$ ,  $\eta=0.01583t_{\text{Leg}}$ , and hole doping  $p=12.5\%$ . (a) and (f) correspond to (16,17,20,28), (b) and (g) to (6,12,13,17), (c) and (h) to (1,12,24,31), and (d) and (i) to (7,14,15,24). The averaged  $S(\mathbf{q}, \omega+i\eta)$  and  $\tilde{N}(\mathbf{q}, \omega+i\eta)$  of the four sets are shown in panel (e) and (j), respectively.

For Sr1.8Ca12.2, we use a 16x2 ladder with the same  $m$  and artificial broadening parameter as Sr14. The maximum truncation error is reduced to  $10^{-8}$ . To simulate the localization effects observed from the RIXS spectra of Sr1.8Ca12.2, a potential  $V_c=0.5U$  is applied to four randomly chosen sites in the ladders. We then calculate both spin and modified charge structure factors for four different disorder configurations (16,17,20,28), (6,12,13,17), (1,12,24,31), (7,14,15,24) [Figure 3:12], where each number in a set corresponds to the site index where the additional potential is introduced. Here, the sites are labelled from 0 to 31, with even and odd number sites corresponding to the upper and lower legs of the ladder, respectively. The final structure factor is then obtained by averaging the spectra produced by each of these disorder configurations. To settle the exact magnitude of impurity potentials, this will require a full quantum chemistry calculation which is beyond the scope of this work. We postulate that the increasing Ca content modulates the electrical potentials for the non-magnetic atomic layers, which redistribute the holes to the ladder subsystem as predicted by former studies. However, from our results we argue that these holes are not freely distributed and remain localized, which is consistent with the reported transport behavior [97]. These “impurity » sites will now have reduced electron occupation, or in other words will be predominantly hole-occupied. The particle number is conserved for our model calculations, and hence the hole occupation can be concluded accordingly. We confirm this by calculating the occupation number per site  $\hat{n}_i$ . The strength of the potential  $V_{\text{imp}}$  and the number of impurity sites were chosen as  $0.5U$  and 4, respectively, which is in reasonable agreement with the associated energy scales for magnetic systems with spin impurities.

Our interpretation of the localized hole content in the ladders of Sr1.8Ca12.2 is further supported by polarimetric analysis of the RIXS measurements. In order to assess the character of charge and spin scattering in the low-energy excitation profile in SCCO, we performed polarization-dependent Cu  $L_3$ -edge RIXS [60–65]. Here we apply the method



established in [60] to disentangle the  $\Delta S=1$  and  $\Delta S=0$  channels of the 2T response, which was previously demonstrated for the two-spinon excitations of  $\text{CaCu}_2\text{O}_3$ . The RIXS intensity  $I(\epsilon, q)$  can be expressed as combination of  $\Delta S=1$  and  $\Delta S=0$  dynamical structure factors  $G(\Delta S, \epsilon, q, \omega)$  multiplied by form factors  $F(\epsilon, q)$  of the scattering processes (see section 2.5.1). Here  $\omega$ ,  $\epsilon$ , and  $q$  represent the energy loss, polarization of incident X-rays and momentum-transfer, respectively, while the light polarization corresponds to  $\sigma$  or  $\pi$ . Following ref. [60], we approximate  $F(\epsilon, q)$  by the local spin flip  $P_{\text{SF}}(\epsilon, q)$  and elastic scattering probabilities  $P_{\text{EL}}(\epsilon, q)$  [132–134], which can be calculated in a simple single-ion model [66]. Thus, we can extract the  $\Delta S=1$  and  $\Delta S=0$  channels by solving the equations of the polarization-dependent RIXS intensity.

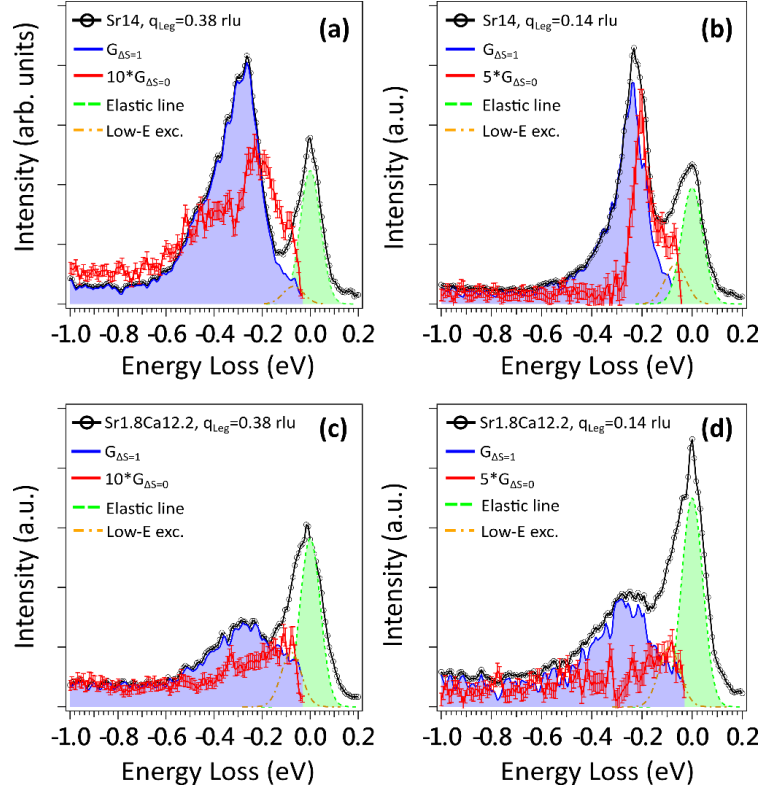


Figure 3:13 RIXS spectra with  $\Delta S=1$  (blue-shaded) and  $\Delta S=0$  (red line) channels disentangled for (a)-(b) Sr14 and (c)-(d) Sr1.8Ca12.2 taken at  $q_{\text{leg}} = 0.38$  rlu [(a) and (c)] and  $q_{\text{leg}} = 0.14$  rlu [(b) and (d)]. Experimental data shown here are taken with  $\pi$  polarization in grazing emission geometry.

In order to decompose the  $\Delta S=1$  and  $\Delta S=0$  scattering of 2T excitations with overlapping energies [91], we measure RIXS spectra with incident X-rays in  $\sigma$  and  $\pi$  polarization at the same geometry. For practical purposes, we follow ref. [60] to perform the  $\Delta S=1$  and  $\Delta S=0$  scattering disentanglement in the grazing emission geometry ( $q_{\text{leg}} > 0$ ). This reduces the errors from intensity fluctuations or unphysical results due to the small differences between  $I(\sigma, q < 0)$  and  $I(\pi, q < 0)$  in the grazing incidence geometry. Additionally, the spectral differences from self-absorption effects by applying  $\sigma$  and  $\pi$  polarization for the incident X-rays are also reduced in grazing emission geometry [60]. With the lack of theories considering carrier mobility effects on the polarization-resolved RIXS cross section, here we also assume that the extracted momentum-dependent RIXS cross section in a single ion (without holes) is in reasonable agreement with the squared-planar lattices in underdoped two-leg ladders of Sr14 and Sr1.8Ca12.2. The atomic symmetries of core-hole p and valence d orbitals for the  $\text{Cu}^{2+}$  ion are taken into account in these calculations. For the given RIXS response probed at the XAS  $3d^9$  white line, this agrees with the majority of  $\text{Cu}^{2+}$  electronic contributions from the underdoped ladder subsystem ( $n_{\text{ladder}}$  of 5~15% and  $n_{\text{chain}}$  of 40~50%, see previous section). Here we normalize the RIXS spectra with respect to the theoretical dd cross section before evaluating  $G(\Delta S, \epsilon, q, \omega)$ . The error bars for evaluating the extracted spectra are assuming Poisson statistics. The raw RIXS spectra measured for selected momenta and varied polarization of incident X-rays are shown in Figure 3:14(a)-(d). The elastic line is removed from the RIXS spectra before the dynamical structure factors  $G(\Delta S, \epsilon, q, \omega)$  are evaluated from the RIXS intensities  $I(\epsilon, q)$ . The disentangled spin-resolved channels in the main text are shown in the energy regime above the elastic line to exclude possible contributions from the quasi-elastic scattering.

In Figure 3:13, we compare the  $\Delta S=1$  and  $\Delta S=0$  signal for  $q_{\text{Leg}} = 0.38$  and  $0.14$  rlu and find that the  $\Delta S=1$  channel indeed provides the major contribution of the magnetic signal for both Sr14 and Sr1.8Ca12.2. In Sr14 [Figure 3:13(a)-(b)], the  $\Delta S=0$  scattering is dominated by a sharp mode at slightly reduced energy compared to the  $\Delta S=1$  channel. Additionally, a broad component of  $400\sim 600$  meV appears to be more pronounced near the zone boundary, coinciding with the momentum region where the excitation profiles show a stronger high-energy tail [Figure 3:12(a)]. These excitations have comparable energy scales with the charge and  $\Delta S=0$  multi-triplon (MT) excitations predicted in recent theories, which would be of interest for future RIXS studies at O K-edge [26,91]. On the contrary, the  $\Delta S=0$  channel in Sr1.8Ca12.2 is essentially a structure-less background below 1 eV. As shown in Figure 3:13(c)-(d), the low-energy spin-conserving weight of Sr1.8Ca12.2 is significantly reduced compared to Sr14. This suppression of spectral contributions from the low-energy charge and  $\Delta S=0$  MT excitations signifies a likely suppressed charge mobility, which would preferentially lift the spectral weight to the higher-energy regime. Such tendency is also observed in the calculated dynamical charge response. As a result, the observed non-dispersive damped magnetic spectra in Sr1.8Ca12.2 can thereby be reconciled by a hole-immobilized ladder picture despite an increased carrier density.

Our results have important consequences for understanding the starting condition from which the SC state in SCCO is established with high Ca content and elevated pressures. The ingredients of a complete theory must now take into account the role of Sr-Ca substitution, inducing charge localization in Ca-doped SCCO. To further elucidate the overall effects of Sr-Ca replacement in SCCO, we suggest future experiments using INS for measuring momentum-resolved magnetic excitations with elevated pressure, which will help to clarify the underlying electronic correlations connected to pairing in SCCO.

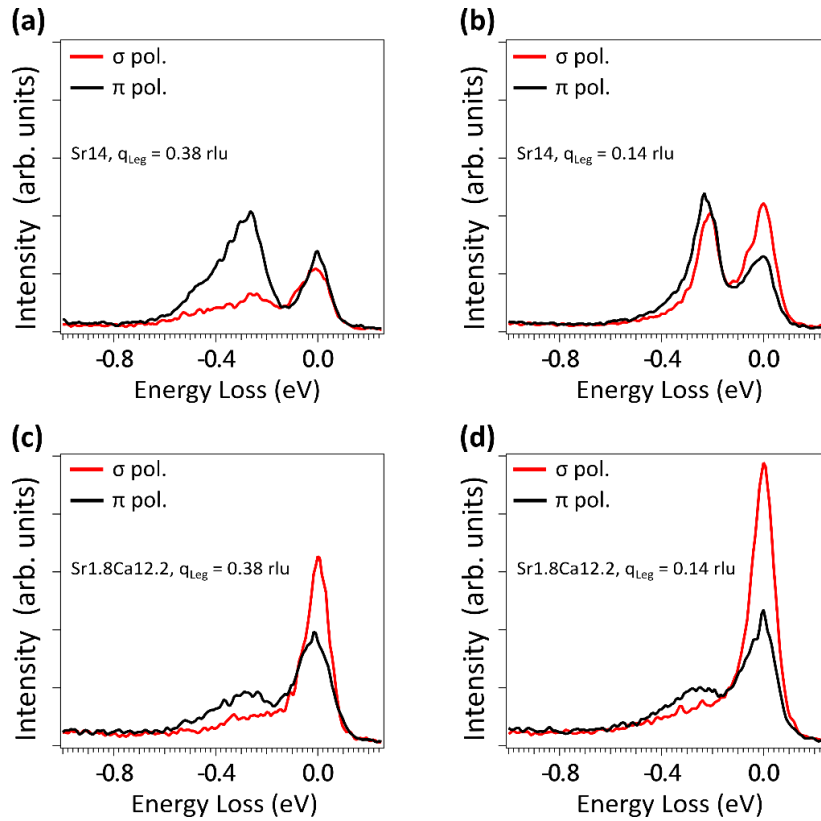


Figure 3:14 (a)-(d) Polarization-dependent Cu  $L_3$ -edge RIXS spectra zoomed in around the low-energy excitations. Here the experimental data are normalized to the total spectral weight of dd excitations with respect to the theoretical cross sections.

### 3.7 Conclusion

We have performed Cu  $L_3$ -edge RIXS measurements on the spin ladder material SCCO. From the momentum dependent RIXS spectra, we reveal a crossover in the magnetic excitation spectrum. In particular, the dispersive collective 2T excitations in pristine Sr14 evolve into a high-energy gapped magnetic mode in doped Sr1.8Ca12.2, showing a nearly flat dispersion and sizable damping in the spectral lineshape. From O K-edge XAS, we obtained an estimate of the hole

distribution in the material as a function of Ca-doping. We then compared the experimental data with DMRG model calculations, using as input the experimentally obtained hole distribution. Upon introducing an impurity potential to mimic charge localization, we obtain the best agreement with the experimental data. Therefore, we conclude that the flattened dispersion of the magnetic mode upon doping reflects a considerable carrier immobility. To further explore this effect, we have performed polarization-dependent RIXS measurements, revealing that the  $\Delta S=0$  channel evolves from well-defined charge and MT excitations in Sr14 to a featureless background in Sr1.8Ca12.2. Our results provide a microscopic view of the dynamical response in the doped cuprate ladders. This work gives valuable information on the magnetic and charge dynamics of q-1D cuprate ladders, as well as their relation to the competing electron-pairing hypotheses.

### 3.8 Acknowledgement

The experiments have been performed at the ADRESS beamline of the Swiss Light Source at the Paul Scherrer Institut (PSI). The work at PSI is supported by the Swiss National Science Foundation through project no. 200021\_178867, the NCCR MARVEL and the Sinergia network Mott Physics Beyond the Heisenberg Model (MPBH) and SNSF Research Grants CRSII2\_160765/1 and CRSII2\_141962. Y.T and T.S would like to thank V. Bisogni for valuable discussions. A. N. acknowledges the supported by the Canada First Research Excellence Fund. J. T. and S. J. are supported by the National Science Foundation under Grant No. DMR-1842056. This work used computational resources supported by the University of Tennessee and Oak Ridge National Laboratory Joint Institute for Computational Sciences, and computational resources and services provided by Advanced Research Computing at the University of British Columbia.

# Chapter 4 Spectroscopic fingerprint for holon-spinon and spin-singlet multi-triplon excitations in the hole-doped ladders of $\text{Sr}_{14}\text{Cu}_{24}\text{O}_{41}$

## 4.1 Project Contribution

The content of this chapter is at the time of the thesis submission undergoing the paper submission process as a journal article. In this chapter, I investigate the  $\Delta S=0$  charge and magnetic excitations in the self-hole-doped two-leg ladders of the chain-ladder cuprate  $\text{Sr}_{14}\text{Cu}_{24}\text{O}_{41}$  using O K-edge RIXS. In this work, I, Yi Tseng, am responsible for the experiment planning, preparation of the single crystal samples, performing the RIXS measurements and experimental data analysis. The paper is written by me as the main responsible with input from all the other co-authors. Section 4.2 serves as an additional introduction giving extended background knowledge for the context within this work, including the figures 4:1 to 4:3. The corresponding article in preparation of submission includes the content of section 4.3 to 4.8, including the figures 4:4 to 4:11.

## 4.2 Preamble

This chapter comprises two major achievements. One is the experimental observation of the spin-conserving  $\Delta S=0$  magnetic and charge excitations in doped cuprate ladders, and the other focuses on its spectroscopic identification granted by the O K-edge RIXS sensitivity. The former highlights the peculiar excitation spectrum originating from the unique dimensionality of doped ladders, providing insight to the character of their 1D and 2D counterparts, i.e. spin-chains and 2D cuprates. The latter concerns the RIXS spectral capability for probing different aspects of the dynamical structure factor, with access to different parameters of the phase space (e.g. momentum sensitivity, element/site selectivity, non-spin-conserving  $\Delta S=1$  and spin-conserving  $\Delta S=0$  channel, different lifetime scales, etc.)

For non-interacting q-1D spin-chains, the low-energy physics is governed by the disentangled elementary quasiparticles [135]. The separated spin, charge and orbital degrees of freedom has been revealed by early photoemission and RIXS experiments [59,136,137]. In real electronic materials, however, one has to take into account perturbations beyond such idealized low-dimensional systems. In this aspect, doped spin ladders serve as ideal material realizations to understand how q-1D spin systems respond to non-negligible (inter-chain) interactions at the lowest-order. Even-leg spin ladders in general show a gapped magnetic excitation spectrum consisting of  $S=1$  triplons due to a sizable intra-ladder magnetic exchange [9–11]. With sizable charge doping, early theories suggested that the interactions between holons and spinons become crucial in the low-energy Hamiltonian [27–29]. Tsunetsugu et al. and Troyer et al. showed that a holon-spinon coupled mode will emerge in lightly hole-doped ladders, where the interaction length and excitation energy are scaled by the intra-ladder (rung) exchange coupling [28,29]. This positions spin ladders close to the so-called Luther-Emery liquid class of materials, which capture the physical picture of hard-core interacting bosons [29]. Specifically, this contrasts to the spin-charge separation present in the Tomonaga-Luttinger liquid realized in q-1D spin-chains [135]. The inclusion of such holon-spinon quasiparticles in addition to the triplons persisting with doping has helped to reconcile the inconsistency between early mean-field and numerical works on the dynamical structure factor (DSF) in doped ladders [10,27,93,94]. It is worth notice that the contribution of the holon-spinon mode to the DSF is still smaller than the  $S=1$  triplons when lightly doped, as the spectral weight is approximately scaling with the hole doping [28,29].

On the other hand, the interacting quasiparticles may also help to pave the way for understanding the dynamical response towards higher dimensions. The differences between spin ladders and the usual Luther-Emery liquid arise from the attraction between bound hole pairs in doped ladders [29]. This leads to d-wave superconductivity and an excitation spectrum with co-existent  $S=1$  magnetic fluctuations and particle-hole like excitations, which connect to the similarities in the low-energy excitations between spin ladders and 2D cuprates discussed in section 3.2 [9–11]. Early

theories further pointed out that the holon-spinon coupled excitations may play a significant role for mediating the modified d-wave superconductivity in the doped ladders [27–29]. This was argued from their similar formalism with the Bogoliubov quasiparticles established in BCS superconductors with particle-hole symmetry [28,29]. Additionally, the low-energy regime of doped ladders shares similar charge and pair density fluctuations proposed for the HTSC in cuprates [27]. Therefore, the identification of such particle-hole like charge excitations, alongside their interplay with periodic charge density fluctuations, will give valuable information for understanding HTSC in cuprates. This also extends to the relationship between dynamical charge correlations and the proposed competition between CDW and HTSC in cuprates, which remains intensively debated in recent RIXS studies [83,138–142]. It was predicted that the holon-spinon quasiparticles possess appreciable spectral weight in the simulated spectral function near the Fermi surface upon sizable band filling with doped holes [28,29].

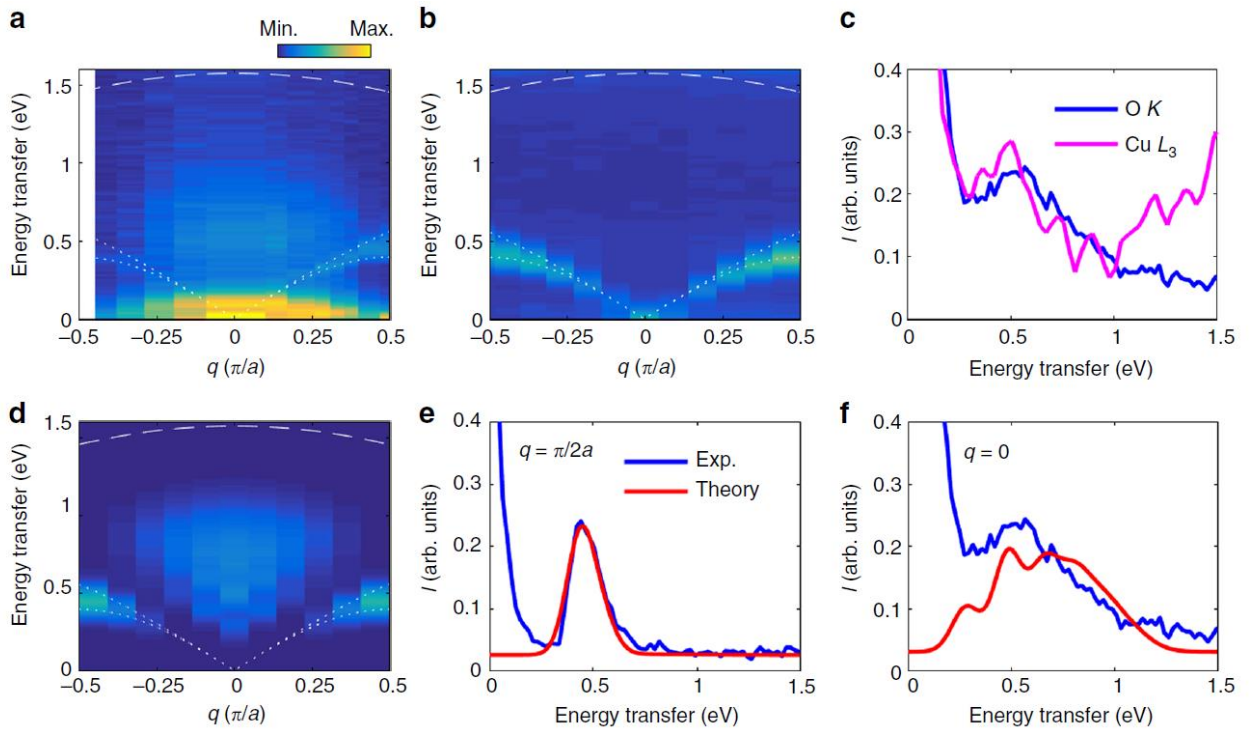


Figure 4:1 (a) Four-spinon continuum excitations outside the Two-spinon continuum boundary in  $\text{Sr}_2\text{CuO}_3$  probed by O K-edge RIXS from ref. [77], in comparison with the former Cu  $L_3$ -edge RIXS results [59] shown in (b). The O K- and Cu  $L_3$ -edge RIXS spectra taken at zone center are displayed in (c). (d) Calculated  $\Delta S=0$  RIXS spectra using DMRG on a 22 site t-J chain with periodic boundary conditions. The RIXS intensity is calculated with the Kramers-Heisenberg formalism with core-hole lifetime effects considered. (e)-(f) The comparison between experimental and theoretical O K-edge RIXS response with  $q=0.25$  and  $q=0$  (r.l.u), respectively (Open access available at: Springer Nature publishing group, Nature Communications, Schlappa J. et al., 9, 5394, 2018).

The unique capability to probe excitation modes in different phase space of the DSF with RIXS was previously demonstrated. Particularly, q-1D systems provide a good benchmark for understanding the intricate electronic interactions with reduced complications for theoretical studies. This has been demonstrated previously in Cu  $L_3$ - and O K-edge RIXS studies on q-1D spin-chain compound  $\text{Sr}_2\text{CuO}_3$  shown in Figure 4:1 [59,77]. Predominant  $\Delta S=1$  two-spinon (2S) continuum excitations were revealed by Cu  $L_3$ -edge RIXS at the  $3d^9$  resonance [59], whereas the  $\Delta S=0$  four-spinon (4S) continuum outside the 2S continuum boundary can sensitively be probed with the O K-edge RIXS spectra at the upper Hubbard band (UHB) [77]. This is utilized by the weak spin-orbit coupling (SOC) and the longer core-hole lifetime of the O 1s core-level, which preferentially enhances the high-order  $\Delta S=0$  double spin-flip (SF) processes that are generally short-lived [Figure 4:2] [77,122]. Such non-local multiple SF excitations can be probed at O K-edge through the UHB RIXS processes. Strong hybridization between Cu 3d and O 2p orbitals and a moderate O 1s core-hole lifetime enable double SF based on inter-site virtual hopping [77,122]. Such microscopic scenario describes the scattering cross section beyond two-site correlation functions. Upon doping, significant charge scattering is also expected in the RIXS signal with the  $\Delta S=0$  scattering channel that is relevant at the O K-edge [122]. Recently, exact-diagonalization (ED) calculations

for the dynamical structure factor of doped ladders suggested a series of collective excitations in the K-edge RIXS signal [26], revealing spectral signatures of MT excitations in the  $\Delta S=0$  sector (see caption in Figure 4:3).

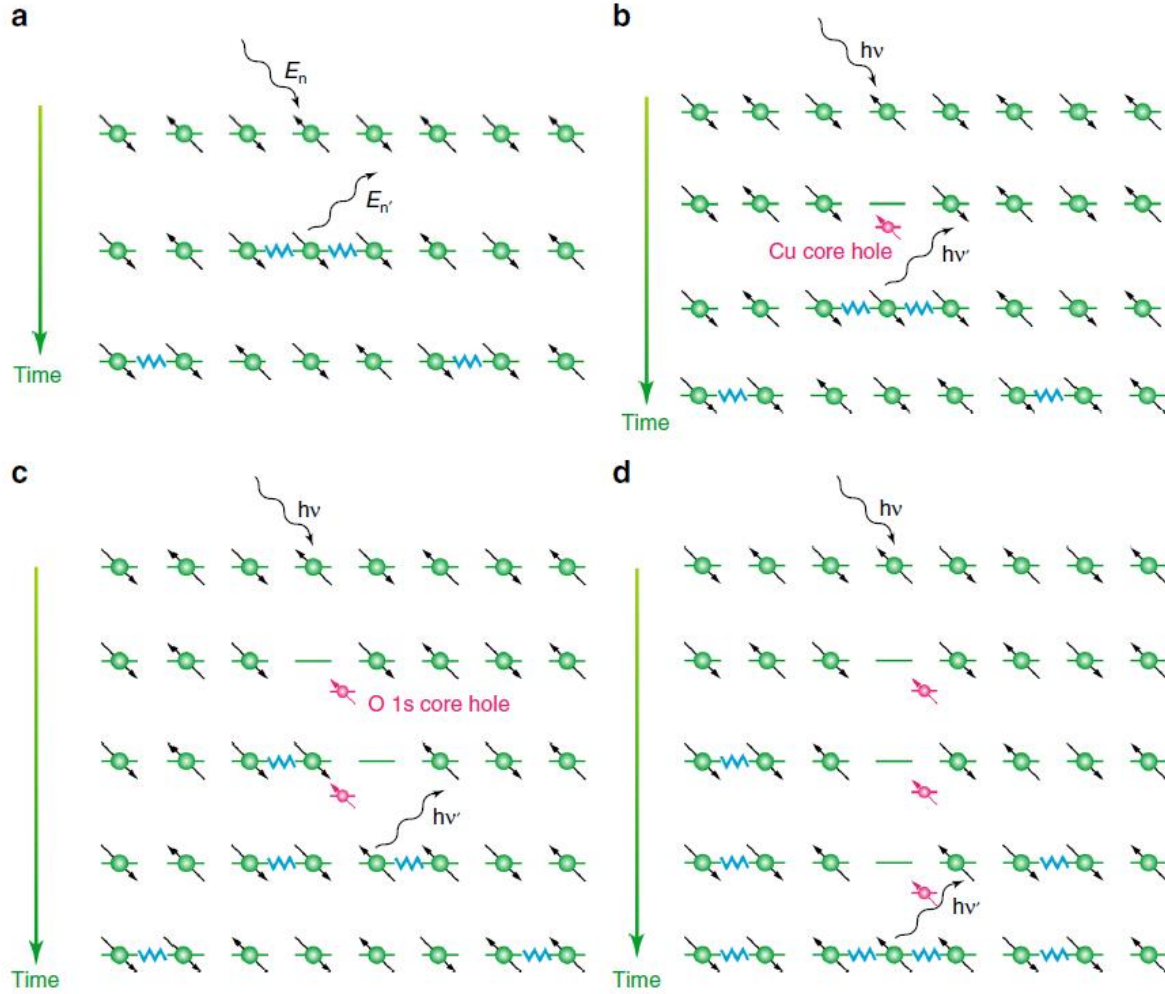


Figure 4:2 Schematics for (a) single  $\Delta S=1$  processes in INS and (b) Cu L<sub>3</sub>-edge RIXS measurements denoted in the hole picture. The 2S and 4S continuum excitations via indirect double spin-flip processes by O K-edge RIXS are shown in (c) and (d), respectively, which are granted by the distinct core-hole potentials of Cu 2p<sub>3/2</sub> and O 1s edges [77] (Open access available at: Springer Nature publishing group, Nature Communications, Schlappa J. et al., 9, 5394, 2018).

In this chapter, I report the UHB O K-edge RIXS spectral response of holon-spinon and  $\Delta S=0$  multi-triplon excitations in Sr<sub>14</sub>Cu<sub>24</sub>O<sub>41</sub>. Despite the speculation of a large Fermi surface from early theories, clear spectral assignment of a band due to holon-spinon quasiparticles is so far lacking in the existing photoemission studies on doped ladder materials [143–146]. The predicted significant weight from holon-spinon quasiparticles in the spectral function was rationalized by its particle-hole character, which is naturally reflected in the charge-removal processes in photoemission experiments [28,29]. In the following sections of this chapter I will show that the O K-edge RIXS results of lightly doped ladders feature a dispersing sharp mode with similar excitation energies of the predominant  $\Delta S=1$  triplons in the DSF. O K-edge RIXS only allows  $\Delta S=0$  spin-conserving scattering processes involving the triplons [26,122]. The spectral assignment of holon-spinon composite-excitations is corroborated by recent DMRG calculations, for which a gapless holon-spinon mode with similar excitation energy as the  $\Delta S=1$  2T excitations in Cu L<sub>3</sub>-edge RIXS spectra was simulated [26,27,29]. This assignment is further supported by the temperature-dependent RIXS measurements performed within the thesis work that show a weight suppression for this mode  $\sim 280$  K. This spectral change occurs below the relevant energy scale of the ladder magnetic exchange  $\sim 130$  meV, but surpasses the CDW melting temperature  $\sim 162$  K revealed from the increased conductivity in the optical measurements [147]. This may indicate that the observed weight suppression is compatible with change in the dynamical charge response due to the enhanced itinerancy. In this work, we fix the scat-



tering geometry to  $q_{\text{Rung}}=0$  such that the holon-spinon response in the bonding band will be preferentially excited [13,108]. Upon hole doping, the originally at half-filling degenerate bands of holon-spinon quasiparticles, with bonding and anti-bonding orbital geometries, will be separated with the latter lifted to higher-energy [26,27]. The former is expected to remain gapless while possessing similar excitation energy with the lowest-lying  $\Delta S=1$  2T excitations in vicinity to the isotropic limit ( $r=J_{\text{Rung}}/J_{\text{Leg}}=1$ ) [26]. On the other hand, the O K-edge RIXS measurements in this chapter reveal a substantial weight for high-order MT scattering outside the lower boundary of 2T continuum. By comparison with triplon spectral density calculations under the framework of continuous unitary transformation (CUT), we conclude that the observed high-energy incoherent damped component is mostly contributed by the upper boundary of 2T continuum [91]. This is in stark contrast to the Cu  $L_3$ -edge RIXS results in the same scattering geometry (see chapter 3 and ref. [13]), which is ascribed to the long core-hole lifetime of the O 1s core-level compared to the Cu 2p one [77,122].

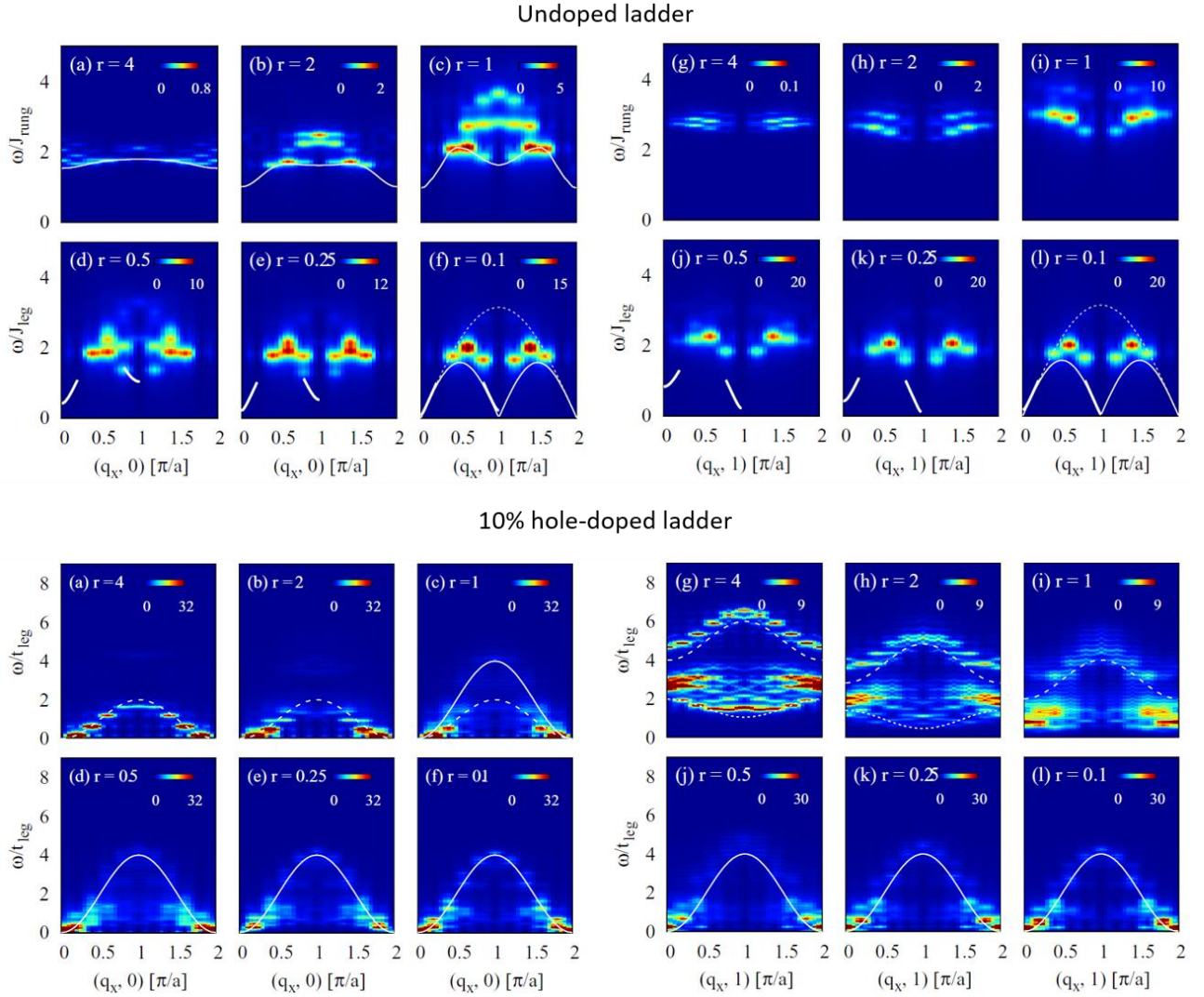


Figure 4.3: Calculated modified dynamical charge structure factor ( $\Delta S=0$ ) for undoped and 10% hole-doped t-J ladder  $10 \times 2$  site clusters using ED [26]. For both the upper and lower panels, (a)-(f) and (g)-(l) represent the excitations at  $q_{\text{Rung}}=0$  and  $q_{\text{Rung}}=0.5$ , separately. The  $r$  value corresponds to the ratio of the nearest-neighbour magnetic exchange between the rung and leg orientations ( $r=J_{\text{Rung}}/J_{\text{Leg}}$ ). Upper panel: The solid white lines in (a)-(c) indicate the  $\Delta S=0$  2T bound state from the strong to isotropic ( $r=1$ ) rung coupling regime. The solid (dotted) line segments in (d)-(f) and (j)-(l) mark the lower (upper) multi-spinon continuum boundary for the weak rung coupling regime. Lower panel: The white dashed lines in (a)-(c) and (g)-(i) represent the gapless and gapped holon-spinon excitations in the bonding and anti-bonding band from strong to isotropic coupling, respectively. The dotted white lines in (g)-(h) illustrate the boundary for 1T excitations. The solid white lines in (c)-(f) and (j)-(l) highlight the holon excitations when approaching the weak rung coupling limit [Reprinted figure with permission from: Umesh Kumar, Alberto Nocera, Elbio Dagotto, and Steven Johnston, Physical Review B, 99, 205134 (2019). Copyright (2019) by the American Physical Society. (<https://doi.org/10.1103/PhysRevB.99.205130>)].

### 4.3 Abstract

We perform O K-edge resonant inelastic X-ray scattering (RIXS) on the self-hole-doped chain-ladder cuprate  $\text{Sr}_{14}\text{Cu}_{24}\text{O}_{41}$ . We identify a dispersing sharp mode  $\sim 270$  meV that is disentangled from a damped incoherent component  $\sim 400$ -500 meV. By comparison with model DMRG calculations of RIXS cross section on doped ladder clusters from literature [26], the dispersing sharp mode shows correspondence to the holon-spinon quasiparticles in the doped ladders, accompanied by the spectral contribution of the spin-singlet two-triplon (2T) bound state with similar excitation energies. The higher-energy component, on the other hand, shows close resemblance to the upper boundary of 2T continuum in our experimental RIXS results. The observed sharp and broad modes are also in close agreement with the simulated multi-triplon (MT) density within the framework of continuous unitary transformation (CUT) [91]. With the RIXS sensitivities, these findings will give valuable information to the dynamical charge and spin correlations that is complementary to other experimental studies.

### 4.4 Introduction

Given the similarities in electronic instabilities with layered cuprates, quasi-one-dimensional (q-1D) spin ladders are ideal model systems to study the high-temperature superconductivity (HTSC) in cuprates with reduced complications [9–11]. In the even-leg spin ladders with doped holes, the gapped magnetic excitation spectrum with bound hole pairs of rung-singlets have been long considered as promising evidence for pairing fluctuations [27–29]. The bound hole pairs can be understood as a direct consequence for minimizing the total energy cost while moving the hole carriers in the antiferromagnetic environment [28]. Several theories for doped ladders have shown the tendency of a ground state of resonance-valence-bond (RVB) character to evolve towards modified d-wave superconductivity (SC) [24,27–29]. Furthermore, the electron pairing in spin ladders has been materialized in the hybrid chain-ladder materials  $\text{Sr}_{14-x}\text{Ca}_x\text{Cu}_{24}\text{O}_{41+\delta}$  for  $x > 11$  with elevated pressure of few GPa [19,20].

Understanding the corresponding electron pairing glue, however, requires a detailed look into the low-energy excitations. With a sizable intra-ladder (rung) exchange coupling, early studies demonstrated that the doped ladder excitation spectrum is composed of a spin-triplet mode (triplon) persisting with doping, along with a quasiparticle (QP) carrying charge  $|e|$  and spin  $S=1/2$  that emerges upon doping (see Figure 4:5(a)-(b)) [27–29]. The latter was rationalized as two separate holes binding to the neighbouring spins from adjacent rungs upon the dissociation of bound hole pairs (Figure 4:5(b)) [28,29]. In the present work, we refer to holon-spinon excitations as QP unless specified otherwise. At low-doping, mean-field studies showed that these QPs tend to form a dilute Fermi gas with attractive binding of their electron-hole counterparts across the Fermi surface [28,29]. This resembles the Bogoliubov formalism with particle-hole symmetry in BCS superconductors [28,29]. Therefore, it is believed that characterizing the QPs will provide insight to the mechanism of pairing fluctuations in doped ladders, as well as their interplay with the  $S=1$  triplon mode and other low-energy excitations [8].

Despite extensive theoretical and experimental studies suggesting the crucial role of the intertwined dynamical magnetic and charge correlations, the experimental interpretation has remained unclear in current literature. Despite the well-defined magnetic exchange in the cuprate ladders, studies with different experimental probes on the doping evolution of  $\Delta S=1$  triplon mode have been inconclusive [104–107,110]. For the charge dynamics, former theories predicted significant spectral weight of the QPs near the Fermi surface upon doping. However, the existing photoemission studies on doped cuprates did not reveal signatures of these QPs [143–146]. On the other hand, infrared and Raman measurements on the hole-doped ladders of SCCO revealed additional excitation modes compared to the hole-depleted  $\text{Ca}_{14-x}\text{La}_x\text{Cu}_{24}\text{O}_{41}$  ( $x \geq 4$ ), which could not be explained by  $\Delta S=0$  magnetic excitations or modulations originating from charge order formation [148]. Experiments using high-pressure nuclear magnetic resonance (NMR) also uncovered a gapless mode exhibiting linear dependence of the Knight shift on temperature, that is indicative of a new exciton emerging with increasing hole carriers [149]. It is tempting to correlate these experimental observations with NMR to the fingerprint of holon-spinon and multi-triplon excitations in the  $\Delta S=0$  scattering channel as speculated in the aforementioned references, yet the understanding of the relevant scattering cross section for detecting these excitations in RIXS is still lacking.



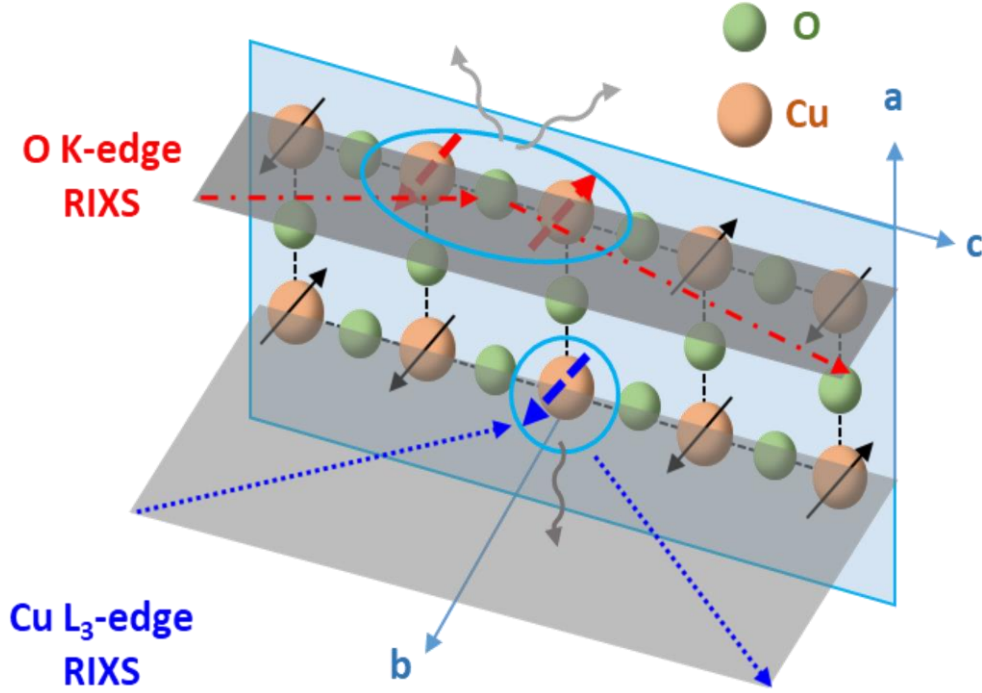


Figure 4:4 RIXS experimental geometry with the orientation of the two-leg  $\text{Cu}_2\text{O}_3$  ladders in Sr14. The ladder-leg direction is along c-axis, with lattice constant  $c \sim 3.93 \text{ \AA}$ . Inter-site double SF ( $\Delta S=0$ ) and single SF ( $\Delta S=1$ ) processes are indicated by gray arrows in the schematics.

In this paper, we present a study on the low-energy excitations in the ladder subsystem of a q-1D chain-ladder cuprate Sr14 using O K-edge resonant inelastic X-ray scattering (RIXS). The RIXS capability for probing collective magnetic and charge excitations in spin ladders has been established theoretically [26]. With two-step photoelectric scattering processes, RIXS is capable of probing various elementary excitations in a charge-neutral fashion. Thus, the spectral signal is not hindered by the lack of Fermi surface formation in a large fraction of the phase diagram for SCCO. At the upper Hubbard band (UHB) resonance  $\sim 529.3 \text{ eV}$ , we report the observation of a sharp excitation  $\sim 270 \text{ meV}$ , at comparable energy scale as the two-triplon (2T) excitations in the ladders previously revealed by inelastic neutron scattering (INS) and Cu  $L_3$ -edge RIXS [12,13,150]. By comparing with the literature of calculated RIXS cross section using density matrix renormalization group (DMRG) on doped ladders, we ascribe the observed mode  $\sim 270 \text{ meV}$  to holon-spinon QPs, and likely also to the spin-singlet 2T bound state with similar excitation energies. The excitations  $\sim 270 \text{ meV}$  are clearly separated from the lower-energy optical phonons and higher-energy 2T continuum. When lightly doped, the dynamical structure factor (DSF) in ladders is expected to be dominated by the triplons, while QPs show little weight which is approximately scaling with the hole doping [28]. Our results highlight the RIXS capability to selectively probe the QPs and long-lived  $\Delta S=0$  2T excitations (O K-edge) from the predominant  $S=1$  two-triplons (Cu  $L_3$ -edge) enabled by the fundamentally different correlation functions. Such versatility, beyond a conventional two-site correlation function, has been recently demonstrated in the RIXS studies of the magnetic excitations in q-1D spin-chain compound  $\text{Sr}_2\text{CuO}_3$  [59,77].

## 4.5 Experimental Method

We performed O K-edge RIXS and XAS measurements at ADRESS beamline at the Swiss Light Source (SLS), Paul Scherrer Institut (see section 3.5). The photon-in-photon-out RIXS technique has developed as an advanced spectroscopic tool for differentiating various low-energy elementary excitations [49]. The two-step RIXS processes consist of exciting the core-level electrons to the valence band, and the subsequent de-excitation of the valence electrons to annihilate the short-lived intermediate core-hole state [49]. When the incident X-rays are tuned to XAS resonances this leads to a finite cross section of an excited final state, and allows detection of charge-neutral dynamical processes with element,

orbital, and momentum selectivity [49]. Details for the growth of Sr<sub>14</sub> single crystal samples can be found elsewhere [16]. The total achieved energy resolution with the RIXS spectrometer operated at the O K-edge ( $\sim 530$  eV) was 55 meV. The scattering angle  $2\theta$  was fixed at  $130^\circ$ . All measurements are taken at base temperature  $\sim 20$  K unless specified. Top-post cleavage of the samples is performed *in-situ* at a vacuum pressure of better than  $5 \times 10^{-10}$  mbar before all measurements. As shown in Figure 4:4, the RIXS geometry is fixed with b- and c- axis oriented in the scattering plane as the same in chapter 3. This will excite the multi-triplon (MT) excitations with even-parity [13,91,108], and holon-spinon QP in the bonding band [27–29]. By rotating the sample stage with respect to the a-axis (ladder-rungs), we perform momentum-dependent RIXS measurements along the in-plane c-axis (ladder-legs). RIXS measurements are acquired with 1 hour per spectrum in  $\sigma$  polarization with grazing incidence geometry. XAS spectra are recorded with total fluorescence yield (TFY) mode.

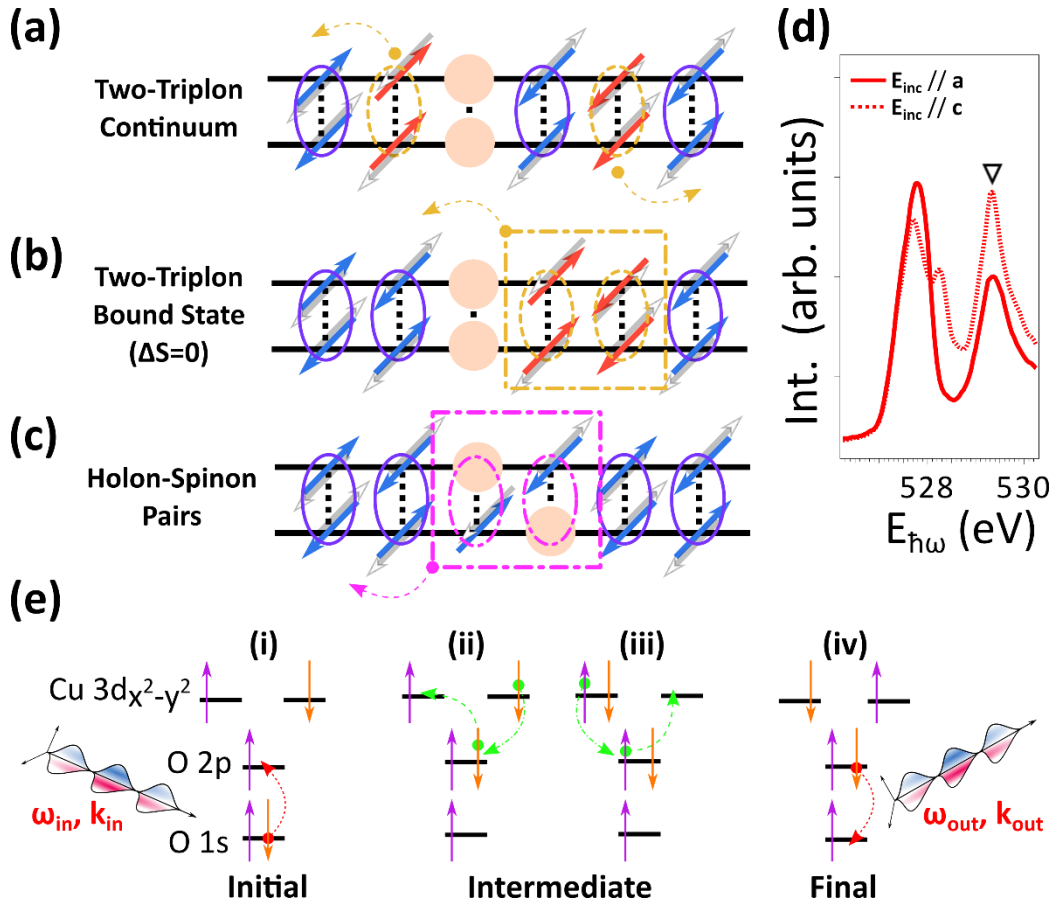


Figure 4:5 (a)-(c) Schematics for the two-triplon continuum,  $\Delta S=0$  two-triplon bound state and holon-spinon excitations in a hole-doped two-leg ladder (from top to bottom, respectively). The ground state rung-singlets (purple ellipses with spin as blue/gray arrows, also see Figure 3:4) can excite into the interacting  $S=1$  triplons (orange dashed-line ellipses with spin-triplets, with flipped spins marked as red arrows). This will result in either two delocalized triplons moving away from each other, forming the two-triplon continuum, or two bound triplons with a total spin  $S=0, 1$  or  $2$ . In this chapter, the  $\Delta S=0$  two-triplon bound state (orange dashed-dotted-line square) is of focus given the O K-edge RIXS sensitivity. The formation of triplons do not require holes (pink filled circles). On the other hand, holon-spinon QPs emerge upon the dissociation of bound hole pairs. As the holes hop without spin-flips, the dissociation of hole pairs leave behind two holon-spinon QPs (magenta dashed-dotted-line square) with a total spin-singlet (magenta dashed-line ellipses). (d) O K-edge XAS spectra with UHB marked (black triangle). (e) Schematics of UHB RIXS processes. (ii) and (iii) show the inter-site electron hopping between the adjacent Cu 3d<sub>x<sup>2</sup>-y<sup>2</sup></sub> orbitals through the Cu-O-Cu superexchange.

## 4.6 Results and Discussions

### 4.6.1 $\Delta S=0$ spin-conserving excitation modes and O K-edge UHB RIXS processes

Figure 4:5(a)-(c) display the two dominant excitation modes in doped spin ladders, namely the triplon and holon-spinon excitations. In two-leg ladders, the interacting  $S=1$  triplons can form either the two-particle continuum band or

bound state (Figure 4.5(a)-(b)), propagating along leg orientation with  $q_{\text{Rung}}=0$  [9]. This can be generalized to the dynamics of even-leg ladders with more than two coupled-chains. Figure 4.5(c) depicts the formation of holon-spinon QPs with doping. It starts with the separation of bound hole pairs, which leaves behind two mobile holes and is subsequently coupling to neighbouring electron spins. This results in a QP pair which favours a singlet-pairing scenario, where the mode energy and interaction length between pairs are scaling with the rung-to-leg exchange ratio  $r=J_{\text{Rung}}/J_{\text{Leg}}$  [28,29]. A typical coherence length of a few lattice spacing's for  $r \sim 1$  was demonstrated in recent theories [151]. The interacting hard-core bosons for the bound hole pairs in spin ladders is characteristic for the Luther-Emery class of q-1D systems [29] (also see section 4.2). Figure 4.5(d) shows the XAS spectra taken at O K-edge. In this work, we focus on the RIXS spectra probed at the resonance  $\sim 529.3$  eV, which corresponds to the upper Hubbard band (UHB) [99]. The pre-edge double-peak structure of  $527.5 \sim 528.5$  eV give information on the hole content in the chain and ladder subsystems, respectively [99].

Figure 4.5(e) shows the schematics of UHB RIXS processes in cuprates. A photo-excited electron initiated in a  $O\ 1s \rightarrow 2p$  transition can hop in between the neighbouring Cu  $3d_{x^2-y^2}$  orbitals due to Cu-O hybridization. This can lead to a  $\Delta S=0$  final state with two spins at adjacent sites flipped after the de-excitation of the O  $2p$  valence electron, which relies on the virtual hopping mediated through Cu-O-Cu superexchange [26,122]. In step (i) shown in Figure 4.5(d), an electron is resonantly excited from O  $1s$  to O  $2p$  states. Then, the intermediate state can be described by the mixed states of overlapping Cu-O-Cu orbitals [step (ii) and (iii) in Figure 4.5], consisting of different configurations where the electron hopping is allowed through Cu-O hybridization. In the second-order perturbative approach, this "virtual" electron hopping, which is essentially based on the mixing of ground state wavefunctions, is only allowed for the anti-parallel spin arrangement for the adjacent Cu ions, leading to an effective magnetic exchange interaction. As a result, the intermediate state in UHB RIXS processes possess a finite cross section for the double SF final state with  $\Delta S=0$  [step (iv) in Figure 4.5(d)]. Previous O K-edge UHB RIXS studies on layered cuprates have revealed magnetic excitations in the  $\Delta S=0$  scattering channel [69,74–77]. This is in contrast to the  $\Delta S=1$  dominant magnetic excitations in cuprates measured by Cu  $L_3$ -edge RIXS. O K RIXS involves only weak spin-orbit coupling (SOC) in the O  $1s$  core-level and is therefore restricted to the  $\Delta S=0$  scattering channel [49].

#### 4.6.2 O K-edge RIXS spectra with comparison to Cu $L_3$ -edge RIXS results

O K-edge RIXS spectra of Sr14 are shown in Figure 4.6(a)-(b), in comparison with the Cu  $L_3$ -edge RIXS results in chapter 3. We observe spectral components from charge transfer (CT) excitations ranging from 3 to 10 eV loss. Around 2 eV loss, the UHB RIXS signal resembles the combined contribution of inter-orbital crystal-field excitations, and charge-transfer excitons with similar character as Zhang-Rice singlets (ZRS) in 2D cuprates [69,74].

In this work, we focus on the energy regime below 1 eV loss [Figure 4.6(b)]. Close to the elastic line around 0 eV loss, the weakly-dispersive excitations about  $\sim 65$  and  $130$  meV closely resemble the harmonics of Cu-O bond-stretching phonons in the chains and ladders, with similar mode frequencies in respective subsystems [Figure 4.6(c)] [152,153]. The UHB resonance does not possess linear dichroism in XAS signal for separating the oxygen contributions of chains/ladders, and therefore contain the oxygen contributions from both the chain and ladder subsystems (see analysis for Figure 3:9). Multi-phonon scattering can be detected as harmonic satellites using RIXS (see section 2.6.1), where similar RIXS spectral response occurs in other q-1D cuprates [154,155].

Around the energy regime expected for  $\Delta S=0$  MT excitations with  $J_{\text{Leg}} \sim 100$  meV scale [26,91], we observe a sharp peak  $\sim 270$  meV on top of a damped spectral component peaked around  $400 \sim 500$  meV. One can see that the broad high-energy component in the O K-edge RIXS spectra extends to higher energy loss compared to the 2T profile in Cu  $L_3$ -edge RIXS [Figure 4.6(b)]. Both the sharp and broad modes in the energy scale of  $200 \sim 600$  meV appear to be enhanced in  $\sigma$  polarization with grazing incidence geometry. The momentum-dependent O K-edge RIXS measurements in Figure 4.6(d) further resolve the character of these two magnetic excitations. The sharp peak disperses towards lower-energy when approaching the zone center, and is then overlapping with the optical phonons for  $|q_{\text{Leg}}| < 0.13$  (r.l.u). On the contrary, the energy dispersion for the high-energy damped peak is essentially flat across the momentum-space.

In Figure 4:7, we show the multi-peak fitting for the O K-edge RIXS spectra measured at UHB resonance. The elastic line in the momentum-dependent O K-edge RIXS map [Figure 4:8(a)] of the data is subtracted with a resolution function of the same spectral intensity as the elastic line. A global fitting procedure across all the momentum-transfer points is

not feasible due to the changing recognizable number of peaks at different measured momentum-transfer points. We apply the following fitting procedure for  $q_{\text{Leg}} = -0.175, -0.196, -0.215, -0.233$  and  $-0.249$  (rlu) for the O K-edge RIXS data [Figure 4:7], where the sharp peak  $\sim 270$  meV is clearly disentangled from the lower-energy phonons and the higher-energy broad mode. In Figure 4:6(c), the elastic line and phonon excitations are well fitted by resolution-limited Gaussians. Three equally-spaced satellites of mode energy about  $65\sim 70$  meV are taken as the initial parameters for fitting the phonons in our UHB RIXS spectra. The mode energies and intensities of high-order phonon overtones, up to the third order, are progressively deviating from the ideal harmonic oscillator. This possibly originates from anharmonic interactions in the lattice, or differences in the momentum-dependent electron-phonon coupling (EPC) for the different phonon modes probed [79]. For  $|q_{\text{Leg}}| > 0.13$  rlu, the dispersing sharp peak is fitted with a Lorentzian function. As for the high-energy weakly-dispersive component  $\sim 400\text{--}500$  meV, we evaluate the peak position by taking the centroid up to 80% of the maximum intensity for the residual weight after subtracting the elastic line, phonons, dispersing sharp peak and a Gaussian background. The latter background is motivated from the complex line shape in the high-energy loss regime and is modelled with a Gaussian of fixed peak position and width. As the dispersive sharp peak  $\sim 270$  meV cannot be recognized for  $|q_{\text{Leg}}| < 0.13$  (rlu), the center of gravity for the high-energy broad mode is evaluated without considering the sharp mode when approaching zone center.

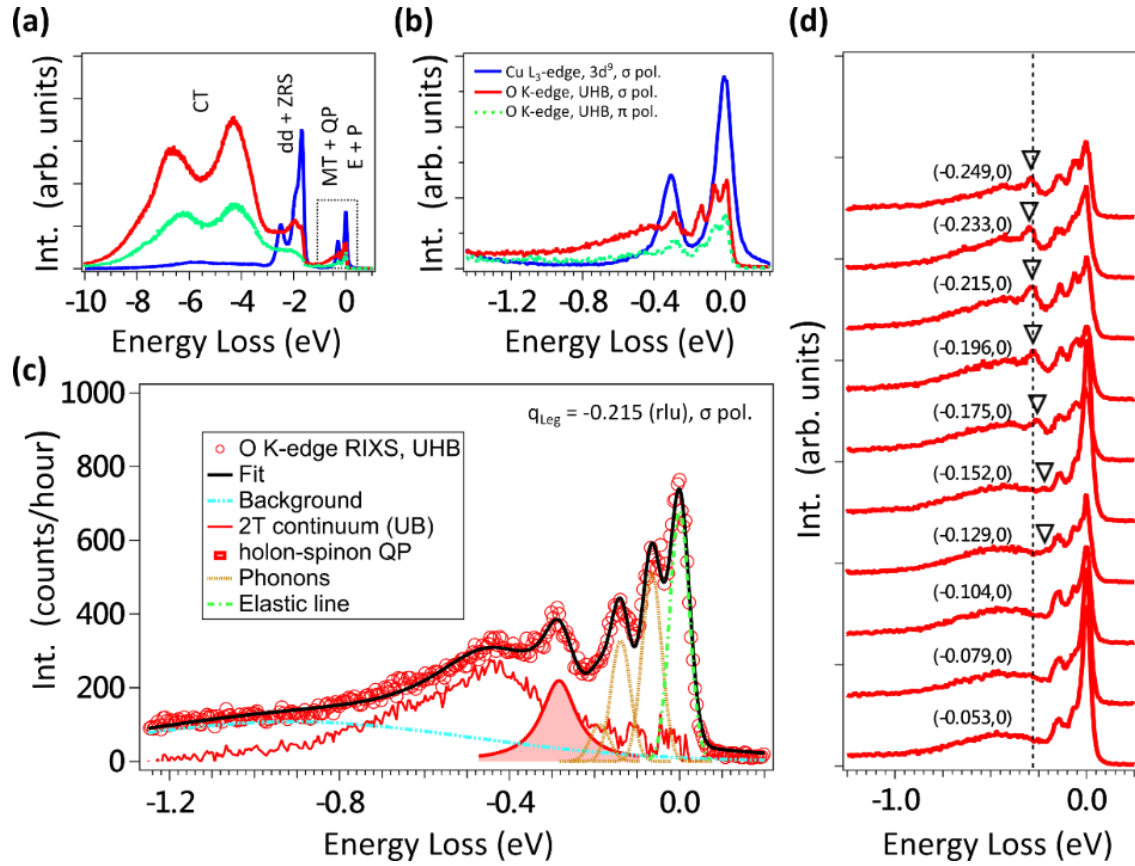


Figure 4:6 (a) RIXS spectra taken Cu  $3d^9$  and UHB resonances of a momentum-transfer  $q_{\text{Leg}} = -0.215$  (rlu). (b) A zoom to the low-energy region, including the elastic line (E), phonons (P), MT and QP modes. (c) The corresponding spectral assignment for UHB RIXS spectra. (d) Momentum-dependent UHB RIXS in  $\sigma$  polarization with  $(q_{\text{Leg}}, q_{\text{Run}})$  labelled. Black triangles serve as a guide-to-eye for the dispersing sharp peak  $\sim 270$  meV, while the peak maximum at  $q_{\text{Leg}} = -0.215$  (rlu) is marked by a black dotted-line. The “negative” momentum-transfer here indicates that the RIXS spectra are recorded in grazing incidence geometry

#### 4.6.3 Experimental interpretation with holon-spinon and $\Delta S=0$ multi-triplon excitations

To assign and interpret the excitations in our experimental O K RIXS spectra, we compare to recently published calculations of the RIXS cross section using density matrix renormalization group (DMRG) [50–52], and simulated MT density employing the continuous unitary transformation (CUT) method [91]. CUT has recently been extended to describe the RIXS response of MT excitations in the spin ladders in both the odd- and even-parity scattering channels [156].

The underdoped two-leg ladder system Sr14 was previously identified to follow an intermediate rung-coupling behaviour close to the isotropic limit ( $r = J_{\text{Rung}}/J_{\text{Leg}} \sim 0.85$ ) [26]. This determined  $r$  value is also consistent with the existing structural data [16,125].

For the broad mode  $\sim 400$ -500 meV, we interpret it as the higher-energy 2T continuum. The flat dispersion with momentum-independent damped profiles capture the character of the high-order upper boundary (UB) for the short-lived 2T continuum [Figure 4:9]. From Figure 4:8, we observe that the broad non-dispersive mode in O K-edge RIXS data are absent in the Cu  $L_3$ -edge RIXS results taken from chapter 3. Similar phenomena were reported in an O K-edge RIXS study on the q-1D spin-chain  $\text{Sr}_2\text{CuO}_3$ , where the four-spinon continuum excitations outside the two-spinon continuum boundary were enhanced due to a longer core-hole lifetime for the O 1s core-level [77]. The observations of these high-energy MT excitations in the spin-singlet  $\Delta S=0$  channel highlight the spectral capability of RIXS to provide complementary insight in the DSF compared to INS. Interestingly, the MT scattering in spin ladders shares similarities with several novel phenomena in mathematical formulation, e.g. Higgs mode in the 2D Heisenberg environments [157–159], Majorana excitations in the Kitaev quantum spin liquid [160–162] (also see section 7.2.2), etc.

For the dispersing sharp mode  $\sim 270$  meV, it may be contributed by two type of excitations. One is the composite holon-spinon QP. Recent calculations of the  $\Delta S=0$  RIXS response on doped t-J ladders have shown a dispersing mode emerging with hole doping along  $\mathbf{q}=(q_{\text{Leg}}, q_{\text{Rung}}=0)$ , being gapless at the zone center, that is persisting from the strong ( $r \gg 1$ ) to the nearly isotropic regime ( $r \sim 1$ ) [26]. This mode can be well described by a Bloch-like quasiparticle derived from the tightly-bound electron spin and a dissociated hole, with its dispersion relation  $\omega(\mathbf{q}) \sim t_{\text{Rung}}(1 - \cos(q_{\text{Leg}}))$  where  $t_{\text{Rung}}$  is the electron hopping along the rungs [29]. The ladder hole density of Sr14 is determined to be  $\sim 6\%$  using the method established in ref. [99] (see the analysis for Figure 3:9). This is corroborated by a sufficiently large  $r$  that is close to the isotropic limit, leading to a sizable coupling between the holons and spinons..

The other possibility to explain the sharp spectral component  $\sim 270$  meV is based on the  $\Delta S=0$  spin-conserving 2T bound state. For the undoped ladders, a spin-singlet 2T bound state was revealed in the calculated RIXS response for the  $\Delta S=0$  scattering channel, accompanied by diffuse incoherent RIXS intensity distributed at higher-energy regime that was assigned to higher-order MT continuum [26]. In this scenario, it can be perceived that the experimentally reported  $\Delta S=1$  2T excitations are reasonably close to the undoped limit such that these  $\Delta S=0$  MT magnetic excitations possess sizable spectral weight. Following from these theory predictions, the underdoped ladders in Sr14 are expected to represent an ideal material realization to search for QPs excitations.

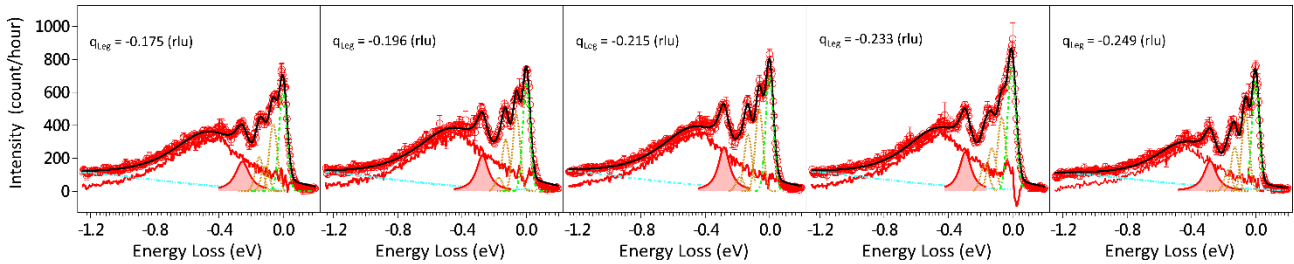


Figure 4:7 Multi-peak fitting for the O K-edge UHB RIXS spectra at selected momentum-transfer points, where the holon-spinon QP (red shaded peak) is clearly separated from the optical phonons and the 2T continuum.

#### 4.6.4 Spectral fingerprint of holon-spinons and $\Delta S=0$ 2T bound state with overlapping energies: Comparison to theories

In Figure 4:8, the dispersing sharp mode in O K-edge RIXS spectra shares similar mode energy and dispersion with the  $\Delta S=1$  2T excitations measured by Cu  $L_3$ -edge RIXS (see chapter 3). Due to the distinct energies of magnetic exchange in the ladder ( $\sim 100$  meV) and chain ( $\sim 10$  meV) subsystems [17], the magnetic RIXS response on the energy scale of hundreds of meV is ascribed to the ladder spin fluctuations [13]. From Figure 4:8 and Figure 4:9, the mode energies and momentum dispersion are compatible with the predicted QPs. Upon charge doping, the dynamical charge correlations are expected to outweigh the concurrent  $\Delta S=0$  magnetic scattering in the RIXS signal [26]. From this, it is unlikely that the sharp mode  $\sim 270$  meV is due to long-lived  $\Delta S=0$  magnetic excitations [26,91]. Furthermore, the reported insulating



charge gap  $\sim 2$  eV and plasma edge  $\sim 400$  meV in Sr14 indicate that our sharp RIXS response  $\sim 270$  meV cannot be reconciled with the inter-band particle-hole excitations or plasmonic response [97,163]. As for the possible spectral contribution for the chain subsystem, the respective charge dynamics in the chains were previously identified as localized charge excitations  $\sim 1$  eV [28,29,143–146], which are inconsistent with the dispersing sharp mode  $\sim 270$  meV.

In order to clarify our RIXS response, we also compare our experimental results with the existing literature that observed  $\Delta S=0$  magnetic excitations in Sr14 and isostructural cuprate compounds. With coupling to phonons, it was demonstrated that infrared absorption measurements can probe long-lived spin-singlet magnetic mode, where the cross section is governed by the two-magnon density weighted by the van Hove singularity [164,165]. Such mode was also recently suggested to be detectable by RIXS with appreciable intensity in undoped ladders [26].

However, the spectral weight of the  $\Delta S=0$  2T bound state is expected to cease with decreasing momentum-transfer towards the zone center. This was due to the decay of bound states when overlaps with the lowest-lying 2T continuum with decreasing momentum (see caption in Figure 4:9) [91]. Furthermore, the existing O K-edge RIXS studies on 2D cuprates have not revealed such sharp spin-singlet magnetic excitations, and are mostly dominated by the  $\Delta S=0$  bimagnon continuum [69,74–76,166]. With the comparison in Figure 4:9, it is yet clear if the sharp mode  $\sim 270$  meV is mainly contributed by the QPs or the  $\Delta S=0$  2T bound state. Further comparison is required. .

Firstly, we extend our comparison to the optical studies. The spectral signature of interacting holons and spinons were previously speculated in the infrared and Raman spectra of doped cuprate ladders. From hole-depleted  $\text{Ca}_{14-x}\text{La}_x\text{Cu}_{24}\text{O}_{41}$  to lightly hole-doped ladders in Sr14, additional excitations were uncovered [148]. While some modes can be explained by the modulations from charge order formation [167], a new mode  $\sim 224$  meV in the infrared spectra of Sr14 was found to be incompatible with this charge order superstructure [148]. This new mode was speculated to be a localized polaronic charge excitation suggested for underdoped  $\text{YBa}_2\text{Cu}_3\text{O}_{6+\delta}$  [168] or the spectral signature of QPs [28,29]. The clear dispersion and energy of the sharp mode  $\sim 270$  meV observed in the present momentum-dependent O K-edge RIXS results is incompatible with the physical picture of localized polaronic excitations.

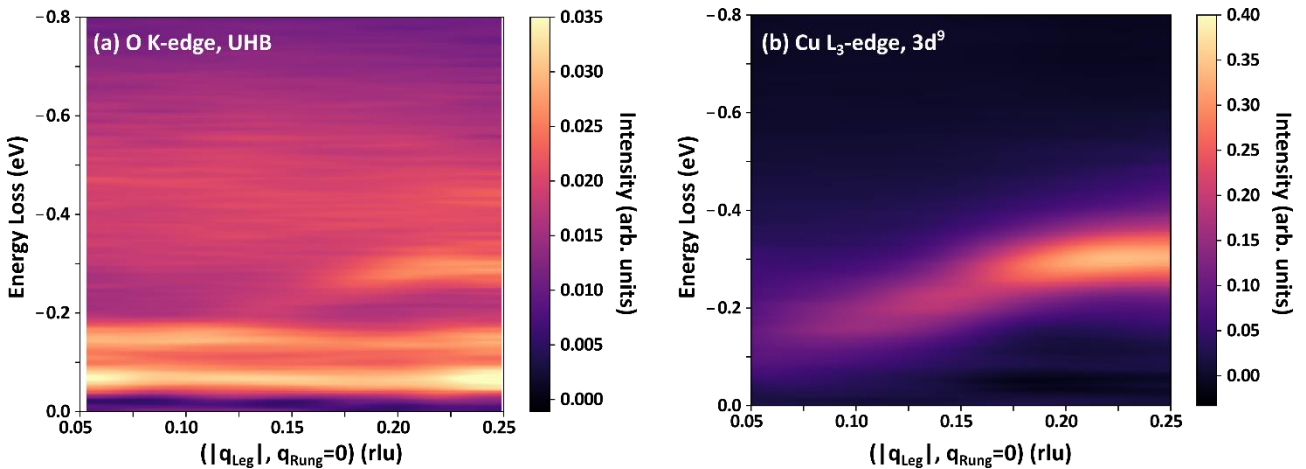


Figure 4:8 (a) Normalized momentum-dependent O K-edge RIXS in this work. (b) Cu L<sub>3</sub>-edge RIXS results in ref. [150]. The experimental data are interpolated along  $q_{\text{Leg}}$  with bicubic approximation, and the elastic line is subtracted for clarity.

Additionally, the temperature-dependent RIXS measurements revealed more information that make our observed sharp mode compatible with the observation of QPs. In Figure 4:10, O K-edge RIXS data taken at higher temperature  $\sim 280$  K show a melting of the sharp mode  $\sim 270$  meV compared to RIXS spectra taken at  $\sim 20$  K. Considering that the associated magnetic energy scale in the ladders of Sr14 is high, with  $J_{\text{Leg}} \sim 130$  meV ( $\sim 1500$  K) and an one-triplon (1T) gap  $\sim 32$  meV ( $\sim 370$  K) [17], suggests that this spectral suppression upon increasing the temperature is not of magnetic origin. Similar spectral behaviour was recently reported in O K-edge RIXS on the perovskite iridate  $\text{Sr}_2\text{IrO}_4$  [80]. An excitation mode  $\sim 400$  meV was found to suppress with increasing temperature and was connected to its electron-hole continuum origin [80]. The mode energy was comparable to the edge of electron-hole continuum, while it showed decreasing intensity with increasing temperature. Such behaviour was consistent with the broadening of the threshold for electron-hole continuum observed from optical measurements, with enhanced metallicity [80]. Additionally, a slight spectral broadening near the sharp onset about  $\sim 2$  eV [see Figure 4:6(a)] can be seen from our RIXS spectra taken at

280 K (Figure 4:10). This is also compatible with the scenario of increasing carriers populated over the charge gap, as the mode energy of  $\sim 2$  eV is consistent with the insulating gap for Sr14 [97]. On the other hand, one should not fully exclude the possibility of decreased Cu-O hybridization due to thermal expansion upon heating. This can lead to the spectral damping for the dd excitations, which are also expected in the energy regime  $\sim 2$  eV for Sr14 with O K-edge UHB RIXS [69,74]. Nevertheless, the temperature-dependent UHB RIXS results are compatible with the possibility that the observed sharp mode  $\sim 270$  meV is related to charge dynamics.

This connects to the characterization of the dc resistivity for Sr14, in which the optical conductivity is enhanced when heating above  $\sim 162$  K [147]. The activation of an additional charge conductivity channel at about 162 K was explained as the gap melting for the charge density wave (CDW), derived from the dissociation of localized hole pairs in the ladders [147]. As covered in chapter 5, a commensurate charge order  $\sim 0.2$  (rlu) has been previously confirmed in the ladders of Sr14 (see Figure 5:4 and Figure 5:7 in chapter 5). As the ladder-rung hole-pairs upon doping are required for both the QPs and charge order, we ascribe the spectral melting of the observed sharp mode to a disruption of the hole-pairs with enhanced itineracy, which lead to the disappearance of CDW as well as suppression for QPs.

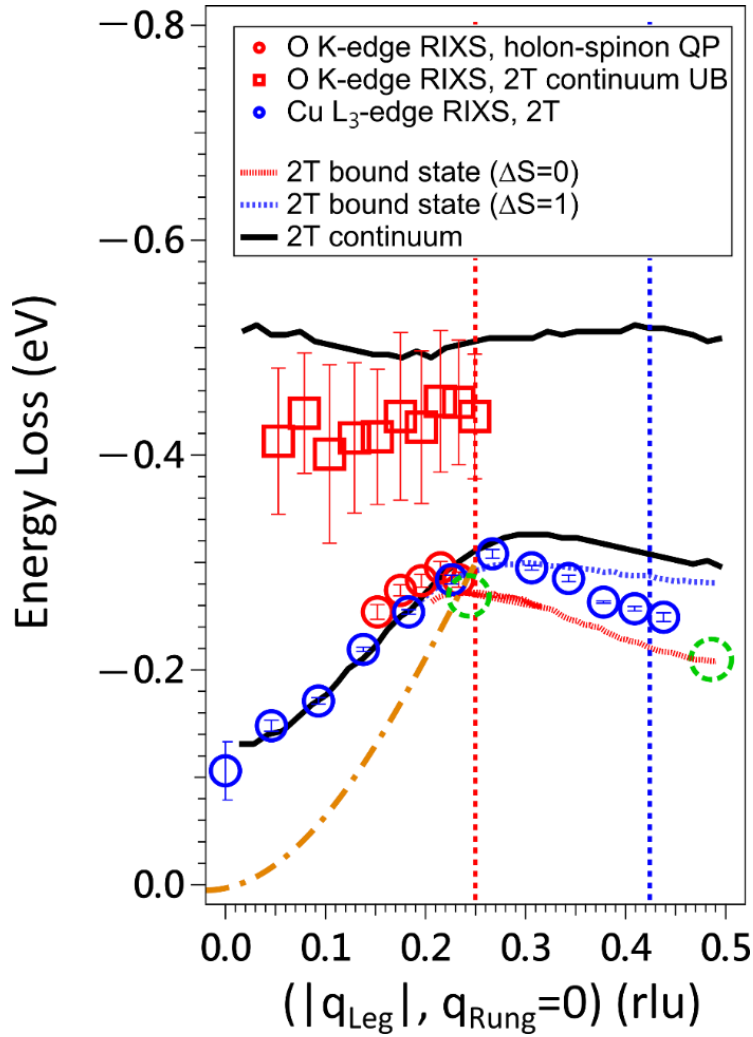


Figure 4:9 Fitted peak positions from O K-edge (this work) and Cu L<sub>3</sub>-edge RIXS from chapter 3, overlaid with the energies of the calculated MT scattering densities using CUT ( $J_{\text{Leg}}=130$  meV and  $r=J_{\text{Rung}}/J_{\text{Leg}}=1$ ) modified from ref. [91]. Red (blue) vertical dotted lines indicate the momentum-transfer of  $10^\circ$  grazing incidence at the O 1s (Cu 2p<sub>3/2</sub>) edge, serving as references of the experimental kinematic limit of the reachable momentum-space. The orange dot-dashed curve shown from  $q_{\text{Leg}}=0$  to  $q_{\text{Leg}}=0.25$  (rlu) depicts the holon-spinon QPs with the energy dispersion  $\omega(q)=t_{\text{Rung}}(1-\cos(q_{\text{Leg}}C_{\text{Leg}}))$  with sizable  $J_{\text{Rung}}$  [29], where the dispersion branch is shown within the kinematic limit of O K-edge RIXS in this work. Here  $t_{\text{Rung}}$  is taken as 300 meV. The optical signal of  $\Delta S=0$  2T bound state for the hole-depleted ladders in  $\text{Ca}_{14-x}\text{La}_x\text{Cu}_{24}\text{O}_{41}$  from ref. [169] is mostly contributed by the van Hove singularity of 2T DOS weighted by its coupling with phonons, which are peaked at the zone boundary and the maximum of the energy dispersion for  $r \sim 1$  (green dashed circles). The calculated  $\Delta S=0$  2T bound state shows appreciable weight only for  $q_{\text{Leg}} \geq 0.2$  rlu. This momentum region belongs to where the  $\Delta S=0$  2T bound state (red dotted curve) has separated energies from the lower 2T continuum boundary (black solid curve), and therefore free from decaying into the 2T continuum.

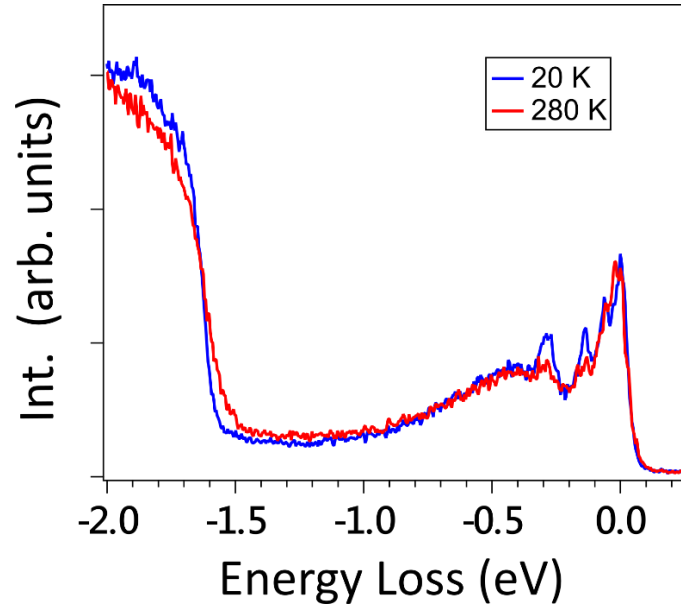


Figure 4:10 Temperature-dependent O K-edge RIXS spectra taken with  $q_{\text{Leg}} = -0.215$  (rlu) at 20 K (blue) and 280 K (red). RIXS spectra are normalized to total integrated intensity (see caption of Figure 4:8)

Lastly, we discuss the evidence that supports our observed sharp mode  $\sim 270$  meV to have spectral contributed from the  $\Delta S=0$  2T bound state. To be more specific for comparing our RIXS results with the MT scattering, we compare our RIXS results with MT spectra using perturbative CUT with magnetic exchange couplings closed to the  $r$  value of Sr14 ( $\sim 0.85$ , also see analysis in Figure 3:8) [26]. Additionally, the four-spin cyclic ring exchange is included in the results shown in Figure 4:11. Despite its lack of RIXS cross section, the  $\Delta S=0$  MT density is in close agreement with our experimental RIXS results. The predominant lowest-lying  $\Delta S=0$  2T bound state follows the energy dispersions with our observed sharp mode  $\sim 270$  meV (see caption of Figure 4:11), while the weakly-dispersing damped mode at higher-energy  $\sim 400$ -500 meV is well reproduced by the 2T continuum boundary. The spectral signature of  $\Delta S=0$  triplon bound state and continuum modes were also reported in recent CUT studies with RIXS matrix elements implemented [156].

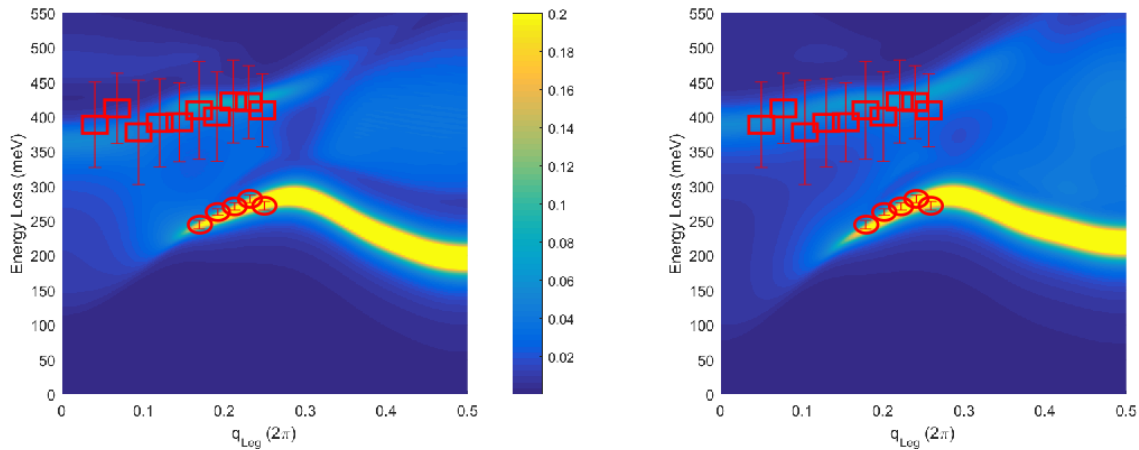


Figure 4:11 Calculated spectral density for the MT scattering in the  $\Delta S=0$  sector (the calculation data are provided with courtesy by Kai Phillip Schmidt). The rung-to-leg ratio of magnetic exchange  $r=0.8$  is close to the value estimated from the local structural distances ( $r \sim 0.85$  from ref. [26]). The effects of including a cyclic four-spin ring exchange, here defined by  $r_c = J_{\text{Ring}}/J_{\text{Rung}}$ , is taken into consideration with  $r_c=0$ , in the left panel and  $r_c=0.1$  in the right panel, respectively. The momentum- and energy-resolved spectral intensity is similar between the two panels with insignificant dependence on the inclusion of ring exchange. For comparing with the experimental O K-edge RIXS data in this chapter, a  $J_{\text{Rung}}$  value of  $\sim 120$  and  $145$  meV is taken for the left and right panels, respectively, which are compatible with the magnetic exchange couplings observed in Sr14 [26].

Combining the current knowledge from theory and optical experiments with our present study, we assign the dispersing sharp mode  $\sim 270$  meV of largely contributed by QPs and/or  $\Delta S=0$  2T bound state in our UHB O K-edge RIXS spectra. However, one should note that the DMRG [26] and CUT [91] theories that we use to compare with our



experimental results are not strictly equivalent to the O K-edge RIXS cross section. Firstly, with narrow resonance like O K-edge, a recent O K-edge RIXS study has confirmed that it is essential to consider core-hole lifetime effects in the calculated RIXS intensity [77], which are still lacking in current literature of doped ladders. Furthermore, in order to disentangle the charge and  $\Delta S=0$  magnetic scattering channels in the doped ladders, one has to calculate the polarization-resolved scattering channels, which will require multi-orbital cluster models [52]. Therefore, future theoretical works that involve the intermediate state effects in the doped multi-orbital ladders are needed to clarify our RIXS results in chapter 4.

## 4.7 Conclusion

We presented a O K-edge RIXS study of the ladder subsystem of Sr14. By comparison with model calculations of RIXS cross section and magnetic spectral density within CUT, our experimental results are compatible with the holon-spinon QPs and  $\Delta S=0$  MT excitations that were recently speculated at the K-edge RIXS signal. The RIXS sensitivities to these excitations highlight the unique spectral capability, and complements the current literature for elementary excitations in doped spin ladders, which share numerous electronic instabilities with the high- $T_c$  cuprates. The possibilities to measure interacting holon-spinons and MT excitations in the doped ladders will help to provide valuable details for the dynamical charge/magnetic correlations. Particularly, the holon-spinon QPs were predicted to be associated with the charge and pair density fluctuations in spin ladders.

## 4.8 Acknowledgement

The experiments have been performed at the ADRESS beamline of the Swiss Light Source at the Paul Scherrer Institut (PSI). The work at PSI is supported by the Swiss National Science Foundation through project no. 200021\_178867, the NCCR MARVEL and the Sinergia network Mott Physics Beyond the Heisenberg Model (MPBH) and SNSF Research Grants CRSII2\_160765/1 and CRSII2\_141962. A.N. acknowledges the supported by the Canada First Research Excellence Fund. J.T. and S.J. are supported by the National Science Foundation under Grant No. DMR-1842056. This work used computational resources supported by the University of Tennessee and Oak Ridge National Laboratory Joint Institute for Computational Sciences, and computational resources and services provided by Advanced Research Computing at the University of British Columbia.

# Chapter 5 Enhanced charge-stripe order with magnetic impurities in the chain-ladder cuprates $\text{Sr}_{14}(\text{Cu}_{1-x}\text{Co}_x)_{24}\text{O}_{41}$

## 5.1 Projection Contribution

The content of this chapter is undergoing at the time of the thesis submission preparations for the paper submission process as a journal article. In this chapter, I investigate the charge density wave (CDW) and phonon excitations in the self-hole-doped two-leg ladders of chain-ladder cuprate  $\text{Sr}_{14}(\text{Cu}_{1-x}\text{Co}_x)_{24}\text{O}_{41}$  using O K-, Cu L<sub>3</sub>- and Co L<sub>3</sub>-edge RIXS. In this work, I, Yi Tseng, am responsible for the experiment planning, preparation of the single crystal samples for the synchrotron experiments, performing the RIXS measurements and experimental data analysis. The paper is written by me as the main responsible with input from all the other co-authors. Section 5.2 serves as an additional introduction giving extended background information for the context of this work, including the figures 5:1 to 5:3. The corresponding article in preparation of submission includes the content from section 5.3 to 5.8, including the figures 5:4 to 5:18 and the tables 5.1-5.2, except for figure 5:9 and 5:11 that are taken from literature for comparison serving as references.

## 5.2 Preamble

One of the compelling hypotheses for high-temperature superconductivity (HTSC) pairing mechanism in cuprates is intertwined charge and pair density fluctuations [23]. This has been established by the seemingly ubiquitous formation of charge density wave (CDW) order in the superconducting (SC) dome of the phase diagram of various cuprates [23]. However, constructing a unified picture accurately describing CDW behavior has remained challenging. Several properties of the CDW order have been shown to vary among different types of cuprates, as well as its possible entanglement with other factors [23]. For instance, for the La-Cu-O cuprates with 214 stoichiometry and charge-stripe formation, the CDW ordering wavevector is positively correlated to the amount of doped holes, which is opposed to the real-space CDW order for (Y,Nd)-Ba-Cu-O compound, the so-called 123 cuprate family, and the Bi-, Tl- and Hg-based multi-layer cuprates [23] [Figure 5:1]. Additionally, the CDW correlation length can be also highly material-dependent and varies from several tens of unit cells for the static order in  $\text{La}_{2-x}\text{Ba}_x\text{CuO}_4$  to short-range charge fluctuations in  $\text{Bi}_2\text{Sr}_2\text{CaCu}_2\text{O}_{8+x}$  of a few lattice units [23]. Furthermore, whether the structural distortions and electron-phonon coupling (EPC) are crucially at play is still debated. The former question was put forward by diffraction and has remained the central topic for cuprate studies on charge-stripe order [170–174]. The latter was suggested by photoemission experiments, showing the omnipresence of significant phonon interactions concluded from the kinks of the quasiparticle dispersions [175]. On the other hand, various theories have been proposed to describe the CDW formation in cuprates. Connected to the band structure point of view, a Fermi-surface reconstruction with Fermi-arcs near the pseudogap temperature was observed in Bi-based SC cuprates [176]. But this observation failed to be extended to all cuprate families as far as current experimental literature can tell [176,177]. The detailed CDW texture including symmetry properties has also been discussed but remains elusive, including the possible multi-orbital texture or a topological crossover based on rotational-symmetry breaking [178,179]. Recent experiments even pointed out likely quantum critical scattering near the optimal doping of CDW order, along with competing components of different interaction-length scales [139,180]. Lastly, possible contributions from magnetic fluctuations may also need to be considered. Early studies have shown that the hourglass magnon excitations observed in 2D SC cuprates are intimately connected to the charge-stripe order [21,22,92].

One unique perspective to investigate the HTSC in cuprates is the role of defects and inhomogeneity. The SC state requires non-stoichiometric charge carriers doped in the  $\text{CuO}_2$  planes [181–183], while defects generally provide scattering centers for magnetic vortices and pinning of electronic order [184]. For samples with magnetic impurities doped at Cu sites, experiments using neutron diffraction and muon spin rotation have revealed enhanced static charge and

spin orders [185–187]. Moreover, this comes together with the observation of a further suppression for the superconducting transition temperature  $T_c$  in the cuprate phase diagram [185–187]. As shown in Figure 5:2, the  $1/8$  anomaly of the cuprate phase diagram was considered as a characteristic feature for the La-based cuprates with four-lattice-unit charge- and spin-stripes [170], but turned out to be achievable also in other types of cuprates by magnetic impurities [182]. These findings have led to the speculation that an universal charge-stripe order with  $T_c$  anomaly is general for cuprates and tuneable by magnetic doping [182]. The stabilization of fluctuating charge and spin orders in cuprates by introducing magnetic defects has also widely been confirmed [188].

Similar with 2D cuprates, the spin ladders were proposed to host competing CDW and SC states upon charge doping [9–11]. This has been confirmed in the two-leg ladders of the hybrid chain-ladder materials  $\text{Sr}_{14-x}\text{Ca}_x\text{Cu}_{24}\text{O}_{41+\delta}$  in experiments using resonant elastic X-ray scattering (REXS) [18,31] and high-pressure transport [19,20], respectively. More importantly, the CDW in spin ladders provides an ideal standard model that closely reproduces the unidirectional spin-charge cooperative stripe order. Coupled-ladders have been applied in theoretical studies simulating charge- and spin-stripes in 2D SC cuprates [21,22,92]. Therefore, it is intriguing to investigate the magnetic doping effects on the CDW in ladder materials. Motivated by that the cuprate ladder is one of the few materials without  $\text{CuO}_2$  planar structure that achieves a SC state upon doping, the magnetic doping evolution of the ladder CDW will provide valuable information for the proposed hypothesis, based on an omnipresent electronic stripe order in cuprates by impurity tuning [182] [Figure 5:3].

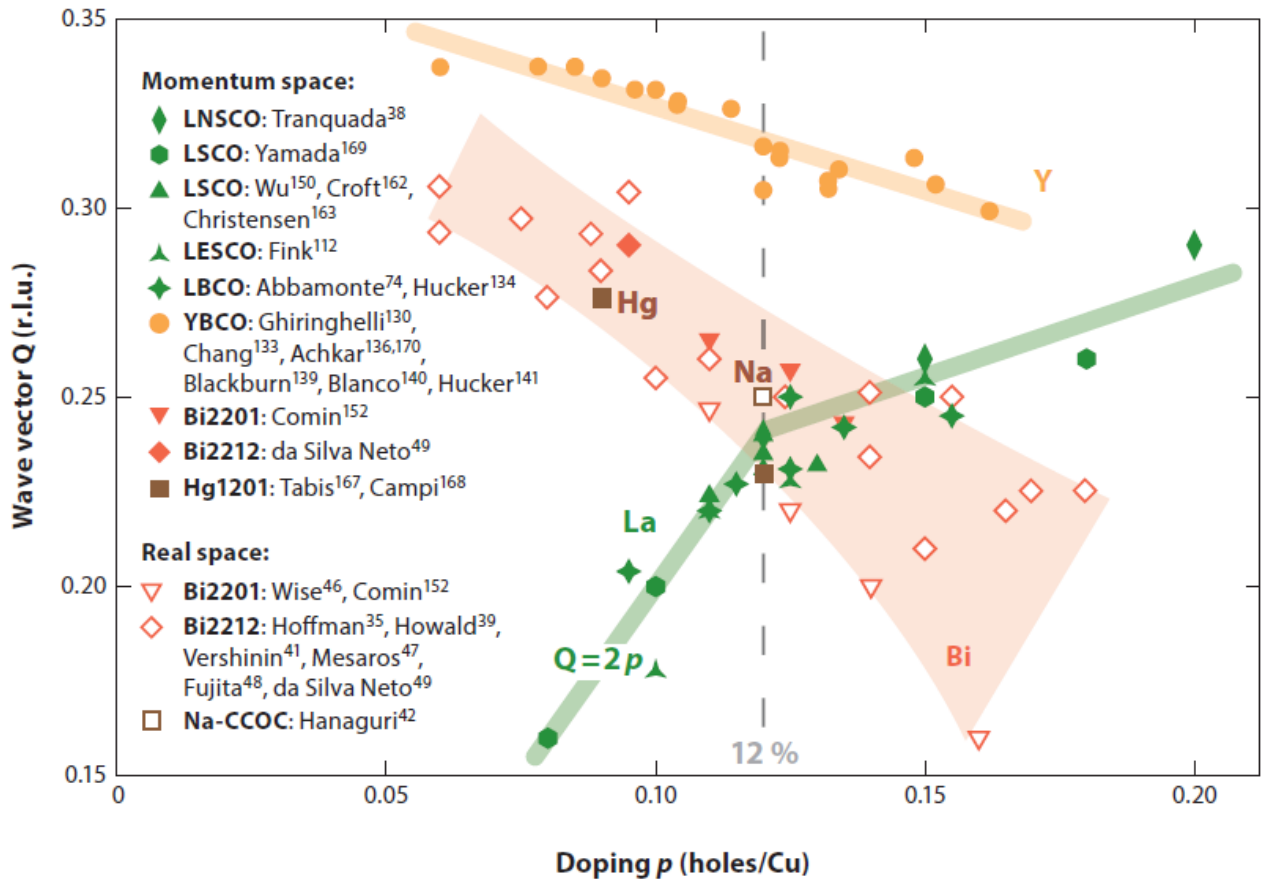


Figure 5:1 The CDW ordering wavevectors  $q_{\text{CDW}}$  as a function of hole-doping  $p$  across a wide span of SC cuprates taken from ref. [23] (Permissions from Annual Reviews, Annu. Rev. Condens. Matter Phys., R. Comin and A. Damascelli, 7, 369–405, 2016). Two major evolutions are highlighted in the plot. The  $q_{\text{CDW}}$  increase with elevated hole density for the momentum-space ordering type cuprates, coinciding with the La-based cuprates hosting charge-spin cooperative stripe orders. On the contrary, the Bi-, Hg- and Y-based multi-layer cuprates generally show an opposite trend, where the  $q_{\text{CDW}}$  decrease with increasing hole content and are referred to as the real-space ordering cuprates in ref. [23].

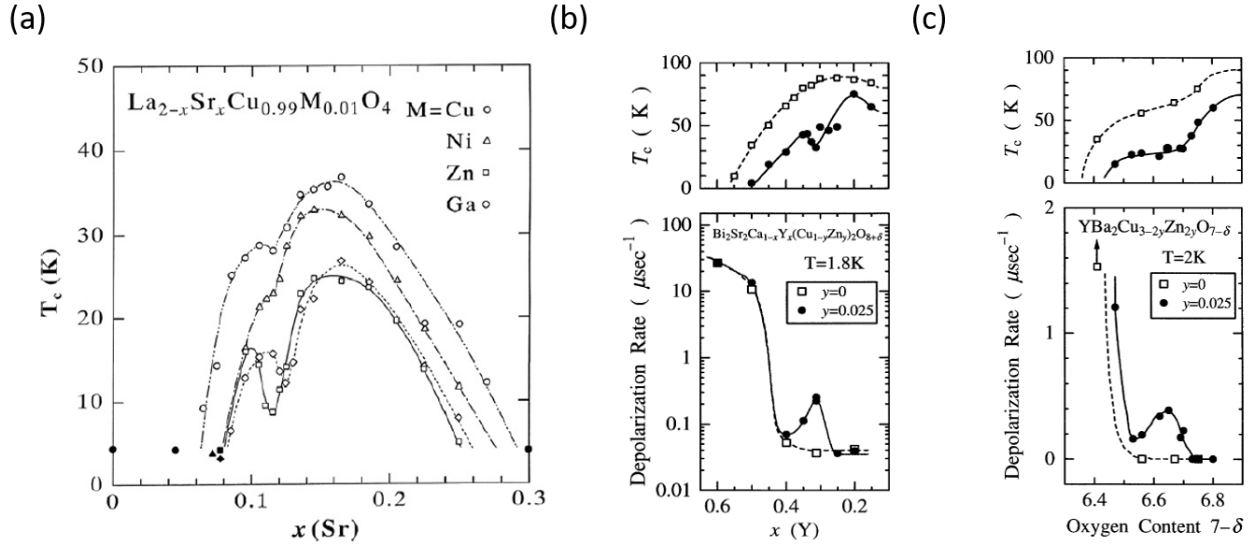


Figure 5:2 (a) The SC transition temperature  $T_c$  as a function of hole doping in  $\text{La}_{2-x}\text{Sr}_x\text{Cu}_{0.99}\text{M}_{0.01}\text{O}_4$  ( $\text{M}=\text{Cu}, \text{Ni}, \text{Zn}$  and  $\text{Ga}$ ) from ref. [182]. (b)-(c) show  $T_c$  and the depolarization rate (asymmetry ratio) in  $\mu\text{SR}$  measurements as a function of hole-doping for Bi- and Y-based cuprates from ref. [182]. The latter can be translated to the measure of local magnetic field strength. Despite different units for the hole-doping for (b)-(c) compared to (a), a significant suppression of  $T_c$  can be inferred around the  $1/8$  hole-doping level with 1-3% of magnetic doping at the Cu sites for all the measured cuprates (Reprinted by permission from Elsevier publishing group, Physica C: Superconductivity, Koike Y. and Adachi T., 481, 115-124, 2012).

This chapter reports RIXS spectra with systematic doping effects of Cu-Co substitution in the two-leg ladder subsystem of the  $\text{Sr}_{14}(\text{Cu}_{1-x}\text{Co}_x)_{24}\text{O}_{41}$ . From the elastic signal in RIXS spectra, the ladder CDW is observed at both the O K- and Cu  $L_3$ -edge, probed at the pre-edge ladder hole peak and charge ligand band with  $3d^{10}\underline{L}$  configuration ( $\underline{L}$  denotes a hole in the oxygen ligand), respectively [18,31]. In the low-energy inelastic energy loss region, the phonon harmonics for the Cu-O bond-stretching mode  $\sim 65\text{-}70\text{ meV}$  are clearly resolved in the O K-edge RIXS spectra [152,153]. At the O K-edge, the CDW is enhanced with increasing content of Co impurities, while the ordering wavevector  $q_{\text{CDW}}$  is continuously reduced. Additionally, the concomitant phonon softening at the CDW ordering wavevector is gaining strength with Co doping. These findings are accompanied by overall decreasing chain and ladder hole densities with increasing Co impurities, as determined from the O K-edge XAS results [99–102]. These results are connected to a strengthened CDW and enhanced phonon interactions with magnetic doping, which are consistent with recent magnetic susceptibility measurements [16,189] and theories on charge-stripe formation [190–192]. The reduced  $q_{\text{CDW}}$  with decreasing hole content is in line with the phase diagram of La-based cuprates with charge-stripe order [23]. Additionally, the electron-doped regime in cuprate ladders was recently predicted to energetically favor superconducting pairing [193,194], which was not discussed in previous studies using REXS [18,31]. Despite that the measured samples all remain reasonably hole-doped, it is a question for further investigations if the enhancement of CDWs by Co dopants leading to effective electron-doping effects is directly connected to this prediction. Former studies on the pristine two-leg ladders  $\text{SrCu}_2\text{O}_3$  (without chain layers) failed to tackle this question, as it is difficult to achieve high crystallinity in this compound with doped charge carriers [195].

The electronic character of the charge order in the ladders of  $\text{Sr}_{14}(\text{Cu}_{1-x}\text{Co}_x)_{24}\text{O}_{41}$  is confirmed in this thesis by RIXS measurements with varied incoming photon energy and temperature. The latter further uncovers an ordering melting accompanied by changes in the CDW linewidth incorporating likely multiple ordering components. These results connect to recent RIXS reports on 2D cuprates, suggesting the short-range charge fluctuations to pervade the phase diagram with low-temperature static order and to persist in the non-SC states [139,180]. These potential competing orders with different correlation length, which are in close relation to the multi-scale inhomogeneities via dopants or structural mismatch [196,197], are also reminiscent of the diffraction studies in SC cuprates [198–201]. These results imply that the similar criticality with a spatial competition of CDWs in SC cuprates may be extended to the cuprate ladders in non-SC phases, providing valuable information to revisit and formulate the pairing mechanism based on these hypotheses.

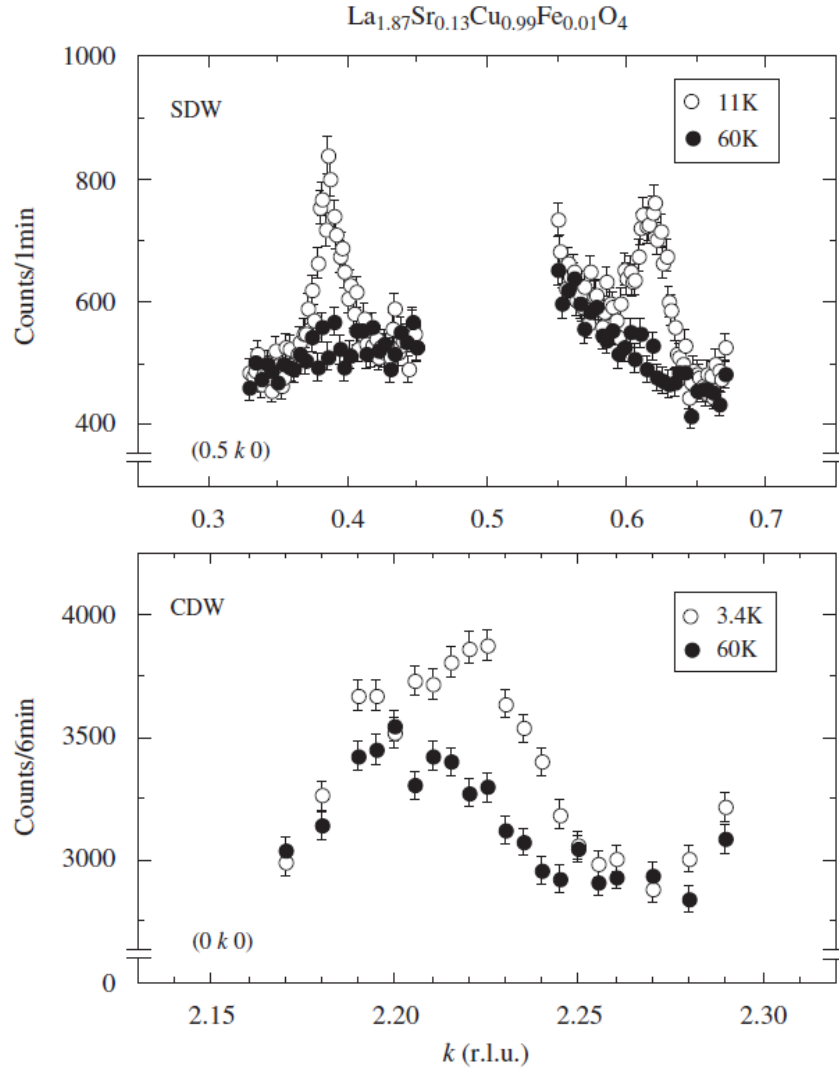


Figure 5:3 The incommensurate SDW and CDW orders observed in the Fe-doped LSCO using neutron diffraction obtained from ref. [202]. The CDW order observed along  $(0 \ 2\pm\epsilon \ 0)$  with  $\epsilon=0.224\pm0.002$  is about twice of the SDW order revealed along  $(0.5 \ 0.5\pm\delta \ 0)$  with  $\delta=0.115\pm0.003$ , while both orders melt with increasing temperature  $\sim 60$  K. This justifies that the enhanced incommensurate CDW and SDW orders that are absent in the Fe-free LSCO can be induced by magnetic impurity doping (Reprinted by permission from Elsevier publishing group, Journal of Physics and Chemistry of Solids, Fujita M., Enoki M., and Yamada K., 69, 3167-3170, 2008).

## 5.3 Abstract

We study charge density wave (CDW) order accompanied by phonon softening in the two-leg ladders of the hybrid chain-ladder materials  $\text{Sr}_{14}(\text{Cu}_{1-x}\text{Co}_x)_{24}\text{O}_{41}$  ( $x \leq 0.05$ ) using resonant inelastic X-ray scattering (RIXS). By monitoring the energy-resolved elastic intensity, the diffraction peak due to static charge order with long-range correlations along the in-plane ladder-leg direction is observed to strengthen with light Co doping content. The ordering wavevector continuously reduces with increasing Co-doping concentration, while the ladder hole content decreases with Co impurities. Melting of this charge order upon heating reveals possible critical-scattering behaviour. At elevated Co doping of 5%, our RIXS measurements uncover a stronger phonon softening  $\sim 10$  meV for the bond-stretching vibrations  $\sim 65$ -70 meV at the CDW wavevector. Furthermore, the electron-phonon coupling (EPC) is analysed as a function of Co-doping and momentum from the observed phonon excitations. We conclude that combined electronic and magnetic doping effects from the Cu-Co substitution are invoked in the enhancement of charge order, as well as the enhanced electron-phonon interactions. Our study demonstrates how the charge-stripes and phonons in cuprate ladders can effectively be manipulated via Co dopants, which may share similar mechanism with the existing reports in superconducting (SC) cuprates with magnetic impurities.

## 5.4 Introduction

The assessment of the electronic order parameter intertwined with high-temperature superconductivity (HTSC) has been a research focus in cuprate studies. Among the competing electronic instabilities with symmetry-broken ground states at low-temperature, the omnipresent charge and spin density wave (CDW & SDW) spanning across various cuprates have been suggested crucial for the high- $T_c$  pairing [23]. However, the distinct ordering vectors found in different types of cuprates, along with their inconsistent doping and structural dependence, hamper the formulation of unified theories for electron pairing in cuprates based on charge density fluctuations [23].

One of the crucial parameters that can help understanding HTSC in cuprates is the density of impurities and electronic inhomogeneity. In cuprates, non-stoichiometric charge doping is essential for the emergence of a superconducting (SC) phase, while chemical disorder generally acts as pinning centers for vortices and generally increases the critical current [184]. Additionally, the experimentally confirmed impurity effects on the SC phase and entangled electronic orders, such as the enhancement of  $T_c$  or pinning of fluctuating charge and spin order, provide a unique aspect to study the pairing mechanism in cuprates [181–183]. Particularly, recent experiments have revealed that an universal anomaly with a suppression of  $T_c$  around 1/8 hole-doping can be achieved in different types of cuprates by adequate addition of magnetic impurities [182,183]. Furthermore, this coincides with the experimental observation of enhanced static incommensurate SDW and CDW orders [185–187,202–204]. The 1/8 anomaly was firstly revealed in the La-based cuprates with an unidirectional charge-spin cooperative stripe order [205], which was later confirmed in early neutron experiments [170]. Additionally, the charge-stripe phase was predicted as the major competing electronic state against HTSC in theories using coupled-ladder models [21,22].

This motivates our study on the doped two-leg cuprate ladders with magnetic impurities. Serving as the minimal interaction model describing the charge-stripe correlations in two-dimensional (2D)  $\text{CuO}_2$  planes, quasi-one-dimensional (q-1D) ladders possess several similarities with the 2D cuprates in their low-energy physics [9–11]. In the hybrid chain-ladder materials  $\text{Sr}_{14-x}\text{Ca}_x\text{Cu}_{24}\text{O}_{41+\delta}$ , the CDW and SC states were confirmed using resonant elastic X-ray scattering (REXS) for  $x=0, 10, 11$  and  $12$  [18,31] and high-pressure transport measurements for  $x>11$  [19,20], respectively. The electronic origin of the observed ladder CDW was further supported by theoretical studies on t-J models with inter-ladder Coulomb repulsion [206–208]. Therefore, it is intriguing to see if the tuning of CDW order with magnetic impurities can be observed in doped cuprate ladders, as such studies are still lacking. Our results would also expand the proposed scenario of an universal  $T_c$  anomaly and its interplay with charge-stripe order possibly to doped spin ladders.

Here we present a study on the evolution of CDW and phonon excitations in  $\text{Sr}_{14}(\text{Cu}_{1-x}\text{Co}_x)_{24}\text{O}_{41}$  using resonant inelastic X-ray scattering (RIXS). O K- and Cu  $L_3$ -edge RIXS both reveal the CDW formation in  $\text{Sr}_{14}(\text{Cu}_{1-x}\text{Co}_x)_{24}\text{O}_{41}$ . From the O K-edge RIXS spectra measured at the ladder hole electronic configuration, the enhanced elastic signal due to CDW becomes more pronounced with increasing Co dopants, and develops into a long-range order at a reduced ordering wavevector. The temperature-dependent O K-edge RIXS measurements confirm an electronic character with the ordering melting upon heating. Additionally, our results further reveal a possible critical-scattering from the temperature-dependent width for the observed in-plane diffraction signal, reminiscent of the recent studies on 2D SC cuprates [139,180,209,210]. Accompanying the strengthened static CDW from Co impurities, the phonon softening for the optical vibrations of 65~70 meV at the ordering wavevector is found to be enhanced in the O K-edge RIXS spectra. The momentum-resolved electron-phonon coupling (EPC) is also evaluated across all Co doping levels. From recent magnetic susceptibility and photoelectron spectroscopy measurements on  $\text{Sr}_{14}(\text{Cu}_{1-x}\text{Co}_x)_{24}\text{O}_{41}$ , we observed the combined magnetic and electronic doping effects of the Co impurities [16,189]. This supports a suggested scenario for the pinning of charge-stripe order via magnetic dopants, which were previously proposed for the SC cuprates [185,187]. Furthermore, the electron-doping effects may be connected to the recent theories that predicted energetically favoured pairing correlations towards the electron-doped regime of the cuprate ladders [193,194]. Lastly, the enhanced phonon-softening response with Co doping is in line with the speculation that the lattice distortion has a crucial role for the charge- and spin-stripes formation [190–192].

## 5.5 Experimental Method

$\text{Sr}_{14}(\text{Cu}_{1-x}\text{Co}_x)_{24}\text{O}_{41}$  ( $x=0, 0.01, 0.03$  and  $0.05$ ) single crystals are grown with the traveling-solvent floating zone method [16,189]. Top-post cleavage is performed *in-situ* before all measurements, with a vacuum pressure about  $5 \times 10^{-10}$  mbar. RIXS and XAS measurements are performed at the Advanced Resonant Spectroscopies (ADRESS) beamline at the Swiss Light Source (SLS), Paul Scherrer Institut [54–56]. The total RIXS energy resolution of 50 meV and 95 meV are achieved with the 3000 line/mm grating for the RIXS spectrometer at the O K- ( $\sim 530$  eV) and Cu L<sub>3</sub>-edge ( $\sim 930$  eV), respectively. To characterize the environments of Co dopants, we apply Co L<sub>3</sub>-edge ( $\sim 780$  eV) RIXS measurements carried out with the 1500 line/mm grating for the RIXS spectrometer, achieving a total RIXS energy resolution of 105 meV. The scattering angle  $2\theta$  is fixed at  $130^\circ$ . The photon-in-photon-out RIXS technique has demonstrated its unique capability for probing various collective electronic excitations, with element and orbital selectivity [49]. By separating the elastic scattering from the inelastic signal, RIXS is capable of simultaneously measuring the energy-resolved (ER) REXS signal and low-energy excitations [211]. This allows direct assessment of the elementary excitations in vicinity to the underlying electronic orders [64,83,138,140–142].

The RIXS experimental geometry is fixed with b- and c- axis oriented in the scattering plane, where the c-axis (ladder-leg) is parallel to the in-plane momentum-transfer. In order to resonantly select the hole content in the ladder subsystem in the given RIXS geometry [99–102],  $\pi$  polarization is applied for the incident X-rays. This ensures a finite projection along the leg direction (c-axis) for the electromagnetic field of the incident X-rays at the O K-edge [99–102]. Cu L<sub>3</sub>-edge RIXS, on the other hand, preferentially enhances the charge scattering in layered cuprates with  $\pi$  polarization in the grazing incidence scattering [66,133,134]. The RIXS measurements are performed in the grazing incidence geometry. RIXS spectra are corrected for self-absorption effects. XAS spectra are recorded with total fluorescence yield (TFY) mode and normalized up to 70 eV above the main resonances from the tabulated photo-absorption cross-sections [85].

## 5.6 Results and Discussions

### 5.6.1 Energy-Resolved REXS and RIXS probed: CDW order and phonon excitations

Figure 5:4 shows the overview of the XAS profiles and ER-REXS signal from RIXS measurements taken at the O K- and Cu L<sub>3</sub>-edge for  $x=0$  and  $x=0.03$ . Following the previous REXS studies on  $\text{Sr}_{14-x}\text{Ca}_x\text{Cu}_{24}\text{O}_{41+6}$ , we measured the elastic scattering intensity as a function of momentum-transfer at the ladder hole peak and the charge transfer ligand band at O K- and Cu L<sub>3</sub>-edge, respectively [18,31]. At the O K-edge, the pre-edge double peaks of 527.5-528.2 eV was argued to consist of the combined electronic configuration of hole content in the chains and ladders [99–102]. It has been perceived that the linear dichroism corresponds to the distinct Cu-O-Cu bonding environments between the edge-sharing chains and two-leg ladders, enabling the disentanglement of the hole content between the two subsystems [99–102]. At the Cu L<sub>3</sub>-edge, the ligand environments for chains and ladders show overlapping energy scales with marginal linear dichroism in XAS, where the chain ligand sites host the majority of the holes [99,102]. For  $x=0$ , a commensurate CDW with an ordering wavevector  $q_{\text{CDW}} \sim 0.2$  (rlu) is inferred [Figure 5:4(b) and (e)], in accordance with the former REXS reports [18,31]. At  $x=0.03$ , we observe a diffraction signal appearing at a reduced ordering wavevector  $\sim 0.135$  (rlu) for both O K- and Cu L<sub>3</sub>-edge. This diffraction peak at the O K-edge is stronger and sharper with 3% Co impurities. The detailed discussions for Cu L<sub>3</sub>-edge RIXS results, including the experimental data taken at the 3d<sup>9</sup> resonance  $\sim 931$  eV, will be covered in later sections (see section 5.6.8).

To systematically investigate the Co doping dependence of the charge order and the relevant dynamical response, we focus on the O K-edge RIXS results from section 5.6.2 to section 5.6.7. We observe an enhancement of the ladder CDW signal and distinct changes in the phonon excitations as a function of Co doping content in the RIXS overview (Figure 5:5). We will firstly address the observed in-plane diffraction signal, evaluated from the energy- and momentum-resolved elastic enhancement in different aspects in section 5.6.2-5.6.5. The phonon excitations will be covered in section 5.6.6-5.6.7. Further discussions on the Cu L<sub>3</sub>- and Co L<sub>3</sub>-edge RIXS results are shown in section 5.6.8 and 5.6.9, respectively.

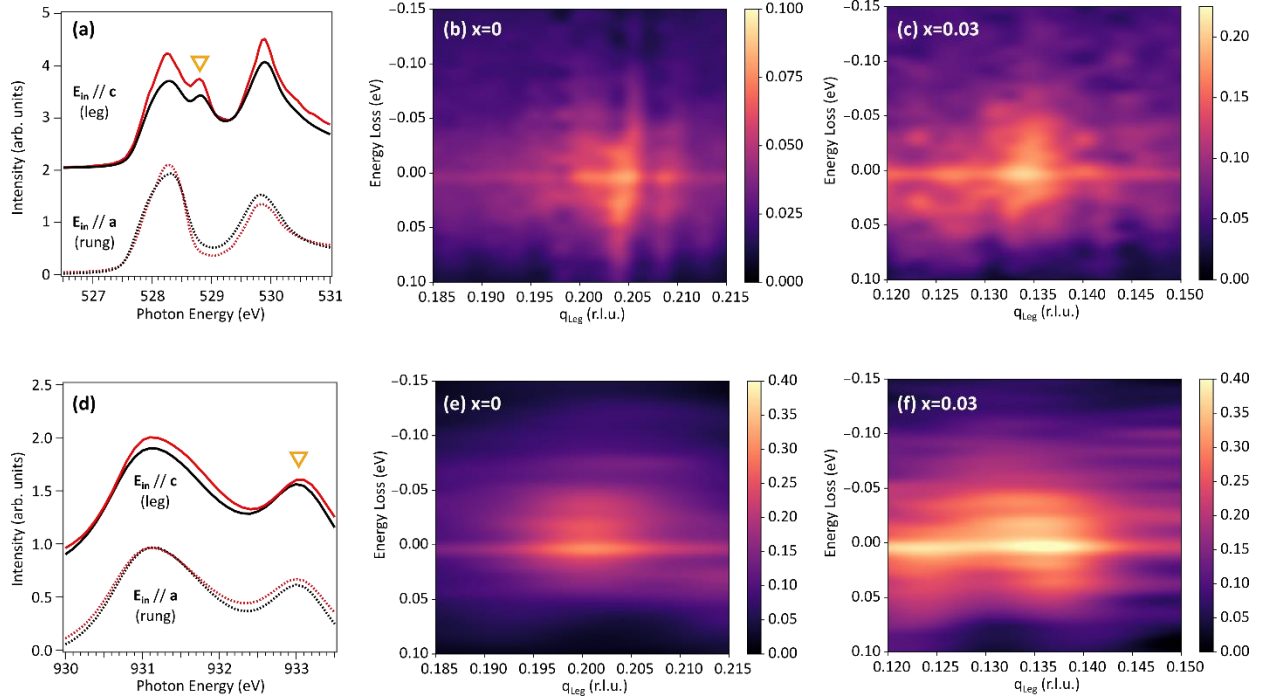


Figure 5:4 (a)-(c) O K-edge XAS and RIXS spectra showing the probed resonance and the energy-resolved (quasi-) elastic signal. The O K-edge RIXS spectra are recorded at the ladder hole peak  $\sim 528.6$  eV (orange triangle). (d)-(f) Cu  $L_3$ -edge XAS and RIXS spectra showing the probed resonance and the energy-resolved (quasi-) elastic signal. The Cu  $L_3$ -edge RIXS spectra are recorded at the charge-transfer ligand band  $\sim 933$  eV (orange triangle). The chosen XAS resonances at O K- and Cu  $L_3$ -edge are in agreement with the previous REXS reports on SCCO [18,31]. Both measurements are performed with  $\pi$  polarization in the grazing incidence geometry. (b) and (e) reproduce the commensurate ladder CDW  $\sim 0.2$  (r.l.u.) reported for  $x=0$  in ref. [18]. (c) and (f) show an enhanced elastic signal near  $q_{\text{Leg}} \sim 0.135$  (r.l.u.) for  $x=0.03$ , where the diffraction signal is more pronounced at the O K-edge.

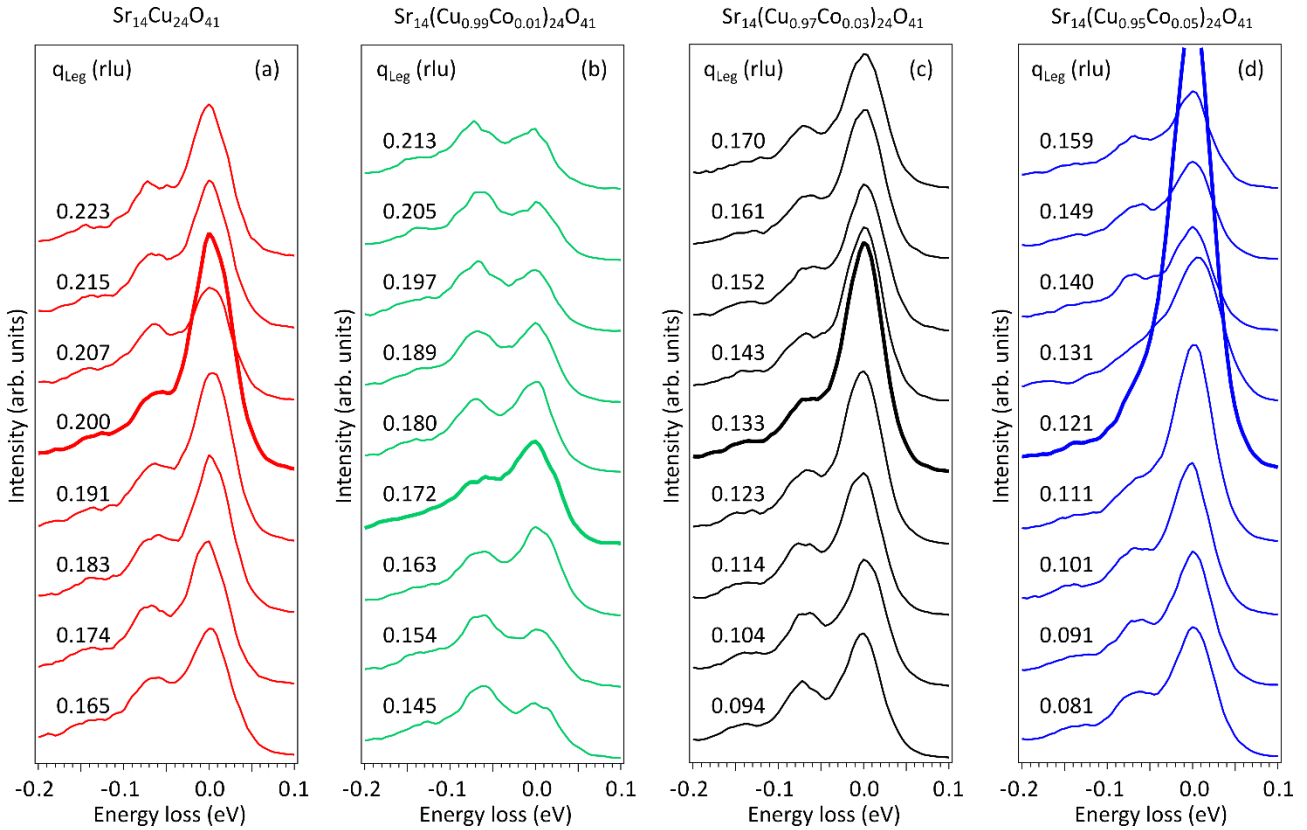


Figure 5:5 (a)-(d) Momentum-dependent O K-edge RIXS spectra revealing the enhanced elastic scattering at certain wavevectors (highlighted by thick solid lines) with optical phonons ( $\sim 65$  meV) across all Co doping levels.



### 5.6.2 O K-edge Energy-Resolved REXS: Change of ladder CDW with Co-doping

From the RIXS measurements taken in a wider momentum range in Figure 5:6(a), this diffraction response is clearly enhanced with increasing Co doping concentration. In particular, the width for the CDW profile seems to show a sharpening upon Co-doping. To further clarify the nature of the observed elastic signal with Co doping, we plot the intensity of the elastic scattering as a function of incident X-ray energy for momentum-transfer vectors where the elastic signal is maximized for each doping level. As shown in Figure 5:6(b)-(c), the observed diffraction signal is resonantly enhanced at the ladder hole peak for all Co doping levels, giving a clear fingerprint of its electronic character of ladder CDW. To our surprise, the observed elastic signal with electronic origin seem to suggest that the periodic charge modulations are not interfered but rather stabilized by a low-doping of Co impurities. Additionally, these in-plane diffraction signal have not been revealed in the isostructural cuprate ladders in former studies using energy-integrated REXS [18,31].

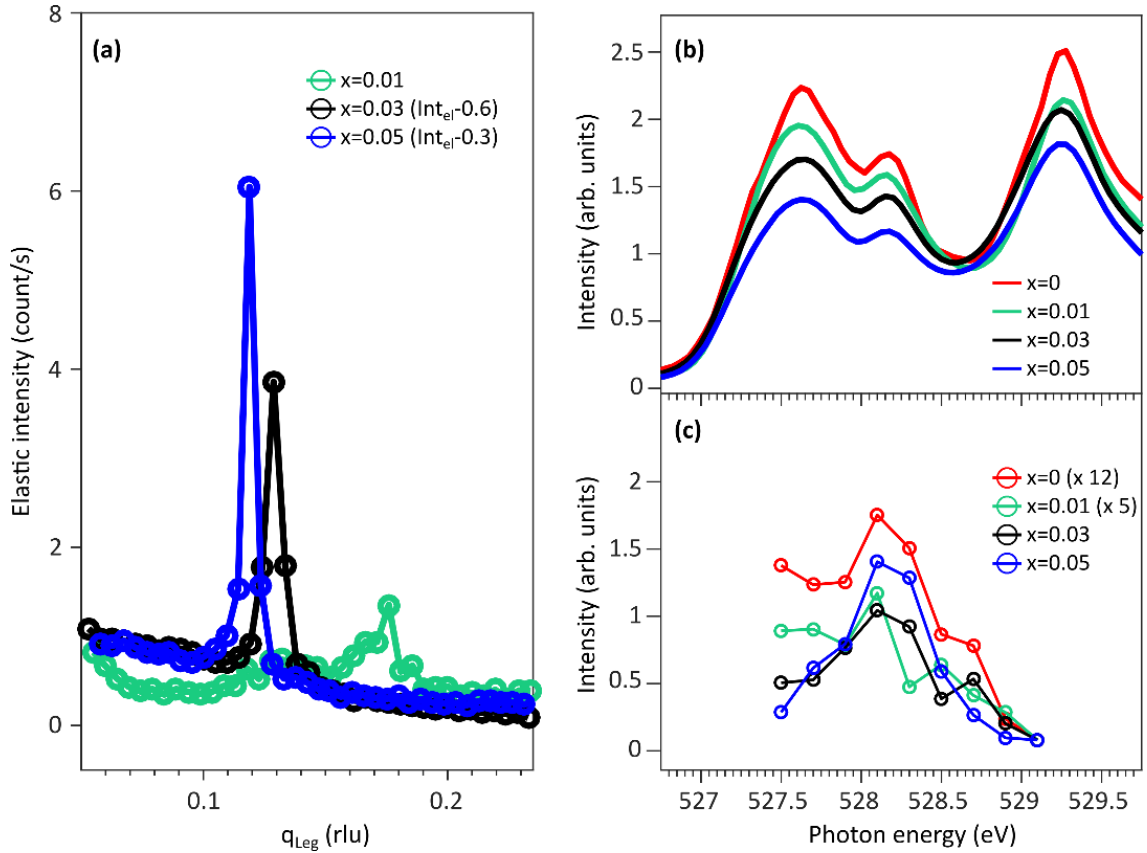


Figure 5:6 (a) Momentum-dependent O K-edge RIXS measurements showing the in-plane elastic signal in the leg direction for different Co-doped samples. (b)-(c) Normalized O K-edge XAS spectra (see main text) and elastic intensity across the main XAS resonances, respectively, measured in the leg direction for all Co doping levels. The elastic intensities in (c) are recorded at the wavevectors where the elastic signal is maximized for each doping level as shown in (a), while the data are normalized to the integrated RIXS intensity from 10 eV loss to 1 eV gain. The elastic signal taken at the post-edge near UHB ( $\sim 529.3$  eV) is used as the normalization background for comparing the resonant profile of in-plane elastic scattering.

Another experimental finding from Figure 5:6 (a) and (b) is a reducing CDW wavevector with slightly decreased hole density, which follows the charge-stripe order relation in the phase diagram of La-based cuprates (see section 5.2). In Figure 5:6(b), the Cu-Co substitution does not drastically modify the XAS resonances, but slightly decrease the pre-edge spectral weight for the doped holes in both chains and ladders [99–102]. Using the modelling of ref. [99], the evaluated ladder hole densities slightly decrease from  $\sim 6\%$  to below  $5\%$  (Table 5.1) from  $x=0$  to  $x=0.05$ . By comparing with Figure 5:1, we notice that the relation between CDW ordering wavevector and ladder hole density in  $\text{Sr}_{14}(\text{Cu},\text{Co})_{24}\text{O}_{41}$  follows the trend of La-based 2D cuprates with charge-spin cooperative stripe order (see section 5.2). Namely, the CDW wavevector decreases with reduced hole density (Figure 5:1). This would naturally connect our observations in cuprate ladders to the layered SC cuprates, and supports the cuprate studies based on ladder models. On the other hand, one

should not fully exclude the possibility that the decreasing ordering wavevector with Co-doping may be affected by impurity percolations, which was previously studied in Fe-based superconductors [212]. To clarify such scenario will require structural refinements and high-resolution diffraction measurements to elucidate the Co dopant distribution between chain and ladder subsystems, which is beyond the scope of this thesis. In section 5.6.9, we will present further discussions for the elastic scattering and inelastic response of Co dopants using Co  $L_3$ -edge RIXS (also see Figure 5:17).

Additionally, with the electron-doping by Co dopants, the enhanced ladder CDW signal is consistent with the recent speculation that the pairing correlations are energetically favoured towards electron-doped regime [193,194]. The predominant static CDW order at low temperature has been considered as a characteristic feature for pairing formation in the cuprate phase diagram [23]. As the measured  $\text{Sr}_{14}(\text{Cu}_{1-x}\text{Co}_x)\text{O}_{41}$  are reasonably hole-doped (Table 5.1) and insulating (Figure 5:7), it is still an open question that if the cuprate ladders show similar competition between CDW and SC states towards the hole-depleted or electron-doped phases as predicted in ref. [193,194]. In Table 5:1, the evaluated hole content ( $x=0, 0.03$  and  $0.05$ ) and their respective hole-doping levels are reasonably away from the  $1/8$  hole-doping concentration. This would suggest that additional factors beyond the  $1/8$  anomaly in hole-doping is required to explain our observations of enhanced CDW.

Samples	Total number of holes (p.c.f.)	Number of chain holes (p.c.f.)	Number of ladder holes (p.c.f.)	Ladder hole density (1/Cu ion)
$\text{Sr}_{14}\text{Cu}_{24}\text{O}_{41}$	6.00	5.15	0.85	6.0%
$\text{Sr}_{14}(\text{Cu}_{0.97}\text{Co}_{0.03})_{24}\text{O}_{41}$	5.61	4.87	0.74	5.3%
$\text{Sr}_{14}(\text{Cu}_{0.95}\text{Co}_{0.05})_{24}\text{O}_{41}$	4.78	4.08	0.70	4.9%

Table 5:1 The hole densities in the chain and ladder subsystems evaluated from the O K-edge XAS results based on the model from ref. [99]. The unit p.c.f. indicates that the number is evaluated per chemical formula of  $\text{Sr}_{14}(\text{Cu},\text{Co})_{24}\text{O}_{41}$ .

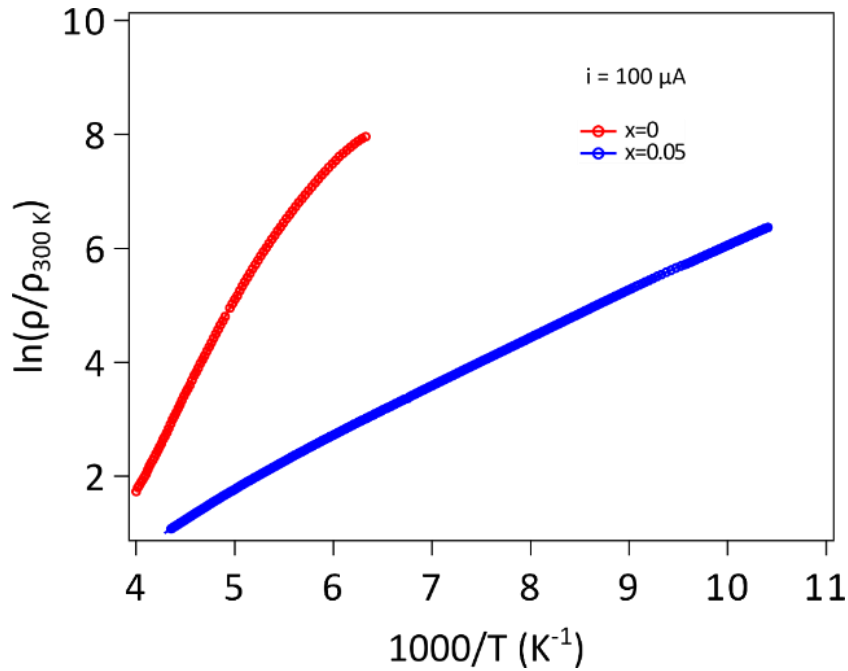


Figure 5:7 Electrical transport measurements without magnetic field on the single crystal  $\text{Sr}_{14}(\text{Cu}_{1-x}\text{Co}_x)\text{O}_{41}$  samples for  $x=0$  and  $x=0.05$  (data courtesy: Surjeet Singh and Rabindranath Bag). The horizontal axis represents the inverse of temperature multiplied by 1000, whereas the vertical axis is the resistivity normalized to room-temperature value expressed in the natural logarithmic scale. An overall increased metallicity is inferred with Co doping.

In Figure 5:8 (a)-(d), we present finer sampling in momentum vectors around the observed ordering wavevectors for all Co-doping levels. To evaluate the ladder CDW correlations as a function of Co-doping, we fit the in-plane diffraction profiles with a Lorentzian function [brown solid curves in Figure 5:8(a)-(d)] on top of a linear background [dotted straight lines in Figure 5:8(a)-(d)]. Alongside the fitted diffraction peak positions that decrease with Co-doping [Figure 5:8(e)], the peak intensities and widths are also displayed [Figure 5:8(f)]. the slight downturn of the leg correlation length for  $x \leq 0.03$  and monotonic increase for the integrated intensity may indicate that the Co dopants activate other types of (electronic) diffraction processes with different spatial and magnetic correlations compared to  $x=0$ . From marginally

modified lattice parameters (Table 5:2) and recent structural characterization [16], we conclude that neither the structural changes or additional Bragg peaks lead to such elastic enhancement in our RIXS measurements.

To make a short summary at this stage, we observe the enhanced ladder CDW signal which develops a sharper linewidth with Co-doping (Figure 5:8). Additionally, it seems that there may be two or more diffraction components involved from the slight asymmetry of CDW profiles (Figure 5:8). In the following paragraphs, we argue that these observations are connected to a physical scenario that the CDW signal is pinned and strengthened by magnetic doping effects, and may involve the emergence of multiple diffraction components with distinct spatial and magnetic correlations.

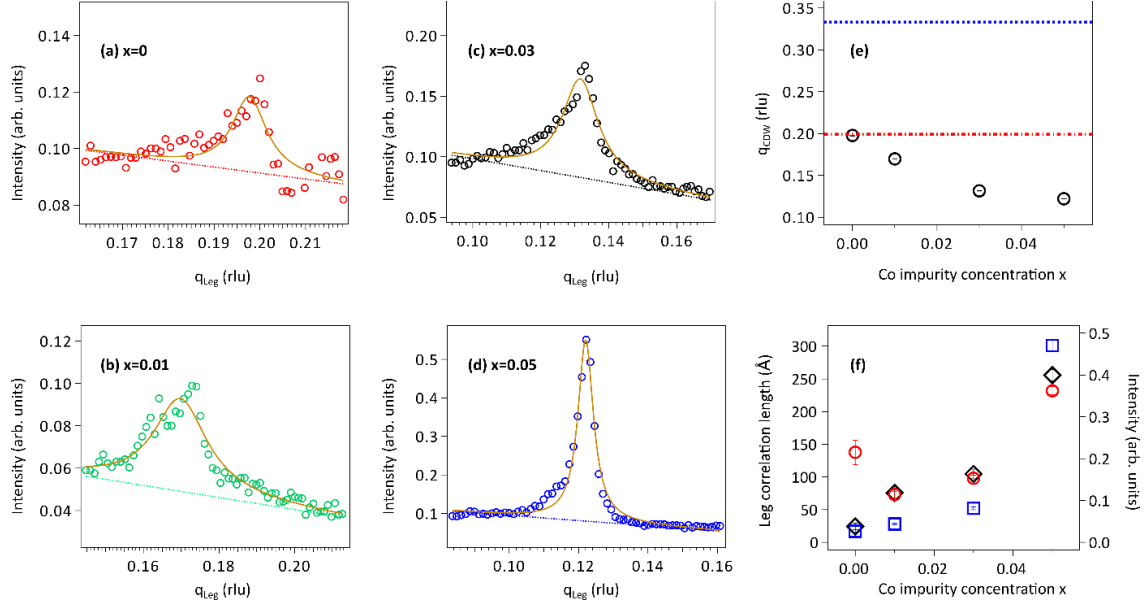


Figure 5:8 (a)-(d) Momentum-dependent O K-edge RIXS measurements for the in-plane rocking curves around the CDW wavevectors for all Co doping levels (see fitting schemes in section 5.6.2). The elastic intensities are normalized to the integrated RIXS spectral weight from 10 eV loss to 1 eV gain. (e) The evaluated ordering wavevectors (black circles) as a function of Co doping concentration. (f) The fitted CDW correlation lengths (red circles), maximum intensity (blue squares) and integrated intensity (black diamonds) for the ladder CDW as a function of Co doping concentration. The CDW signal is fitted by a Lorentzian function with a linear background. The horizontal lines in (e) represent the  $q_{\text{CDW}}$  obtained from the previous REXS studies on  $\text{Sr}_{14-y}\text{Ca}_y\text{Cu}_{24}\text{O}_{41}$ , where  $q_{\text{CDW}} \sim 0.2$  rlu for  $y=0$  (red dot-dashed) and  $q_{\text{CDW}} \sim 0.33$  rlu for  $y$  of 10~12 (blue dashed) [18,31].

### 5.6.3 Charge order pinning by magnetic impurities?

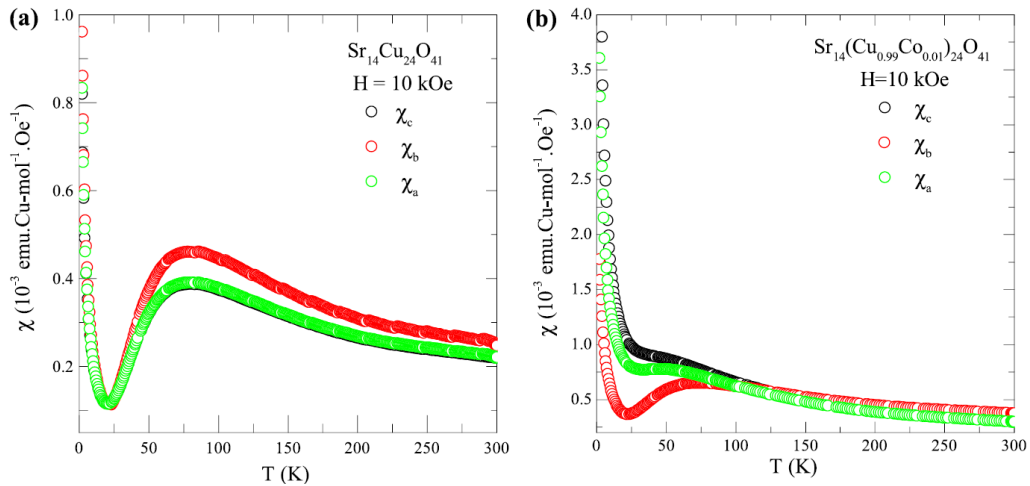


Figure 5:9 Magnetic susceptibility for  $\text{Sr}_{14}(\text{Cu}_{1-x}\text{Co}_x)_{24}\text{O}_{41}$  from ref [16], showing an enhanced Curie-Weiss weight in the low-temperature regime upon Co-doping (also see Figure 6 in ref. [213]). This indicates an increased magnetic moment from Co dopants that disrupts the isotropic spin-liquid ground state for the cuprate ladder subsystem, while the increased moment shows clear in-plane/out-of-plane anisotropy. (Reprinted by permission from Elsevier publishing group, Journal of Crystal Growth, Bag R., Karmakar K., and Singh S., 458, 16-26, 2017).

Samples	a(Å)	b(Å)	c <sub>leg</sub> (Å)	Cell volume V (Å <sup>3</sup> )
$\text{Sr}_{14}\text{Cu}_{24}\text{O}_{41}$	11.4689(6)	13.4004(8)	3.9327(3)	604.42(5)
$\text{Sr}_{14}(\text{Cu}_{0.99}\text{Co}_{0.01})_{24}\text{O}_{41}$	11.4660(6)	13.3936(8)	3.9343(3)	604.19(5)
$\text{Sr}_{14}(\text{Cu}_{0.97}\text{Co}_{0.03})_{24}\text{O}_{41}$	11.4648(7)	13.3871(8)	3.9378(5)	604.37(7)
$\text{Sr}_{14}(\text{Cu}_{0.95}\text{Co}_{0.05})_{24}\text{O}_{41}$	11.4624(7)	13.3827(8)	3.9378(5)	604.19(7)

Table 5:2 Structural lattice parameters for the single crystal samples of  $\text{Sr}_{14}(\text{Cu}_{1-x}\text{Co}_x)_{24}\text{O}_{41}$  obtained from ref. [16].

We firstly start from the connection between magnetic impurities and enhanced CDW orders. By looking at the former studies on 2D SC cuprates with magnetic doping, those results remind on the possible scenarios for strengthening CDWs in layered cuprates (see section 5.2). It has been shown that the presence of defects and impurities can stabilize dynamically fluctuating stripes in SC cuprates [188]. This was observed in neutron and muon spin rotation ( $\mu\text{SR}$ ) experiments on cuprates with Cu substituted by 1-2% of Fe or Zn [185–187]. Additionally, our observations connect to the spin-freezing mechanism for quenching the spin fluctuations, which are proposed to compete with pairing correlations [214–216]. The role of remnant AFM correlations with spin-freezing in hole-doped 2D cuprates was recently suggested crucial for understanding the pseudogap phase in SC cuprates, with the observed glassy spin-freezing behavior energetically favoured for charge-stripe formation [217]. Therefore, we believe that our energy-resolved REXS results in Figure 5:8 provide the ideal bridge between the q-1D ladders and 2D SC cuprates, with the tuning of charge order by magnetic impurities. The enhanced spin and charge orders with magnetic impurities are often interpreted as the magnetic impurity quench of the fluctuating SDWs, and thereby affecting the CDWs via the compensated hole content with respect to the stripe structural deformations. With magnetic dopants, the observation of strengthened long-range static charge order *at a reduced ordering wavevector* (Figure 5:8) was also found in the neutron studies on Fe-doped LSCO [202,204]. This suggests that a similar scenario may be present in our experimental results in this chapter.

In order to tackle this question, we will start by aiming for investigating the characterization on magnetic properties of  $\text{Sr}_{14}(\text{Cu}_{1-x}\text{Co}_x)_{24}\text{O}_{41}$ . In the low-dimensional chains and ladders, magnetic impurities can potentially percolate across the lattices, and introduce intercalated spin-spin correlations forming real-space ordering [218]. On the other hand, one should note that even the magnetic doping in respective copper-oxide subsystems may affect each other. For instance, in the hybrid chain-planar structures of Co-doped  $\text{YBa}_2\text{Cu}_3\text{O}_{7-x}$  (YBCO), Tarascon et al. showed that the suppressed  $T_c$  in the 2D  $\text{CuO}_2$  planes was accompanied by the preferential Cu-Co replacement for the Cu sites with Co in chain layers [219]. This can be conceptualized by Co dopants in the chains providing magnetic vortices, which can still effectively suppress the SC state in the 2D  $\text{CuO}_2$  plaquettes and promote the static stripe formation like when applying a magnetic field [220–222]. With this, an enhanced incommensurate SDW has been reported in YBCO, which may very likely affect the charge density correlations as well [185].

With these experimental observations, we look into the existing characterization of magnetic susceptibility in  $\text{Sr}_{14}(\text{Cu}_{1-x}\text{Co}_x)_{24}\text{O}_{41}$ . The magnetic doping effects in the chain subsystem were clearly shown in the magnetic susceptibility measurements (Figure 5:9), where the spin dimerization was found to be disrupted and shifted towards lower temperature [16,189]. The Curie-Weiss term was found to be enhanced differently with Co doping for the in-plane and out-of-plane contribution [16,189]. This led to the suggestion that a magnetic anisotropy is induced likely from a single-ion like magnetic correlations with Co doping [16,189]. Previous electron diffraction measurements also suggested a predominant fraction of Cu-Co replacement in the chains with only marginally modified diffraction of ladder sites [223,224]. The increased Curie term and magnetic impurities are ascribed to a contribution of the chains, sharing similar magnetic doping effects in YBCO [219,225]. One should notice that this does not rule out the possibility for a finite amount of Co dopants residing in the ladders, which will be discussed below sections. A possible explanation for the enormously strong CDW signal at  $x=0.05$  may suggest that a direct Cu-Co replacement occurs at the ladder sites when  $x \geq 0.05$ . Given the scarcity and complications for studies with mixed  $\text{Co}^{2+}/\text{Co}^{3+}$  coordination in the square planar environments, characterization of the exact chain- and ladder-site Co distribution with their spin states will require further investigations. The nearly identical scattering cross section in X-ray diffraction between Cu and Co hinders the quantitative assessment of Co dopant distribution with structural refinements [16]. Furthermore, the complexity of the incommensurate chain-ladder structural misfit can induce additional superstructure reflections [16].

### 5.6.4 Cooperating or competing mechanism of CDW with different spatial and magnetic correlations?

In this paragraph, we then deal with the origin of a slightly asymmetric lineshape in CDW signal with Co-doping. We choose the RIXS data taken for  $x=0.03$ , as the experimental results take in  $x=0$  and  $x=0.01$  are relatively noisy for this purpose. This is studied with temperature-dependent O K-edge RIXS measurements (Figure 5:10). The fitting of CDW profiles follow the strategy sued in Figure 5:8. At  $x=0.03$ , a ordering melting  $\sim 200$  K can be seen for the in-plane ER-REXS signal [Figure 5:10(a)-(b)]. Additionally, there are spectral signatures of damping and asymmetry in the CDW profiles with increasing temperature [Figure 5:10(c) and (e)]. This was not observed in previous REXS studies on  $\text{Sr}_{14-x}\text{Ca}_x\text{Cu}_{24}\text{O}_{41+\delta}$  [18,31]. On the contrary, a recent study featuring Eu-doped LSCO pointed out that these CDW orders are of electronic origin with a spontaneous symmetry-breaking, where the CDW signal was found to melt and broaden with a temperature-independent integrated intensity [210]. By fitting a Lorentzian function for the CDW profile, the conclusions from ref. [210] seem to agree with our observation for the ladder CDW [Figure 5:10(d)-(f)].

Additionally, recent Cu  $L_3$ -edge RIXS studies on SC YBCO, LSCO and  $\text{La}_{2-x}\text{Ba}_x\text{CuO}_4$  (LBCO) also show similar temperature dependence for the in-plane CDW rocking curves, which further revealed an anti-symmetric line shape for the CDW signal [139,180,209,210]. These findings share similarities to our temperature evolution of the CDW correlation lengths (Figure 5:10), which might suggest the possibility that other types of charge order/fluctuations may be induced by the Co dopants. In Figure 5:10(c), the CDW broadening along with ordering melting in our experimental RIXS results at 160 K and 200 K are reminiscent of the reports [139,180,209,210].

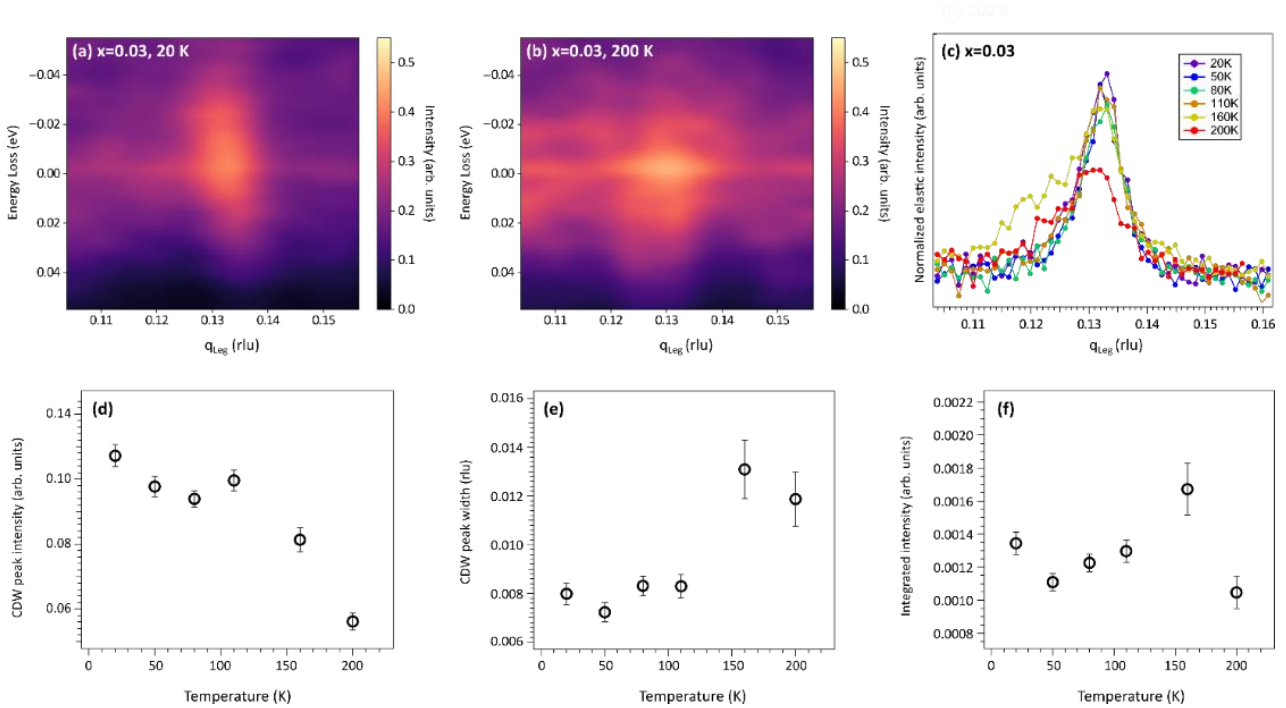


Figure 5:10 O K-edge RIXS measurements showing the ER-REXS signal around the elastic line for  $x=0.03$  taken at (a) 20 K and (b) 200 K. (c) The CDW rocking curves for  $x=0.03$  are displaying the in-plane resonant diffraction signal for a series of temperatures. The fitting scheme follows Figure 5:8. A linear background is fitted and subtracted from the data. (d)-(f) The fitted peak intensity, peak width and integrated intensity of area below the peak, respectively, for the CDW profiles as a function of temperature.

One proposal for such temperature-dependent CDW correlation length is related to charge fluctuations pervading across the CDW transition temperature [139,180,209]. In this scenario, the CDW is expected to be dynamically critical, with the short-range charge fluctuations spanning across the phase diagram and persist in the non-SC phases [180]. Another possible mechanism for explaining our temperature-dependent results in Figure 5:10 relies on the competing CDWs and SDWs with different correlation lengths, which co-exist with a peculiar metallic state in the cuprates [198–201]. This was previously demonstrated in the three-dimensional (3D) CDWs of YBCO, where a manipulation with magnetic field was achieved for these spatially-inhomogeneous charge- and spin-orders [198–201].

Following these proposed scenarios from ref. [139,180,209] and ref. [198–201], our observations with similar broadened line shapes from the CDW melting may imply that these proposals can exist in the non-SC cuprate ladders without  $\text{CuO}_2$  plaquette structures. Given the close relationships between the 2D SC cuprates and q-1D cuprate ladders, our results support that the tuning of multiple CDW components can be achieved by magnetic and electronic inhomogeneity in doped cuprate ladders. To clarify this, we suggest high-resolution single crystal X-ray and neutron diffraction measurements for diffraction peaks around our probed momentum regions. This will help to separate our observed electronic orders from structural Bragg reflections, as well as their interplay with magnetic field and pressure in the presence of Co dopants. The studies on spatially-competing CDW orders in cuprates and their connection to magnetic impurities are still lacking. Therefore, our study shall provide information for examining the role and evolution for charge order and fluctuations in cuprates with different structures and stoichiometry.

### 5.6.5 Evaluation of CDW profiles according to co-existent charge order and charge density fluctuations

In Figure 5:11, we apply the model from ref. [180] to analyse the temperature dependence of the CDW profiles. It was previously proposed that the CDW with critical scattering around the optimal doping phases may provide a possible explanation for mediating the HTSC in cuprates [139,180,209]. Another proposal is formulated on the possibility of multiple CDWs competing with different spatial correlations and magnetism [198–201]. In the former picture, the charge correlations persist as short-range fluctuations up to the non-SC high-temperature phases, whereas the static charge order melts with increasing temperature. Despite the lack of SC phases in the  $\text{Sr}_{14}(\text{Cu},\text{Co})_{24}\text{O}_{41}$  materials, this model provides a pictorial approach for differentiating multiple (electronic) orders that may compete at distinct temperature and spatial scales, therefore providing a good framework for understanding our experimental RIXS results. The fitting constraint for the two-component model is taken from the experimental RIXS data taken at 160 K, where the spectral components for the static sharp peak (SP) and a broad peak (BP) reflective of the charge fluctuations are both clearly presented. Both the peak positions and widths of BP are assumed to be temperature-independent. On the other hand, the peak position for the SP is fixed, and then we evaluate the temperature evolution of the peak intensities and widths of SP. Based on the model in ref. [180], the BP component shows no critical scattering with temperature. Therefore, in the enclosed analysis of this work, the peak width ( $\sim 0.17$  rlu) and position of the BP are kept fixed throughout all temperature points with respect to the 160 K data.

We compare the fitting results of our experimental RIXS data with one- and two-Lorentzian profiles for the predominant SP of the CDW signal. In ref. [139,180], the SP was observed to become broader across the SC transitions and melt upon heating in YBCO and LBCO. On the other hand, the BP was proposed as the seeding precursor of charge density fluctuations, representative of the pre-formed pairing that pervades the entire phase diagram. In our results of  $\text{Sr}_{14}(\text{Cu}_{1-x}\text{Co}_x)\text{O}_{41}$ , however, the BP is not consistently present as a temperature-independent component throughout all the temperature range. The BP peak intensity is generally below  $\sim 0.01$  [unit in Figure 5:11(a)] for temperatures below 110 K, reasonably within the signal fluctuations in the background, but shows a sudden increase when exceeding 160 K ( $\sim 0.035$  and  $0.015$  for 160 K and 200 K, respectively). This could indicate that the source of anti-symmetric CDW line shape in our RIXS results may not share the same mechanism as ref. [139,180,209], suggesting other types of diffraction processes with distinct temperature dependence may need to be considered here. The possibility of beam instability and intensity fluctuations at 160 K, on the other hand, cannot be completely excluded here. The SP intensity is generally unaffected by the inclusion of the BP in the fitting scheme. As for the peak width of SP, the spike of increase at 160 K and 200 K seems here to be compensated by considering an additional spectral component for BP. The tendency of an overall increasing peak width for the long-range static charge order (SP) upon heating, due to interactions with fast oscillations of charge density (BP), is qualitatively in agreement with ref. [180]. Additionally, by adapting the two-peak fitting model for the CDW signal, the integrated intensity for the SP also evolves towards a smoother trend with temperature, which gradually decreases with increasing temperature.

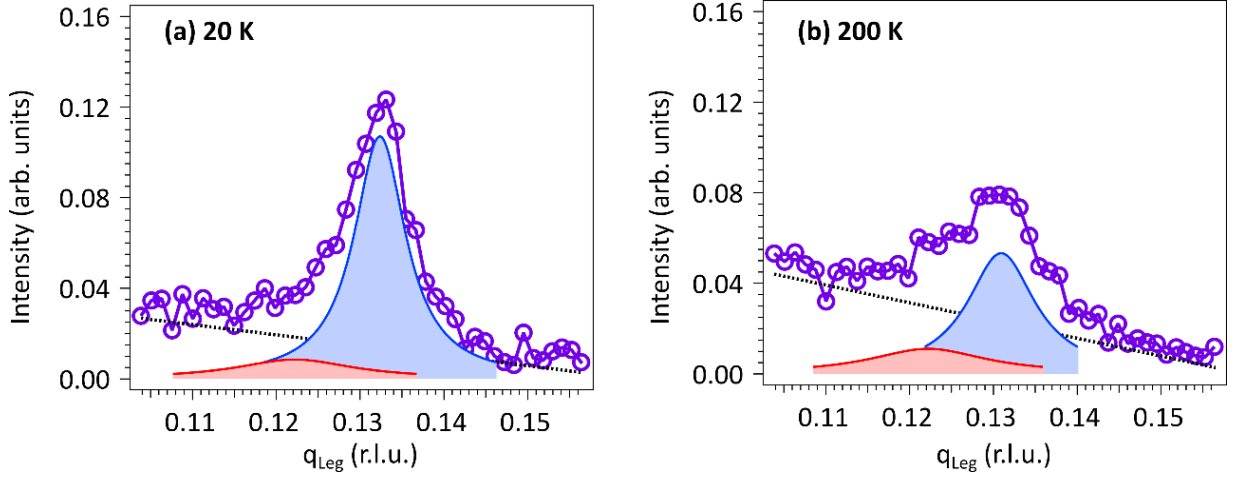


Figure 5:11 (a)-(b) CDW fitting with two Lorentzian functions for  $x=0.03$  in  $\text{Sr}_{14}(\text{Cu}_{1-x}\text{Co}_x)_{24}\text{O}_{41}$  taken at 20 K and 200 K, respectively. The fitting scheme is taken from the ref. [180]. Following ref. [180], the BP (red) is assumed to be the temperature-independent charge fluctuations, where the peak position and width are fixed for different temperatures. The SP (blue) is assigned to be the static charge order component that melts with increasing temperature, and its peak position is fixed for all temperatures.

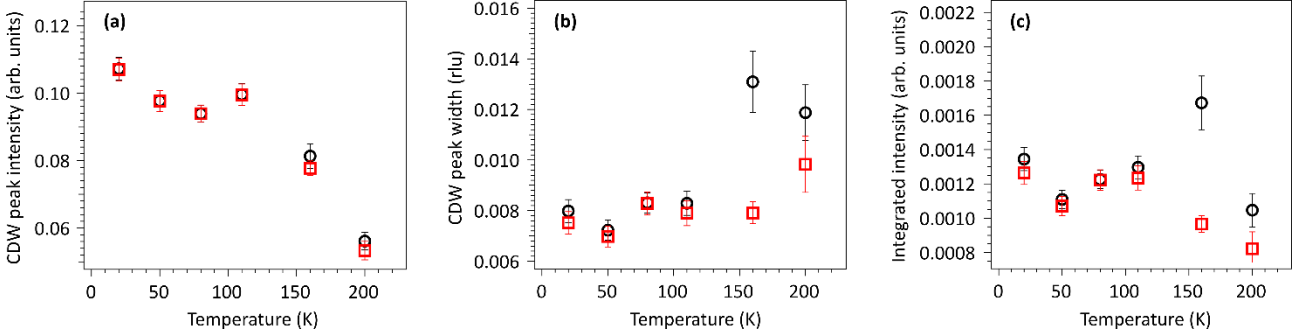


Figure 5:12 (a)-(c) The fitted peak intensity, peak width and integrated intensity for the SP (red squares) compared to the fitting results with one Lorentzian function for the CDW signal shown in Figure 5:10.

### 5.6.6 O K-edge RIXS spectra: Phonon excitations vs. Co-doping

A natural further question to be addressed is if and how corresponding lattice excitations are connected to the enhanced charge-stripe order with Co doping. Despite that the HTSC in cuprates cannot be solely explained by the phonon-mediated electron-pairing in BCS theory, the observed strong softening and broadening for the bond-stretching and low-energy acoustic phonons in the vicinity to CDW ordering, suggest that the electron-phonon interactions still have a more crucial role in the pairing correlations in cuprates [226–229]. As RIXS is capable to detect multi-phonon processes as harmonic satellites in the energy-loss spectrum, it is a very promising probe to elucidate the relation between phonons and charge ordering [78]. The direct access to momentum-resolved EPC, without integrating the respective phonon spectral weight and analysing the broadening, sets RIXS apart from other experimental probes for measuring phonons, e.g. optical probes, photoemission spectroscopy, non-resonant inelastic X-ray scattering (IXS), etc [53,78]. The RIXS sensitivity to phonons is achieved by a re-arrangement of the charge clouds via electron-phonon interactions during the RIXS intermediate state. The matrix elements for the scattering cross section are described in a Frank-Condon picture for the excited vibrational modes (see section 2.6.1).

In Figure 5:13, we study the phonon excitations of  $\text{Sr}_{14}(\text{Cu}_{1-x}\text{Co}_x)_{24}\text{O}_{41}$  as a function of Co doping  $x$  by taking advantage of the strong EPC signal in the O K-edge RIXS spectra, with clear high-order harmonic contributions. Compared to the transition-metal L-edge, the longer core-hole lifetime at the O K-edge grants substantial weight for the short-lived high-order phonon overtones, which have been observed in the low-dimensional cuprates [154,155]. This comes alongside with the improvements in the soft X-ray RIXS instrumentation in recent years, where the detection of concurrent CDW and softening of phonon modes  $\sim 35\text{--}70$  meV have been widely demonstrated in layered cuprates [83,138,140,142].



This will give direct access to tackle the role of phonons for CDW in the doped ladders. This is of particular importance as the phonon interactions were not included in the early theories for the CDW in  $\text{Sr}_{14-x}\text{Ca}_x\text{Cu}_{24}\text{O}_{41+6}$  [206–208].

In Figure 5:13(c), we observe a phonon-softening response for the vibrational mode of 65–70 meV that is particularly strong for  $x=0.05$  [152,153]. The 15–20% of softening in energy agrees with the softening of the Cu–O bond-stretching mode observed in 2D cuprates by RIXS [83,138,140,142]. Figure 5:13(a)–(b) show the line fitting of elastic and phonon components for  $x=0$  and  $x=0.03$ . With increasing  $x$ , a slightly reduced phonon intensity is inferred and may be associated with the enhanced metallicity from electron-doping of the  $\text{Co}^{3+}$  dopants (Figure 5:7). The concomitant CDW and phonon softening is observed across all Co doping levels, where the phonon-softening becomes stronger with increasing Co doping and a strengthening long-range charge-stripe order. The unquenched orbital momentum from magnetic site impurities may introduce a single-ion like magnetic anisotropy [106,191,217]. Such magnetic doping effects were previously suggested to be responsible for the lattice distortions, which can help for unidirectional charge modulations in the SC cuprates [16,189,218]. Additionally, the anomalous softening and broadening of the longitudinal oxygen bond-stretching vibrations were reported to be manifested within the SC phases in cuprates, which was believed to be intimately associated with the dynamical charge-stripe formation that is different from the static charge/spin stripes [226–229]. Our experimental findings in a doped spin ladder not only support the crucial role of phonons for stabilizing the likely formation of broken-symmetry dynamical charge order in cuprates, but likely expand this physical scenario to non-SC phases [190–192]. In our O K-edge RIXS results, it is noticeable that a marginal signature of phonon broadening near  $q_{\text{CDW}}$  or a Fano-type phonon anomaly away from  $q_{\text{CDW}}$  is observed, which was recently reported in the Cu  $L_3$ -edge RIXS studies on Bi-based SC cuprates [83,138,142]. The former may be reconciled by a spectral broadening within the spectral functions in our RIXS measurements, as the fundamental phonon  $\sim 65$ –70 meV can be reasonably fitted by resolution-limited Gaussians (see next paragraph). On the other hand, Fano-like responses with quantum fluctuations are formulated for stabilizing the pairing correlations in ref. [83,142], while the SC state is absent in our measured samples. This effect may also be material-dependent, as the recent Cu  $L_3$ -edge RIXS study on LSCO did not observe this spectral behaviour [140].

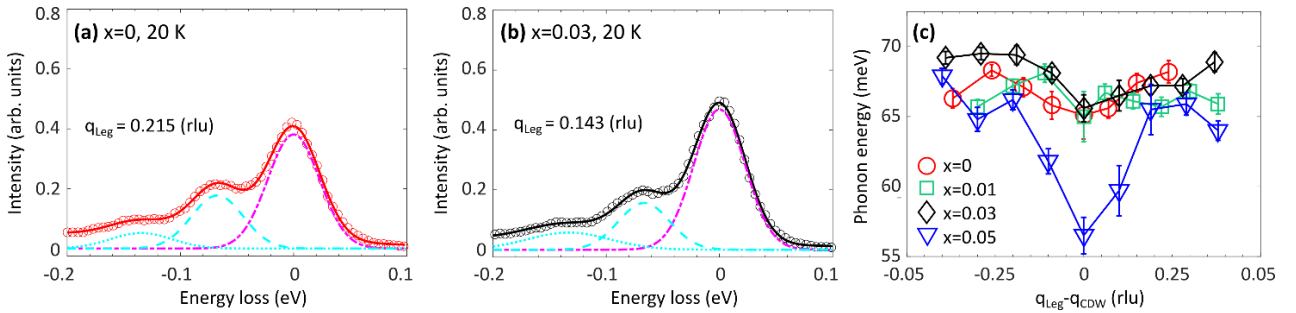


Figure 5:13 (a)–(b) O K-edge RIXS spectral line fitting. The elastic scattering (purple dot-dashed lines) and the fundamental phonon around 65–70 meV (cyan dashed lines) are well described by two resolution-limited Gaussian functions. The higher-energy peak above 100 meV (cyan dotted lines) is damper than the lower-energy modes, which may originate in high-order multi-phonon scattering or other excitation modes. (c) Momentum-resolved phonon energy for all Co doping levels.

We introduce the fitting scheme for the low-energy quasi-elastic scattering and phonon excitations in Figure 5:14. With the spectral capability of O K-edge RIXS, we are able to fit the low-energy spectra with clearly resolved elastic scattering and phonon excitations. A background with linear slope is taken into consideration for the line fitting (green dotted line). The RIXS experimental data are normalized to the total integrated RIXS intensity from 10 eV energy loss to 1 eV energy gain. The elastic line in each spectrum (red dot-dashed curve) is fitted with a resolution-limited Gaussian function. The first fundamental phonon around 60–70 meV (blue dashed curve) shows a negligible broadening beyond the instrumental resolution width ( $\sim 55$  meV), while the higher-energy spectral modes above 100 meV (blue dotted curve) may be contributed by high-order phonon overtones or other excitations. Both inelastic modes are fitted with Gaussian functions, and the widths for both modes are found to be insignificantly broader than the instrumental energy resolution  $\sim 50$  meV.



The initial fitting criteria assumes that the higher-energy excitation mode is mostly contributed by the second harmonic of the multi-phonon scattering. Namely, the energy position between the elastic line and the fundamental phonon is kept the same as the distance between the fundamental phonon and the high-energy mode. This provides a reasonable fit and does not show significant differences after the relaxation of peak positions  $\sim 2\%$ , while the spectral signature of phonon softening and broadening in the vicinity to the charge order wavevector sustains in the RIXS spectra in general.

Additionally, it should be noted that the phonon excitations measured in this work likely involve multiple vibrational modes within the spectral response. This means that the spectral broadening for the phonons probed by RIXS may also be explained by various modes with different EPC strength and their overlapping harmonics. The analysis for Figure 5:13 and Figure 5:14 includes the assumption that the high-energy mode is mainly contributed by the second phonon harmonic to constrain the spectral mode energies. This comes with the postulation of negligible phonon broadening by assigning the same width for the phonon and elastic line, which is allowed to change by less than 5% about the energy resolution. The later scheme assumes that the phonon broadening with proximity to the charge order may be insignificant in our RIXS measurements.

Nevertheless, one has to be aware that this fitting strategy is not uniquely defined and may fail to explain certain details in experimental data. For instance, the fitted phonon intensity is twice as larger at  $q_{CDW}$  than the neighboring momentum-transfer points for  $x=0.05$  (Figure 5:14). This is compatible with the recent studies on Eu-doped LSCO, where the RIXS phonon intensity and EPC were found to co-enhance at the CDW ordering [230]. However, the evaluation of phonon energy at  $q_{Leg}=0.121$  for  $x=0.05$  relies on the asymmetric weight inside the elastic line, which can be mixed with quasi-elastic scattering and creating estimation errors. Although phonon softening is also inferred from the neighboring momentum vectors (i.e.  $q_{Leg}=0.111$  and  $0.131$  rlu) for  $x=0.05$  with separated elastic line and phonons, one cannot rule out the possibilities that our observations may be explained by lattice coupling to other lower-energy excitations (e.g. charge fluctuations) near CDW ordering [83,138,142]. Such mechanism does not necessarily require an enhanced phonon-softening. To clarify this, future RIXS experiments with higher energy resolution are required.

### 5.6.7 Evaluation of EPC

From the observed phonon excitations, we evaluate the EPC strength from the RIXS signal shown in Figure 5:15 using the model in ref. [78] (also see section 2.6.1). One should note that the modelling for our RIXS results here is a simplified approach with the following assumptions: (i) the material is well-insulating, (ii) the phonon spectrum is dominated by a single Einstein phonon, (iii) the higher-energy inelastic signal is mainly contributed by phonon overtones, (iv) the electron scattering does not occur between different sites and orbitals, and (v) the core-hole lifetime effects are not considered. With these one can diagonalize the RIXS phonon amplitude that is taken as the fitting model here. By constraining the phonon energies from the fit in Figure 5:15 and fixing the inverse core-hole lifetime as a constant with respect to energy transfer (taken as 180 meV from ref. [231]), we assess the remaining free parameters including the EPC self-energy and an overall intensity scaling as demonstrated in ref. [79]. The fitted EPC is generally weakly dependent on momentum and Co-doping [Figure 5:15]. The EPC self-energy is slightly enhanced for Co-doped samples.

### 5.6.8 Cu $L_3$ -edge energy-resolved REXS and RIXS results

To further explore the electronic origin of the observed CDW orders, we revisit the experimental results at the Cu  $L_3$ -edge and show the energy-dependent CDW profiles from the RIXS measurements [Figure 5:16]. At the  $3d^{10}\underline{L}$  configuration ( $\sim 933$  eV) in the XAS spectra, reflective of the charge-transfer band involving the oxygen ligand through Cu-O hybridization, both the pristine and Co-doped samples show sizable elastic enhancement about the same ordering wavevectors observed from the O K-edge RIXS results [Figure 5:6(b) and (e)]. This is consistent with the previous REXS studies on SCCO [18,31]. One should note that the ligands for chain and ladder subsystems both contribute here, as the bonding environments show marginal dichroism for the XAS matrix elements of  $Cu\ 2p_{3/2} \rightarrow 3d$  transitions. At the  $3d^9$  white line, on the contrary, the CDW signal is clearly revealed at  $x=0$  while it nearly disappears at  $x=0.03$  [Figure 5:6(a) and (c)]. This seems to suggest that the Cu-Co substitution affects the sub-lattices of electronic orders at the Cu and O sites differently, where similar behaviour has also been observed in existing literature for 2D SC cuprates. Early REXS studies on LBCO and YBCO have formulated a possible explanation based on the co-existent s- and d-wave symmetry of the CDW orders,

suggested to be projected onto the O and Cu sub-lattices, respectively [178,232]. However, the microscopic interaction model to account for resonant diffraction from electronic order has yet remained elusive. One empirical scenario is that the charge order pinning may possess slight phase differences from the given lattice deformations, differentiated among the excited elements and orbitals [232]. This may provide the explanation for distinct correlations of electronic orders probed at different elemental sub-lattices, suggesting that the different spectral sensitivities to the atomic sites and orbitals cannot be ignored. A recent RIXS report on  $\text{Bi}_2\text{Sr}_{1.4}\text{La}_{0.6}\text{CuO}_{6+\delta}$  cuprates revealed comparable in-plane correlation lengths at the Cu  $L_3$ - and O K-edge [138]. A consolidated understanding of the potential multi-orbital nature of CDW orders in cuprates will definitely require further investigations [179,232].

In the following we give the interpretation of our findings within a crude picture. The coherence volume for electronic modulations at the Cu sites may be directly sensitive to the Co dopants and thus get directly disrupted, thereby interfering with the corresponding charge correlations at the  $3d^9$  resonance. It is reasonable to conclude that the majority of electronic configurations at the Cu sites of the ladders are  $3d^9$  for  $\text{Sr}_{14}(\text{Cu},\text{Co})_{24}\text{O}_{41}$ , which would explain the significantly suppressed CDW correlations from Cu sub-lattice for  $x=0.03$ . Despite that most of the Co impurities were believed to reside in the chain Cu sites from prior experiments, the Co dopants in the chains can also provide effective magnetic impurity pinning, similar with the previous studies on YBCO [219]. Such magnetic impurity effects with strong anisotropy have been confirmed from the characterization of the magnetic susceptibility [16,189]. On the other hand, the hole content is mainly governed by its oxygen 2p character in the wavefunction. Therefore, the electronic diffraction at the O sites may be relatively robust against perturbations that do not largely involve changes in the hole content. Although this assumes that the Cu-Co substitution alters the O 2p electronic densities insignificantly, it does not entirely exclude the possibility of Co-O hybridization channels. In fact, the latter may explain our experimental RIXS results at the Co  $L_3$ -edge (see section 5.6.9). Therefore, the CDW signal is present for both the ladder hole resonance at the O K-edge and the charge ligand environments at the Cu  $L_3$ -edge. In Figure 5:16(e), the Cu  $L_3$ -edge RIXS probed at  $3d^9$  resonance uncover minor spectral differences for the low-energy magnetic excitations with Co dopants. It has been previously shown that the two-tripion (2T) excitations in the ladders, with mode energy of hundreds of meV, dominate the RIXS response at the  $3d^9$  configuration (see chapter 3). The negligible spectral differences for the magnetic 2T excitations are in agreement with a recent study concluding that the Co dopants mainly affect the spin fluctuations in the chains for low-doping of  $x \leq 0.03$  [16,189].

### 5.6.9 Co $L_3$ -edge energy-resolved REXS and RIXS results

Lastly, we characterize the Co dopant environments using the Co  $L_3$ -edge XAS and RIXS for the Co-doped samples. In Figure 5:17(a), the observed XAS resonances have different shapes compared to the reported pristine  $\text{Co}^{3+}$  and  $\text{Co}^{2+}$  in octahedral crystal environments [233], with marginal linear dichroism. The energy-dependent RIXS spectra reveal a series of Raman-like modes [Figure 5:17(b)], which may be derived from the inter-orbital excitations from the Co impurities affected by the local bonding environments. From in-plane ER-REXS measurements at the Co  $L_3$ -edge, no elastic enhancement is found across the XAS resonances. This suggests that the Co dopants may not tend to form a quasi-crystal like order. In other words, this indicates that the strengthened CDW orders with Co doping, observed at the O K-edge, are not driven by periodically arranged Co. Our observations will give valuable information of further investigations on the role of Co dopants, including the potential impurity percolation effects and their interplay with charge orders.

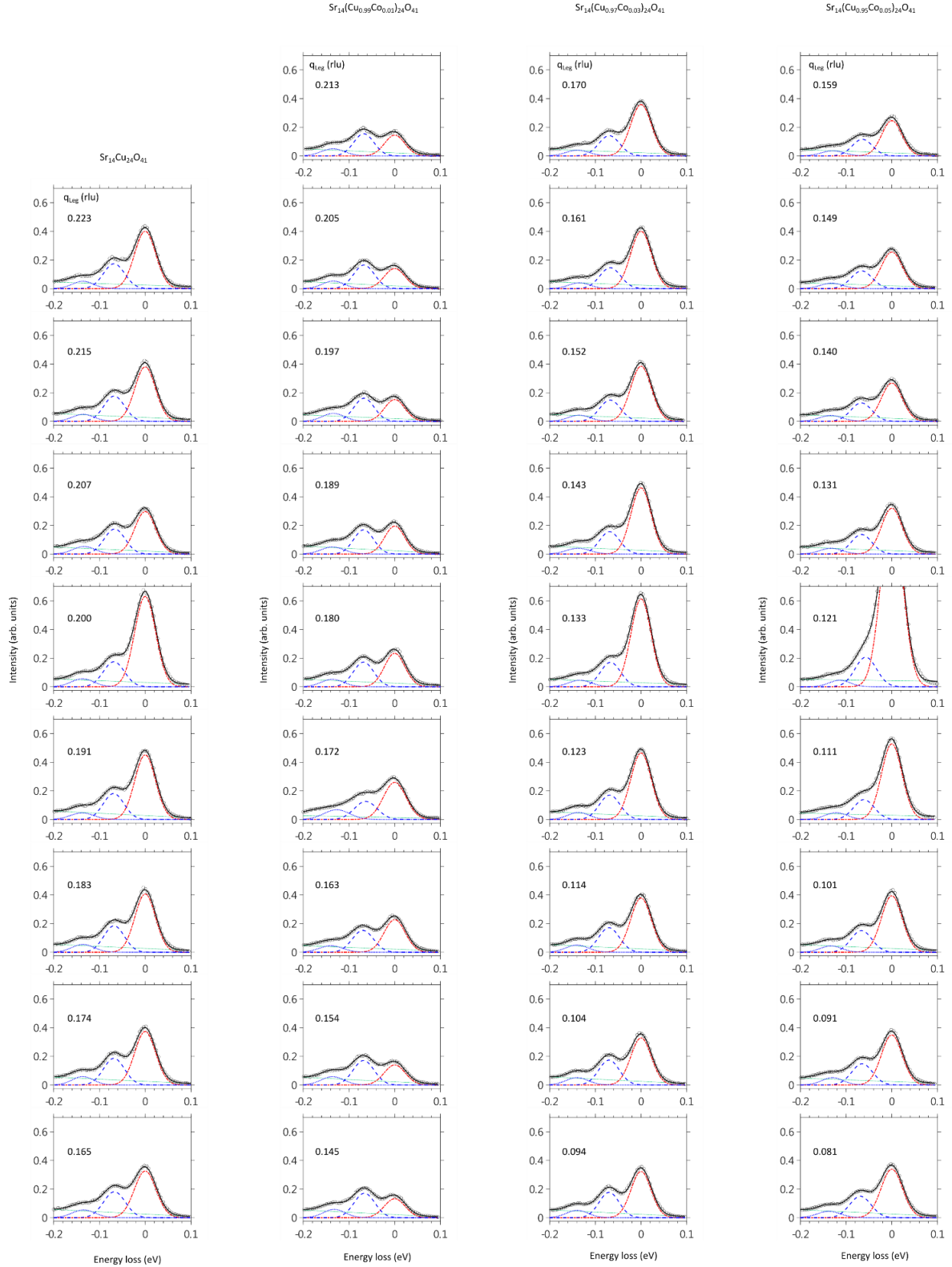
The comparison between the O K- and Co  $L_3$ -edge RIXS spectra for Co-doped samples shows an additional intriguing connection. Around 270 meV, an excitation mode appears at both the ladder hole content of O K-edge and Co  $L_3$ -edge resonances [Figure 5:17(b) and (d)]. The spectral intensity of this mode is scaling with Co doping concentration, and absent for  $x=0$ . These experimental results show correspondence with the magnetic susceptibility of  $\text{Sr}_{14}(\text{Cu}_{1-x}\text{Co}_x)\text{O}_{41}$ , where Co dopants are suggested to reside also in the ladder Cu sites for higher doping ( $x \geq 0.03$ ) [16,189]. We interpret these findings as the direct consequences of altered local Cu-O bonding environments in the ladders from Co impurities, which is detected at the O K-edge through the electronic hybridization.

## 5.7 Conclusion

In this chapter we present a RIXS study on the impurity effects of the ladder CDW and phonon excitations in  $\text{Sr}_{14}(\text{Cu}_{1-x}\text{Co}_x)_{24}\text{O}_{41}$  materials. From the O K- and Cu  $L_3$ -edge RIXS spectra, we observe an enhanced CDW that develops an increased leg correlation length at a reduced wavevector  $q_{\text{CDW}}$  with increasing Co dopants. At the O K-edge, this is accompanied by the concomitant phonon softening at the CDW ordering, which is also found to be enhanced with Co impurities. With a decreasing ladder hole density determined from our O K-edge XAS results, we report a strengthened charge-stripe order and phonon softening originating from combined magnetic and electronic doping effects. The magnetic impurity doping leads, consistent with susceptibility measurements and our Co  $L_3$ -edge RIXS results, to pinning of fluctuating CDW and SDW. On the other hand, the predominant long-range CDW with effective electron doping may be connected to energetically-favoured pairing correlations, recently predicted for cuprate ladders approaching an electron-doped regime. The stronger phonon softening for increasing Co doping is in line with recent theories suggesting a crucial role for the lattice distortions to stabilize symmetry-broken charge- and spin-strips. Additionally, the electronic character for the Co-doping persisting CDW is confirmed by detuning and temperature-dependent O K-edge RIXS measurements. The CDW melting upon heating further reveals a possible critical scattering that has been recently observed in the SC cuprates. To verify the relation between our results on cuprate ladders and current studies of SC cuprates, it would be worth revisiting the temperature evolution of CDW profiles systematically among different families of cuprates. These experimental findings are consistent with the physical scenario for an unified charge-stripe formation with a  $T_c$  anomaly for different types of cuprates. The enhancement (suppression) of charge-strips (SC) phases was speculated to be achievable by magnetic impurity tuning, inspired by the neutron and  $\mu\text{SR}$  results across a wide species of cuprates. Our results expand the hypothesis of universal charge-stripe formation of SC cuprates to the non-SC cuprate ladders that provide a suitable framework for studying the interplay between CDW and HTSC. This also demonstrates the richness of spin ladders for exploring the entangled electronic degrees of freedom.

## 5.8 Acknowledgement

The experiments have been performed at the ADRESS beamline of the Swiss Light Source at the Paul Scherrer Institut (PSI). The work at PSI is supported by the Swiss National Science Foundation through project no. 200021\_178867, the NCCR MARVEL and the Sinergia network Mott Physics Beyond the Heisenberg Model (MPBH) and SNSF Research Grants CRSII2\_160765/1 and CRSII2\_141962. Y.T and T.S would like to thank R. Comin, J. Pelliciari, K. Wohlfeld, J. Chang, and S. Johnston for valuable discussions.


 Figure 5:14 Line fitting for the elastic line and phonon excitations for  $\text{Sr}_{14}(\text{Cu}_{1-x}\text{Co}_x)_{24}\text{O}_{41}$  across all doping levels and momentum-transfer points.

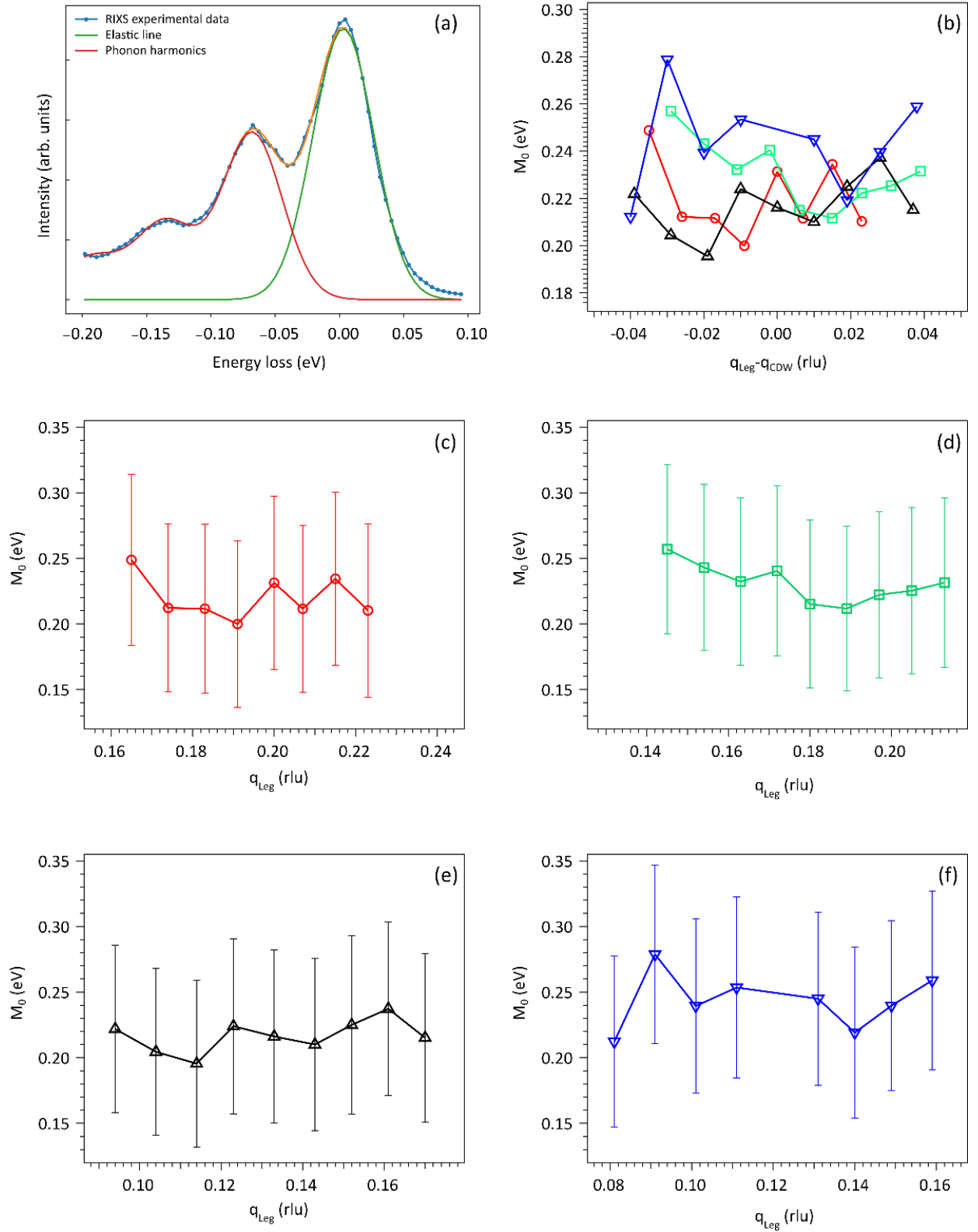


Figure 5:15 Fitting results of the electron-phonon interactions from the observed phonon excitations in the RIXS spectra. (a) Representative fit for the experimental RIXS results taken for  $x=0.03$  with  $q_{\text{Leg}}=0.094$  (r.u.). (b) The summary of momentum-resolved EPC as the phonon self-energy across all Co doping levels. The error bars are removed for visual clarity. (c)-(f) The fitted EPC around the CDW ordering vector for  $x=0, 0.01, 0.03$  and  $0.05$ , where the error bars are included.

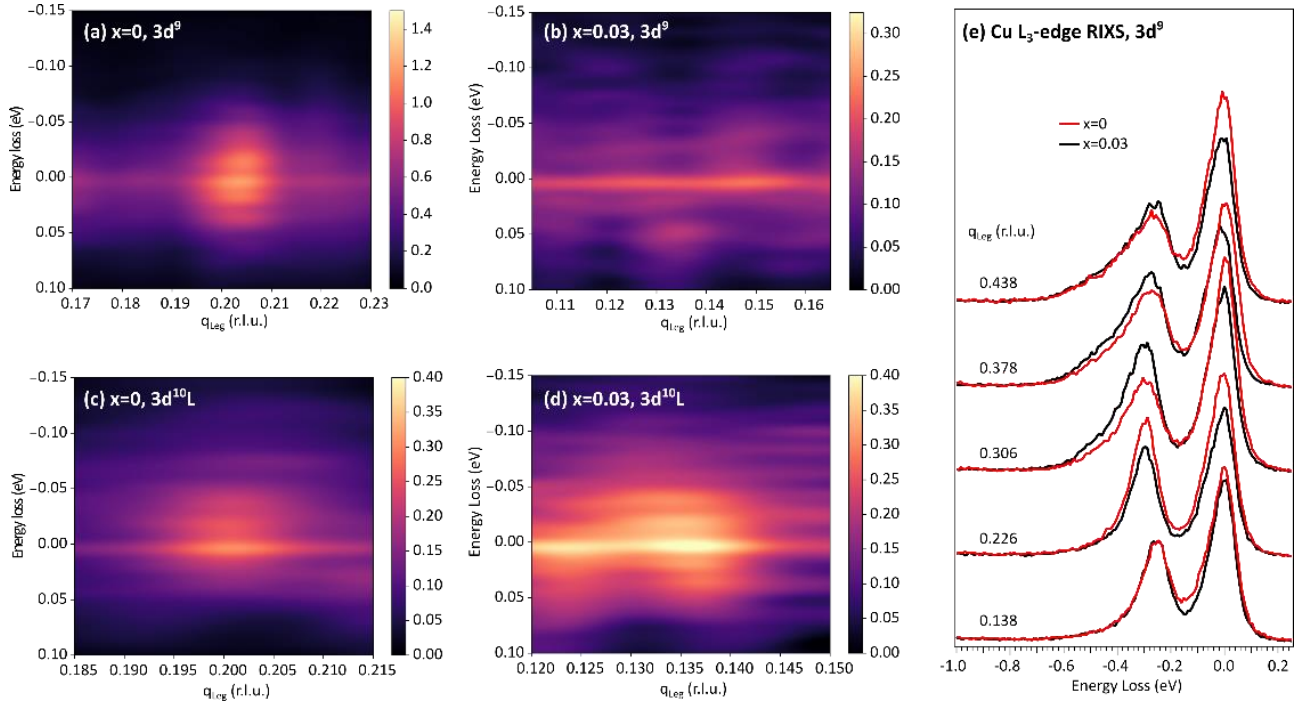


Figure 5:16 (a)-(d) Energy-resolved elastic scattering in  $\text{Sr}_{14}(\text{Cu}_{1-x}\text{Co}_x)\text{O}_{41}$  ( $x=0$  and  $0.03$ ) probed by Cu  $L_3$ -edge RIXS at the  $3d^9$  ( $\sim 931$  eV) and  $3d^{10}\text{L}$  ( $\sim 933$  eV) resonances, respectively. (e) Momentum-dependent Cu  $L_3$ -edge RIXS measurements of the 2T magnetic excitations for  $x=0$  and  $x=0.03$ .

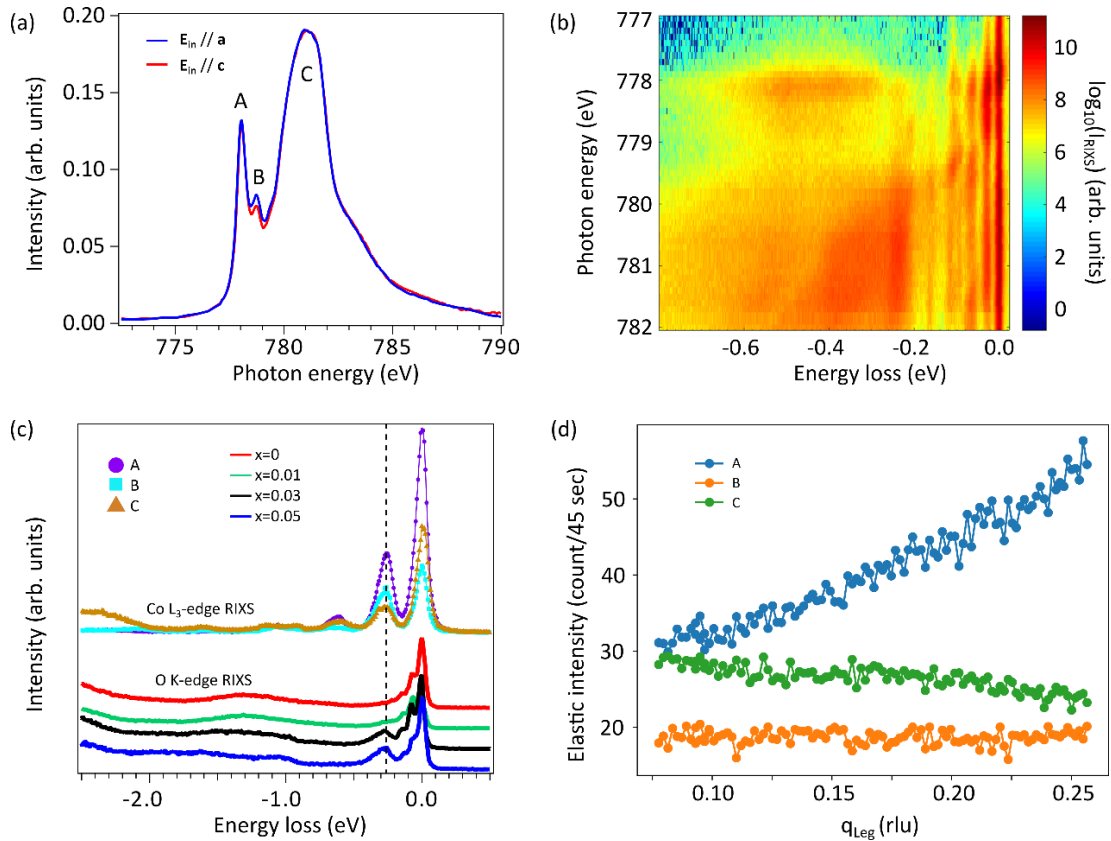


Figure 5:17 (a)-(b) Co  $L$ -edge XAS and RIXS measurements for  $x=0.03$ , where the RIXS intensity is plotted for varied incident X-ray energies across the Co  $L_3$ -edge in (b). Both measurements are taken in the grazing  $20^\circ$  incidence geometry. (c) Comparison between O  $K$ -edge (ladder hole peak for  $x \leq 0.05$ ) and Co  $L_3$ -edge RIXS spectra (the 3 main resonances labelled in (a) for  $x=0.03$ ). The Co-doping induced peak  $\sim 270$  meV is highlighted (black dashed line) in the O  $K$ -edge RIXS experimental data, matching the localized excitations observed in Co  $L_3$ -edge RIXS results. (d) Co  $L_3$ -edge ER-REXS signal for  $x=0.03$  at the 3 main resonances.



# Chapter 6 Electronic structure and electron-phonon coupling of the layered honeycomb nickelate $\text{Na}_2\text{Ni}_2\text{TeO}_6$

## 6.1 Projection Contribution

The content of this chapter is at the time of the thesis submission undergoing the paper submission process as a journal article. In this chapter, I investigate the electron-phonon coupling and inter-orbital excitations in the layered honeycomb lattice of the nickel oxide compound  $\text{Na}_2\text{Ni}_2\text{TeO}_6$  using Ni  $L_3$ - and O K-edge RIXS. In this work, I, Yi Tseng, am responsible for the experiment planning, preparation of the experimental setup, alignment and in-situ cleaving of the samples, performing the RIXS measurements and the experimental data analysis. The paper is written by me as the main responsible with input from all the other co-authors. Section 6.2 serves as an additional introduction giving extended background knowledge on the context of this work, including the figures 6:1 - 6:4. The corresponding article in preparation of submission includes the content of section 6.3 - 6.8, including the figures 6:5 - 6:12, except for figure 6:6 and figure 6:8 that are taken from literature for the purpose of comparison to references.

## 6.2 Preamble

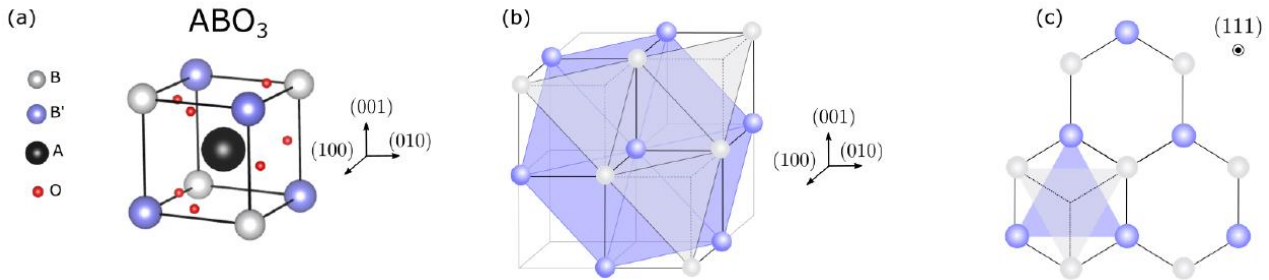


Figure 6:1 (a) Schematic of  $\text{A}(\text{B},\text{B}')\text{O}_3$  cubic in perovskites with (b) truncated projection along  $(111)_{\text{pc}}$  [234]. (c) Effective hexagonal environments along  $(111)_{\text{pc}}$  [Open access for the reprint of figure available from: Online Publikationen der Universität Stuttgart, Matthias Hepting, PhD dissertation, Ordering phenomena in nickelate heterostructures studied by elastic and inelastic photon scattering, 2016 (<http://dx.doi.org/10.18419/opus-8969>)].

Correlated oxides with honeycomb structures have received great attention owing to their exotic magnetic ground state. The hexagonal geometry is in close relationship with the frustrated triangular and Kagome lattices [38], related to several emergent phases, e.g. Kosterlitz–Thouless (KT) transition [38] and bond-directional exchange interactions [235]. These properties are promising for designing new devices with tailored functionalities. Therefore, detailed understanding of the underlying electron correlations is urgently required. Similar structures have recently been studied in the rare-earth nickelate  $\text{RENiO}_3$  (RE=rare earth ion). One can realize such honeycomb lattices in  $\text{RENiO}_3$  by truncating along the pseudocubic (pc)  $(111)$  orientation in a perovskite structure (Figure 6:1). Numerous thin films and heterostructures in  $(111)_{\text{pc}}$  orientation revealed unexpected interplay between spin, orbital, charge and lattice degrees of freedom (DOFs) in these nickelates, e.g., orbital order [236], interfacial magnetism [237], ferroelectricity [238], etc. It is, therefore, of high importance for fundamental and applied research to understand the low-energy excitations of nickelates sharing the same crystallographic environment with  $(111)_{\text{pc}}$  oriented  $\text{RENiO}_3$ . With RIXS, studies on  $\text{RENiO}_3$  successfully revealed the evolution of elementary excitations across the metal-insulator transition (MIT) [239,240]. RIXS can probe the phonon and orbital excitations, proven to be directly connected to the breathing distortion in buckled  $\text{NiO}_6$  octahedra [239,240]. By Ni  $L_3$ -edge RIXS, one directly detects the Ni 3d valence from the local crystal field excitations, as well as the orbital response with respect to structural distortion [239] (Figure 6:2). On the contrary, O K-edge RIXS probes the charge degree of freedom on the oxygen ligand, shown to be extremely sensitive to the EPC [240] (Figure 6:3).



In this chapter, an intrinsically crystallized hexagonal lattice in nickelate  $\text{Na}_2\text{Ni}_2\text{TeO}_6$  is studied using RIXS. Recent experiments suggested a predominant spin-lattice relaxation in its AFM phase [38]. Particularly, the structural connectivity between Ni-O bonds in honeycomb lattices is expected to contribute to strong EPC [234]. For instance, in the (111)pc oriented  $\text{RENiO}_3$  (see Figure 6:1), each  $\text{NiO}_6$  shares three oxygen atoms with the neighbouring octahedra, as compared to 1-shared atom when truncated along the (100) orientation [234]. Magnetic susceptibility and neutron diffraction measurements on  $\text{Na}_2\text{Ni}_2\text{TeO}_6$  showed a three-dimensional (3D) antiferromagnetic transition  $\sim 27$  K alongside with zero-thermal expansion along c-axis, coinciding with an onset temperature in the magnetic response deviating from the Curie-Weiss law [38,241]. These findings raise the speculation of predominant SPC, which is in line with the spin-lattice relaxation reported by NMR spectroscopy [242]. Present neutron and X-ray studies still fail to clarify if spin-Peierls physics exists in  $\text{Na}_2\text{Ni}_2\text{TeO}_6$ . Thus, measuring the phonon response across the AFM transition using O K-edge RIXS will assess if a significant SPC is indeed at play. With the lack of understanding on the electronic valence configuration of Ni 3d shell in  $\text{Na}_2\text{Ni}_2\text{TeO}_6$ , the RIXS probe will determine the valence state and the local crystal field, and assess the phonon and orbital excitations with their development across  $T_{\text{Néel}}$ . This clarifies contributions of the predicted spin-phonon coupling (SPC) in  $\text{Na}_2\text{Ni}_2\text{TeO}_6$ , and provide insight on the honeycomb nickelates on a fundamental ground. Another point worth noticing is that the effective moment, extracted from susceptibility measurements ( $\sim 3.4 \mu\text{B}$ ), is larger than a spin-only modelling value ( $\sim 2.8 \mu\text{B}$ ) [38], indicating a sizable spin-orbital interaction. Another open problem is the proof of existence of a Kitaev spin liquid phase with bond-directional magnetic interactions in  $\text{Na}_2\text{Ni}_2\text{TeO}_6$ . A KT-like transition was reported in a similar compound  $\text{BaNi}_2\text{V}_2\text{O}_8$  [40], but the current experimental evidence for such topological excitations is still lacking in  $\text{Na}_2\text{Ni}_2\text{TeO}_6$ . On the other hand, orbital rearrangement across the AFM transition was observed in  $\text{Ni}_3\text{TeO}_6$ , which also contains honeycomb stacking layers [243,244]. Ni  $L_3$ -edge RIXS is ideal for evaluating if an orbital reconstruction due to structural deformation is also occurring in  $\text{Na}_2\text{Ni}_2\text{TeO}_6$ .

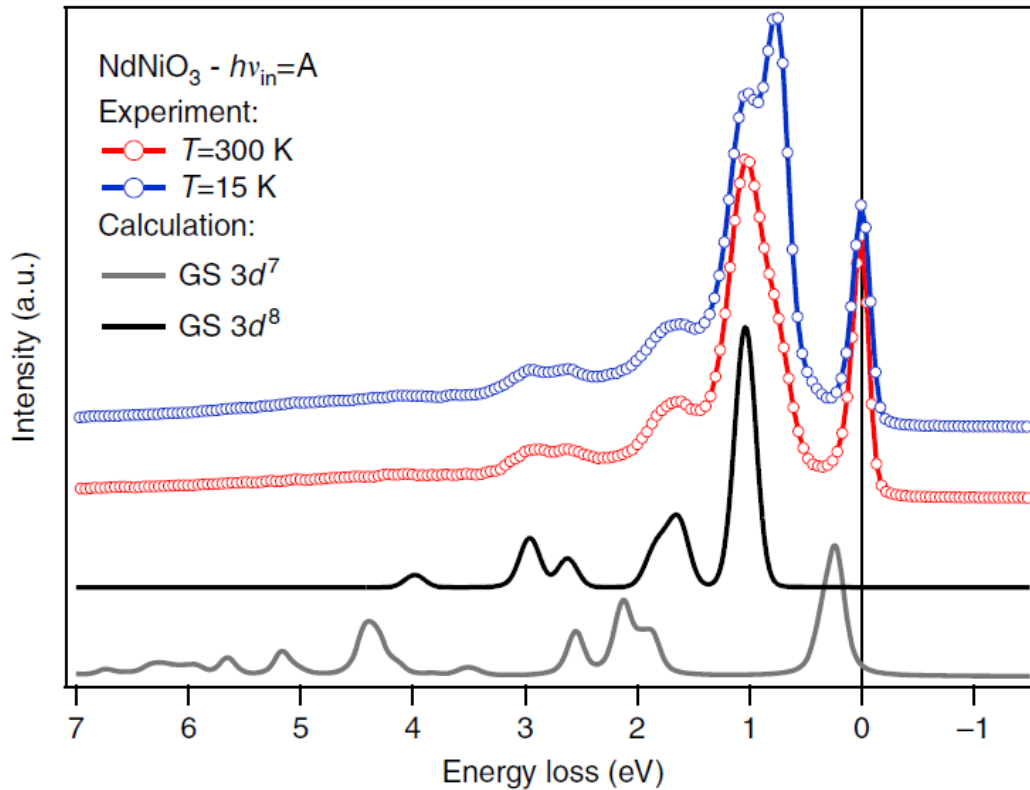


Figure 6:2 Ni  $L_3$ -edge RIXS spectra on  $\text{NdNiO}_3$  and calculated RIXS response for the Ni  $3d^8\bar{L}$  ( $\bar{L}$  is denoted for ligand hole) and  $3d^7$  ground state from ref. [239], respectively. The RIXS spectra are taken at  $3d^8$  electronic configuration, which is labelled as the A resonance in ref. [239] (Open access available at: Springer Nature publishing group, Nature Communications, Bisogni V. et al., 7, 13017, 2016).

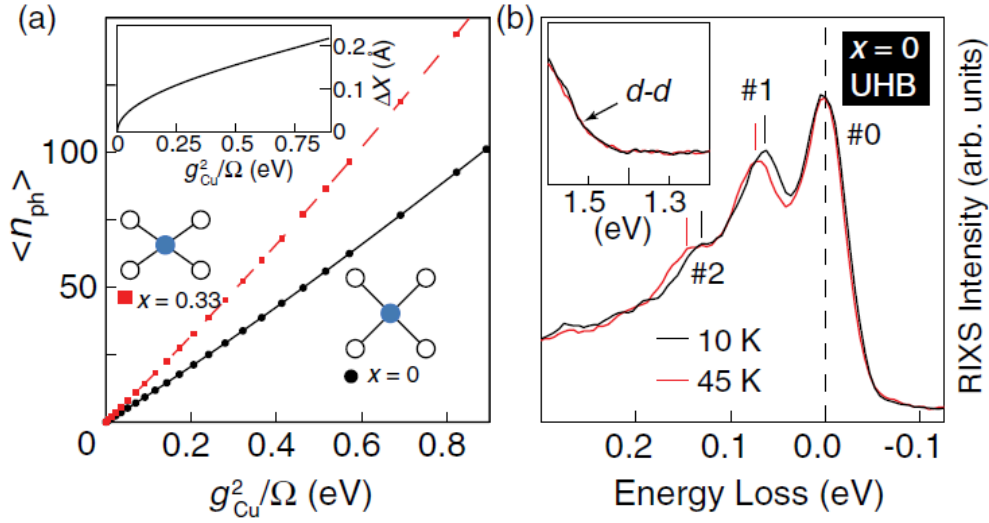


Figure 6:3 O K-edge RIXS study on the phonon excitations of Ca<sub>2+5x</sub>Y<sub>2-5x</sub>Cu<sub>5</sub>O<sub>10</sub> showing the intertwine lattice, charge and spin degrees of freedom from ref. [154]. (a) The doping-dependent phonon population as a function of EPC strength for  $x=0$  and  $x=0.33$ , which was attributed to the lattice distortions for the O-Cu-O bonds that are sensitive to the charge carrier concentration. (b) The phonon softening for the Cu-O bond-stretching vibrational mode across the Neel temperature  $\sim 30$  K, suggesting the RIXS sensitivities to the re-arranged electron-phonon interactions with respect to the magnetic transitions [Reprinted figure with permission from: W. S. Lee et al., Physical Review Letters, 110, 265502 (2013). Copyright (2013) by the American Physical Society. (<https://doi.org/10.1103/PhysRevLett.110.265502>)].

With the RIXS capability, the orbital and phonon excitations of Na<sub>2</sub>Ni<sub>2</sub>TeO<sub>6</sub> are characterized at the Ni L<sub>3</sub>- and O K-edge, respectively. In the Ni L<sub>3</sub>-edge RIXS spectra, the Raman-like localized excitations from 1 to 4.5 eV loss are the predominant spectral components, with mode energies comparable to the inter-orbital crystal-field splitting for the Ni 3d valence. By comparing with the theoretical and experimental literature on the Ni L<sub>3</sub>-edge multiplets, the observed localized excitations well resemble the octahedra NiO<sub>6</sub> environments [245,246]. On the other hand, O K-edge RIXS measurements reveal clearly resolved multi-phonon overtones up to the fifth harmonic for the optical vibrational mode, with fundamental frequency  $\sim 80$  meV. The momentum-dependent measurements show that these multi-phonon modes are weakly-dispersive, matching well the optical lattice vibrations for oxygen ions. By comparing with the existing literature of phonon excitations measured by Raman spectroscopy, the observed predominant optical phonon is closely reflective of the O-Ni-O bond stretching mode, in agreement with the recent RIXS report on isostructural iridate  $\alpha$ -Li<sub>2</sub>IrO<sub>3</sub> [79]. With the high-resolution RIXS probe, the indication of sizable low-energy spectral weight between the elastic scattering and phonon excitations (30~40 meV) is also uncovered. This mode may be composed of phonons at lower-energy or spin-conserving ( $\Delta S=0$ ) bimagnon continuum, as suggested in recent calculations on Kagome/honeycomb/triangular antiferromagnets. The temperature-dependent O K-edge RIXS results show marginal changes for the phonon excitations and low-energy mode across the AFM transitions, which may reflect that the correspondent spectral changes with respect to magnetism may be insignificant for the energy regime of dd and optical phonons in the presented RIXS measurements.

### 6.3 Abstract

The potential spin-phonon coupling in magnetically frustrated materials, alongside its corresponding relevance to novel magnetic ground states formulated in recent theories, have raised the attention to investigate the interplay between magnetism and lattice response. We present a Ni L<sub>3</sub>- and O K-edge RIXS study on the orbital and lattice dynamics of the layered honeycomb antiferromagnet Na<sub>2</sub>Ni<sub>2</sub>TeO<sub>6</sub>, a compound predicted to host spin-Peierls physics in the quasi-2D hexagonal planes. By studying the dependence of the RIXS spectra on the light polarization, momentum-transfer in high-symmetry directions, and temperature, we characterize the local spin-orbital structure and the electron-phonon coupling. In Ni L<sub>3</sub>-edge RIXS, localized excitations of 1-4 eV are revealed with comparable energies of the octahedral crystal-field splitting for the Ni<sup>2+</sup> configuration, in agreement with the studies on nickel compounds with 2+ electronic states [246]. The O K-edge RIXS response, on the other hand, is dominated by multi-phonon scattering of clearly re-

solved harmonics, with a fundamental frequency of  $\sim 80$  meV. The mode energy and weakly-dispersive nature are reminiscent of the optical oxygen vibrations inferred from optical spectroscopy. Additionally, we observe the spectral signature of sizable quasi-elastic weight which may be connected to the lower-energy phonon or spin-conserving bimagnon continuum excitations that were recently predicted in hexagonal frustrated magnets. The temperature-dependent O K-edge RIXS measurements show little differences for the observed inelastic response across the AFM transition  $\sim 28$  K. These findings provide information to the dynamical orbital and lattice correlations across the magnetic transition, which will help to elucidate the underlying spin texture among the magnetically frustrated systems.

## 6.4 Introduction

An active lattice degree of freedom that can potentially couple to the charge, spin, and orbital sector represents the driving force for numerous exotic many-body phenomena in the strongly correlated materials. This leads to the opportunities of device engineering based on new electronic phases with flexibility in material synthesis and fabrication. For instance, a sizable SPC has been considered crucial for various emergent phenomena (e.g. multiferroics, colossal magnetoresistance, HTSC, etc [175,247–250]) and relevant for spintronics applications [251,252]. A number of novel electronic ground states have been proposed with the experimental signature of a significant role of the lattice fluctuations. In particular, the magnetically frustrated materials represent the ideal demonstration for such category with rich electronic and magnetic phase diagram [253–255]. Recently, it was proposed that fingerprints of fractionalized excitations may be inferred from the phonon excitation spectra of a Kitaev quantum spin liquid through the coupling between spinons and phonons [256–258]. The proposed material candidates for Kitaev quantum spin liquid like honeycomb iridates, where the spin Hamiltonian is governed by the bond-directional exchange interactions, have been reported to host Fano-type response from the phonon excitations revealed by optical spectroscopy [259]. These observations were interpreted as the characteristic of strong coupling between the phonons and a continuum of spin excitations. Additionally, several experimental works have pointed out the unusual transport behavior and thermal Hall effects in similar compounds [255,260], which were argued to be closely related to a considerable spin-phonon scattering.

In this work, we investigate the electronic structure and elementary excitations of the q-2D honeycomb nickelates  $\text{Na}_2\text{Ni}_2\text{TeO}_6$  using Ni  $L_3$ - and O K-edge XAS and RIXS. This is a compound where the structure is stacked with honeycomb layers of rotated  $\text{NiO}_6$  octahedra in the pseudo-cubic (111) orientation notation (Figure 6:4) [38]. Derived from the stoichiometric variation of the battery materials  $\text{Na}_x\text{CoO}_2$ , the  $\text{Na}_2\text{Ni}_2\text{TeO}_6$  compound was previously regarded as a promising material for thermoelectric application [261]. A short-range AFM order below  $\sim 28$  K was previously observed by magnetic susceptibility and neutron diffraction measurements [38,241], while early NMR experiments revealed a predominant spin-phonon relaxation across the magnetic transition in this material [242].

In recent years, RIXS has been demonstrated to be powerful for probing the local crystal-field and phonon excitations in the transition metal oxides [49]. Therefore, the RIXS study on  $\text{Na}_2\text{Ni}_2\text{TeO}_6$  provides a suitable platform for assessing the Ni 3d valence that is central to the spin texture, as well as the potential SPC from the RIXS phonon signal across the AFM transition. At the Ni  $L_3$ -edge, the inter-orbital transitions about 1-3 eV loss from the RIXS spectra highlight the electronic structure that is dominated by the  $\text{Ni}^{2+} 3d^8$  state with octahedral site environments. This is consistent with the XAS spectra, where the two main resonances near the  $L_3$ -edge representing the Ni spin exchange fields are clearly observed [245,246]. In the Ni  $L_3$  post-edge region, we reveal the spectral signature of an anti-bonding configuration with high charge-transfer excitations from both the XAS and RIXS spectra. As for the O K-edge, intense multi-phonon overtones with the fundamental phonon frequency  $\sim 80$  meV are revealed from the RIXS spectra, when the incoming photon energy is tuned to the Ni-O hybridization band. This is observed alongside the high-energy fluorescence-like charge excitations that are reflective of the O 2p band transitions. From the momentum-dependent O K-edge RIXS measurements, the multi-phonon excitations are essentially flat in energy dispersions, reminiscent of the optical vibrational modes for the oxygen ions. Given the well-resolved phonon satellites in the energy loss functions, the momentum-resolved EPC is evaluated along with the an-harmonicity, defined by the deviations from the harmonic oscillator for the high-order overtones. Additionally, we unveil the spectral signature of low-energy excitations in the quasi-elastic regime. By comparison with literature, this mode may result from phonons at lower energy or spin-conserving ( $\Delta S=0$ ) bimagnon excitations. In general, the observed spectral modes show insignificant temperature dependence across the

AFM transition. This behaviour may result from the high energy scale of such modes, rendering them insensitive to the energy regime characteristic of the AFM fluctuations and correspondent lattice distortions.

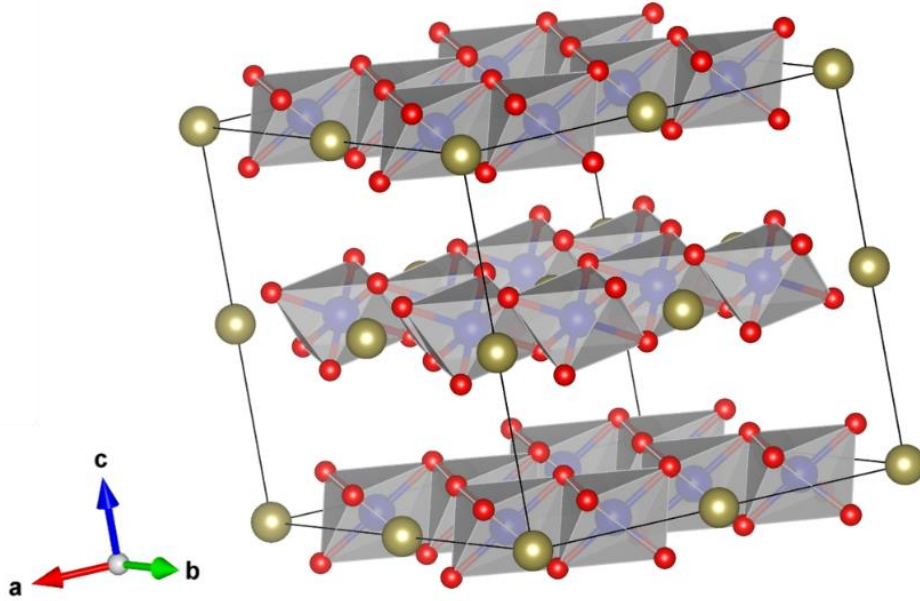


Figure 6:4 Crystallographic structure of  $\text{Na}_2\text{Ni}_2\text{TeO}_6$  generated by VESTA [262]. The layers of  $\text{NiO}_6$  octahedra are highlighted with polyhedral surface (Ni: blue spheres; O: red spheres). Te atoms are labelled as clay-brown spheres, while the Na atomic layers are hidden for visible clarity for the  $\text{NiO}_6$  structures.

## 6.5 Experimental Method

Flakes of  $\text{Na}_2\text{Ni}_2\text{TeO}_6$  single crystals with planar dimension of 2-3 mm are grown with the self-flux method [38]. Top-post cleavage is performed *in-situ* before all measurements, with the vacuum pressure about  $5 \times 10^{-10}$  mbar. RIXS and XAS measurements are performed at the ADRESS beamline at the Swiss Light Source (SLS), Paul Scherrer Institut [54–56]. The total RIXS energy resolution of 50 meV and 110 meV are achieved with the 1500 line/mm grating for the RIXS spectrometer at the O K- ( $\sim 530$  eV) and Ni  $L_3$ -edge ( $\sim 854$  eV), respectively. The scattering angle  $2\theta$  is fixed at  $130^\circ$ . The sample is mounted with the high-symmetry orientations (1,0) and (1,1) along the in-plane momentum-transfer. The RIXS measurements are performed in the grazing incidence geometry. RIXS spectra are corrected for self-absorption effects. XAS spectra are recorded with TFY mode.

## 6.6 Results and Discussions

Figure 6:4 depicts the crystallographic structure of the  $\text{Na}_2\text{Ni}_2\text{TeO}_6$  compound, consisting of a network of  $\text{NiO}_6$  octahedra oriented along the  $(111)_{\text{pc}}$  orientation. This gives rise to the stacking layers of quasi-2D honeycomb sheets projected onto the hexagonal a-b plane. The Na atomic layers are intercalated between the  $\text{NiO}_6$  and Te layers, which has been a crucial issue for studying the potential for applications in battery materials. In Figure 6:5, we show the Ni  $L_3$ -edge experimental XAS and RIXS results. To understand the major RIXS excitation profiles, the energy-detuning RIXS measurements with varying incident photon energies are applied across the Ni  $L_3$ -edge XAS resonances (Figure 6:5(b)). The characteristic spectral modes are the localized excitations ranging from 1 to 5 eV energy loss. These excitations show energies that are independent of the incident photon energies, resembling the Stokes lines in Raman spectroscopy. Despite forbidden in the scattering cross section for the optical measurements, the inter-orbital transitions are generally direct RIXS processes at the 3d metal L-edge and therefore strong in spectral intensity. This finding has established a unique way to investigate the metal d valence, which is central to the exotic many-body properties in strongly correlated electronic materials with transition-metal ions. In Figure 6:5(c), the spectral differences in intensity with the polarization of the incident X-rays may be reflective of the projection of different orbitals with respect to the X-ray polarization.

In general, the XAS response at the Ni  $L_3$ -edge is mainly of  $Ni^{2+}$  character. The two main resonances  $\sim 854$ - $856$  eV closely resemble the  $3d^8$  state with its spin-flip excited state for a local  $Ni^{2+}$  ion. In Figure 6:5(c), the RIXS spectrum probed at the Ni  $L_3$ -edge XAS maximum is shown. The dominant spectral component is the mode around 1 eV. At the higher-energy regime, we observe multiplets of excitations about 2 and 2.5 eV loss with 2-3 sub-bands, and a single-peak structure of 4.5 eV. The energy scales are consistent with the inter-orbital splitting derived from the local crystal field excitations [245,246,263]. By comparison with the theoretical and experimental literature shown in Figure 6:6, we assure the RIXS spectral response is dominated by the multiplets of  $Ni^{2+}$  crystal field excitations in the octahedral lattice environments. Despite the slight shifts in the overall energy differences, the experimentally recognizable peaks in the RIXS spectra are qualitatively in agreement with the present literature [246,263]. The shift in peak energies towards higher energy range, compared to other 2+ compounds, may be affected by the differences in the metal-ligand bond lengths for the Ni ions (see NiO and  $NiCl_2$  in Figure 6:6(b)). The predominant excited states of  $^3T_2$  symmetry show comparable mode energy, as well as similar energy dependence with varying incident X-ray energies, to the 1 eV peak from our RIXS results.

On the other hand, the excitation multiplets above 2 eV loss are enhanced at the second resonance in the Ni  $L_3$ -edge XAS signal ( $\sim 855.5$  eV), which also follows the energy dependence for the higher-energy excited states of  $^3T_1 + ^1E$  symmetry shown in Figure 6:6(a) [245]. At the higher-energy regime near the shoulder of the second main XAS peak ( $\sim 856.8$  eV), the RIXS spectral weight at  $\sim 1.5$  eV loss may not be solely attributed to the standard  $Ni^{2+}$  octahedral crystal field observed in NiO and  $NiCl_2$  (Figure 6:6(b)). This might suggest the electronic structure is partially contributed by the  $Ni^{1+}$  state in the XAS signal with overlapping energy with the second  $L_3$ -edge resonance  $\sim 855.5$  eV, resulting in a  $3d^9$  electronic configuration, as in the layered cuprates with a sharp dd excitation located near  $\sim 1.5$  eV [264]. This is consistent with the observed ratio of integrated intensity between the second ( $\sim 855.5$  eV) and first ( $\sim 854$  eV) Ni  $L_3$ -edge resonances, which seems to be higher than the reports on NiO and  $NiCl_2$ . Nevertheless, the potential self-absorption effects on the Ni  $L_3$ -edge first XAS resonance cannot be fully ignored here.

The XAS peak about 867 eV may contain contributions from the Te  $M_2$ -edge [85]. On the other hand, the post-edge side band  $\sim 859$ - $860$  eV is likely to be the electronic configuration that involves the charge-transfer at the Ni sites with the surrounding screening environments [49]. This is supported by the RIXS spectrum taken at this resonance, which shows spectral signature of the high-energy charge transfer excitations  $\sim 7$ - $8$  eV loss range, matching the energy differences between this XAS resonance and the  $Ni^{2+}$  main peak about 854 eV. Such electronic state can be conceptualized as the  $3d^9\bar{L}$  configuration, where  $\bar{L}$  represents the anti-bonding configuration for the Ni sites here in general [49]. The XAS peak around 864 eV may share similar origin with the mode about 859 eV, however, a detailed interpretation will require dedicated calculations. To sum up, the present XAS and RIXS measurements reveal a predominant  $Ni^{2+}$  configuration and octahedral site symmetry for the layered  $Na_2Ni_2TeO_6$ , consistent with the reported nickel compounds with  $Ni^{2+}$  configuration [246].

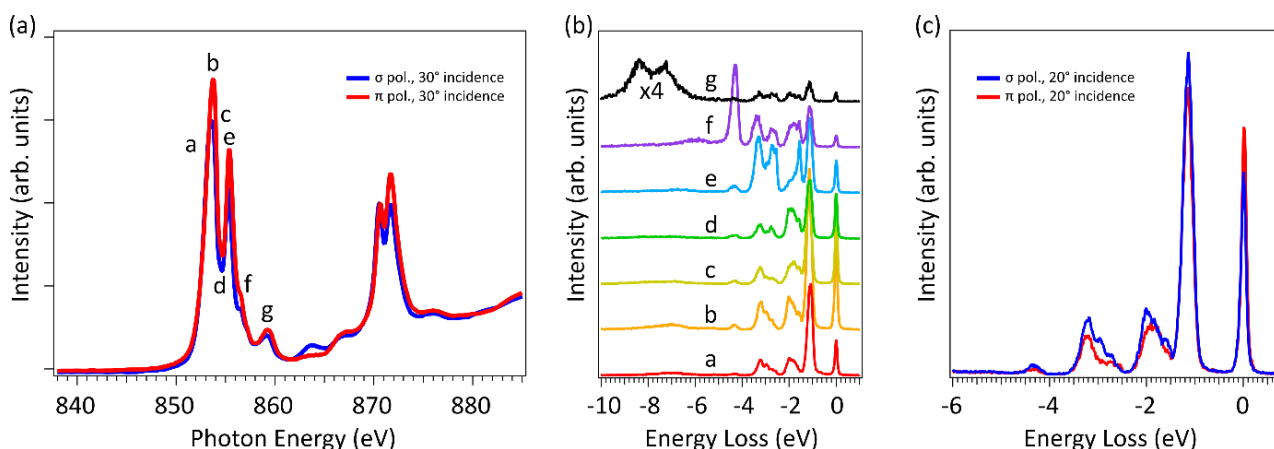


Figure 6:5 (a) Ni  $L$ -edge XAS spectra normalized at post-edge  $\sim 885$  eV with both  $\sigma$  and  $\pi$  polarization. (b) RIXS spectra taken at selected incident X-ray energies as marked in (a) with  $\sigma$  polarization. (c) A zoom to the local Raman-like excitations in the RIXS spectra measured with  $\sigma$  and  $\pi$  polarization, probed at the Ni  $L_3$ -edge XAS maximum ( $\sim 854$  eV, b resonance).

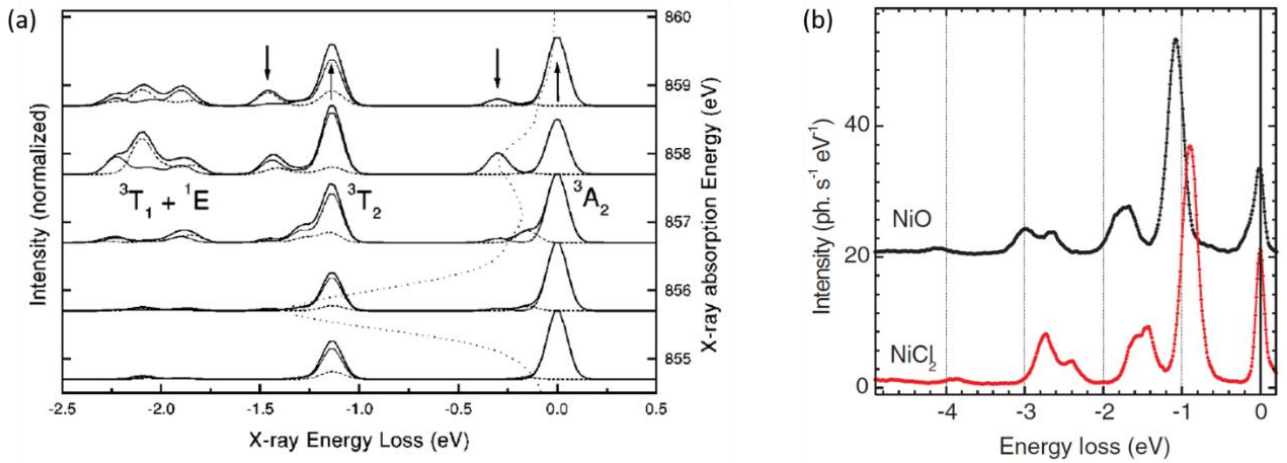


Figure 6:6 (a) Calculated local crystal field excitations for a  $\text{Ni}^{2+}$  ion with octahedral lattice environments from ref. [245] [Reprinted figure with permission from: F. M. F. de Groot, P. Kuiper, and G. A. Sawatzky, *Physical Review B*, 57, 14584 (1998). Copyright (1998) by the American Physical Society. (<https://doi.org/10.1103/PhysRevB.57.14584>)]. The crystal field splitting is taken as 1 eV, while the exchange field for the local spin-flips for the Ni ions is set to be 0.25 eV. The dot-dashed line across simulated RIXS spectra probed at different incident X-ray energies corresponds to the Ni  $L_3$ -edge XAS profiles. (b) Ni  $L_3$ -edge RIXS spectra taken for NiO and  $\text{NiCl}_2$  from ref. [246], where both compound possess octahedra crystal-field environments for the  $\text{Ni}^{2+}$  ions (Reprinted by permission from Springer Nature publishing group, *The European Physical Journal - Special Topics*, Ghiringhelli G. et al., 169, 199-205, 2009).

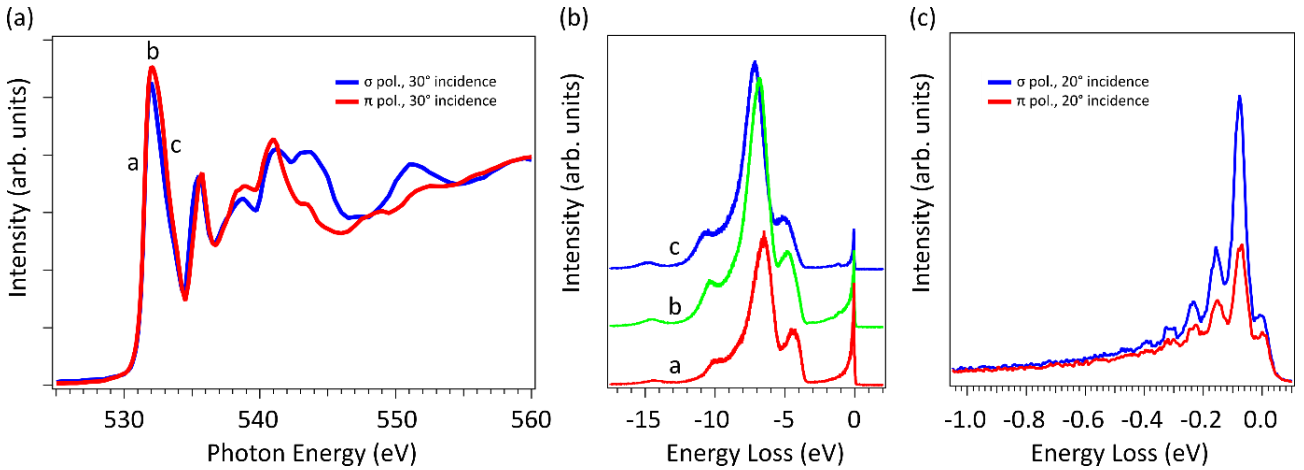


Figure 6:7 (a) O K-edge XAS spectra normalized at post-edge  $\sim 560$  eV with both  $\sigma$  and  $\pi$  polarization. (b) RIXS spectra taken at selected incident X-ray energies as marked in (a) with  $\sigma$  polarization. The zoom to low-energy regime (below 1 eV loss) are shown in (c) measured with  $\sigma$  and  $\pi$  polarization. High-energy spectral modes (above 4 eV) are basically fluorescence-like charge excitations, whereas clear multi-phonon overtones for the optical vibrational mode  $\sim 80$  meV are observed.

We then move onto the O K-edge XAS and RIXS results. In Figure 6:7(a), the O K-edge XAS spectra are measured with both  $\sigma$  and  $\pi$  polarization. In this work, we focus on the RIXS spectral response around the main edge  $\sim 532$  eV. Compared to the literature for nickelate materials with  $\text{Ni}^{2+}$  ions, this main edge shows similar energy scale with the Ni-O hybridization in the octahedral  $\text{NiO}_6$  environments [265]. We collect RIXS spectra by detuning the incoming energy across the O K-edge XAS resonances to map out the excitation profiles (Figure 6:7(b)). The excitation spectra are dominated by fluorescence-like modes at energy loss higher than 4 eV loss, similar to the charge-transfer excitations reported in NiO [265,266]. Below 1 eV energy loss, the RIXS spectra show intense multi-phonon overtones, where the higher-energy peaks are well described as high-order harmonics with mode frequency  $\omega_v \approx (v+1)\omega_0$ . Here,  $\omega_0$  is about 80 meV, and  $v$  is denoted for the  $v$ -th order of the multi-phonon scattering of a single vibrational mode. The representative RIXS spectra, taken at  $\sim 531.5$  eV with both  $\sigma$  and  $\pi$  polarization, are shown in Figure 6:7(c). Such an intense phononic response, reminiscent of the one observed in O K-edge RIXS spectra of molecules, is a striking result and likely due to the weak charge screening in geometrically frustrated honeycomb lattices. Additionally, the strong signal for multi-phonon satellites highlights the sufficiently long O 1s core-hole lifetime for the RIXS intermediate states, enabling the probing of phonon excitations with short-lived high-order overtones. The fundamental phonon energy of  $\sim 80$  meV is consistent with the optical phonon modes revealed by Raman spectroscopy [267]. The vibrational modes from  $640$  to  $670\text{ cm}^{-1}$



(~79-83 meV), well resembling our RIXS spectral function, were assigned to O-Ni-O bond-stretching vibrations [267]. Such strong EPC of clearly resolved multi-phonon overtones, combining with the energy dependence for the phonon intensities, were also observed in the recent O K-edge RIXS study on the isostructural honeycomb iridate  $\alpha$ -Li<sub>2</sub>IrO<sub>3</sub> [79].

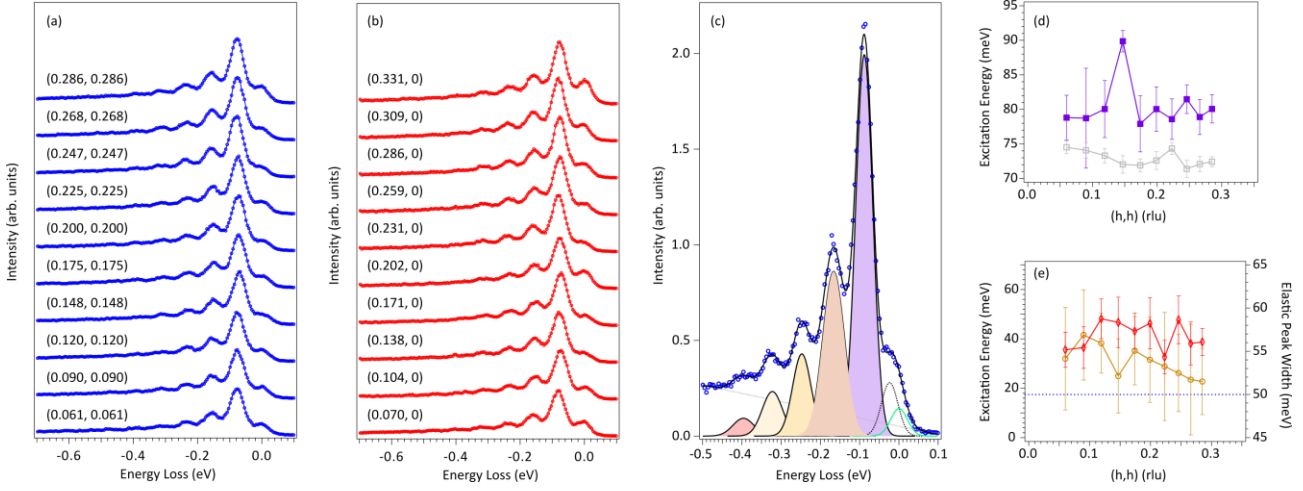


Figure 6:8 Momentum-dependent O K-edge RIXS measurements taken along the (a) (1, 1) and (b) (1, 0) high-symmetry orientations. The predominant RIXS response are weakly-dispersive multi-phonon excitations from the optical phonon modes, reminiscent of the molecular vibrational spectra. (c) Line fitting for the O K-edge RIXS spectrum taken at (0.148, 0.148) rlu. (d) Fitted phonon energy along the (1,1) orientation with two (filled purple squares) Gaussian functions as shown in (c) and one Gaussian function (open gray squares) to account for the quasi-elastic regime below ~75 meV loss. (e) Fit for the mode energy of the quasi-elastic component about 25~35 meV (open brown circles, left axis) with two-component assignment for the elastic line. This is plotted with the peak width of elastic line when it is fitted with only one Gaussian function (open red diamonds, right axis). If the quasi-elastic regime is only fitted with one spectral component, a significant broadening for the elastic peak width of 15~20% compared to the instrumental energy resolution ~50 meV (horizontal blue dotted line) is inferred. Alongside the underestimated phonon energy with one-component quasi-elastic fitting, the two-component assignment for the elastic line in (c) justifies a sizable spectral weight for the low-energy excitations between the elastic scattering and the predominant multi-phonon overtones.

We continue to characterize the multi-phonon excitations by momentum-dependent O K-edge RIXS measurements. In Figure 6:8 (a)-(b), the phonon response are probed along the high-symmetry orientations (1,1) and (1,0), respectively. The representative fit for the multi-phonon overtones in the O K-edge RIXS spectrum is shown in Figure 6:8(c). Five Gaussian functions are applied to fit the inelastic phonon overtones. An ideal simple harmonic oscillator is taken as the initial fitting input. Namely, the energy spacing between the multi-phonon peaks are initially assumed to be the same, which is later relaxed to optimize the fit. To set up the fitting constraint throughout all the momentum-transfer points, the peak widths for the fourth and fifth phonon overtones are set to be the same for all momentum vectors, which provide a reasonable fit as an initial input. The first fundamental phonon is essentially resolution limited, while the phonon broadening is generally no more than 10~15% larger than the energy resolution (~50 meV) up to the fourth harmonic. On the other hand, the fifth harmonic may be mixed with other elementary excitations and show significant broadening about 70~75 meV in FWHM, and seemingly overwhelmed by the background level when approaching the zone center. In general, the multi-phonon excitations are weakly-dispersive, characteristic of the typical optical phonon modes. The fitted peak positions are shown in Figure 6:9(a)-(b). The fundamental phonon intensity is found to gradually increase with elevated momentum-transfer for both orientations (Figure 6:9(c)-(d)), in agreement with the calculated RIXS cross section for a single optical bond-stretching phonon in previous theoretical RIXS studies [268]. Furthermore, the excitation energies of the high-energy multi-phonon overtones are compared with the fundamental phonon frequency at each given momentum-transfer point. This was previously evaluated as the reference for quantifying anharmonicity for the lattice vibrations, characterized by the mode energy ratio  $\omega_v/(v+1)\omega_0$  [79]. When the anharmonicity is large, the high-order harmonics would possess progressively lower mode energies compared to the expected values for a simple harmonic oscillator. This is plotted as a function of momentum-transfer in Figure 6:9 (e)-(f).

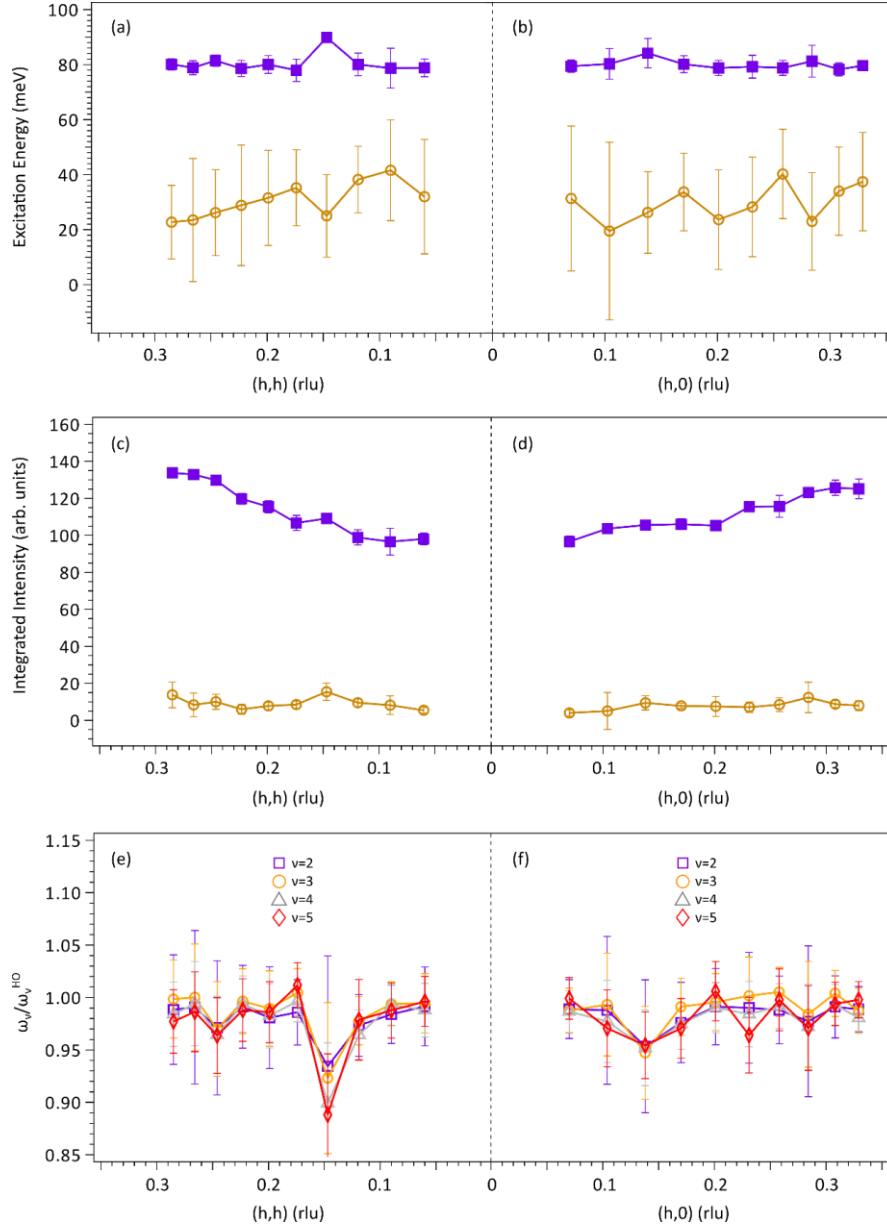


Figure 6:9 (a)-(b) Momentum-resolved fitted peak positions for the fundamental frequency of optical phonon (filled purple squares) and the low-energy mode in the quasi-elastic regime (open brown circles). (c)-(d) Momentum-resolved integrated intensities for the fitted excitation modes. The symbols for notifying the phonon and low-energy excitations follow (a)-(b). (e)-(f) An-harmonicity defined as the deviation for multi-phonon overtones away from the expected energies for a simple harmonic oscillator, which are plotted as the function of momentum-transfer and the  $v$ th-order of phonon harmonics.

Along with the phonon excitations, we also observe an anomalous broadening of the quasi-elastic scattering beyond the experimental resolution, particularly visible at certain momentum-transfer vectors in Figure 6:8(a)-(b). To elucidate the spectral contribution of low-energy excitations in the quasi-elastic regime (below 75 meV here), we compare the fitting results for the low-energy RIXS spectra with two scenarios. One is to account for the quasi-elastic scattering by a single Gaussian function where the width is allowed to vary, while the other considers two separate, resolution-limited Gaussian lineshapes. In the first scenario, the elastic line width is progressively larger than the instrumental response by up to 20% (Figure 6:8(e)). On the other hand, the two-component scheme for the quasi-elastic regime yields a low-energy mode around 25-40 meV in energy. The spectral intensity for this low-energy mode shows insignificant momentum-dependence, while the momentum region that shows larger mode energies seem to coincide with the momentum vectors of stronger elastic broadening in the one-component fitting scheme. By comparison with the current literature, the possible source for the observed low-energy excitations can be other phonon modes at lower-energy (e.g. stretching



vibrations in the  $\text{TeO}_6$  octahedra) [267], or partially contributed by the spin-conserving magnetic excitations, e.g.  $\Delta S=0$  bimagnon continuum [79]. The latter was recently predicted in several magnetically frustrated systems and expected to be detectable by K-edge RIXS [269]. Additionally, optical experiments on other honeycomb oxides have shown indications of Fano-type response in phonon lines that are sensitive to magnetic transition temperature, which were interpreted as coupling to a fractionalized spinon continuum [259]. A similar low-energy excitonic mode  $\sim 25$  meV was also observed in a recent O K-edge RIXS study on the honeycomb iridates [79].

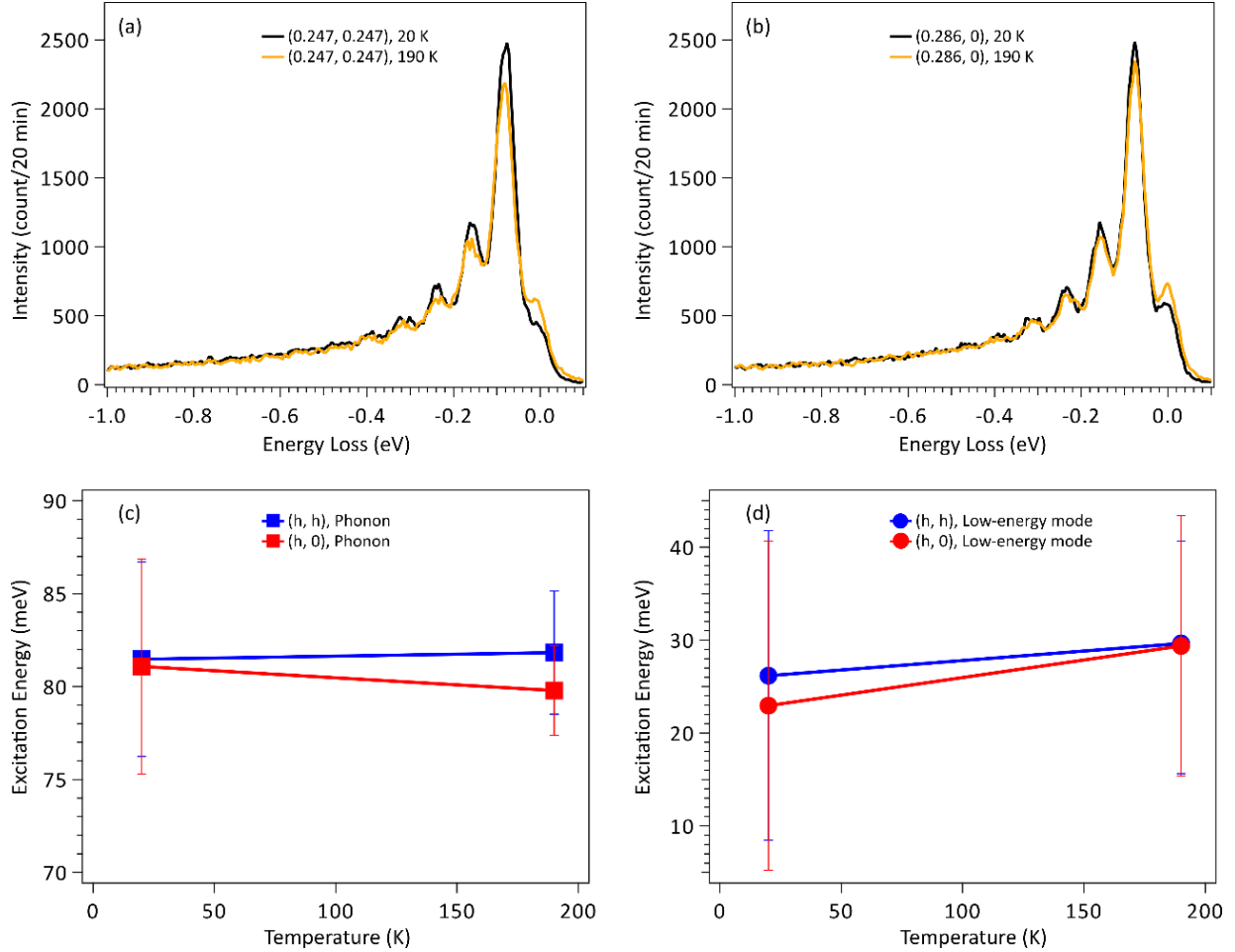


Figure 6:10 Temperature-dependent O K-edge RIXS measurements along  $(h,0)$  orientation with (a)  $\sigma$  and (b)  $\pi$  polarization, respectively. Marginal spectral changes are inferred from the optical phonons  $\sim 80$  meV, which is in agreement with the previous Raman experiments.

As shown in Figure 6:9(e)-(f), the anharmonicity in the phononic response is different between the  $(1,1)$  and  $(1,0)$  orientations. Such effect might be connected to the magnetic order expected along the  $(0.5, 0, 1)$  direction [241]. Another consequence of anharmonicity is the presence of phonon softening in the high-temperature regime. The previous O K-edge RIXS study on the isostructural iridates [79] revealed the opposite trend for the bond-stretching phonon excitations across the AFM temperature, observing increase in mode energies upon heating and was suggested to reflect a possible SPC [79]. In Figure 6:10, we present the temperature dependence of the RIXS spectra and the fitted peak positions for the optical phonon and low-energy excitation mode in both  $(1,1)$  and  $(1,0)$  orientations. Figure 6:10(a)-(b) shows that when the temperature is increased from 20 K to 190 K, the spectral intensity for the phonons slightly decrease while the elastic scattering is slightly enhanced. The latter may result from enhanced thermal fluctuations and diffuse scattering upon increasing temperature. In Figure 6:10(c), the phonon frequency shows marginal differences with respect to temperature, where a small softening around  $\sim 2$  meV is inferred at  $\mathbf{q}=(0.286,0)$  upon heating. This may indicate that the SPC is less significant in the measured honeycomb nickelate compound, or the relevant magneto-elastic coupling simply involves lower-frequency phonons. Given the recent availability of single-crystal NNT0 honeycomb compound [38], we believe that future optical studies on the phonon excitations across the AFM transitions may

shed light on this aspect. Similar phenomena were previously observed in the double-layered perovskite  $\text{Ni}_3\text{TeO}_6$  with honeycomb stacking layers, where the melting of a magneto-electric mode  $\sim 25$  meV was inferred that melted across the Néel temperature  $\sim 52$  K [270]. From Figure 6:10(d), the low-energy mode show a slight hardening  $\sim 5$  meV in both (1,0) and (1,1) directions at the selected momentum-transfer points.

Lastly, we analyse the EPC from the observed multi-phonon excitations by the intensity decay of the higher-energy overtones [Figure 6:11]. The fit adopts the modelling of a single Einstein phonon from ref. [78] to account for the predominant localized optical phonons in the RIXS spectra (also see section 2.6.1). For simplicity, we assume that the vibrations do not include the scattering of electrons between different orbitals and sites, while the effects of intermediate core-hole potentials are not considered here [86]. In this case, the RIXS amplitude for phonon scattering can be diagonalizable and provide an estimate to the EPC in a Frank-Condon fashion [86]. We fix the inverse of core-hole lifetime to be 180 meV taken from ref. [231], and assume that it is a constant with respect to energy transfer and photon energy [271]. This leaves behind the free parameters of the EPC phonon self-energy and the phonon amplitude as an overall intensity scale. A representative fit to the RIXS spectrum is shown in Figure 6:11(a). The fourth and fifth harmonics are not included in the fit because the spectral appearances are not well-defined throughout all momentum-transfer points in the RIXS measurements. Additionally, the damping of high-order harmonics in the RIXS spectra may also be affected by the mixing with other excitation modes, rather than solely derived from their short-lived nature. The fitted EPC are expressed with the phonon self-energies  $M_0$  as a function of momentum-transfer [Figure 6:11(b)-(c)]. Generally, the evaluated EPC shows weak momentum-dependence, similar to the case of the isostructural iridate  $\alpha\text{-Li}_2\text{IrO}_3$  [86]. One should note that the evaluated EPC from our RIXS results assume the major contribution from a single optical phonon branch. Indeed, the presence of other vibrational modes may affect the estimation of the EPC [272]. From the evaluated phonon frequency  $\sim 80$  meV and EPC self-energy  $\sim 280$  meV, we obtain a dimensionless EPC strength  $g=(M_0/\omega_0)^2 \sim 12$ , which is also consistent with the previous RIXS work on the honeycomb iridate  $\alpha\text{-Li}_2\text{IrO}_3$  [86].

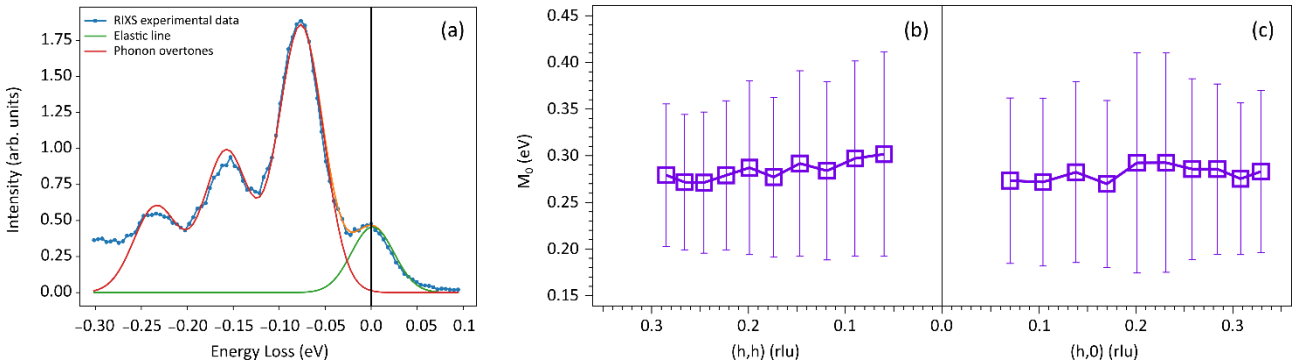


Figure 6:11 Analysis of EPC from the multi-phonon overtones observed for the oxygen vibrations. (a) illustrates the schematic fit at  $\mathbf{q}=(0.06, 0.06)$  rlu, where the RIXS intensity for the multi-phonon scattering adopts the modelling in ref. [78]. (b)-(c) show the momentum-resolved phonon self-energy  $M_0$  along (1,1) and (1,0) directions, respectively..

## 6.7 Conclusion

We explore the Ni 3d electronic structure and the electron-phonon coupling in the layered honeycomb antiferromagnet  $\text{Na}_2\text{Ni}_2\text{TeO}_6$  using RIXS and XAS. From the Ni L-edge XAS spectra, we establish a predominant  $\text{Ni}^{2+}$  configuration in an octahedral site environment, with a possible partial contribution from a  $\text{Ni}^{1+}$  configuration. The dominant 2+ component is supported by the observed dd excitations around 1-3 eV loss in Ni  $L_3$ -edge RIXS, reminiscent of the previous experimental reports on NiO and  $\text{NiCl}_2$ . At the O K-edge, we focus on the RIXS spectral modes arising from the XAS resonance that is characteristic of the Ni-O hybridization band. A series of intense multi-phonon overtones, with fundamental frequency  $\sim 80$  meV, dominate the spectral response suggesting the presence of a high EPC. With the clearly resolved phonon overtones up to the 5-6 harmonics, we use a model of a single Einstein phonon to extract the large EPC value  $\sim 285$  meV, comparable with the recent O K-edge study on the isostructural iridate  $\alpha\text{-Li}_2\text{IrO}_3$  [79]. In addition, our measurements reveal the presence of low-energy elementary excitations  $\sim 25$ -40 meV, which may be composed of lower-energy phonons or by a spin-conserving  $\Delta S=0$  bimagnon continuum. The observed phonon (and quasi-elastic)

RIXS response shows marginal temperature dependence across the AFM transition. This would help to elucidate the excitation modes that are directly sensitive to the magnetic transitions.

## 6.8 Acknowledgement

The experiments have been performed at the ADRESS beamline of the Swiss Light Source at the Paul Scherrer Institut (PSI). The work at PSI is supported by the Swiss National Science Foundation through project no. 200021\_178867, the NCCR MARVEL and the Sinergia network Mott Physics Beyond the Heisenberg Model (MPBH) and SNSF Research Grants CRSII2\_160765/1 and CRSII2\_141962.

# Chapter 7 Conclusion

## 7.1 Achieved Results

In this thesis, the electronic structure and elementary excitations of q-1D chain-ladder cuprates  $\text{Sr}_{14-x}\text{Ca}_x(\text{Cu}_{1-y}\text{Co}_y)_{24}\text{O}_{41}$  (chapter 3-5) and 2D honeycomb nickelates  $\text{Na}_2\text{Ni}_2\text{TeO}_6$  (chapter 6) are investigated by means of XAS and RIXS. In studies on the magnetic and charge dynamics of the hole-doped two-leg spin ladders, the momentum-resolved  $\Delta S=1$  magnetic excitations in the ladders of  $\text{Sr}_{14-x}\text{Ca}_x\text{Cu}_{24}\text{O}_{41}$  ( $x=0$  and  $12.2$ ) are compared (chapter 3). At the O K-edge, the  $\Delta S=0$  magnetic and charge dynamics for the ladders are revealed in  $\text{Sr}_{14}\text{Cu}_{24}\text{O}_{41}$  (chapter 4). By monitoring the quasi-elastic and inelastic RIXS response as a function of momentum, the spectral signature of concomitant CDW order and soft-phonon anomalies are observed for the two-leg ladders in  $\text{Sr}(\text{Cu}_{1-y}\text{Co}_y)_{24}\text{O}_{41}$  ( $y=0, 0.01, 0.03$  and  $0.05$ ) using O K-edge RIXS (chapter 5). Lastly, the Ni 3d electronic structure and the O vibrational modes of  $\text{Na}_2\text{Ni}_2\text{TeO}_6$  are studied by XAS and RIXS at Ni  $L_{3-}$  and O K-edge, respectively (chapter 6).

In chapter 3, the Cu  $L_{3-}$  edge RIXS measurements probed at the  $3d^9$  white line revealed a drastic flattening of dispersion and broadening of the collective 2T magnetic excitations upon heavy Ca-doping in  $\text{Sr}_{14-x}\text{Ca}_x\text{Cu}_{24}\text{O}_{41}$  ( $x=0$  and  $12.2$ ). The excitation energy scales  $\sim 200$ - $300$  meV match the large Cu-O-Cu superexchange in the two-leg ladders ( $\sim 100$  meV) and are much above the scale of the edge-sharing chains ( $\sim 10$  meV) for both  $x=0$  and  $x=12.2$ . Moreover, the polarization-dependent RIXS measurements revealed predominant  $\Delta S=1$  non-spin-conserving scattering for the observed excitations at both  $x=0$  and  $x=12.2$ . From the polarization analysis, the disentangled  $\Delta S=0$  scattering channel, representative of spin-conserving magnetic excitations becomes suppressed and structureless at the low-energy regime (below 1 eV) for  $x=12.2$  compared to  $x=0$ . From the localized magnetic excitations and depletion of low-energy spectral weight of charge dynamics at  $x=12.2$ , these observations suggest an overall localization for the hole carriers in the ladder subsystem upon doping. This is examined and supported by DMRG calculations of the RIXS response through the dynamical spin and charge structure factors of doped Hubbard models, where the localization is simulated by the addition of impurity site potentials. These findings will help to reconcile the role of momentum-dependent spin (and charge) fluctuations for the pairing correlations of doped cuprate ladders  $\text{Sr}_{14-x}\text{Ca}_x\text{Cu}_{24}\text{O}_{41}$  in the heavily Ca-doped phases. For further investigations, the assessment of magnetic and charge excitations across a wide range of chemical doping, i.e. Sr replaced by Ca, Y, or La, should provide a systematic fingerprint to examine the role of spin and charge fluctuations for the pairing correlations of cuprate ladders. Furthermore, experiments with polarimetric analysis of the polarization dependence of the scattered light would consolidate the conclusions obtained from the polarization-dependent RIXS measurements in chapter 3, as those results were obtained only by varying the light polarization of only the incident X-rays.

At the Cu-O hybridization UHB band in the O K-edge XAS signal, the corresponding RIXS measurements on  $\text{Sr}_{14}\text{Cu}_{24}\text{O}_{41}$  in chapter 4 revealed a series of elementary excitation modes that are different from the RIXS spectral response at the Cu  $L_{3-}$  edge. With the weak spin-orbit interactions and longer intermediate state lifetime of O 1s core-level, the RIXS response is dominated by  $\Delta S=0$  magnetic and charge scattering in the doped ladders of  $\text{Sr}_{14}\text{Cu}_{24}\text{O}_{41}$ , giving different sensitivity to the dynamical properties compared to the Cu  $L_{3-}$  edge RIXS results. This was previously shown for the q-1D spin-chain cuprate  $\text{Sr}_2\text{CuO}_3$ , where the lowest-lying  $\Delta S=1$  two-spinon continuum and the high-energy  $\Delta S=0$  four-spinon and higher-order continuum excitations were captured by Cu  $L_{3-}$  and O K-edge RIXS, respectively.

In chapter 4, a dispersing sharp exciton of  $\sim 270$  meV and a weakly-dispersive broad mode about 400-500 meV are observed at the UHB resonance using O K-edge RIXS in  $\text{Sr}_{14}\text{Cu}_{24}\text{O}_{41}$ . The dispersing sharp mode, with comparable energy to the previously reported  $\Delta S=1$  magnetic excitations, is in agreement with composite QPs between holons and spinons predicted in lightly hole-doped ladders. Given the weak spin-orbit interaction of the O 1s core-levels, the O K-edge RIXS cross section will preferentially suppress the predominant  $\Delta S=1$  triplons of the Cu  $L_{3-}$  RIXS response and is interpreted to give rise to sizable spectral weight for the holon-spinon QPs. On the other hand, the significant weight at high-energy in O K-edge compared to Cu  $L_{3-}$  edge naturally speaks for a better sensitivity to short-lived high-order MT scattering, with the relatively long core-hole lifetime of O 1s core-levels. By monitoring the O K- and Cu  $L_{3-}$  edge RIXS spectral response in the same energy regime for  $\text{Sr}_{14}\text{Cu}_{24}\text{O}_{41}$ , the spectral evolution closely resembles the recent RIXS studies on the q-1D cuprate chain compound  $\text{Sr}_2\text{CuO}_3$ . In comparison to theoretical studies of the magnetic and charge dynamics for

doped ladders, the sharp and broad RIXS modes are in reasonable agreement with the holon-spinon QPs and 2T continuum boundary, respectively. These observed excitations are generally inaccessible by other experimental probes that can detect the low-energy dynamics of spin ladders, e.g. INS, Raman spectroscopy, infrared optical absorption, etc. Our study demonstrates the versatility of RIXS in investigating various elementary excitations in correlated electronic materials, with spectral sensitivity to dynamics of different lifetimes, spin character, momentum-space region, etc. As a future outlook, polarization-resolved RIXS cross section calculations, with the core-hole lifetime effects taken into account, will be crucial for further elucidating the  $\Delta S=0$  magnetic and charge excitations with overlapping energies. Additionally, future studies on undoped or hole-depleted ladders would provide the ideal benchmark for clarifying the RIXS spectral response discussed in this thesis.

In chapter 5, the CDW order in the ladders and its interplay with the phonon excitations are studied as a function of Co dopant concentration in  $\text{Sr}(\text{Cu}_{1-y}\text{Co}_y)_{24}\text{O}_{41}$  ( $y=0, 0.01, 0.03$  and  $0.05$ ). The CDW formation in the hole-doped ladders has been previously revealed by O K- and Cu L<sub>3</sub>-edge resonant diffraction in  $\text{Sr}_{14-x}\text{Ca}_x\text{Cu}_{24}\text{O}_{41}$ . This was in line with the proposed scenario of competing charge and pairing density fluctuations to explain HTSC in the early studies of 2D cuprates. In this thesis, the unique opportunity to tune the CDW order via magnetic impurities is discussed for cuprate ladders. At the ladder hole resonance, the CDW formation persists with Cu-Co substitution up to low-doping levels of  $y \leq 0.05$ . Specifically, the CDW signal develops a stronger long-range order at a decreasing ordering wavevector continuously with increasing Co doping, manifested by increasing CDW peak intensity compared to the pristine  $\text{Sr}_{14}\text{Cu}_{24}\text{O}_{41}$ . Energy-detuned and temperature-dependent RIXS measurements confirmed the electronic character of the observed in-plane diffraction peak across all doping levels. Additionally, this coincides with a stronger phonon softening for the bond-stretching vibrational mode ( $\sim 65\text{-}70$  meV) for the elevated Co impurity levels. These experimental findings are consistent with a physical scenario based on an enhanced stripe-like order mediated by significant soft-lattice vibrations, which are seemingly stabilized by the magnetic impurities. This is also compatible with measurements of the magnetic susceptibility, reporting a single-ion like anisotropy via Co dopants in  $\text{Sr}(\text{Cu}_{1-y}\text{Co}_y)_{24}\text{O}_{41}$  [16,189].

Despite a clear experimental development with Co-doping, there are interesting questions that remain open. Firstly, the exact distribution of Co impurities will require more X-ray and neutron diffraction studies involving the structural refinements in the future. This will enable theoretical studies on the influence of magnetic impurities percolating in q-1D systems on electronic order and electron-phonon interactions. Furthermore, the temperature-dependent RIXS measurements reveal a broadening of CDW width with increasing temperature, with spectral signatures that likely represent multiple diffraction components having different temperature and spatial correlations. This has also been observed in recent RIXS studies on 2D SC cuprates, and interpreted as evidence of charge and pair density waves that host quantum critical scattering in the vicinity to optimal doping in the phase diagram. With high-resolution X-ray and neutron diffraction measurements, it will be interesting to check if the CDW temperature evolution in chapter 5 is connected to the proposed hypothesis of pairing correlations mediated by quantum-critical charge density fluctuations. Lastly, the CDW orders probed by Cu L<sub>3</sub>-edge RIXS show different Co-doping dependence at the 3d<sup>9</sup> white line and the ZRS charge-transfer configuration of 3d<sup>10</sup> $\bar{L}$ , whereas the latter XAS resonance is generally weak in 2D cuprates. This will give unique opportunities to study the electronic origin of CDW probed by resonant X-ray probes, as there are several issues remaining elusive in the microscopic modeling of the energy- and element-dependent CDW correlations.

In chapter 6, the Ni 3d electronic configuration and the O vibrations of the 2D honeycomb nickelate  $\text{Na}_2\text{Ni}_2\text{TeO}_6$  are studied by XAS and RIXS at the Ni L<sub>3</sub>- and O K-edge. The importance of assessing the excitations in the Ni 3d valence shell and phonon excitations is motivated by the identification of a crucial role of spin-phonon interactions in the recent studies on magnetically frustrated materials. From the RIXS spectra across the Ni L<sub>3</sub>-edge, it is attested that the localized Raman-like excitations in the 1-3 eV range are similar to the inter-orbital dd excitations in NiO and NiCl<sub>2</sub>, dominated by a Ni<sup>2+</sup> configuration with octahedral site symmetry. This can also be inferred from the two main XAS resonances at Ni L<sub>3</sub>-edge that are characteristic of the Ni<sup>2+</sup> state of NiO<sub>6</sub> octahedra, with an energy difference  $\sim 1.5$  eV that is close to the combined energy splitting of the  $e_g\text{-}t_{2g}$  transition and the local spin-flip exchange for the Ni<sup>2+</sup> ions. The additional spectral components between the Ni L<sub>3</sub>- and L<sub>2</sub>-edge XAS resonances may be attributed to charge-transfer anti-bonding configurations and emission lines from Te M-edge, where the former may be dominated by Ni 3d<sup>8</sup>-3d<sup>9</sup> $\bar{L}$  transitions. This characterization of the Ni 3d valence configuration is crucial for understanding the magnetism in  $\text{Na}_2\text{Ni}_2\text{TeO}_6$  that is hosted by the Ni 3d shell.

From the O K-edge RIXS spectra, high-energy fluorescence-like excitations and predominant multi-phonon overtones of oxygen vibrational modes are revealed, which are probed at the main XAS resonance  $\sim 531$  eV that is reminiscent of the Ni-O hybridization peak in other nickelates with  $\text{Ni}^{2+}$  states. The molecular-like strong EPC  $\sim 285$  meV for the oxygen vibrations ( $\sim 80$  meV for the fundamental frequency) are reminiscent of the isostructural iridates  $\alpha\text{-Li}_2\text{IrO}_3$   $\sim 260$  meV [79], showing weakly momentum-dispersive optical phonon satellites. In addition to the dominant phonon harmonics in  $\text{Na}_2\text{Ni}_2\text{TeO}_6$ , a sizable quasi-elastic scattering  $\sim 25\text{-}40$  meV between the fundamental phonon and the elastic scattering at 0 eV loss is uncovered, which may be contributed by phonon modes at lower-energy, magneto-elastic coupled excitations, or a  $\Delta S=0$  bimagnon continuum that has been reported for other frustrated oxide antiferromagnets. The temperature-dependent RIXS measurements show only marginal spectral contrast across the Néel temperature, leaving open the question of which modes are reflective of the magnetic phase transition. The RIXS response of orbital and charge-transfer excitations, as well as momentum-resolved EPC, characterize the dynamics that are difficult with other experimental techniques for the energy regime discussed in chapter 6. For clarifying the inelastic spectral fingerprint associated with the magnetic transitions, further studies using optical spectroscopy for measuring the lower-energy phonons and the  $\Delta S=0$  bimagnon continuum excitations, as a function of temperature and magnetic field, should give insight to this open question.

## 7.2 Future Development

Section 7.2.1 I address possible extensions of RIXS studies on the magnetic excitations of the cuprate ladders in  $\text{Sr}_{14}\text{Cu}_{24}\text{O}_{41}$ . The main idea is based on the RIXS capability for resolving the multi-tripion scattering with separate odd- and even-parity channels, which can be achieved by employing different scattering geometry. Section 7.2.2-7.2.3 gives a future outlook based on the RIXS results presented in this thesis, and extend the discussion to the ongoing developments in the RIXS field that are relevant for in the context. This will include the connection of the demonstrated experimental achievements to other promising fields where RIXS has great potential for scientific breakthrough, as well as a brief overview of the relevant developments in current literature. Given the rapid progress in instrumental performance and understanding of the scattering cross-section in the RIXS field, this will open up several new opportunities to study many-body physics in correlated electronic materials. In the following two sub-sections, two examples will be given that are associated with the experimental results shown in this thesis.

### 7.2.1 Extended research

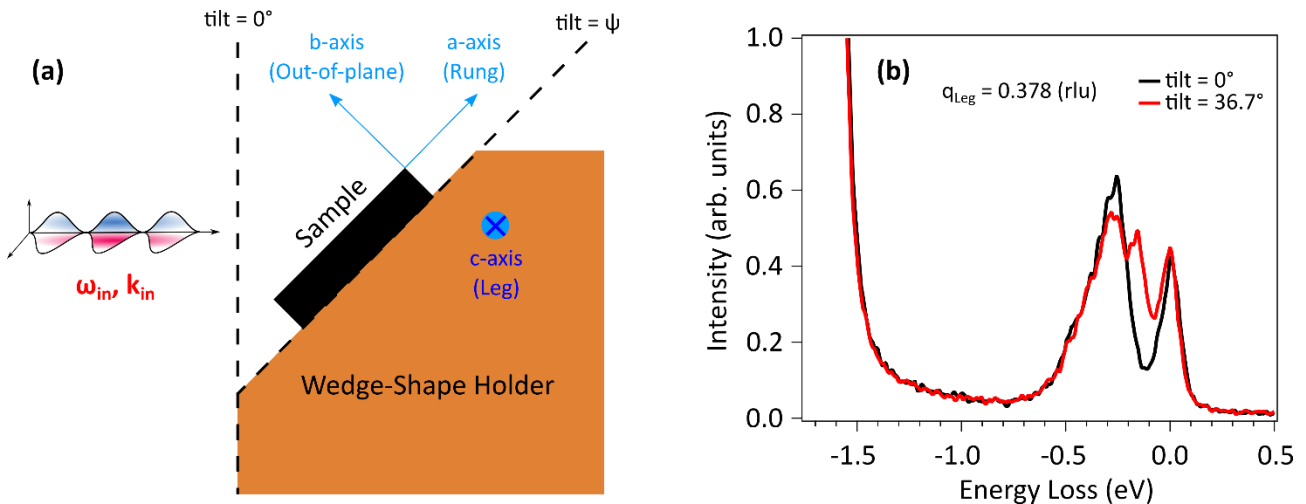


Figure 7:1 (a) RIXS experimental geometry for probing triplon excitations in the odd-parity scattering channel. The tilted orientation ensures a finite momentum-transfer along the ladder-rung direction (a-axis) for horizontally incident X-rays. (b) The Cu  $L_3$ -edge RIXS measurements performed on  $\text{Sr}_{14}\text{Cu}_{24}\text{O}_{41}$  taken with and without a rung tilt-angle, while the momentum-transfer along ladder-leg (c-axis) is fixed at  $q_{\text{Leg}}=0.378$  (rlu).

For the presented RIXS results in chapter 3 to 5, the experiments were performed in a geometry where the scattering plane lies within the a-b plane (see Figure 3:4 and 4:4). In this geometry, the momentum-transfer along the ladder-rung

is zero for horizontally incident X-rays as shown in Figure 7:1(a), and the magnetic excitations are dominated by multi-triplon scattering in the even-parity as previously demonstrated [13]. This was understood through the selection rules in the scattering cross section for momentum- and energy-resolved spectroscopies, e.g. INS and RIXS [108]. The separation of the lowest-lying one- and two-triplon magnetic spectra has been reported for the hole-depleted ladders in  $\text{Sr}_4\text{La}_{10}\text{Cu}_{24}\text{O}_{41}$  using INS, where the disentanglement between the odd- and even-parity was achieved by applying the structural modulation factors onto the momentum- and energy-resolved time-of-flight (TOF) datasets for the scattered neutron [12]. For RIXS measurements, it was theoretically formulated that a non-zero momentum-transfer along the rung orientation is required to give a finite cross section of one-triplon and higher-order triplon scattering in the odd-parity channel [108].

In principle, one needs to fix the rung momentum-transfer at the zone boundary ( $q_{\text{Rung}}=0.5$  rlu) to fully suppress the two-triplon RIXS signal. In practice, this can be achieved by either varying the tilt angle along the rung direction with respect to different incidence angles for the leg momentum-transfer (see Figure 7:1(a)), or tweaking the scattering angle between the incident and outgoing photon when mapping out the full energy dispersion along the ladder-leg [108]. The latter option requires a continuous rotation between the experimental UHV chamber from the beamline side (incident X-rays) and RIXS spectrometer (outgoing X-rays). For the former case, exemplary RIXS spectra are taken for a fixed leg momentum-transfer  $q_{\text{Leg}} \sim 0.378$  (rlu) as shown in Figure 7:1(b). With a tilt angle of  $\sim 37^\circ$  ( $q_{\text{Rung}} \sim 0.227$  rlu), an additional peak  $\sim 100$  meV arises in the energy range of triplon excitations in the cuprate ladders of SCCO. The peak energy  $\sim 100$  meV is in close agreement with the INS report for the one-triplon excitations in hole-depleted  $\text{Sr}_4\text{La}_{10}\text{Cu}_{24}\text{O}_{41}$  at the same leg momentum-transfer [12]. One should note that here the tilt angle is chosen such that the RIXS signal shows a mixture between the two- and one-triplon magnetic scattering. For the given Cu  $L_3$ -edge photon energy and Cu-Cu lattice spacing of SCCO, a larger scattering angle  $2\theta \geq 138^\circ$  is required to probe the pure one-triplon energy dispersion using RIXS [108], which was not possible for the largest scattering angle available in the experimental setup used in this thesis. With  $2\theta$  of  $150^\circ$ , the one-triplon dispersion through about 15~20% of the Brillouin zone can be reached for the cuprate ladders of SCCO using Cu  $L_3$ -edge RIXS [108].

### 7.2.2 Quantum spin liquid and Majorana excitations

In this section, the relation between the RIXS results in chapter 4 and quantum spin liquid (QSL) states is discussed. It is intriguing to compare the O K-edge RIXS results on  $\text{Sr}_{14}\text{Cu}_{24}\text{O}_{41}$  in chapter 4 to the recent theories of RIXS response on the QSLs of Kitaev character [160–162]. For more comprehensive reading for the experimental response of QSLs, the readers are referred to ref. [273]. QSL is an exotic magnetic phase where there is no magnetic order in the ground state, while a product state cannot describe its low-energy spin Hamiltonian due to the long-range entanglement. The excitation spectrum of QSLs is characterized by the so-called Majorana quasiparticles, where the antimatter for these particles are exactly themselves. The experimental demand for probing these Majorana modes has been increasing in recent years, given their potential for realizing the memory unit of quantum computation. INS is able to capture the momentum-independent continuum of two immobile Majorana fermions [274,275], while Raman measurements can detect the two-particle scattering fractionalized excitations of at the zone center [276]. On the other hand, disentanglement between different flavors of excitations, such as the gapless Majorana mode and gapped vison, were expected to be achievable by resolving the  $\Delta S=1$  and  $\Delta S=0$  RIXS scattering channels [160]. The generic  $\Delta S=0$  RIXS response of QSLs is suggested as the dispersive sharp lower-energy edge along with a higher-energy continuum (Figure 7:2), where the latter could persist in the magnetically-ordered state [160]. While the ladder excitation spectra can be taken as the suitable model systems to map onto multiple Majorana fermions accordingly [277], the calculated multi-particle Majorana modes resemble the  $\Delta S=0$  MT bound state and continuum [160], where the latter have been predicted to be detectable by RIXS [26]. The zero-energy bound states with pairs of Majorana vortices in non-Abelian QSLs are predicted as the ideal building blocks for quantum information [273]. In fact, recent theories demonstrated the robustness of these modes against perturbation over parametrically wide regions in inhomogeneous ladders [278]. These connect our results to the RIXS capabilities for probing interacting fractionalized excitations in the presence of non-local ground state degeneracy. The experimental evidence of effective Kitaev-Heisenberg interactions in the QSL candidate  $\text{Na}_2\text{IrO}_3$  was recently revealed using Ir  $L_3$ -edge RIXS [279]. Along with the improvements of RIXS instrumental

setups, understanding of the MT bound state and continuum in spin ladders will help to understand the long-range-entangled nature in QSLs.

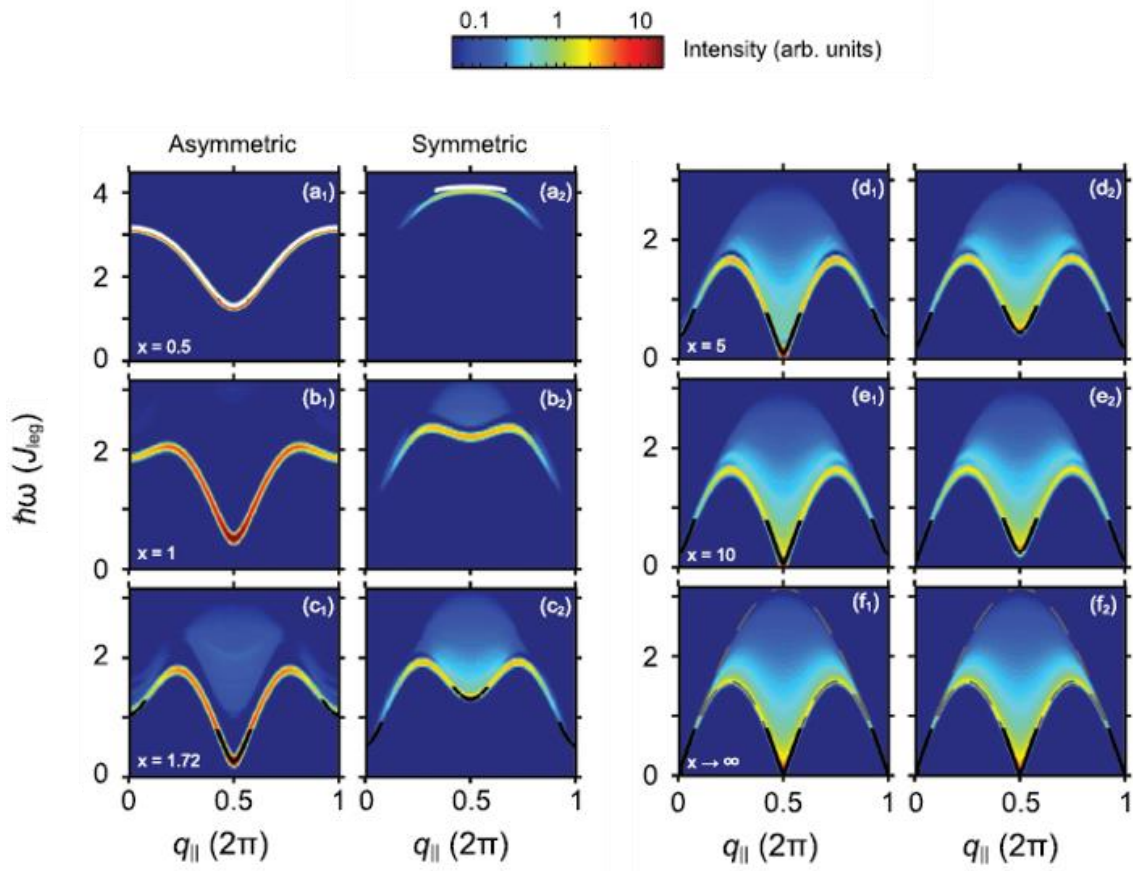


Figure 7:2 Magnetic excitation spectra of an undoped two-leg ladder calculated as a function of the ratio of magnetic exchange between leg and rung orientations (modified from ref. [277]). The black solid lines highlight the boundaries of the multi-particle continuum that follow the formalism of interacting Marojana fermions, which emerge from the intermediate to weak coupling regime. (Note that here  $x \equiv J_{\text{leg}}/J_{\text{rung}}$ , which is different with the definition of  $r$  value in chapter 3 and 4). [Reprinted figure with permission from: D. Schmidiger et al., Physical Review B, 88, 094411 (2013). Copyright (2013) by the American Physical Society. (<http://dx.doi.org/10.1103/10.1103/PhysRevB.88.094411>)]

### 7.2.3 Further insight into electron-phonon coupling

In this section, recent developments of the capability for studying the momentum-resolved EPC strength using RIXS are reported. This concerns mainly energy-detuning RIXS measurements, which were proposed aiming at providing an alternative approach for the quantification of the EPC in the absence of clearly observable multi-phonon overtones and strong electron-phonon interactions. The advantages and drawbacks of this alternative experimental method are discussed.

In chapter 5 and 6, the development of the large EPC is quantified for the oxygen vibrational modes in q-1D cuprate ladders and a 2D frustrated honeycomb nickelate. In the present work the EPC strength is determined from the decay of the higher-order phonon overtones with respect to the first fundamental phonon. However, this is only achievable when the phonon satellites are clearly detectable in the energy loss spectrum. For most cases, the high-order vibrational overtones can only be observed in gases or materials with lighter elements when probed at narrow resonances with sufficiently long core-hole lifetime for the intermediate states. Early theories formulated the fundamental phonon intensity to be approximately proportional to the square of EPC constant  $g$  [138,140,230,268]. Recently, Cu  $L_3$ -edge RIXS studies on 2D cuprates demonstrated another approach to estimate EPC without the need to observe high-energy phonon overtones [272,280]. The RIXS intensity for the probed inelastic excitations are generally maximized at the XAS resonances. For convenience, a simple case of one Einstein phonon is considered in the following discussions. If one assumes the RIXS phonon response of interest can be described by a single phonon in the localized picture, it is feasible



to evaluate the EPC strength by assessing the RIXS phonon intensity as a function of detuning-energy  $\Omega$  of the incident X-rays. Under these assumptions, the simplified analytical form for the RIXS intensity can be written as [78,271]

$$I \propto \frac{e^{-2g}}{g} \left| \sum_{n=0}^{\infty} \frac{g^n (n-g)}{n! (\Omega + i\Gamma + (g-n)\omega_0)} \right|^2.$$

Equation 7:1 RIXS intensity for considering a single Einstein phonon mode as a function of detuned-energy for the incident X-rays.

The phonon frequency  $\omega_0$  for the investigated vibrational mode can be directly inferred from the RIXS experiments. Therefore, if one assumes the inverse core-hole lifetime  $\Gamma$  changes negligibly across the XAS resonances with detuning, one can extract the phonon self-energy  $M$  by mapping the phonon intensity with respect to the detuned-energy through numerical optimization, e.g. a standard least-square fit, and thereby also determine the dimensionless EPC constant  $g=(M/\omega_0)^2$ .

This method, however, has its own suitable parameter space for applying to RIXS experiments. In order to assess the EPC using the detuning RIXS approach, it assumes a moderately large inverse core-hole lifetime  $\Gamma$  and small EPC. This leads to the direct consequence of disregarding intermediate state and core-hole lifetime effects, and the intensity ratio between the high-order overtone and fundamental phonon will start to diverge within the theoretical framework of a single Einstein phonon from ref. [78]. This happens when  $M/\Gamma$  is reasonably large such that an analytical solution cannot exist. Recently, Vale et al argued that the detuning RIXS approach would reasonably describe the EPC with Einstein phonon for  $M/\Gamma < 1$ , namely the phonon self-energy has to be sufficiently small compared to the inverse core-hole lifetime [79]. From ref. [272,280], the  $M/\Gamma$  value is  $\sim 0.28$  at the Cu  $L_3$ -edge for the layered cuprates is significantly smaller compared to the oxygen vibrations for the honeycomb iridate  $\alpha$ - $\text{Li}_2\text{IrO}_3$  in ref. [79] with  $1 \leq M/\Gamma \leq 1.35$ . In ref. [79], the fundamental phonon and the second harmonic of oxygen vibrations in honeycomb iridates barely suppress in intensities when detuned away from resonance by about 200 meV. Additionally, by mapping the detuning RIXS signal, a heavily underestimated EPC strength is obtained with poorly fitted  $M$  and  $g$  for the measured samples. A similar scenario is inferred for the phonon excitations of the honeycomb nickelate  $\text{Na}_2\text{Ni}_2\text{TeO}_6$  in chapter 6, where the observed strong EPC and phonon overtones for the bond-stretching vibrations do not follow the energy dependence as described in the detuning Cu  $L_3$ -edge RIXS measurements on the 2D cuprates. These observations indicate that more elaborate theories for simulating the RIXS phonon response is urgently in need. Namely, a single Einstein phonon for localized systems (ref. [78]) may not be sufficient. The RIXS phonon cross section has been recently extended with the consideration of interacting phonon models [281], and effects of carrier mobility [282]. Alongside the rapidly improved energy resolution from the RIXS instrumentation, this will enable detection of lower-energy phonons with their overtones, as well as the de-convolution of different phonon modes and their respective EPC strength.

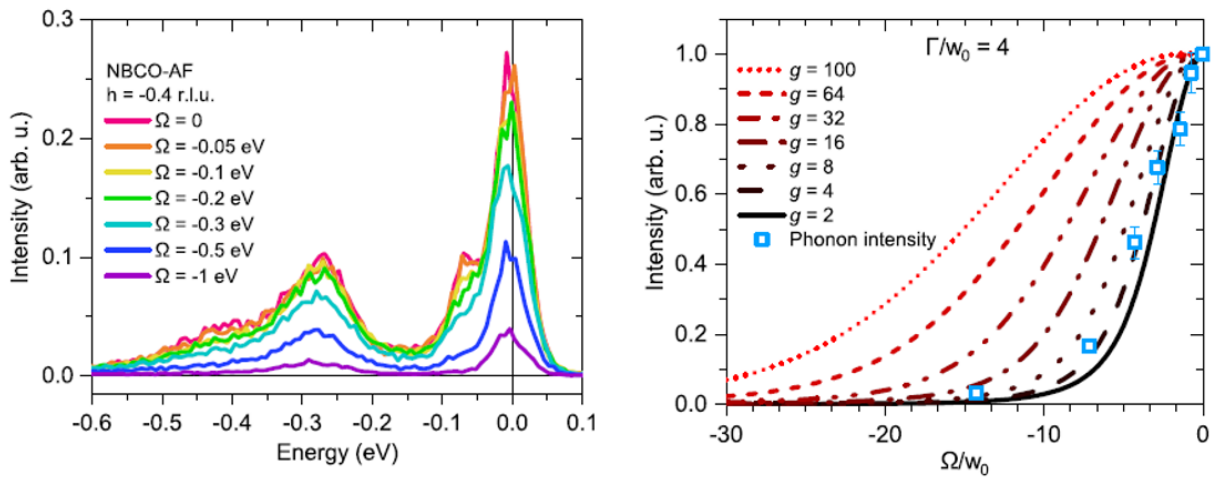


Figure 7:3 Energy-detuning Cu  $L_3$ -edge RIXS measurements of the Cu-O bond-stretching phonon in the AFM  $\text{Nd}_{1-x}\text{Ba}_x\text{Cu}_3\text{O}_{7-\delta}$  cuprate, modified from ref. [272]. (Left) The phonon intensity is monotonically suppressed with the detuning  $\Omega$  of the incident photon energy towards the pre-edge of the Cu  $L_3$ -edge XAS response. (Right) The dimensionless EPC constant  $g$  is compared for a variety of extracted values based on the model from Ament et al. in ref. [78] with a Einstein phonon. [Open access for the reprinted figure is available from: L. Braicovich et al., Physical Review Research, 2, 023231 (2020). Copyright (2020) by the American Physical Society. (<http://dx.doi.org/10.1103/PhysRevResearch.2.023231>)]

## References

- [1] N. W. Ashcroft and N. Mermin, *Solid State Physics* (New York, 1976).
- [2] S. Blundell, *Magnetism in Condensed Matter* (Oxford University Press, 2001).
- [3] H. A. Kramers, *Physica* **1**, 182 (1934).
- [4] P. W. Anderson, *Phys. Rev.* **79**, 350 (1950).
- [5] J. B. Goodenough, *Phys. Rev.* **100**, 564 (1955).
- [6] J. B. Goodenough, *J. Phys. Chem. Solids* **6**, 287 (1958).
- [7] J. Kanamori, *J. Phys. Chem. Solids* **10**, 87 (1959).
- [8] M. Eschrig, *Adv. Phys.* **55**, 47 (2006).
- [9] E. Dagotto and T. M. Rice, *Science* **271**, 618 (1996).
- [10] E. Dagotto, J. Riera, and D. Scalapino, *Phys. Rev. B* **45**, 5744 (1992).
- [11] T. M. Rice, S. Gopalan, and M. Sigrist, *Europhys. Lett.* **23**, 445 (1993).
- [12] S. Notbohm, P. Ribeiro, B. Lake, D. A. Tennant, K. P. Schmidt, G. S. Uhrig, C. Hess, R. Klingeler, G. Behr, B. Büchner, M. Reehuis, R. I. Bewley, C. D. Frost, P. Manuel, and R. S. Eccleston, *Phys. Rev. Lett.* **98**, 027403 (2007).
- [13] J. Schlappa, T. Schmitt, F. Vernay, V. N. Strocov, V. Ilakovac, B. Thielemann, H. M. Rønnow, S. Vanishri, A. Piazzalunga, X. Wang, L. Braicovich, G. Ghiringhelli, C. Marin, J. Mesot, B. Delley, and L. Patthey, *Phys. Rev. Lett.* **103**, 047401 (2009).
- [14] R. S. Eccleston, M. Azuma, and M. Takano, *Phys. Rev. B* **53**, R14721 (1996).
- [15] T. Imai, K. R. Thurber, K. M. Shen, A. W. Hunt, and F. C. Chou, *Phys. Rev. Lett.* **81**, 220 (1998).
- [16] R. Bag, K. Karmakar, and S. Singh, *J. Cryst. Growth* **458**, 16 (2017).
- [17] R. S. Eccleston, M. Uehara, J. Akimitsu, H. Eisaki, N. Motoyama, and S. I. Uchida, *Phys. Rev. Lett.* **81**, 1702 (1998).
- [18] P. Abbamonte, G. Blumberg, A. Rusydi, A. Gozar, P. G. Evans, T. Siegrist, L. Venema, H. Eisaki, E. D. Isaacs, and G. A. Sawatzky, *Nature* **431**, 1078 (2004).
- [19] M. Uehara, T. Nagata, J. Akimitsu, H. Takahashi, N. Môri, and K. Kinoshita, *J. Phys. Soc. Japan* **65**, 2764 (1996).
- [20] T. Nagata, M. Uehara, J. Goto, J. Akimitsu, N. Motoyama, H. Eisaki, S. Uchida, H. Takahashi, T. Nakanishi, and N. Môri, *Phys. Rev. Lett.* **81**, 1090 (1998).
- [21] M. Vojta and T. Ulbricht, *Phys. Rev. Lett.* **93**, 127002 (2004).
- [22] M. Greiter and H. Schmidt, *Phys. Rev. B* **82**, 144512 (2010).
- [23] R. Comin and A. Damascelli, *Annu. Rev. Condens. Matter Phys.* **7**, 369 (2016).
- [24] P. W. Anderson, *Science* **235**, 1196 (1986).
- [25] T. Senthil and M. P. A. Fisher, *Phys. Rev. Lett.* **86**, 292 (2001).
- [26] U. Kumar, A. Nocera, E. Dagotto, and S. Johnston, *Phys. Rev. B* **99**, 205130 (2019).
- [27] M. Sigrist, T. M. Rice, and F. C. Zhang, *Phys. Rev. B* **49**, 12058 (1994).
- [28] H. Tsunetsugu, M. Troyer, and T. M. Rice, *Phys. Rev. B* **49**, 16078 (1994).
- [29] M. Troyer, H. Tsunetsugu, and T. M. Rice, *Phys. Rev. B* **53**, 251 (1996).
- [30] E. M. McCarron, M. A. Subramanian, J. C. Calabrese, and R. L. Harlow, *Mater. Res. Bull.* **23**, 1355 (1988).

- 
- [31] A. Rusydi, P. Abbamonte, H. Eisaki, Y. Fujimaki, G. Blumberg, S. Uchida, and G. A. Sawatzky, *Phys. Rev. Lett.* **97**, 016403 (2006).
  - [32] M. Matsuda and K. Katsumata, *Phys. Rev. B* **53**, 12201 (1996).
  - [33] M. Matsuda, K. Katsumata, H. Eisaki, N. Motoyama, S. Uchida, S. M. Shapiro, and G. Shirane, *Phys. Rev. B* **54**, 12199 (1996).
  - [34] G. Blumberg, P. Littlewood, A. Gozar, B. S. Dennis, N. Motoyama, H. Eisaki, and S. Uchida, *Science* **297**, 584 (2002).
  - [35] S. Sahling, G. Remenyi, C. Paulsen, P. Monceau, V. Saligrama, C. Marin, A. Revcolevschi, L. P. Regnault, S. Raymond, and J. E. Lorenzo, *Nat. Phys.* **11**, 255 (2015).
  - [36] M. Kato, K. Shiota, T. Adachi, and Y. Koike, *Czechoslov. J. Phys.* **46**, 2701 (1996).
  - [37] E. Dagotto, *Reports Prog. Phys.* **62**, 1525 (1999).
  - [38] R. Sankar, I. P. Muthuselvam, G. J. Shu, W. T. Chen, S. K. Karna, R. Jayavel, and F. C. Chou, *CrystEngComm* **16**, 10791 (2014).
  - [39] J. S. Gardner, M. J. P. Gingras, and J. E. Greedan, *Rev. Mod. Phys.* **82**, 53 (2010).
  - [40] M. Heinrich, H. A. Krug von Nidda, A. Loidl, N. Rogado, and R. J. Cava, *Phys. Rev. Lett.* **91**, 137601 (2003).
  - [41] A. Yu. Kitaev, *Ann. Phys.* **303**, 2 (2002).
  - [42] L. Balents, *Nature* **464**, 199 (2010).
  - [43] F. M. F. de Groot, *Coord. Chem. Rev.* **249**, 31 (2005).
  - [44] F. M. F. de Groot, *Chem. Rev.* **101**, 1779 (2001).
  - [45] F. M. F. de Groot and A. Kotani, *Core Level Spectroscopy of Solids* (CRC Press, 2008).
  - [46] D. Attwood, *Soft X-Rays and Extreme Ultraviolet Radiation* (2007).
  - [47] A. Kotani and S. Shin, *Rev. Mod. Phys.* **73**, 203 (2001).
  - [48] J. Als-nielsen and D. Mcmorrow, *Elements of Modern X-Ray Physics Elements of Modern X-Ray Physics Second Edition* (John Wiley & Sons, Ltd, 2001).
  - [49] L. J. P. Ament, M. van Veenendaal, T. P. Devereaux, J. P. Hill, and J. van den Brink, *Rev. Mod. Phys.* **83**, 705 (2011).
  - [50] S. R. White, *Phys. Rev. Lett.* **69**, 2863 (1992).
  - [51] S. R. White, *Phys. Rev. B* **48**, 10345 (1993).
  - [52] A. Nocera, U. Kumar, N. Kaushal, G. Alvarez, E. Dagotto, and S. Johnston, *Sci. Rep.* **8**, 11080 (2018).
  - [53] T. P. Devereaux, A. M. Shvaika, K. Wu, K. Wohlfeld, C. J. Jia, Y. Wang, B. Moritz, L. Chaix, W. S. Lee, Z. X. Shen, G. Ghiringhelli, and L. Braicovich, *Phys. Rev. X* **6**, 041019 (2016).
  - [54] V. N. Strocov, T. Schmitt, U. Flechsig, T. Schmidt, A. Imhof, Q. Chen, J. Raabe, R. Betemps, D. Zimoch, J. Krempasky, X. Wang, M. Grioni, A. Piazzalunga, and L. Patthey, *J. Synchrotron Radiat.* **17**, 631 (2010).
  - [55] V. N. Strocov, T. Schmitt, U. Flechsig, L. Patthey, and G. S. Chiuzbăian, *J. Synchrotron Radiat.* **18**, 134 (2011).
  - [56] G. Ghiringhelli, A. Piazzalunga, C. Dallera, G. Trezzi, L. Braicovich, T. Schmitt, V. N. Strocov, R. Betemps, L. Patthey, X. Wang, and M. Grioni, *Rev. Sci. Instrum.* **77**, 1 (2006).
  - [57] T. Schmidt, M. Calvi, T. Schmitt, V. N. Strocov, and D. Zimoch, *J. Phys. Conf. Ser.* **425**, 032020 (2013).
  - [58] T. Schmitt, V. N. Strocov, K. J. Zhou, J. Schlappa, C. Monney, U. Flechsig, and L. Patthey, *J. Electron Spectros. Relat. Phenomena* **188**, 38 (2013).
  - [59] J. Schlappa, K. Wohlfeld, K. J. Zhou, M. Mourigal, M. W. Haverkort, V. N. Strocov, L. Hozoi, C. Monney, S. Nishimoto, S. Singh, A. Revcolevschi, J.-S. Caux, L. Patthey, H. M. Rønnow, J. van den Brink, and T. Schmitt, *Nature* **485**, 82 (2012).

- 
- [60] V. Bisogni, S. Kourtis, C. Monney, K. J. Zhou, R. Kraus, C. Sekar, V. N. Strocov, B. Büchner, J. van den Brink, L. Braicovich, T. Schmitt, M. Daghofer, and J. Geck, *Phys. Rev. Lett.* **112**, 147401 (2014).
  - [61] M. Minola, G. Dellea, H. Gretarsson, Y. Y. Peng, Y. Lu, J. Porras, T. Loew, F. Yakhou, N. B. Brookes, Y. B. Huang, J. Pelliciari, T. Schmitt, G. Ghiringhelli, B. Keimer, L. Braicovich, and M. Le Tacon, *Phys. Rev. Lett.* **114**, 217003 (2015).
  - [62] C. Jia, K. Wohlfeld, Y. Wang, B. Moritz, and T. P. Devereaux, *Phys. Rev. X* **6**, 021020 (2016).
  - [63] M. Hepting, L. Chaix, E. W. Huang, R. Fumagalli, Y. Y. Peng, B. Moritz, K. Kummer, N. B. Brookes, W. C. Lee, M. Hashimoto, T. Sarkar, J. F. He, C. R. Rotundu, Y. S. Lee, R. L. Greene, L. Braicovich, G. Ghiringhelli, Z. X. Shen, T. P. Devereaux, and W. S. Lee, *Nature* **563**, 374 (2018).
  - [64] E. H. da Silva Neto, M. Minola, B. Yu, W. Tabis, M. Bluschke, D. Unruh, H. Suzuki, Y. Li, G. Yu, D. Betto, K. Kummer, F. Yakhou, N. B. Brookes, M. Le Tacon, M. Greven, B. Keimer, and A. Damascelli, *Phys. Rev. B* **98**, 161114 (2018).
  - [65] R. Fumagalli, L. Braicovich, M. Minola, Y. Y. Peng, K. Kummer, D. Betto, M. Rossi, E. Lefrançois, C. Morawe, M. Salluzzo, H. Suzuki, F. Yakhou, M. Le Tacon, B. Keimer, N. B. Brookes, M. M. Sala, and G. Ghiringhelli, *Phys. Rev. B* **99**, 134517 (2019).
  - [66] M. Moretti Sala, V. Bisogni, C. Aruta, G. Balestrino, H. Berger, N. B. Brookes, G. M. DeLuca, D. DiCastro, M. Grioni, M. Guarise, P. G. Medaglia, F. Miletto Granozio, M. Minola, P. Perna, M. Radovic, M. Salluzzo, T. Schmitt, K. J. Zhou, L. Braicovich, and G. Ghiringhelli, *New J. Phys.* **13**, 043026 (2011).
  - [67] M. Kang, J. Pelliciari, Y. Krockenberger, J. Li, D. E. McNally, E. Paris, R. Liang, W. N. Hardy, D. A. Bonn, H. Yamamoto, T. Schmitt, and R. Comin, *Phys. Rev. B* **99**, 045105 (2019).
  - [68] J. Zaanen, G. A. Sawatzky, and J. W. Allen, *Phys. Rev. Lett.* **55**, 418 (1985).
  - [69] Y. Harada, K. Okada, R. Eguchi, A. Kotani, H. Takagi, T. Takeuchi, and S. Shin, *Phys. Rev. B* **66**, 165104 (2002).
  - [70] C. Monney, V. Bisogni, K. J. Zhou, R. Kraus, V. N. Strocov, G. Behr, J. Málek, R. Kuzian, S. Drechsler, S. Johnston, A. Revcolevschi, B. Büchner, H. M. Rønnow, J. van den Brink, J. Geck, and T. Schmitt, *Phys. Rev. Lett.* **110**, 087403 (2013).
  - [71] K. Ishii, T. Tohyama, S. Asano, K. Sato, M. Fujita, S. Wakimoto, K. Tustsui, S. Sota, J. Miyawaki, H. Niwa, Y. Harada, J. Pelliciari, Y. Huang, T. Schmitt, Y. Yamamoto, and J. Mizuki, *Phys. Rev. B* **96**, 115148 (2017).
  - [72] A. Nag, M. Zhu, M. Bejas, J. Li, H. C. Robarts, H. Yamase, A. N. Petsch, D. Song, H. Eisaki, A. C. Walters, S. M. Hayden, and K. J. Zhou, *Phys. Rev. Lett.* **125**, 257002 (2020).
  - [73] A. Singh, H. Y. Huang, C. Lane, J. H. Li, J. Okamoto, S. Komiya, R. S. Markiewicz, A. Bansil, A. Fujimori, C. T. Chen, and D. J. Huang, *arXiv:2006.13424* (2020).
  - [74] V. Bisogni, L. Simonelli, L. J. P. Ament, F. Forte, M. Moretti Sala, M. Minola, S. Huotari, J. van den Brink, G. Ghiringhelli, N. B. Brookes, and L. Braicovich, *Phys. Rev. B* **85**, 214527 (2012).
  - [75] V. Bisogni, M. Moretti Sala, A. Bendounan, N. B. Brookes, G. Ghiringhelli, and L. Braicovich, *Phys. Rev. B* **85**, 214528 (2012).
  - [76] M. Magnuson, T. Schmitt, and L. C. Duda, *J. Electron Spectros. Relat. Phenomena* **224**, 38 (2018).
  - [77] J. Schlappa, U. Kumar, K. J. Zhou, S. Singh, M. Mourigal, L. Patthey, H. M. Rønnow, S. Johnston, and T. Schmitt, *Nat. Commun.* **9**, 5394 (2018).
  - [78] L. J. P. Ament, M. van Veenendaal, and J. van den Brink, *Europhys. Lett.* **95**, 27008 (2011).
  - [79] J. G. Vale, C. D. Dashwood, E. Paris, L. S. I. Veiga, A. Nag, A. C. Walters, K. J. Zhou, I. Pietsch, A. Jesche, P. Gegenwart, R. C. Oldea, T. Schmitt, and D. F. Mcmorrow, *Phys. Rev. B* **100**, 224303 (2019).
  - [80] X. Lu, P. Olalde-velasco, Y. Huang, V. Bisogni, J. Pelliciari, S. Fatale, M. Dantz, J. G. Vale, E. C. Hunter, J. Chang, V. N. Strocov, R. S. Perry, M. Grioni, D. F. Mcmorrow, H. M. Rønnow, and T. Schmitt, *Phys. Rev. B* **97**, 041102 (2018).
  - [81] P. Abbamonte, L. Venema, A. Rusydi, G. A. Sawatzky, G. Logvenov, and I. Bozovic, *Science* **297**, 581 (2002).
  - [82] P. Abbamonte, A. Rusydi, S. Smadici, G. D. Gu, G. A. Sawatzky, and D. L. Feng, *Nat. Phys.* **1**, 155 (2005).
  - [83] L. Chaix, G. Ghiringhelli, Y. Y. Peng, M. Hashimoto, B. Moritz, K. Kummer, N. B. Brookes, Y. He, S. Chen, S. Ishida, Y. Yoshida, H. Eisaki, M. Salluzzo, L. Braicovich, Z. X. Shen, T. P. Devereaux, and W. S. Lee, *Nat. Phys.* **13**, 952 (2017).

- 
- [84] S. K. Moser, The Nature of the Quasiparticles in Two Benchmark Transition Metal Oxides; A Spectroscopic Study of Anatase  $\text{TiO}_2$  and Tetragonal  $\text{CuO}$ , Ph.D. Thesis, École polytechnique fédérale de Lausanne, 2014.
  - [85] J. J. Yeh and I. Lindau, *At. Data Nucl. Data Tables* **32**, 1 (1985).
  - [86] Y. Y. Peng, G. Dellea, M. Minola, M. Conni, A. Amorese, D. DiCastro, G. M. DeLuca, K. Kummer, M. Salluzzo, X. Sun, X. J. Zhou, G. Balestrino, M. Le Tacon, B. Keimer, L. Braicovich, N. B. Brookes, and G. Ghiringhelli, *Nat. Phys.* **13**, 1201 (2017).
  - [87] M. Minola, Y. Lu, Y. Y. Peng, G. Dellea, H. Gretarsson, M. W. Haverkort, Y. Ding, X. Sun, X. J. Zhou, D. C. Peets, L. Chauviere, P. Dosanjh, D. A. Bonn, R. Liang, A. Damascelli, M. Dantz, X. Lu, T. Schmitt, L. Braicovich, G. Ghiringhelli, B. Keimer, and M. Le Tacon, *Phys. Rev. Lett.* **119**, 097001 (2017).
  - [88] M. Vojta, *Adv. Phys.* **58**, 699 (2009).
  - [89] B. Keimer, S. A. Kivelson, M. R. Norman, S. Uchida, and J. Zaanen, *Nature* **518**, 179 (2014).
  - [90] N. Motoyama, T. Osafune, T. Kakeshita, H. Eisaki, and S. Uchida, *Phys. Rev. B* **55**, R3386 (1997).
  - [91] K. P. Schmidt and G. S. Uhrig, *Mod. Phys. Lett. B* **19**, 1179 (2005).
  - [92] J. M. Tranquada, H. Woo, T. G. Perring, H. Goka, G. D. Gu, G. Xu, M. Fujita, and K. Yamada, *Nature* **429**, 534 (2004).
  - [93] R. M. Noack, S. R. White, and D. J. Scalapino, *Phys. Rev. Lett.* **73**, 882 (1994).
  - [94] D. Poilblanc, H. Tsunetsugu, and T. M. Rice, *Phys. Rev. B* **50**, 6511 (1994).
  - [95] S. Wakimoto, K. Yamada, J. M. Tranquada, C. D. Frost, R. J. Birgeneau, and H. Zhang, *Phys. Rev. Lett.* **98**, 247003 (2007).
  - [96] M. P. M. Dean, G. Dellea, R. S. Springell, K. Kummer, N. B. Brookes, X. Liu, Y. Sun, J. Strle, T. Schmitt, L. Braicovich, G. Ghiringhelli, I. Božović, and J. P. Hill, *Nat. Mater.* **12**, 1019 (2013).
  - [97] T. Osafune, N. Motoyama, H. Eisaki, and S. Uchida, *Phys. Rev. Lett.* **78**, 1980 (1997).
  - [98] Y. Mizuno, S. Maekawa, T. Tohyama, and S. Maekawa, *J. Phys. Soc. Japan* **66**, 937 (1997).
  - [99] N. Nücker, M. Merz, C. A. Kuntscher, S. Gerhold, S. Schuppler, R. Neudert, M. S. Golden, J. Fink, D. Schild, S. Stadler, V. Chakarian, J. Freeland, Y. U. Idzerda, K. Conder, M. Uehara, T. Nagata, J. Goto, J. Akimitsu, N. Motoyama, H. Eisaki, S. Uchida, U. Ammerahl, and A. Revcolevschi, *Phys. Rev. B* **62**, 14384 (2000).
  - [100] A. Rusydi, M. Berciu, P. Abbamonte, S. Smadici, H. Eisaki, Y. Fujimaki, S. Uchida, M. R. Übhausen, and G. A. Sawatzky, *Phys. Rev. B* **75**, 104510 (2007).
  - [101] E. Kabasawa, J. Nakamura, N. Yamada, K. Kuroki, H. Yamazaki, M. Watanabe, J. D. Denlinger, S. Shin, and R. C. C. Perera, *J. Phys. Soc. Japan* **77**, 034704 (2008).
  - [102] M. J. Huang, G. Deng, Y. Y. Chin, Z. Hu, J. G. Cheng, F. C. Chou, K. Conder, J. S. Zhou, T. W. Pi, J. B. Goodenough, H. J. Lin, and C. T. Chen, *Phys. Rev. B* **88**, 014520 (2013).
  - [103] V. Ilakovac, C. Gougoussis, M. Calandra, N. B. Brookes, V. Bisogni, S. G. Chiuzbaian, J. Akimitsu, O. Milat, S. Tomić, and C. F. Hague, *Phys. Rev. B* **85**, 075108 (2012).
  - [104] S. Katano, T. Nagata, J. Akimitsu, M. Nishi, and K. Kakurai, *Phys. Rev. Lett.* **82**, 636 (1999).
  - [105] G. Deng, N. Tsyrlin, P. Bourges, D. Lamago, H. Ronnow, M. Kenzelmann, S. Danilkin, E. P. Omjakushina, and K. Conder, *Phys. Rev. B* **88**, 014504 (2013).
  - [106] K. Magishi, S. Matsumoto, Y. Kitaoka, K. Ishida, and K. Asayama, *Phys. Rev. B* **57**, 11533 (1998).
  - [107] H. Mayaffre, P. Auban-Senzier, M. Nardone, D. Jérôme, D. Poilblanc, C. Bourbonnais, U. Ammerahl, G. Dhalenne, and A. Revcolevschi, *Science* **279**, 345 (1998).
  - [108] T. Nagao and J. I. Igarashi, *Phys. Rev. B* **85**, 224436 (2012).
  - [109] E. Dagotto, *J. Electron Spectros. Relat. Phenomena* **117–118**, 223 (2001).
  - [110] K. I. Kumagai, S. Tsuji, M. Kato, and Y. Koike, *Phys. Rev. Lett.* **78**, 1992 (1997).

- 
- [111] G. Deng, D. M. Radheep, R. Thiyagarajan, E. Pomjakushina, S. Wang, N. Nikseresht, S. Arumugam, and K. Conder, *J. Cryst. Growth* **327**, 182 (2011).
  - [112] W. S. Lee, J. J. Lee, E. A. Nowadnick, S. Gerber, W. Tabis, S. W. Huang, V. N. Strocov, E. M. Motoyama, G. Yu, B. Moritz, H. Y. Huang, R. P. Wang, Y. B. Huang, W. B. Wu, C. T. Chen, D. J. Huang, M. Greven, T. Schmitt, Z. X. Shen, and T. P. Devereaux, *Nat. Phys.* **10**, 883 (2014).
  - [113] K. Ishii, M. Fujita, T. Sasaki, M. Minola, G. Dellea, C. Mazzoli, K. Kummer, G. Ghiringhelli, L. Braicovich, T. Tohyama, K. Tsutsumi, K. Sato, R. Kajimoto, K. Ikeuchi, K. Yamada, M. Yoshida, M. Kurooka, and J. Mizuki, *Nat. Commun.* **5**, 3714 (2014).
  - [114] M. Guarise, B. Dalla Piazza, H. Berger, E. Giannini, T. Schmitt, H. M. Rønnow, G. A. Sawatzky, J. van den Brink, D. Altenfeld, I. Eremin, and M. Grioni, *Nat. Commun.* **5**, 5760 (2014).
  - [115] M. P. M. Dean, A. J. A. James, A. C. Walters, V. Bisogni, I. Jarrige, M. Hücker, E. Giannini, M. Fujita, J. Pelliciari, Y. B. Huang, R. M. Konik, T. Schmitt, and J. P. Hill, *Phys. Rev. B* **90**, 220506 (2014).
  - [116] C. Monney, T. Schmitt, C. E. Matt, J. Mesot, V. N. Strocov, O. J. Lipscombe, S. M. Hayden, and J. Chang, *Phys. Rev. B* **93**, 075103 (2016).
  - [117] D. Meyers, H. Miao, A. C. Walters, V. Bisogni, R. S. Springell, M. D'Astuto, M. Dantz, J. Pelliciari, H. Y. Huang, J. Okamoto, D. J. Huang, J. P. Hill, X. He, I. Božović, T. Schmitt, and M. P. M. Dean, *Phys. Rev. B* **95**, 075139 (2017).
  - [118] O. Ivashko, N. E. Shaik, X. Lu, C. G. Fatuzzo, M. Dantz, P. G. Freeman, D. E. McNally, D. Destraz, N. B. Christensen, T. Kurosawa, N. Momono, M. Oda, C. E. Matt, C. Monney, H. M. Rønnow, T. Schmitt, and J. Chang, *Phys. Rev. B* **95**, 214508 (2017).
  - [119] Y. Y. Peng, E. W. Huang, R. Fumagalli, M. Minola, Y. Wang, X. Sun, Y. Ding, K. Kummer, X. J. Zhou, N. B. Brookes, B. Moritz, L. Braicovich, T. P. Devereaux, and G. Ghiringhelli, *Phys. Rev. B* **98**, 144507 (2018).
  - [120] L. Chaix, E. W. Huang, S. Gerber, X. Lu, C. Jia, Y. Huang, D. E. McNally, Y. Wang, F. H. Vernay, A. Keren, M. Shi, B. Moritz, Z. X. Shen, T. Schmitt, T. P. Devereaux, and W. S. Lee, *Phys. Rev. B* **97**, 155144 (2018).
  - [121] A. Nocera, Y. Wang, N. D. Patel, G. Alvarez, T. A. Maier, E. Dagotto, and S. Johnston, *Phys. Rev. B* **97**, 195156 (2018).
  - [122] U. Kumar, A. Nocera, E. Dagotto, and S. Johnston, *New J. Phys.* **20**, 073019 (2018).
  - [123] G. Deng, V. Pomjakushin, V. Petříček, E. Pomjakushina, M. Kenzelmann, and K. Conder, *Phys. Rev. B* **84**, 144111 (2011).
  - [124] M. Bugnet, S. Löffler, D. Hawthorn, H. A. Dabkowska, G. M. Luke, P. Schattschneider, G. A. Sawatzky, G. Radtke, and G. A. Botton, *Sci. Adv.* **2**, e1501652 (2016).
  - [125] J. Etrillard, M. Braden, A. Gukasov, U. Ammerahl, and A. Revcolevschi, *Phys. C Supercond. Its Appl.* **403**, 290 (2004).
  - [126] J. Zaanen and A. M. Oleå, *Phys. Rev. B* **37**, 9423 (1988).
  - [127] Y. Piskunov, D. Jérôme, P. Auban-Senzier, P. Wzietek, and A. Yakubovsky, *Phys. Rev. B* **72**, 064512 (2005).
  - [128] E. Tafra, B. Korin-Hamzić, M. Basletić, A. Hamzić, M. Dressel, and J. Akimitsu, *Phys. Rev. B* **78**, 155122 (2008).
  - [129] M. Le Tacon, G. Ghiringhelli, J. Chaloupka, M. M. Sala, V. Hinkov, M. W. Haverkort, M. Minola, M. Bakr, K. J. Zhou, C. Monney, Y. T. Song, G. L. Sun, C. T. Lin, G. M. DeLuca, M. Salluzzo, G. Khaliullin, T. Schmitt, L. Braicovich, and B. Keimer, *Nat. Phys.* **7**, 725 (2011).
  - [130] M. Montagnese, M. Otter, X. Zotos, D. A. Fishman, N. Hlubek, O. Mityashkin, C. Hess, R. Saint-martin, S. Singh, A. Revcolevschi, and P. H. M. van Loosdrecht, *Phys. Rev. Lett.* **110**, 147206 (2013).
  - [131] D. Bounoua, L. Mangin-thro, J. Jeong, R. Saint-martin, L. Pinsard-gaudart, Y. Sidis, and P. Bourges, *Commun. Phys.* **3**, 123 (2020).
  - [132] L. J. P. Ament, G. Ghiringhelli, M. M. Sala, L. Braicovich, and J. van den Brink, *Phys. Rev. Lett.* **103**, 117003 (2009).
  - [133] M. W. Haverkort, *Phys. Rev. Lett.* **105**, 167404 (2010).
  - [134] L. Braicovich, M. Moretti Sala, L. J. P. Ament, V. Bisogni, M. Minola, G. Balestrino, D. DiCastro, G. M. DeLuca, M. Salluzzo, G. Ghiringhelli, and J. van den Brink, *Phys. Rev. B* **81**, 174533 (2010).

- 
- [135] F. D. M. Haldane, *J. Phys. C Solid State Phys.* **14**, 2585 (1981).
  - [136] C. Kim, A. Y. Matsuura, Z. X. Shen, N. Motoyama, H. Eisaki, S. Uchida, T. Tohyama, and S. Maekawa, *Phys. Rev. Lett.* **77**, 4054 (1996).
  - [137] B. J. Kim, H. Koh, E. Rotenberg, S. Oh, H. Eisaki, N. Motoyama, S. Uchida, T. Tohyama, S. Maekawa, Z. X. Shen, and C. Kim, *Nat. Phys.* **2**, 397 (2006).
  - [138] J. Li, A. Nag, J. Pelliciari, H. C. Robarts, A. C. Walters, M. Garcia-fernandez, H. Eisaki, D. Song, H. Ding, S. Johnston, R. Comin, and K.-J. Zhou, *Proc Natl Acad Sci* **117**, 16219 (2020).
  - [139] H. Miao, R. Fumagalli, M. Rossi, J. Lorenzana, G. Seibold, F. Yakhov-Harris, K. Kummer, N. B. Brookes, G. D. Gu, L. Braicovich, G. Ghiringhelli, and M. P. M. Dean, *Phys. Rev. X* **9**, 031042 (2019).
  - [140] J. Q. Lin, H. Miao, D. G. Mazzone, G. D. Gu, A. Nag, A. C. Walters, M. García-Fernández, A. Barbour, J. Pelliciari, I. Jarrige, M. Oda, K. Kurosawa, N. Momono, K. J. Zhou, V. Bisogni, X. Liu, and M. P. M. Dean, *Phys. Rev. Lett.* **124**, 207005 (2020).
  - [141] B. Yu, W. Tabis, I. Bialo, F. Yakhov, N. B. Brookes, Z. Anderson, Y. Tang, G. Yu, and M. Greven, *Phys. Rev. X* **10**, 021059 (2020).
  - [142] W. S. Lee, K. J. Zhou, M. Hepting, J. Li, A. Nag, A. C. Walters, H. C. Robarts, M. Hashimoto, H. Lu, B. Nosarzewski, D. Song, H. Eisaki, Z. X. Shen, B. Moritz, J. Zaanen, and T. P. Devereaux, *Nat. Phys.* <https://doi.org/10.1038/s41567> (2020).
  - [143] T. Takahashi, T. Yokoya, A. Ashihara, O. Akaki, H. Fujisawa, and A. Chainani, *Phys. Rev. B* **56**, 7870 (1997).
  - [144] T. Sato, T. Yokoya, T. Takahashi, M. Uehara, T. Nagata, J. Goto, and J. Akimitsu, *J. Phys. Chem Solids* **59**, 1912 (1998).
  - [145] T. Yoshida, X. J. Zhou, Z. Hussain, Z. X. Shen, A. Fujimori, H. Eisaki, and S. Uchida, *Phys. Rev. B* **80**, 052504 (2009).
  - [146] A. Koitzsch, D. S. Inosov, H. Shiozawa, V. B. Zabolotnyy, S. V. Borisenko, A. Varykhalov, C. Hess, M. Knupfer, U. Ammerahl, A. Revcolevschi, and B. Büchner, *Phys. Rev. B* **81**, 113110 (2010).
  - [147] S. Hazra, R. Bag, S. Singh, and R. N. Kini, *J. Phys. Condens. Matter* **32**, 275601 (2020).
  - [148] M. S. Windt, *Optical Spectroscopy of Spin Ladders*, Ph.D. Dissertation, Universität zu Köln, 2002.
  - [149] N. Fujiwara, N. Mori, Y. Uwatoko, T. Matsumoto, N. Motoyama, and S. Uchida, *Phys. Rev. Lett.* **90**, 137001 (2003).
  - [150] Y. Tseng, J. Thomas, W. Zhang, E. Paris, P. Puphal, R. Bag, G. Deng, T. C. Asmara, V. N. Strocov, S. Singh, E. Pomjakushina, U. Kumar, A. Nocera, H. M. Rønnow, S. Johnston, and T. Schmitt, paper submitted.
  - [151] S. Liu, H. C. Jiang, and T. P. Devereaux, *Phys. Rev. B* **94**, 155149 (2016).
  - [152] M. V. Abrashev, C. Thomsen, and M. Surtchev, *Phys. C* **280**, 297 (1997).
  - [153] X. Chen, D. Bansal, S. Sullivan, D. L. Abernathy, A. A. Aczel, J. Zhou, O. Delaire, and L. Shi, *Phys. Rev. B* **94**, 134309 (2016).
  - [154] W. S. Lee, S. Johnston, B. Moritz, J. Lee, M. Yi, K. J. Zhou, T. Schmitt, L. Patthey, V. N. Strocov, K. Kudo, Y. Koike, J. van den Brink, T. P. Devereaux, and Z. X. Shen, *Phys. Rev. Lett.* **110**, 265502 (2013).
  - [155] S. Johnston, C. Monney, V. Bisogni, K. J. Zhou, R. Kraus, G. Behr, V. N. Strocov, J. Málek, S. L. Drechsler, J. Geck, T. Schmitt, and J. van den Brink, *Nat. Commun.* **7**, 10653 (2016).
  - [156] G. Ferkinghoff, M. Leanna, G. S. Uhrig, U. Kumar, and B. Fauseweh, *arXiv* 2012.01513 (2020).
  - [157] M. Powalski, G. S. Uhrig, and K. P. Schmidt, *Phys. Rev. Lett.* **115**, 207202 (2015).
  - [158] M. Powalski, K. P. Schmidt, and G. S. Uhrig, *SciPost Phys.* **4**, 1 (2018).
  - [159] T. Ying, K. P. Schmidt, and S. Wessel, *Phys. Rev. Lett.* **122**, 127201 (2019).
  - [160] G. B. Halász, N. B. Perkins, and J. van den Brink, *Phys. Rev. Lett.* **117**, 127203 (2016).
  - [161] W. M. H. Natori, M. Daghofer, and R. G. Pereira, *Phys. Rev. B* **96**, 125109 (2017).
  - [162] G. B. Halász, S. Kourtis, J. Knolle, and N. B. Perkins, *Phys. Rev. B* **99**, 184417 (2019).

- 
- [163] F. Roth, A. Revcolevschi, B. Büchner, M. Knupfer, and J. Fink, *Phys. Rev. B* **101**, 195132 (2020).
  - [164] J. Lorenzana and G. A. Sawatzky, *Phys. Rev. Lett.* **74**, 1867 (1995).
  - [165] J. Lorenzana and G. A. Sawatzky, *Phys. Rev. B* **52**, 9576 (1995).
  - [166] M. Guarise, B. D. Piazza, M. M. Sala, G. Ghiringhelli, L. Braicovich, H. Berger, J. N. Hancock, D. van der Marel, T. Schmitt, V. N. Strocov, L. J. P. Ament, J. van den Brink, P.-H. Lin, P. Xu, H. M. Rønnow, and M. Grioni, *Phys. Rev. Lett.* **105**, 157006 (2010).
  - [167] K. P. Schmidt, C. Knetter, M. Grüninger, and G. S. Uhrig, *Phys. Rev. Lett.* **90**, 167201 (2003).
  - [168] M. U. Grüninger, *Of Spin and Charge in the Cuprates*, Ph.D. Dissertation, University of Groningen, 1999.
  - [169] M. Windt, M. Grüninger, T. Nunner, C. Knetter, K. P. Schmidt, G. S. Uhrig, T. Kopp, A. Freimuth, U. Ammerahl, B. Büchner, and A. Revcolevschi, *Phys. Rev. Lett.* **87**, 127002 (2001).
  - [170] J. M. Tranquada, B. J. Sternllebt, J. D. Axe, Y. Nakamura, and S. Uchida, *Nature* **375**, 561 (1995).
  - [171] M. Hücker, M. V. Zimmermann, M. Debessai, J. S. Schilling, J. M. Tranquada, and G. D. Gu, *Phys. Rev. Lett.* **104**, 057004 (2010).
  - [172] M. Hücker, M. V. Zimmermann, G. D. Gu, Z. J. Xu, J. S. Wen, G. Xu, H. J. Kang, A. Zheludev, and J. M. Tranquada, *Phys. Rev. B* **83**, 104506 (2011).
  - [173] A. J. Achkar, M. Zwiebler, C. McMahon, F. He, R. Sutarto, I. Djianto, Z. Hao, M. J. P. Gingras, M. Hücker, G. D. Gu, A. Revcolevschi, H. Zhang, Y. J. Kim, J. Geck, and D. G. Hawthorn, *Science* **351**, 576 (2016).
  - [174] Z. Zhang, R. Sutarto, F. He, F. C. Chou, L. Udby, S. L. Holm, Z. H. Zhu, W. A. Hines, J. I. Budnick, and B. O. Wells, *Phys. Rev. Lett.* **121**, 067602 (2018).
  - [175] A. Lanzara, P. V. Bogdanov, X. J. Zhou, S. A. Kellar, D. L. Feng, E. D. Lu, T. Yoshida, H. Eisaki, A. Fujimori, K. Kishio, J.-I. Shimoyama, T. Nodak, S. Uchida, Z. Hussain, and Z.-X. Shen, *Nature* **412**, 510 (2001).
  - [176] R. Comin, A. Frano, M. M. Yee, Y. Yoshida, H. Eisaki, E. Schierle, E. Weschke, R. Sutarto, F. He, A. Soumyanarayanan, Y. He, M. Le Tacon, I. S. Elfimov, J. E. Hoffman, G. A. Sawatzky, B. Keimer, and A. Damascelli, *Science* **343**, 390 (2014).
  - [177] Y. Y. Peng, R. Fumagalli, Y. Ding, M. Minola, S. Caprara, D. Betto, M. Bluschke, G. M. DeLuca, K. Kummer, E. Lefrançois, M. Salluzzo, H. Suzuki, M. Le Tacon, X. J. Zhou, N. B. Brookes, B. Keimer, L. Braicovich, M. Grilli, and G. Ghiringhelli, *Nat. Mater.* **17**, 697 (2018).
  - [178] A. J. Achkar, F. He, R. Sutarto, C. McMahon, M. Zwiebler, M. Hücker, G. D. Gu, R. Liang, D. A. Bonn, W. N. Hardy, J. Geck, and D. G. Hawthorn, *Nat. Mater.* **15**, 616 (2016).
  - [179] M. Kang, J. Pelliciari, A. Frano, N. Breznay, E. Schierle, E. Weschke, R. Sutarto, F. He, P. Shafer, E. Arenholz, M. Chen, K. Zhang, A. Ruiz, Z. Hao, S. Lewin, J. Analytis, Y. Krockenberger, H. Yamamoto, T. Das, and R. Comin, *Nat. Phys.* **15**, 335 (2019).
  - [180] R. Arpaia, S. Caprara, R. Fumagalli, G. De Vecchi, Y. Y. Peng, E. Andersson, D. Betto, G. M. DeLuca, N. B. Brookes, F. Lombardi, M. Salluzzo, L. Braicovich, C. DiCastro, M. Grilli, and G. Ghiringhelli, *Science* **365**, 906 (2019).
  - [181] H. Alloul, J. Bobroff, M. Gabay, *Rev. Mod. Phys.* **81**, 45 (2009).
  - [182] Y. Koike and T. Adachi, *Phys. C Supercond. Its Appl.* **481**, 115 (2012).
  - [183] M. Schmid, F. Loder, A. P. Kampf, and T. Kopp, *New J. Phys.* **15**, 073049 (2013).
  - [184] I. Zeljkovic and J. E. Hoffman, *Phys. Chem. Chem. Phys.* **15**, 13462 (2013).
  - [185] A. Suchaneck, V. Hinkov, D. Haug, L. Schulz, C. Bernhard, A. Ivanov, K. Hradil, C. T. Lin, P. Bourges, B. Keimer, and Y. Sidis, *Phys. Rev. Lett.* **105**, 037207 (2010).
  - [186] R. H. He, M. Fujita, M. Enoki, M. Hashimoto, S. Iikubo, S. K. Mo, H. Yao, T. Adachi, Y. Koike, Z. Hussain, Z. X. Shen, and K. Yamada, *Phys. Rev. Lett.* **107**, 127002 (2011).
  - [187] K. Suzuki, T. Adachi, Y. Tanabe, H. Sato, Y. Ishii, T. Suzuki, I. Watanabe, and Y. Koike, *Phys. Procedia* **30**, 275 (2012).
  - [188] G. Xiao, M. Z. Cieplak, J. Q. Xiao, and C. L. Chien, *Phys. Rev. B* **42**, 8752 (1990).



- 
- [189] R. Bag, K. Karmakar, S. Dhar, M. Tripathi, R. J. Choudhary, and S. Singh, *J. Phys. Condens. Matter* **31**, 035801 (2019).
  - [190] G. De Filippis, V. Cataudella, G. Iadonisi, V. M. Ramaglia, C. A. Perroni, and F. Ventriglia, *Phys. Rev. B* **64**, 155105 (2001).
  - [191] Y. Yildirim and A. Moreo, *Phys. Rev. B* **72**, 134516 (2005).
  - [192] Y. Zhang, C. Lane, J. W. Furness, B. Barbiellini, J. P. Perdew, R. S. Markiewicz, A. Bansil, and J. Sun, *Proc Natl Acad Sci* **117**, 68 (2019).
  - [193] K. Kuroki, T. Higashida, and R. Arita, *Phys. Rev. B* **72**, 212509 (2005).
  - [194] H. Sakamoto and K. Kuroki, *Phys. Rev. Res.* **2**, 22055 (2020).
  - [195] Z. Hiroi, M. Azuma, M. Takano, and Y. Bando, *J. Solid State Chem.* **95**, 230 (1991).
  - [196] G. Campi, A. Bianconi, N. Poccia, G. Bianconi, L. Barba, G. Arrighetti, D. Innocenti, J. Karpinski, N. D. Zhigadlo, S. M. Kazakov, M. Burghammer, M. Sprung, and A. Ricci, *Nature* **525**, 359 (2015).
  - [197] L. Cuo, M. Fratini, N. Poccia, A. Ricci, G. Campi, M. Burghammer, G. Aeppli, and A. Bianconi, *Nature* **466**, 841 (2010).
  - [198] S. Gerber, H. Jang, H. Nojiri, S. Matsuzawa, H. Yasumura, D. A. Bonn, R. Liang, W. N. Hardy, Z. Islam, A. Mehta, S. Song, M. Sikorski, D. Stefanescu, Y. Feng, S. A. Kivelson, T. P. Devereaux, Z. X. Shen, C. C. Kao, W. S. Lee, D. Zhu, and J. S. Lee, *Science* **350**, 949 (2015).
  - [199] J. Chang, E. Blackburn, O. Ivashko, A. T. Holmes, N. B. Christensen, M. Hücker, R. Liang, D. A. Bonn, W. N. Hardy, U. Rütt, M. V. Zimmermann, E. M. Forgan, and S. M. Hayden, *Nat. Commun.* **7**, 1 (2016).
  - [200] H. Jang, W. S. Lee, H. Nojiri, S. Matsuzawa, H. Yasumura, L. Nie, A. V. Maharaj, S. Gerber, Y. J. Liu, A. Mehta, D. A. Bonn, R. Liang, W. N. Hardy, C. A. Burns, Z. Islam, S. Song, J. Hastings, T. P. Devereaux, Z. X. Shen, S. A. Kivelson, C. C. Kao, D. Zhu, and J. S. Lee, *Proc. Natl. Acad. Sci.* **113**, 14645 (2016).
  - [201] J. Choi, O. Ivashko, E. Blackburn, R. Liang, D. A. Bonn, W. N. Hardy, A. T. Holmes, N. B. Christensen, M. Hücker, S. Gerber, O. Gutowski, U. Rütt, M. Zimmermann, E. M. Forgan, S. M. Hayden, and J. Chang, *Nat. Commun.* **11**, 990 (2020).
  - [202] M. Fujita, M. Enoki, and K. Yamada, *J. Phys. Chem. Solids* **69**, 3167 (2008).
  - [203] X. Zuo, J. An, and C. Gong, *Phys. Rev. B* **77**, 212508 (2008).
  - [204] M. Fujita, M. Enoki, S. Iikubo, and K. Yamada, *J. Supercond. Nov. Magn.* **22**, 243 (2009).
  - [205] A. R. Moodenbaugh, Y. Xu, M. Suenaga, T. J. Folkerts, and R. N. Shelton, *Phys. Rev. B* **38**, 4596 (1988).
  - [206] K. Wohlfeld, A. M. Oles, and G. A. Sawatzky, *Phys. C* **462**, 1043 (2007).
  - [207] K. Wohlfeld, A. M. Oles, and G. A. Sawatzky, *Phys. Rev. B* **75**, 180501 (2007).
  - [208] K. Wohlfeld, A. M. Oles, and G. A. Sawatzky, *Phys. Rev. B* **81**, 214522 (2010).
  - [209] H. Miao, J. Lorenzana, G. Seibold, Y. Y. Peng, A. Amorese, K. Kummer, N. B. Brookes, R. M. Konik, V. Thampy, G. D. Gu, G. Ghiringhelli, L. Braicovich, and M. P. M. Dean, *Proc Natl Acad Sci* **114**, 12430 (2017).
  - [210] Q. Wang, M. Horio, K. von Arx, Y. Shen, D. J. Mukkattukavil, Y. Sassa, O. Ivashko, C. E. Matt, S. Pyon, T. Takayama, H. Takagi, T. Kurosawa, N. Momono, M. Oda, T. Adachi, S. M. Haidar, Y. Koike, Y. Tseng, W. Zhang, J. Zhao, K. Kummer, M. Garcia-Fernandez, K.-J. Zhou, N. B. Christensen, H. M. Rønnow, T. Schmitt, and J. Chang, *Phys. Rev. Lett.* **124**, 187002 (2020).
  - [211] G. Ghiringhelli, M. Le Tacon, M. Minola, C. Mazzoli, N. B. Brookes, G. M. DeLuca, A. Frano, D. G. Hawthorn, F. He, T. Loew, M. M. Sala, D. C. Peets, M. Salluzzo, E. Schierle, R. Sutarto, G. A. Sawatzky, E. Weschke, B. Keimer, and L. Braicovich, *Science* **337**, 821 (2012).
  - [212] M. Saarela and F. V. Kusmartsev, *Nanoscience and Engineering in Superconductivity* (Springer US, 2010).
  - [213] R. Bag, K. Karmakar, S. Dhar, M. Tripathi, R. J. Choudhary, and S. Singh, *J. Phys. Condens. Matter* **31**, (2019).
  - [214] S. V. Zaitsev-Zotov, G. Remenyi, and P. Monceau, *Phys. Rev. Lett.* **78**, 1098 (1997).
  - [215] K. Biljaković, M. Miljak, D. Starežinić, J. C. Lasjaunias, P. Monceau, H. Berger, and F. Levy, *Europhys. Lett.* **62**, 554 (2003).

- 
- [216] D. F. Mross and T. Senthil, *Phys. Rev. X* **5**, 031008 (2015).
  - [217] M. Frachet, I. Vinograd, R. Zhou, S. Benhabib, S. Wu, H. Mayaffre, S. Krämer, S. K. Ramakrishna, A. P.R eyes, J. Debray, T. Kurosawa, N. Momono, M. Oda, S. Komiya, S. Ono, M. Horio, J. Chang, C. Proust, D. Leboeuf, and M. Julien, *Nat. Phys.* **16**, 1064 (2020).
  - [218] K. Karmakar, M. Skoulatos, G. Prando, B. Roessli, U. Stuhr, F. Hammerath, C. Rüegg, and S. Singh, *Phys. Rev. Lett.* **118**, 107201 (2017).
  - [219] J. M. Tarascon, P. Barboux, P. F. Miceh, L. H. Greene, G. W. Hull, M. Eibschutz, and S. A. Sunshine, *Phys. Rev. B* **37**, 7458 (1988).
  - [220] D. Haug, V. Hinkov, A. Suchaneck, D. S. Inosov, N. B. Christensen, C. Niedermayer, P. Bourges, Y. Sidis, J. T. Park, A. Ivanov, C. T. Lin, J. Mesot, and B. Keimer, *Phys. Rev. Lett.* **103**, 017001 (2009).
  - [221] T. Wu, H. Mayaffre, S. Krämer, M. Horvatić, C. Berthierl, W. N. Hardy, R. Liang, D. A. Bonn, and M. H. Julien, *Nature* **477**, 191 (2011).
  - [222] J. Chang, E. Blackburn, A. T. Holmes, N. B. Christensen, J. Larsen, J. Mesot, R. Liang, D. A. Bonn, W. N. Hardy, A. Watenphul, M. Zimmermann, E. M. Forgan, and S. M. Hayden, *Nat. Phys.* **8**, 871 (2012).
  - [223] Y. Lin, R. Xiong, N. Hu, L. Wang, Z. Yu, W. Tang, and J. Shi, *Phys. B* **400**, 93 (2007).
  - [224] J. Wang, H. Zou, Y. Li, H. Xie, N. Hu, L. Wang, and J. Shi, *Phys. B* **441**, 6 (2014).
  - [225] F. Licci and L. Raffo, *Supercond. Sci. Technol.* **8**, 245 (1995).
  - [226] R. J. McQueeney, Y. Petrov, T. Egami, M. Yethiraj, G. Shirane, and Y. Endoh, *Phys. Rev. Lett.* **82**, 628 (1999).
  - [227] D. Reznik, L. Pintschovius, M. Ito, S. Iikubo, M. Sato, H. Goka, M. Fujita, K. Yamada, G. D. Gu, and J. M. Tranquada, *Nature* **440**, 1170 (2006).
  - [228] M. Le Tacon, A. Bosak, S. M. Souliou, G. Dellea, T. Loew, R. Heid, K. P. Bohnen, G. Ghiringhelli, M. K. Kirsch, and B. Keimer, *Nat. Phys.* **10**, 52 (2013).
  - [229] H. Miao, D. Ishikawa, R. Heid, M. Le Tacon, G. Fabbri, D. Meyers, G. D. Gu, A. Q. R. Baron, and M. P. M. Dean, *Phys. Rev. X* **8**, 011008 (2018).
  - [230] Q. Wang, K. von Arx, M. Horio, D. J. Mukkattukavil, Y. Sassa, T. Schmitt, A. Nag, S. Pyon, T. Takayama, H. Takagi, M. Garcia-Fernandez, K.-J. Zhou, and J. Chang, *arXiv* 2012.10503 (2020).
  - [231] M. Neeb, J. E. Rubensson, M. Biermann, and W. Eberhardt, *J. Electron Spectros. Relat. Phenomena* **67**, 261 (1994).
  - [232] R. Comin, R. Sutarto, F. He, E. H. da Silva Neto, L. Chauviere, A. Frañó, R. Liang, W. N. Hardy, D. A. Bonn, Y. Yoshida, H. Eisaki, A. J. Achkar, D. G. Hawthorn, B. Keimer, G. A. Sawatzky, and A. Damascelli, *Nat. Mater.* **14**, 796 (2015).
  - [233] Y. K. Wakabayashi, Y. Nonaka, Y. Takeda, S. Sakamoto, K. Ikeda, Z. Chi, G. Shibata, A. Tanaka, Y. Saitoh, H. Yamagami, M. Tanaka, A. Fujimori, and R. Nakane, *Phys. Rev. B* **96**, 104410 (2017).
  - [234] Matthias Hepting, *Ordering Phenomena in Nickelate Heterostructures Studied by Elastic and Inelastic Photon Scattering*, Ph.D. Dissertation, University of Stuttgart, 2016.
  - [235] S. H. Chun, J. W. Kim, J. Kim, H. Zheng, C. C. Stoumpos, C. D. Malliakas, J. F. Mitchell, K. Mehlawat, Y. Singh, Y. Choi, T. Gog, A. Al-Zein, M. M. Sala, M. Krisch, J. Chaloupka, G. Jackeli, G. Khaliullin, and B. J. Kim, *Nat. Phys.* **11**, 462 (2015).
  - [236] S. Middey, D. Meyers, D. Doennig, M. Kareev, X. Liu, Y. Cao, Z. Yang, J. Shi, L. Gu, P. J. Ryan, R. Pentcheva, J. W. Freeland, and J. Chakhalian, *Phys. Rev. Lett.* **116**, 056801 (2016).
  - [237] M. Gibert, P. Zubko, R. Scherwitsl, J. Íñiguez, and J.-M. Triscone, *Nat. Mater.* **11**, 195 (2012).
  - [238] T. H. Kim, D. Puggioni, Y. Yuan, L. Xie, H. Zhou, N. Campbell, P. J. Ryan, Y. Choi, J. W. Kim, J. R. Patzner, S. Ryu, J. P. Podkaminer, J. Irwin, Y. Ma, C. J. Fennie, M. S. Rzchowski, X. Q. Pan, V. Gopalan, J. M. Rondinelli, and C. B. Eom, *Nature* **533**, 68 (2016).
  - [239] V. Bisogni, S. Catalano, R. J. Green, M. Gibert, R. Scherwitsl, Y. Huang, V. N. Strocov, P. Zubko, S. Balandeh, J.-M. Triscone, G. Sawatzky, and T. Schmitt, *Nat. Commun.* **7**, 13017 (2016).

- 
- [240] D. E. McNally, S. Catalano, J. Pellicciari, M. Gibert, E. Paris, Y. Tseng, V. N. Strocov, J.-M. Triscone, S. Johnston, and T. Schmitt, paper submitted.
  - [241] S. K. Karna, Y. Zhao, R. Sankar, M. Avdeev, P. C. Tseng, C. W. Wang, G. J. Shu, K. Matan, G. Y. Guo, and F. C. Chou, *Phys. Rev. B* **95**, 104408 (2017).
  - [242] Y. Itoh, *J. Phys. Soc. Japan* **84**, 064714 (2015).
  - [243] R. Sankar, G. J. Shu, B. Karunakara Moorthy, R. Jayavel, and F. C. Chou, *Dalt. Trans.* **42**, 10439 (2013).
  - [244] A. Ghosh, K. H. Chen, X. S. Qiu, S. H. Hsieh, Y. C. Shao, C. H. Du, H. T. Wang, Y. Y. Chin, J. W. Chiou, S. C. Ray, H. M. Tsai, C. W. Pao, H. J. Lin, J. F. Lee, R. Sankar, F. C. Chou, and W. F. Pong, *Sci. Rep.* **8**, 15779 (2018).
  - [245] F. M. F. de Groot, P. Kuiper, and G. A. Sawatzky, *Phys. Rev. B* **57**, 14584 (1998).
  - [246] G. Ghiringhelli, A. Piazzalunga, X. Wang, A. Bendounan, H. Berger, F. Bottegoni, N. B. Christensen, C. Dallera, M. Grioni, J.-C. Grivel, M. M. Sala, L. Patthey, J. Schlappa, T. Schmitt, V. N. Strocov, and L. Braicovich, *Eur. Phys. J. Spec. Top.* **205**, 199 (2009).
  - [247] Y. Tokura and N. Nagaosa, *Science* **288**, 462 (2000).
  - [248] W. Eerenstein, N. D. Mathur, and J. F. Scott, *Nature* **442**, 759 (2006).
  - [249] J. H. Lee, L. Fang, E. Vlahos, X. Ke, Y. W. Jung, L. F. Kourkoutis, J. W. Kim, P. J. Ryan, T. Heeg, M. Roeckerath, V. Goian, M. Bernhagen, R. Uecker, P. C. Hammel, K. M. Rabe, S. Kamba, J. Schubert, J. W. Freeland, D. A. Muller, C. J. Fennie, P. Schiffer, V. Gopalan, E. Johnston-Halperin, and D. G. Schlom, *Nature* **466**, 954 (2010).
  - [250] M. Mochizuki, N. Furukawa, and N. Nagaosa, *Phys. Rev. B* **84**, 144409 (2011).
  - [251] C. Calero, E. M. Chudnovsky, and D. A. Garanin, *Phys. Rev. Lett.* **95**, 166603 (2005).
  - [252] X. Moya and N. D. Mathur, *Nat. Mater.* **16**, 784 (2017).
  - [253] J. S. Lee, T. W. Noh, J. S. Bae, I. S. Yang, T. Takeda, and R. Kanno, *Phys. Rev. B* **69**, 214428 (2004).
  - [254] A. B. Sushkov, O. Tchernyshyov, W. Ratcliff, S. W. Cheong, and H. D. Drew, *Phys. Rev. Lett.* **94**, 137202 (2005).
  - [255] Y. Vinkler-Aviv and A. Rosch, *Phys. Rev. X* **8**, 031032 (2018).
  - [256] M. Ye, G. B. Halász, L. Savary, and L. Balents, *Phys. Rev. Lett.* **121**, 147201 (2018).
  - [257] A. Metavitsiadis and W. Brenig, *Phys. Rev. B* **101**, 035103 (2020).
  - [258] M. Ye, R. M. Fernandes, and N. B. Perkins, *Phys. Rev. Res.* **2**, 033180 (2020).
  - [259] A. Glamazda, P. Lemmens, S.-H. Do, Y. S. Choi, and K.-Y. Choi, *Nat. Commun.* **7**, 12286 (2016).
  - [260] J. Nasu, J. Yoshitake, and Y. Motome, *Phys. Rev. Lett.* **119**, 127204 (2017).
  - [261] F. T. Huang, M. W. Chu, G. J. Shu, H. S. Sheu, C. H. Chen, L. K. Liu, P. A. Lee, and F. C. Chou, *Phys. Rev. B* **79**, 014413 (2009).
  - [262] K. Momma and F. Izumi, *J. Appl. Crystallogr.* **44**, 1272 (2011).
  - [263] G. Ghiringhelli, A. Piazzalunga, C. Dallera, T. Schmitt, V. N. Strocov, J. Schlappa, L. Patthey, X. Wang, H. Berger, and M. Grioni, *Phys. Rev. Lett.* **102**, 027401 (2009).
  - [264] H. M. Hollmark, K. Maher, I. Saadoune, T. Gustafsson, K. Edström, and L. C. Duda, *Phys. Chem. Chem. Phys.* **13**, 6544 (2011).
  - [265] L. C. Duda, T. Schmitt, M. Magnuson, J. Forsberg, A. Olsson, J. Nordgren, K. Okada, and A. Kotani, *Phys. Rev. Lett.* **96**, 067402 (2006).
  - [266] V. I. Anisimov, P. Kuiper, and J. Nordgren, *Phys. Rev. B* **50**, 8257 (1994).
  - [267] V. Kumar, A. Gupta, and S. Uma, *Dalt. Trans.* **42**, 14992 (2013).
  - [268] S. Johnston, F. Vernay, B. Moritz, Z. X. Shen, N. Nagaosa, J. Zaanen, and T. P. Devereaux, *Phys. Rev. B* **82**, 064513 (2010).

- 
- [269] Z. Xiong, T. Datta, and D.-X. Yao, *npj Quantum Mater.* **5**, 78 (2020).
- [270] S. Skiadopoulou, F. Borodavka, C. Kadlec, F. Kadlec, M. Retuerto, Z. Deng, M. Greenblatt, and S. Kamba, *Phys. Rev. B* **95**, 184435 (2017).
- [271] L. Ament, *Resonant Inelastic X-Ray Scattering Studies of Elementary Excitations*, Ph.D. Thesis, Leiden University, 2010.
- [272] L. Braicovich, M. Rossi, R. Fumagalli, Y. Peng, Y. Wang, R. Arpaia, D. Betto, G. M. DeLuca, D. DiCastro, K. Kummer, M. M. Sala, M. Pagetti, G. Balestrino, N. B. Brookes, M. Salluzzo, S. Johnston, J. van den Brink, and G. Ghiringhelli, *Phys. Rev. Res.* **2**, 023231 (2020).
- [273] J. Knolle and R. Moessner, *Annu. Rev. Condens. Matter Phys.* **10**, 451 (2019).
- [274] G. Baskaran, S. Mandal, and R. Shankar, *Phys. Rev. Lett.* **98**, 247201 (2007).
- [275] J. Knolle, D. L. Kovrizhin, J. T. Chalker, and R. Moessner, *Phys. Rev. Lett.* **112**, 207203 (2014).
- [276] J. Knolle, G. W. Chern, D. L. Kovrizhin, R. Moessner, and N. B. Perkins, *Phys. Rev. Lett.* **113**, 187201 (2014).
- [277] D. Schmidiger, S. Mühlbauer, A. Zheludev, P. Bouillot, T. Giamarchi, C. Kollath, G. Ehlers, and A. M. Tsvelik, *Phys. Rev. B* **88**, 094411 (2013).
- [278] N. J. Robinson, A. Altland, R. Egger, N. M. Gergs, W. Li, D. Schuricht, A. M. Tsvelik, A. Weichselbaum, and R. M. Konik, *Phys. Rev. Lett.* **122**, 27201 (2019).
- [279] J. Kim, J. Chaloupka, Y. Singh, J. W. Kim, B. J. Kim, D. Casa, J. Kim, A. Said, X. Huang, and T. Gog, *Phys. Rev. X* **10**, 021034 (2020).
- [280] M. Rossi, R. Arpaia, R. Fumagalli, M. M. Sala, D. Betto, K. Kummer, G. M. DeLuca, J. van den Brink, M. Salluzzo, N. B. Brookes, L. Braicovich, and G. Ghiringhelli, *Phys. Rev. Lett.* **123**, 027001 (2019).
- [281] A. Geondzhian and K. Gilmore, *Phys. Rev. B* **101**, 214307 (2020).
- [282] K. Bieniasz, S. Johnston, and M. Berciu, *arXiv* 2011.05400 (2020).



# Curriculum Vitae

Yi Tseng

Born January 23<sup>rd</sup> 1992, Taipei, Taiwan

## EMPLOYMENT HISTORY

- 04.2017-04.2021: PhD student, **Group of Spectroscopy of Novel Materials (SNM)** in **Swiss Light Source (SLS)**, **Photon Science Division, Paul Scherrer Institut (PSI)**, Villigen, Switzerland (Supervisor: Dr. Thorsten Schmitt)
- 04.2017-04.2021: PhD student, **Laboratory of Quantum Magnetism (LQM)**, **Ecole Polytechnique Fédérale de Lausanne (EPFL)**, Lausanne, Switzerland (Supervisor: Prof. Henrik M. Rønnow)
- 09.2014-08.2016: Master student, Nanomagnetism Laboratory, National Taiwan University, Taipei, Taiwan (Supervisor: Prof. Minn-Tsong Lin)
- 07.2013-08.2013: Undergraduate intern, Advanced Materials and Electronic Structure Laboratory (AMES) in Taiwan Light Source (TLS), National Synchrotron Radiation Research Center (NSRRC), Hsinchu, Taiwan (Supervisor: Prof. Chung-Li Dong and Dr. Ting-Shan Chan)

## EDUCATION

- 2017-2021: PhD, Laboratory of Quantum Magnetism (LQM), Ecole Polytechnique Fédérale de Lausanne (EPFL), Lausanne, Switzerland, "Resonant inelastic X-ray studies of low-dimensional and frustrated 3d transition-metal oxides"
- 2014-2016: M. Sc. Physics, Nanomagnetism Laboratory, National Taiwan University, Taipei, Taiwan, "Surface characterization of 3D Dirac semimetal  $\text{Cd}_3\text{As}_2$  using scanning tunneling microscopy and first-principles calculation"
- 2010-2014: B. Sc. Mechanical Engineering, National Taiwan University, Taipei, Taiwan
- 2007-2010: Wu-Ling Senior High School, Taoyuan, Taiwan

## TEACHING EXPERIENCE

- 09.2020-12.2020: Assistance in supervision, Master semester project of Gabriele Domaine, "Resonant inelastic X-ray scattering study on magnetic van der Waals' materials  $\text{MPS}_3$ "
- 02.2015-06.2015: Teaching assistance, "Nanoscience Lab(I)", National Taiwan University (Lecturer: Prof. Pi-Tai Chou)

## AWARDS

- 2015: BenQ Materials Corp. Research Scholarship

## PUBLICATIONS

### In preparation

- **Y. Tseng**, E. Paris, K. P. Schmidt, W. Zhang, T. C. Asmara, R. Bag, V. N. Strocov, S. Singh, J. Schlappa, H. M. Rønnow, and T. Schmitt, *Spectroscopic fingerprint of multi-tripion and holon-spinon excitations in the lightly hole-doped ladders  $\text{Sr}_{14}\text{Cu}_{24}\text{O}_{41}$* .
- **Y. Tseng**, E. Paris, W. Zhang, R. Bag, T. C. Asmara, V. N. Strocov, S. Singh, H. M. Rønnow, and T. Schmitt, *Enhanced charge-stripe order and soft-phonon anomalies with magnetic impurities in the chain-ladder cuprates  $\text{Sr}_{14}(\text{Cu},\text{Co})_{24}\text{O}_{41}$* .
- **Y. Tseng**, W. Zhang, E. Paris, T. C. Asmara, P. Puphal, V. N. Strocov, E. Pomjakushina, R. Sankar, F.-C. Chou, H. M. Rønnow, and T. Schmitt, *Probing the spin-orbital structure and electron-phonon coupling in the layered antiferromagnetic honeycomb nickelate  $\text{Na}_2\text{Ni}_2\text{TeO}_6$* .
- **Y. Tseng**, J. Thomas, W. Zhang, E. Paris, P. Puphal, R. Bag, G. Deng, T. C. Asmara, V. N. Strocov, S. Singh, E. Pomjakushina, U. Kumar, A. Nocera, H. M. Rønnow, S. Johnston, and T. Schmitt, *Crossover of the high-energy spin fluctuations from collective triplons to localized magnetic excitations in doped  $\text{Sr}_{14-x}\text{Ca}_x\text{Cu}_{24}\text{O}_{41}$  cuprate ladders*.

- X. Lu, W. Zhang, **Y. Tseng**, R. Liu, Z. Tao, E. Paris, D. E. McNally, P. Liu, T. Chen, R. Yu, Q. Si, P. Dai, and T. Schmitt, *Magnetic excitations in the nematic state of detwinned FeSe*.
- D. E. McNally, S. Catalano, J. Pelliciari, M. Gibert, E. Paris, C. Dominguez, **Y. Tseng**, V. N. Strocov, J.-M. Trsicone, S. Johnston, and T. Schmitt, *Evolution of the electron-phonon interactions across the metal-insulator transition of rare-earth nickelate*.
- E. Paris, W. Zhang, **Y. Tseng**, A. Efimenko, V. Favre, V. Strocov, K. Rolfs, T. Shang, M. Medarde, E. Pomjakushina, H. M. Rønnow, M. Radović, and T. Schmitt, *Evidence for short-range antiferromagnetic interactions in the elementary excitation spectrum of SrIrO<sub>3</sub>*.
- Y. Song, W. Wang, E. Paris, X. Lu, J. Pelliciari, **Y. Tseng**, Y. Huang, D. E. McNally, M. Dantz, C. Cao, R. Yu, R. J. Birgeneau, T. Schmitt, and P. Dai, *Spin dynamics in NaFeAs and NaFe<sub>0.53</sub>Cu<sub>0.47</sub>As probed by resonant inelastic X-ray scattering*.
- E. Paris\*, C. W. Nicholson\*, S. Johnston, **Y. Tseng**, M. Rumo, G. Coslovich, S. Zohar, M.-F. Lin, V. N. Strocov, R. Saint-Martin, A. Revcolevschi, A. Kemper, W. Schlotter, G. Dakovski, C. Monney, and T. Schmitt, *Probing the interplay between lattice dynamics and short-range magnetic correlations with femtosecond RIXS*.

Accepted (\* represents equal contribution)

- R. Gaina\*, C. W. Nicholson\*, M. Rumo, S. Sarkar, J. Khmaladze, E. Paris, **Y. Tseng**, W. Zhang, T. C. Asmara, D. E. McNally, C. Piamonteze, E. Weschke, T. Schmitt, C. Monney, and C. Bernhard, *Long-ranged Cu-based order with d<sub>z<sup>2</sup></sub> orbital character at a YBa<sub>2</sub>Cu<sub>3</sub>O<sub>7</sub>/manganite interface*, accepted in npj Quantum Materials.

Published (\* represents equal contribution)

- K. von Arx, F. Forte, M. Horio, V. Granata, Q. Wang, L. Das, Y. Sassa, R. Fittipaldi, C. G. Fatuzzo, O. Ivashko, **Y. Tseng**, E. Paris, A. Vecchione, T. Schmitt, M. Cuoco, and J. Chang, *Resonant inelastic X-ray scattering study of Ca<sub>3</sub>Ru<sub>2</sub>O<sub>7</sub>*, Phys. Rev. B **102**, 235104 (2020).
- E. Paris\*, **Y. Tseng**\*, E. M. Pärshcke\*, W. Zhang, M. H. Upton, A. Efimenko, K. Rolfs, D. E. McNally, L. Maurel, M. Naamneh, M. Caputo, V. N. Strocov, Z. Wang, D. Casa, C. Schneider, E. Pomjakushina, K. Wohlfeld, M. Radović, and T. Schmitt, *Strain engineering of the charge and spin-orbital interactions in Sr<sub>2</sub>IrO<sub>4</sub>*, PNAS **117**, 24764 (2020).
- Q. Wang, M. Horio, K. von Arx, Y. Shen, D. Mukkattukavil, Y. Sassa, O. Ivashko, C. E. Matt, S. Pyon, T. Takayama, H. Takagi, T. Kurosawa, N. Momono, M. Oda, T. Adachi, **Y. Tseng**, W. Zhang, J. Zhao, K. Kummer, M. Garcia-Fernandez, K.-J. Zhou, N. B. Christensen, H. M. Rønnow, T. Schmitt, and J. Chang, *High-temperature charge-stripe correlations in La<sub>1.675</sub>Eu<sub>0.2</sub>Sr<sub>0.125</sub>CuO<sub>4</sub>*, Phys. Rev. Lett. **124**, 187002 (2020).
- S. Parchenko\*, E. Paris\*, D. E. McNally, E. Abreu, M. Dantz, E. M. Bothschafter, A. H. Reid, W. F. Schlotter, M.-F. Lin, S. F. Wandel, G. Coslovich, S. Zohar, G. L. Dakovski, J. J. Turner, S. Möller, **Y. Tseng**, M. Radović, C. Saathe, M. Agaaker, J. E. Nordgreen, S. L. Johnson, T. Schmitt, and U. Staub, *Orbital dynamics during an ultrafast insulator to metal transition*, Phys. Rev. Research **2**, 023110 (2020).
- M. Hepting, D. Li, C. J. Jia, H. Lu, E. Paris, **Y. Tseng**, X. Feng, M. Osada, E. Been, Y. Hikita, Y.-D. Chuang, Z. Hussain, K.-J. Zhou, A. Nag, M. Garcia-Fernandez, M. Rossi, H.-Y. Huang, D.-J. Huang, Z.-X. Shen, T. Schmitt, H. Y. Hwang, B. Moritz, J. Zaanen, T. P. Devereaux, and W.-S. Lee, *Electronic structure of the parent compound of superconducting infinite-layer nickelates*, Nat. Mater **19**, 381 (2020).
- H. Elnaggar, R. Wang, S. Lafuerza, E. Paris, A. C. Komarek, H. Guo, **Y. Tseng**, D. E. McNally, F. Frati, M. W. Haverkort, M. Sikora, T. Schmitt, and F. M. F. de Groot, *Possible absence of trimeron correlations above the Verwey temperature in Fe<sub>3</sub>O<sub>4</sub>*, Phys. Rev. B **101**, 085017 (2020).
- H. Elnaggar, R. Wang, S. Lafuerza, E. Paris, **Y. Tseng**, D. E. McNally, A. C. Komarek, M. W. Haverkort, M. Sikora, T. Schmitt, and F. M. F. de Groot, *Magnetic contrast at spin-flip excitations: An advanced X-ray spectroscopy tool to study magnetic ordering*, ACS Appl. Mater. Interfaces **11**, 36213 (2019).
- O. Ivashko\*, M. Horio\*, W. Wan, N. B. Christensen, D. E. McNally, E. Paris, **Y. Tseng**, N. E. Shaik, H. M. Rønnow, H. I. Wei, C. Adamo, M. Gibert, K. M. Shen, J. M. Tomczak, T. Schmitt, and J. Chang, *Strain-engineering Mott-insulating La<sub>2</sub>CuO<sub>4</sub>*, Nat. Commun. **10**, 786 (2019).
- S. Kang, **Y. Tseng**, B. H. Kim, S. Yun, B. Sohn, B. Kim, D. E. McNally, E. Paris, C. H. Kim, C. Y. Kim, T. W. Noh, S. Ishihara, T. Schmitt, and J.-G. Park, *Orbital-selective confinement effect of Ru 4d orbitals in SrRuO<sub>3</sub> ultrathin film*, Phys. Rev. B **99**, 045113 (2019).
- L. Das, F. Forte, R. Fittipaldi, C. G. Fatuzzo, V. Granata, O. Ivashko, M. Horio, F. Schindler, M. Dantz, **Y. Tseng**, D. E. McNally, H. M. Rønnow, W. Wan, N. B. Christensen, J. Pelliciari, P. Olalde-Velasco, N. Kikugawa, T. Neupert, A. Vecchione, T. Schmitt, M. Cuoco, and J. Chang, *Spin-orbital excitations in Ca<sub>2</sub>RuO<sub>4</sub> revealed by resonant inelastic X-ray scattering*, Phys. Rev. X **8**, 011048 (2018).

- C. J. Butler, Y.-M. Wu, C.-R. Hsing, **Y. Tseng**, R. Sankar, C.-M. Wei, F.-C. Chou, and M.-T. Lin, *Quasiparticle interference in ZrSiS: Strongly band-selective scattering depending on impurity lattice site*, Phys. Rev. B **96**, 196125 (2017).
- C. J. Butler\*, **Y. Tseng\***, C.-R. Hsing, Y.-M. Wu, R. Sankar, M.-F. Wang, C.-M. Wei, F.-C. Chou, and M.-T. Lin, *Observation of surface superstructure induced by systematic vacancies of topological Dirac semimetal Cd<sub>3</sub>As<sub>2</sub>*, Phys. Rev. B **95**, 081410(R) (2017).

## CONFERENCES

- Photon Science Division (PSD) Mini-Symposia 2019; Contributed talk in X-ray scattering session, *Doping evolution of the spin dynamics in two-leg spin ladders probed by resonant inelastic X-ray scattering*; 2019 December 10; Villigen PSI, Switzerland.
- 10th New Generation in Strongly Correlated Electron Systems (NGSCES); Contributed talk in RIXS session, *Electronic and magnetic tuning of charge order and phonon anomaly in a cuprate spin ladder*; 2019 September 2-6, Pescara, Italy.
- Joint Annual Meeting of Swiss Physical Society (SPS) and Austrian Physical Society (APS) 2019; Contributed talk in MaNEP session, *Electronic and magnetic tuning of charge order and phonon anomaly in a cuprate spin ladder*; 2019 August 26-30, Zürich, Switzerland.
- Emergent Phenomena in Correlated Quantum Matter Summer School 2019; Poster presentation, *Electronic and magnetic tuning of charge order and phonon anomaly in the cuprate spin ladder Sr<sub>14</sub>(Cu<sub>1-x</sub>Co<sub>x</sub>)<sub>24</sub>O<sub>41</sub>*; 2019 August 5-17, Cargèse, Corsica.
- The 40th International Conference on Vacuum Ultraviolet and X-ray Physics (VUVX); Contributed talk in Electronic session, *Electronic and magnetic tuning of charge order and phonon anomaly in a cuprate spin ladder*; 2019 July 1-5, San Francisco, United States of America.
- Swiss Physical Society (SPS) Annual Meeting 2020; Contributed talk in Condensed Matter Physics (KOND) session, *Manipulating the spin and hole dynamics in the spin ladder of Co doped Sr<sub>14</sub>Cu<sub>24</sub>O<sub>41</sub>*; 2018 August 28-31, Lausanne, Switzerland.
- 2018 Swiss Workshop on Materials with Novel Electronic Properties (MaNEP); Poster presentation at Quantum and mesoscopic magnetism session, *Manipulating the spin and hole dynamics in the spin ladder of Co doped Sr<sub>14</sub>Cu<sub>24</sub>O<sub>41</sub>*; 2018 August 29-31; Les Diablerets, Switzerland.
- 2018 Workshop, Group of Spectroscopy on Novel Materials; Contributed talk, *Co impurity modification of the magnetic correlation in the spin ladder Sr<sub>14</sub>Cu<sub>24</sub>O<sub>41</sub>*; 2018 January 16-20; Saas-Grund, Switzerland.
- 2nd PSI Condensed Matter Retreat; Poster presentation at Quantum Magnetism session, *Co impurity modification of the magnetic correlation in the spin ladder Sr<sub>14</sub>Cu<sub>24</sub>O<sub>41</sub>*; 2017 November 15-16; Windisch, Switzerland.
- Annual Meeting of the Physical Society of the Republic of China; Poster presentation at Surface Science session, *Atomically Resolved Surface Study of Three-Dimensional Dirac Semimetal Cadmium Arsenide*; 2016 January 25-27; Kaohsiung, Taiwan.
- Joint Seminar of Korea University and National Taiwan University; Poster presentation at Surface Science session, *Atomically Resolved Surface Study of Three-Dimensional Dirac Semimetal Cadmium Arsenide*; 2016 January 19-21; Taipei, Taiwan.